UNIVERSITÀ DEGLI STUDI DI MODENA E REGGIO EMILIA
Dipartimento di Ingegneria "Enzo Ferrari"

International Doctorate in Information and Communication Technologies

XXXIV Cycle

Mathematical Modeling Control and Simulation of Hybrid Electric Vehicles

---

Candidate: Davide Tebaldi

Advisor: Prof. Laura Giarré

Co-Advisor: Prof. Roberto Zanasi

Director of the PhD school: Prof. Sonia Bergamaschi

Contents

Abstract

English: This work of thesis deals with the mathematical modeling, control and simulation of Hybrid Electric Vehicles. First, the classification and description of the main architectures for Hybrid Electric Vehicles are carried out, highlighting pros and cons of the different architectures. The modeling is performed exploiting the properties of the Power-Oriented Graphs modeling technique. Among all the involved physical elements, particular attention is given to the modeling of planetary gear sets, multilevel flying-capacitor converters and permanent magnet synchronous motors. As far as planetary gear sets are concerned, a systematic procedure has been developed for the systematic modeling of any planetary gear set using a unified approach. The proposed procedure allows to obtain two models of the system: a full elastic model, representing a more detailed modeling of the considered planetary gear set accounting for the gears elastic contact points, and a reduced-order model allowing to use fixed-step solvers with a larger simulation step size, which is more suitable for real-time execution. As for multilevel flying-capacitor converters, a compact model is proposed. Next, a robustness assessment when the converter is controlled using a classical minimum distance control is performed, and a new variable-step control strategy allowing to guarantee capacitors voltages balancing is proposed. For what concerns permanent magnet synchronous motors, a power-oriented model is proposed, together with its efficiency analysis based on which model parameters estimation can be performed starting from the motor efficiency map. Some Hybrid Electric Vehicle architectures in the agricultural and construction fields are then proposed as case studies, and a solution for the energy management problem is studied for all of them. Finally, simulation results for each Hybrid Electric

Vehicle architecture are reported and commented in detail.

Italian: Questo lavoro di tesi tratta la modellistica matematica, il controllo e la simulazione di Veicoli Ibridi Elettrici. Innanzitutto, la classificazione e la descrizione delle principali architetture per Veicoli Ibridi Elettrici vengono effettuate, mettendo in evidenza vantaggi e svantaggi delle diverse architetture. La modellistica viene affrontata sfruttando le proprietà della tecnica Power-Oriented Graphs. Fra tutti gli elementi fisici coinvolti, particolare attenzione viene data alla modellistica di planetary gear sets, convertitori multilivello flying-capacitor e motori sincroni a magneti permanenti. Per quanto riguarda le planetary gear sets, una procedura sistematica è stata sviluppata per modellare qualunque planetary gear set utilizzando un approccio unificato. La procedura proposta consente di ottenere due modelli del sistema: un modello intero elastico, che fornisce una modellistica più dettagliata della planetary gear set in esame prendendo in considerazione i punti di contatto elastici fra le ruote dentate, ed un modello ridotto che consente di utilizzare solutori a passo fisso con un passo di simulazione più lungo, quest'ultimo più adatto per l'esecuzione in tempo reale. Per quanto riguarda i convertitori multilivello flying-capacitor, un modello compatto viene proposto. Dopodichè, una valutazione della robustezza del convertitore quando questo è controllato utilizzando un controllo classico a minima distanza viene effettuata, ed una nuova tecnica di controllo che consente di mantenere le tensioni ai capi dei condensatori ai livelli desiderati viene proposta. Per quanto riguarda i motori sincroni a magneti permanenti, un modello power-oriented viene proposto, insieme ad un'analisi di efficienza grazie alla quale una stima dei parametri del modello può essere effettuata partendo dalla mappa di efficienza del motore. Alcune architetture di Veicoli Ibridi Elettrici nei settori agricolo e delle costruzioni vengono poi proposte come casi studio, ed una soluzione per l'energy management problem viene studiata per ciascuna di esse. Infine, i risultati di simulazione per ciascuna architettura vengono riportati e commentati nel dettaglio.

Introduction

The modern trend in the development of new road transportation systems is strongly oriented towards the hybridization of propulsion systems, since this represents the most promising solution allowing to limit the exhaust emissions. This trend holds both in the agricultural, construction and in the automotive fields, as conceptually shown in Fig. 1. The term hybrid vehicle refers to a vehicle equipped with more than one type of energy source, which can be endothermic, electric, hydraulic, etc. Out of the different types of hybrid vehicles, strong interest resides in Hybrid Electric Vehicles (HEVs), thanks to the high efficiency they provide and to the strong development of new technologies for batteries in recent years. A vehicle can be seen as a complex physical system, composed of several physical subsystems interacting with each other. An overview of the main subsystems that can be found in a HEV is given in Fig. 2. The Gear Mesh system describes a gearing system that introduces a constant or time variant (i.e. a gearbox, enabling gearshifting) reduction ratio [1] between the input and the output shafts. The Energy Storage subsystem represents the device which is responsible for storing electrical energy in the vehicle, which can be a battery or a supercapacitor. A Planetary Gear Set (PGS) is a three to n

Figure 1: Transition towards hybridization in different transportation fields.

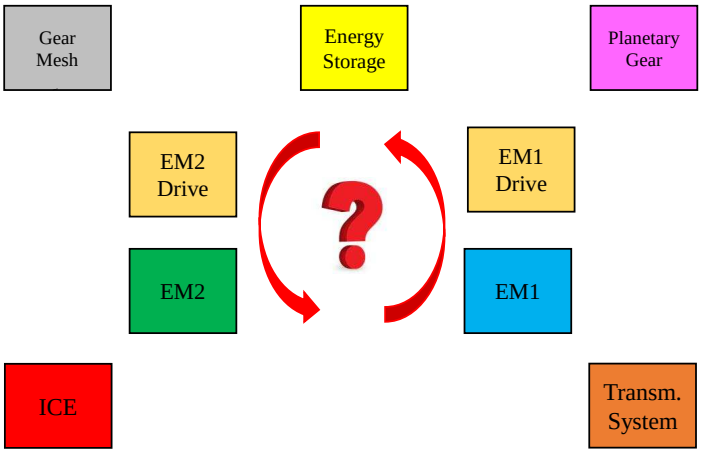

Figure 2: Typical subsystems composing a Hybrid Electric Vehicle.

energetic ports device enabling power-splitting and Electro Continuously Variable Transmission (ECVT) functionalities in Power-Split HEVs. The EM1 and EM2 subsystems describe the electric machines present on board the HEV, which are typically either two or more. The EM1 Drive and EM2 Drive subsystems describe the power electronics which is needed to drive the electric machines, namely the inverter. The ICE system is the one containing the Internal Combustion Engine, which is the main source of energy on board the vehicle. The Transm. System block is the one containing the vehicle transmission system from the output of the transmission shaft all the way down to the vehicle wheels. The red question mark in the figure highlights that the connection of these subsystems with each other depends on the considered vehicle architecture. The classification of HEVs on the basis of the vehicle architecture is quite important especially at system level, since it highlights how the power sources mounted on the vehicle are arranged in order to satisfy the transmission power demand. This classification is addressed in detail in Chap. 2, together with the description of the main advantages and disadvantages offered by the different HEVs architectures.

Once the most suitable architecture has been identified depending on the purpose, the modeling step has to be addressed. Modeling a vehicle architecture is an essential part, as it enables the simulation, testing and performance evaluation of the vehicle before its physical production. In order to obtain a good model

describing the dynamics of the whole vehicle, the mathematical modeling of the different physical subsystems composing it needs to be addressed. There are several approaches in the literature for modeling physical systems, which typically vary depending on the considered system. In this work, the modeling has been performed using the Power-Oriented Graphs (POG) modeling technique [2]-[3]. The latter is a graphical formalism which is very useful for describing the systems dynamic model, as it allows to build block schemes which are directly implementable in the Matlab/Simulink environment and also allows to maintain an excellent control on the power flows within the system [4]. The main properties and characteristics of the main graphical formalisms for modeling physical systems, namely Power-Oriented Graphs (POG), Bong-Graphs (BG) and Energetic Macroscopic Representations (EMR) are described in Chap. 1.

In this work of thesis, the modeling of Planetary Gear Sets (PGSs), Permanent Magnet Synchronous Motors (PMSMs), multilevel converters for electric machine drives and vehicle transmission systems is addressed in detail, exploiting the convenient properties offered by the POG modeling technique. In the following, a description of the contributions of this work of thesis with respect to the literature for the mentioned physical elements is provided.

As far as PGSs are concerned, their modeling is addressed using different approaches in the literature. An interesting approach for easily and quickly determining the kinematics of a coupled epicyclic spur-gear train can be found in [5]. Next, the well-known Lever Analogy was introduced back in 1981 by Benford and Leising [6]. This is still nowadays one of the most effective tools for analyzing the kinematics and the dynamics of planetary gear sets. In fact, several works refer to the Lever Analogy to establish a fundamental understanding of the speed and torque relationships characterizing the considered planetary gear sets [7]-[10]. In [11], the planetary gear set is modeled by using basic physics laws and introducing some simplifying assumptions about the mechanical dynamics, i.e. all the connections in the powertrain are supposed to be rigid. With all these methods, the natural constraints relating the gears angular speeds, as well as the input torques relations at steady-state, can be found. In Chap. 3, a new POG-based approach for modeling

planetary gear sets is proposed [12]-[14]. The presented approach is deemed more effective than the current state of the art for the following reasons: a) the dynamic model is *general* for any planetary gear set and is directly implementable in Matlab/Simulink; b) the user is only required to compute two matrices, which fully and uniquely define the considered planetary gear set; c) the procedure for building the system vectors and matrices is *entirely systematic*; d) the model includes both the friction accounting for the rotation of the gears around their own axes and the *relative friction* associated with the in-contact gears exhibiting a relative movement; e) two state space models are obtained: a full dynamic model accounting for the gears elastic interaction, and a reduced-order model assuming rigid connections between the gears. The latter is proven suitable for fixed-step simulations needed for real-time execution; f) in the reduced-order dynamic model, the time behavior of the tangential forces exchanged between the gears can still be obtained offline, even if the tangential forces are no longer present in the reduced-order model, as proven in App. A; g) in the reduced-order dynamic model, the inherent kinematic speed and torque relations of the considered system automatically turn out.

For what concerns multilevel converters: the need of performing power conversion is present in a large variety of engineering fields. When focusing on electrical power conversions, the cases of DC/DC [15]-[17], AC/DC-DC/AC [18]-[21] power conversions can be distinguished. These types of power conversion find application in many areas, including smart grids [15],[18]-[19], hybrid electric vehicles [22], and many others. The physical modeling of the employed power converter topology is of great importance, as it represents the starting point for understanding its dynamic behavior and developing an effective control strategy. When driving electric machines, multilevel topologies bring several advantages when compared to classical two-level converters, such as a significant distortion reduction in the output voltage waveform and in the drawn input current, a reduction of the dv/dt effect in the output voltage waveform, and the generation of a lower common-mode voltage [23]-[24]. Together with the advantages and potentialities that are brought by multilevel converters comes the difficulty of having more power electronics devices to control. This has led to the development of different modulation algorithms and techniques hav-

ing different trade-offs between the pros and cons [25]-[26]. When dealing with the modeling and control of multilevel converters, the choice of the employed modeling approach represents the first step. Chap. 4 deals with the dynamic modeling, control and robustness assessmemt of multilevel flying-capacitor converters [27]. The modeling is performed using the POG modeling technique [2]-[3], extending the modeling approach that was proposed in [28]. The proposed approach provides a very compact continuous-time model of the considered multilevel converter which can be applied to other converter topologies as well, and establishes a straightforward way of computing the capacitor voltages and currents starting from the Insulated Gate Bipolar Transistors (IGBTs) switching states. Once the modeling is performed, the next step is represented by the control of the considered multilevel converter topology. Focusing on multilevel topologies having floating capacitors involved in their operation, an important aspect is represented by the capacitors voltages balancing. If not properly controlled, the floating capacitors voltages may suffer from ripple [29], which would cause output voltage and current distortion, or even voltages trajectory divergence, thus further compromising the converter operation. An important distinction needs to be made between those multilevel converters having full floating capacitors voltage balancing capability and those not having it, due to topology limitations or lack of redundancy. This latter case is addressed in [29], where a new PWM method was proposed to improve the floating capacitors voltage balancing capability. Multilevel flying-capacitor converters have full floating capacitors voltage balancing capability if properly controlled and if the number of output voltage levels m equals the number of capacitors n plus one (i.e. the number of floating capacitors plus two). An analytical investigation of the voltage balancing characteristics of the flying capacitor converter while using the phase disposition PWM (PDPWM) modulation technique is presented in [30]. An interesting approach to ensure floating capacitors voltage balancing capability is presented in [31], where a modification of the carrier-redistribution PWM (CRPWM) is proposed in order to ensure a low output voltage harmonic content and low voltage ripple, thanks to the symmetric disposition of carriers in every fundamental period. However, the main drawback that is associated with open-loop methods is that they aim at keeping the floating

capacitors voltages as close to the desired value as possible, but do not consider the case of a voltage unbalance occurring because of some unfavorable conditions, such as a fault, for example. In this latter case, a closed-loop control solution is required, in order to drive the capacitors voltages trajectory back to the desired operating point, thus ensuring the correct operation of the converter. The multilevel flying-capacitor converter having a generic number n of capacitors can actually generate all the way up to 2^n output voltage levels, giving rise to what is called "extended operation" [32]-[33]. However, if the number of voltage levels m is greater than $n+1$, then the multilevel flying-capacitor converter loses the property of full floating capacitors voltage balancing capability, and a suitable closed-loop control technique becomes paramount. An example of closed-loop control technique for the multilevel flying-capacitor converter in such operating condition using a "minimum distance" approach is proposed in [33]. However, to the best of my knowledge, there is no proposal in the literature of a metric allowing to perform the robustness assessment of multilevel flying-capacitor converters against the divergence of the flying capacitors voltage trajectory [27]. This becomes especially crucial with the converter working in extended operation, namely with a number m of output voltage levels greater than $n+1$ all the way up to 2^n. In Chap. 4, the following contributions with respect to the literature are addressed [27]: a) the dynamic modeling of multilevel flying-capacitor converters; b) the analysis of all the possible configurations of the converter in terms of capacitors voltage ratio allowing the converter to work in extended operation; c) the robustness assessment of multilevel flying-capacitor converters when working in extended operation and controlled using a classical minimum distance approach; d) the proposal of a divergence index determining the degradation of the converter operation using a minimum distance control as the number of output voltage levels is increased for all the possible capacitors voltages configurations; e) the proposal of a new variable-step closed-loop control strategy for guaranteeing the best flying capacitors voltage balance in any extended operating condition; f) the comparison of the proposed variable-step control strategy for multilevel flying-capacitor converters with a classical minimum distance control approach.

As far as PMSMs are concerned, Chap. 5 deals with the theoretical analysis,

modeling and parameters estimation of three-phase PMSMs [34]-[41] by means of the POG technique [2]-[3]. The dynamics of the three-phase PMSM is presented both in the static reference frame and in a transformed rotating reference frame, which makes the implementation of the motor control easier [34]-[35], [37]. The state-space transformations to be applied in order to turn the system into the rotating reference frame are illustrated and both the POG model in the static reference frame and the POG model in the rotating reference frame are reported and commented in detail. The torque vector analysis is then performed, together with the description of the simplified motor dynamics in the case of star-connected phases and of the optimal way of generating the desired torque. A new procedure for the estimation of the motor parameters is finally illustrated, which is based on the efficiency analysis of physical systems using the unified approach presented in [41]-[42]. Thanks to this procedure, the motor parameters estimation can be performed starting from the motor efficiency map, which is typically made available by the provider through the machine datasheet.

Once the modeling part of the considered HEV architecture has been addressed, a proper solution to the energy management problem must be found. This consists in identifying how to properly control the three power sources to achieve the desired goals: the minimization of the ICE specific fuel consumption, the charge sustaining operation of the vehicle, and the capability of satisfying the power demand from the vehicle transmission system. For this purpose, different HEV architectures in the agricultural and construction fields are taken into account in Chap. 6, both for series HEVs [43]-[45], parallel HEVs [46]-[51] and power-split HEVs [52]-[58], and a solution for the energy management problem is proposed for each of them [59]-[62], in order to be able to satisfy all the requirements.

The structure of this work of thesis is organized as described in the following. Chap. 1 describes the concepts and the basic properties of the POG modeling technique, together with an overview of the main characteristics of BG and EMR. A description of the main HEV architectures is presented in Chap. 2, highlighting the trade-offs between them. The fully systematic procedure for modeling planetary gear set is described in Chap. 3, together with its comparison with a common tool used in

the literature, namely the Lever Analogy. Chap. 4 deals with the modeling, control and robustness assessment of multilevel flying-capacitor converters, whereas Chap. 5 address the modeling, efficiency analysis and parameters estimation of permanent magnet synchronous motors. Next, the modeling, control and simulation of four different types of HEV architectures in the agricultural and construction fields are carried out in Chap. 6, while the conclusions are reported in Chap. 7. The proof that the time behavior of the tangential forces exchanged between the gears can still be obtained in the reduced-order dynamic model of planetary gear sets is given in App. A, whereas the list of publications is finally reported in App. B.

Chapter 1

Power-Oriented Graphs and Other Graphical Formalisms

Power-Oriented Graphs (POG) [2]-[3], Bond-Graph (BG) [63]-[66] and Energetic Macroscopic Representation (EMR) [63], [67]-[69] are the three main graphical formalisms for modeling physical systems exploiting an energetic approach. POG, BG and EMR provide different trade-offs between pros and cons as described in [4], from which it results that EMR is more suitable for simulation and control purposes, BG is more suitable for simulation and design purposes and POG is more suitable for simulation and analysis purposes. The main advantage of EMR is that it provides some inversion rules which make it easier to develop a control structure. The main advantage of BG is that it offers bidirectional connections, making the model more compact. The main advantage of POG is that it gives models which are directly implementable in the Simulink environment with no need of additional libraries using standard Simulink blocks; furthermore, it enables a straightforward analysis of the system power flows.

In this work of thesis, the POG technique is employed because of the advantages it offers [4]. In this chapter, an overview of the main characteristics of BG [63]-[64] and EMR [63], [67] is given, together with a description of the main properties of the POG technique [2]-[3]. The remainder of this chapter is organized as follows. Sec. 1.1 and Sec. 1.2 describe the main characteristics of the BG and EMR techniques,

respectively. Sec. 1.3 describes the main blocks and variables characterizing POG block schemes. In Sec. 1.4, the structure and correct orientation of physical elements to guarantee an integral causality are illustrated. Sec. 1.5 shows the possible connections of physical elements, whereas Sec. 1.6 describes the POG state-space model and Sec. 1.7 summarizes the main properties of POG block schemes.

1.1 BG: main features

The Bond Graphs (BG) graphical formalism employs a uniform notation for all types of physical systems [34]. The power exchanges are denoted by half arrows, i.e. bonds, carrying a couple of power variables. The product of these two power variables, one of which being of the flow type and the other being of the effort type, represents the power exchanged between the physical elements. The edges orientation is represented by a little stroke forming a half arrow with the line (which indicates the positive orientation of the variables). The bong graph labeled nodes are multiport elements which are identified on the basis of their behavior with respect to energy, power, and the conserved quantities typical for an energetic domain. The Bond Graph nodes satisfy the following property: power continuity, meaning that the net power into the node is always equal to zero. The nine basic node types can be classified into five groups: 1) Storage (energy conservation), 2) Supply and demand (boundary conditions), 3) Reversible transformation (inter-domain connections), 4) Distribution (intra-domain connections), 5) Irreversible transformation (dissipation). The causality information is given on each half arrow by means of the causal stroke drawn perpendicularly to the bond.

1.2 EMR: main features

The Energetic Macroscopic Representation (EMR) graphical formalism is based on the action-reaction principle [34]. It allows to give a compact representation of com-

plex electromechanical systems and it is characterized by specific pictograms associated to each power component depending on their function: energy accumulation (rectangle with an oblique bar), conversion without energy accumulation (square for electrical conversion, circle for electromechanical conversion, triangle for mechanical conversion) and interleaved pictograms for energy distribution. The EMR formalism identifies flow variables as those that are associated with a motion (as velocity and current in the mechanical and electrical domains) and effort variables as those that are not associated with a motion (as force and voltage in the mechanical and electrical domains). The EMR technique gives a methodology to build a control structure starting from the model of the system, which can be obtained performing a step-by-step inversion of the system decomposed into elementary subsystems. An advantage of the EMR representation is that it is planar, therefore clearly showing the elements coupling and the system energy flux, and being easy to read. However, it does not show the model mathematical details.

1.3 Main elements characterizing a POG block scheme

The POG technique only uses two ***Basic blocks*** for modeling physical systems, see Fig. 1.1:

a) the ***elaboration block*** (e.b.) is used for modeling all the physical elements that store and/or dissipate energy (i.e. springs, masses, dampers, capacities, inductances, resistances, etc.).

b) the ***connection block*** (c.b.) is used for modeling all the physical elements that "perform lossless power conversion" (i.e. *neutral elements* such as gear reductions, transformers, etc.). In the vectorial case, matrix $\mathbf{K}$ characterizing the connection block can also be rectangular, time varying or function of other variables.

Power sections: the dashed lines in Fig. 1.1 represent the power sections connecting the two POG basic blocks with the external world and with other blocks. There are no restrictions on the choice of the vectors $\mathbf{x}$ and $\mathbf{y}$ involved in each power

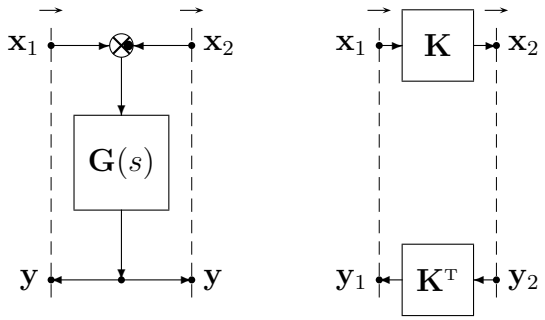

a) *Elaboration block* b) *Connection block*

Figure 1.1: POG blocks: *elaboration block* and *connection block*.

	Electrical	Mech. Tran.	Mech. Rot.	Hydraulic
$\mathcal{D}_e$	C Capacitor	M Mass	J Inertia	C_I Hyd. Capacitor
q_e	Q Charge	p Momentum	p Ang. Momentum	V Volume
v_e	V Voltage	v Velocity	ω Ang. Velocity	P Pressure
$\mathcal{D}_f$	L Inductor	E Spring	E Spring	L_I Hyd. Inductor
q_f	ϕ Flux	x Displacement	θ Ang. Displacement	ϕ_I Hyd. Flux
v_f	I Current	F Force	τ Torque	Q Volume flow rate
$\mathcal{R}$	R Resistor	b Friction	b Ang. Friction	R_I Hyd. Resistor

Figure 1.2: Energetic domains: the physical elements $\mathcal{D}_e$, $\mathcal{D}_f$ and $\mathcal{R}$; the energy variables q_e, q_f; the power variables v_e, v_f.

section, except for the following one: the inner product $\langle \mathbf{x}, \mathbf{y} \rangle = \mathbf{x}^{\mathrm{T}}\mathbf{y}$ must have the physical meaning of *power flowing through that corresponding power section.*

Energetic domains: when modeling physical systems, the main energetic domains are: electrical, mechanical (translational and rotational) and hydraulic. Each energetic domain has its own couple of power variables, see Fig. 1.2.

Power variables: they can be divided into two groups:
1) the *"across-variables"* (i.e. voltage V_p, velocity $\dot{\mathbf{x}}_p$, angular velocity ω_p and pressure P_p) which are defined *"between two points P and 0"* of the space:

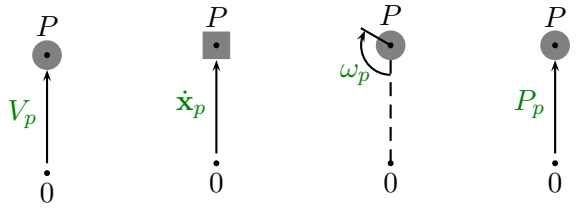

2) The *"through-variables"* (i.e. current I_p, force F_p, torque τ_p and volume flow rate Q_p) which are defined *"in each point P"* of the space:

Dynamic structure of the energetic domains: each *energetic domain* is characterized by three different types of physical elements only:

- Two ***dynamic elements*** D_e and D_f which store the energy (capacitors, inductors, masses, springs, etc.);
- A ***static element*** R which dissipates the energy (i.e. resistors, frictions, etc.);

The system dynamics can be described using four variables:

- Two ***energy variables*** q_e and q_f which define *how much energy is stored* within the *dynamic elements*;
- Two ***power variables*** v_e and v_f which describe *the power flows* entering or exiting the physical element.

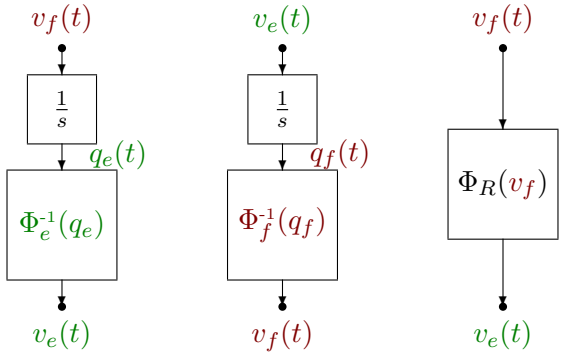

Figure 1.3: *Dynamic elements* D_e, D_f and *static element* R.

The dynamic/static elements and the energy/power variables for the considered energetic domains are shown in Fig. 1.2. The difference between the dynamic elements D_e and D_f is the following: the D_e elements provide the power across-variables v_e as output, the D_f elements provide the power through-variables v_f as output.

1.4 Mathematical structure of the physical elements

The *dynamic element* D_e is characterized by:

1) an internal *energy variable* $q_e(t)$;

2) a *through-variable* $v_f(t)$ as input variable;

3) an *across-variable* $v_e(t)$ as output variable;

4) a *constitutive relation* $q_e = \Phi_e(v_e)$ which links the internal variable $q_e(t)$ to the output variable $v_e(t)$;

5) a *differential equation* $\dot{q}_e(t) = v_f(t)$ which links the internal variable $q_e(t)$ to the input variable $v_f(t)$;

The energy E_e stored in the *dynamic element* D_e is function of the internal *energy variable* q_e only:

$$E_e = \int_0^t v_e(t)\, v_f(t)\, dt = \int_0^{q_e} \Phi_1^{-1}(q_e)\, dq_e = E_e(q_e).$$

In the POG modeling technique, all the dynamic elements are always described by block schemes using *integral causality*, see the first two blocks on the left in Fig. 1.3.

1.5 Connection of power sections: series and parallel

Each Physical Element (PE) interacts with the external world and with other PEs through the power sections associated with its terminals. The two basic power connections of the physical element PE with the external world are shown in Fig. 1.4: a) the *series* connection occurs when the two terminals share the same through-variable $v_f = v_{f1} = v_{f2}$; b) the *parallel* connection occurs when the two terminals share the same across-variable $v_e = v_{e1} = v_{e2}$.

The POG block schemes corresponding to the *series* and *parallel* connections reported in Fig. 1.4 are shown in Fig. 1.5:

a) The summation element present in the POG block diagram of Fig. 1.5.a is a mathematical description of the Voltage Kirchhoff's Law (VKL) applied to the *across variables* v_{e1}, v_{e2} and v_e involved in the *closed path*, which is always present when the PE is connected in series, i.e. the green closed dashed path shown in Fig. 1.4.a.

b) The summation element present in the POG block diagram of Fig. 1.5.b is a mathematical description of the Current Kirchhoff's Law (CKL) applied to the *through variables* v_{f1}, v_{f2} and v_f involved in the "*node*" corresponding to terminal 1 of the PE connected in parallel, see the red closed dashed line shown in Fig. 1.4.b.

A simple example of POG modeling is shown in Fig. 1.6, where a C-parallel element is connected with an R-series element: this is a particular case of "*Parallel - Series*" connection. The circled numbers ①, ② and ③ denote the system power sections.

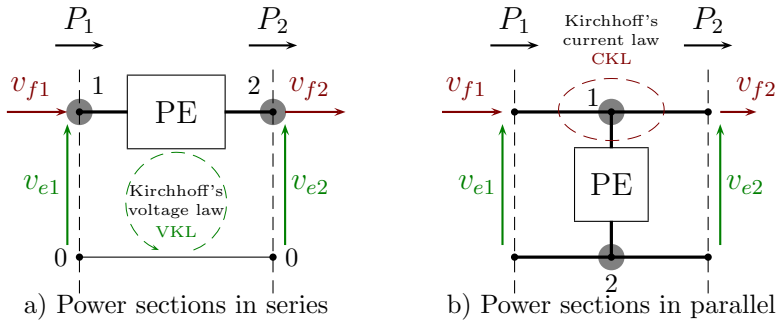

Figure 1.4: Connections of the PE with the external world.

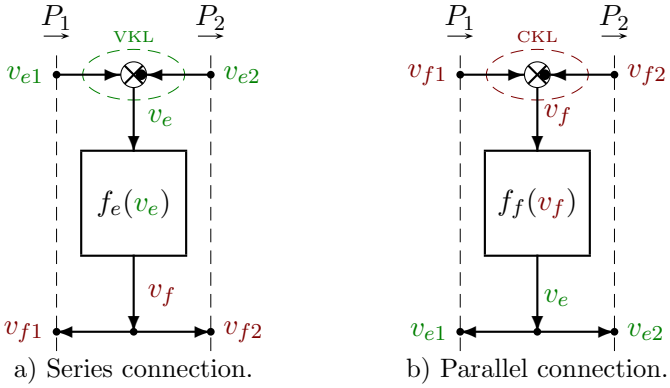

Figure 1.5: POG schemes of the *series* and *parallel* connections.

1.6 POG state-space model

Any linear time-invariant physical system modeled using the POG technique can be written in a POG state-space representation as follows:

$$\begin{cases} \mathbf{L}\,\dot{\mathbf{x}} = \mathbf{A}\,\mathbf{x} + \mathbf{B}\,\mathbf{u} \\ \mathbf{y} = \mathbf{C}\,\mathbf{x} + \mathbf{D}\,\mathbf{u} \end{cases},$$

where $\mathbf{L}$ is the energy matrix, $\mathbf{A}$ is the power matrix, $\mathbf{B}$ is the input matrix, $\mathbf{C}$ is the output matrix and $\mathbf{D}$ is the input-output matrix. The energy matrix $\mathbf{L}$ and the power matrix $\mathbf{A}$ describe the energy E_s stored in the system and the power P_d dissipated in the system, respectively, as shown in Sec. 1.7. When an eigenvalue of the energy matrix $\mathbf{L}$ tends to zero or to infinite, the system model degenerates to a lower dimension, and the reduced model can be obtained by applying a proper

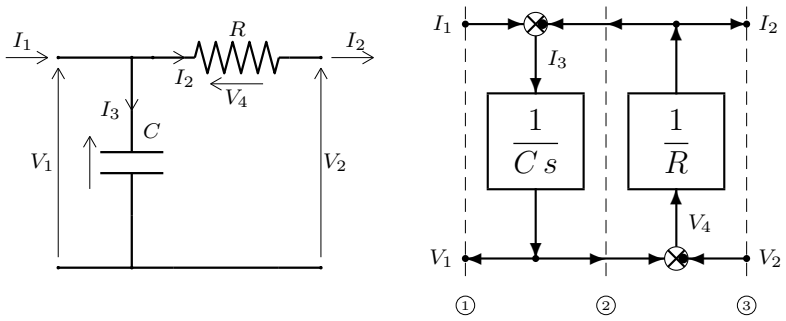

Figure 1.6: POG modeling of an electrical RC circuit.

congruent transformation $\mathbf{x} = \mathbf{T}_1\,\mathbf{x}_1$, where $\mathbf{x}$ is the state vector of the original full model, $\mathbf{x}_1$ is the state vector of the new reduced model and $\mathbf{T}_1$ is a proper rectangular matrix. The new matrices of the reduced model can be directly obtained as follows: $\mathbf{L}_1 = \mathbf{T}_1^{\mathrm{T}}\,\mathbf{L}\,\mathbf{T}_1$, $\mathbf{A}_1 = \mathbf{T}_1^{\mathrm{T}}\,\mathbf{A}\,\mathbf{T}_1$, $\mathbf{B}_1 = \mathbf{T}_1^{\mathrm{T}}\,\mathbf{B}$, $\mathbf{C}_1 = \mathbf{C}\,\mathbf{T}_1$ and $\mathbf{D}_1 = \mathbf{D}$.

1.7 Properties of POG block schemes

The main properties of linear POG block schemes are reported in the following:

1. the energy E_s stored in the system can be expressed as $E_s = \frac{1}{2}\mathbf{x}^{\mathrm{T}}\mathbf{L}\,\mathbf{x}$;
2. the power P_d dissipated in the system can be expressed as $P_d = \mathbf{x}^{\mathrm{T}}\mathbf{A}\,\mathbf{x}$;
3. all the loops present in a POG block scheme contains an "odd" number of minus signs (i.e. of the black spots in the summation elements);
4. the direction of the power flowing through a section is positive if an "even" number of minus signs is present along one of the paths going from the input to the output of the section.

Chapter 2

Hybrid Electric Vehicles Propulsion Systems

Propulsion systems for HEVs can be mainly classified according to the two criteria shown in Table 2.1, [70]-[71]: the degree of hybridization and the considered architecture.

The degree of hybridization of a HEV is dictated by the fraction of electric power in the vehicle with respect to the overall vehicle rated power, which is in turn given by the electric power source combined with the endothermic power source, namely the ICE. Depending on the degree of hybridization, the HEV can be classified into micro, mild, full and plug-in HEV, see Table 2.1. Micro HEVs have the lowest degree of hybridization ($< 5\%$), and the electric motor is mainly employed for start and stop functionality. Mild HEVs exhibit a degree of hybridization which can get up to 10%. In full HEVs, the electric motor provides at least 40% of the engine power. In this case, the electric motor and battery sizes are larger and there is room for improving the engine fuel consumption. Finally, plug-in HEVs are vehicles that can be plugged-in, meaning that an additional external power source which is not on board the vehicle is present in this case.

From the modeling point of view, the classification based on the considered vehicle architecture is of interest, see Table 2.1. The three main vehicle architectures can be described as follows:

Based on Degree of Hybridization	Based on Architecture
Micro Hybrid	Series Hybrid
Mild Hybrid	Parallel Hybrid
Full Hybrid	Power-Split Hybrid
Plug-in Hybrid	

Table 2.1: Classification of Hybrid Electric Vehicles.

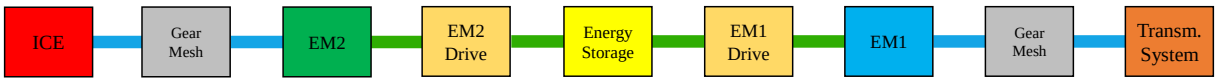

Figure 2.1: Schematic overview of a series architecture for HEVs.

- *Series* architecture, which is characterized by a single hybrid mechanical/electrical power flow from the ICE to the vehicle transmission system, see Fig. 2.1;
- *Parallel* architecture, which is characterized by two parallel power flows, a hybrid mechanical/electrical one and a fully mechanical one, from the ICE to the vehicle transmission system, see Fig. 2.2;
- *Power-Split* architecture, which is still characterized by two parallel power flows, a hybrid mechanical/electrical one and a fully mechanical one, from the ICE to the vehicle transmission system, but introducing more degrees of freedom with respect to the parallel architecture thanks to the use of a power-split device, see Fig. 2.3 and Fig. 2.4.

Series HEVs are a category of hybrid electric vehicles where there is no mechanical coupling between the endothermic engine and the vehicle transmission [59], [72], as it can be seen from the schematic representation in Fig. 2.1. In the figure, the electric machine denoted by EM2 is the one working as a generator only, whereas the one denoted by EM1 is either working as a motor or as a generator, the latter when performing energy recovery. The absence of a direct mechanical power path from the ICE to the transmission represents one of the main advantages of series HEVs:

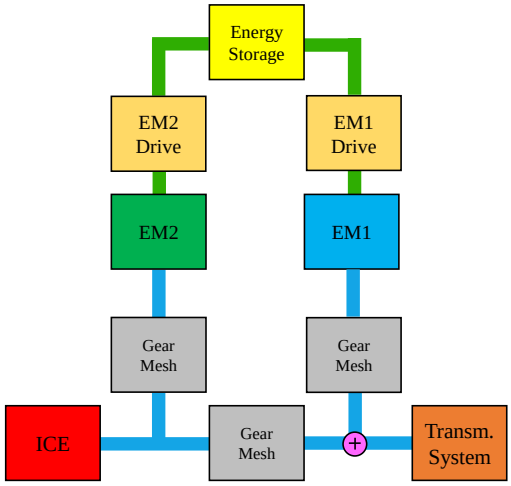

Figure 2.2: Schematic overview of a parallel architecture for HEVs.

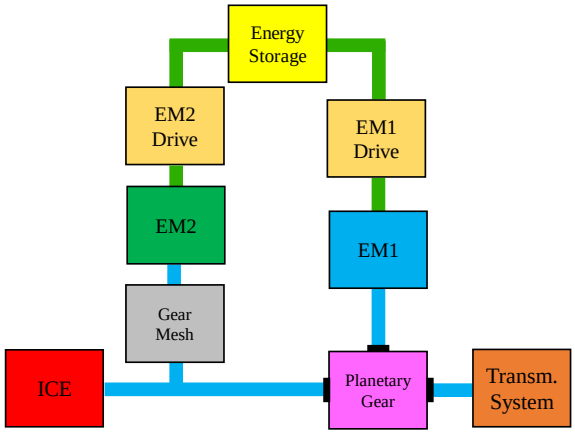

Figure 2.3: Schematic overview of power-split (output split) architecture for HEVs.

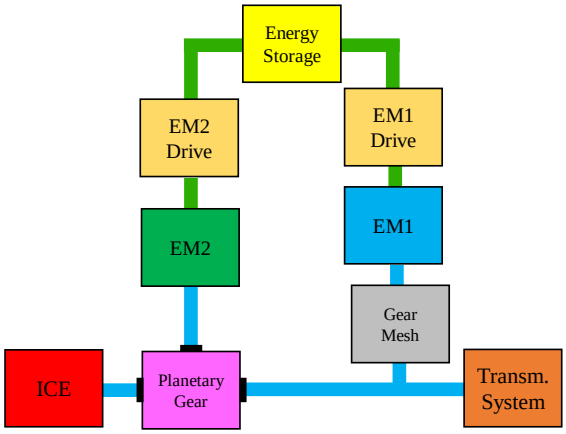

Figure 2.4: Schematic overview of power-split (input split) architecture for HEVs.

the ICE torque and the ICE speed are decoupled from the transmission torque and speed, respectively, and can be exploited as degrees of freedom. The main disadvantage of this architecture is that EM1 must be able to satisfy the entire transmission power demand on its own, meaning that the size of EM1 is going to be consistent.

Parallel HEVs are a category of hybrid electric vehicles characterized by two parallel power paths from the ICE to the vehicle transmission [60], [73], as shown in Fig. 2.2. Note that the parallel architecture shown in Fig. 2.2 is not the classical one since it has two electric machines. The first power path in Fig. 2.2 is a direct mechanical power path, which lets a given fraction of the mechanical power generated by the ICE flow through a gearbox and be delivered to the load. The second one is an indirect mechanical/electrical power path. In this case, a determined fraction of the ICE power undergoes a mechanical-to-electrical energy conversion by means of an electric machine EM2, gets stored in an energy storage device, and eventually undergoes a final electrical-to-mechanical energy conversion performed by another electric machine EM1. The electric machine EM2 plays the role of a generator to recharge the energy storage device. The electric machine EM1 mainly acts as a motor, in order to help the ICE to satisfy the load required power level. This enables both engine and electric machine downsizing, which is an advantage of this architecture. Because of the direct mechanical power path, the ICE and transmission speeds are coupled through the gearbox, therefore one degree of freedom gets lost. The presence of the additional electrical power path allows to decouple the ICE torque from the transmission torque, meaning that the other degree of freedom remains.

Power-Split HEVs [61]-[62], [71] are a category of hybrid electric vehicles characterized by the presence of a power-split device, which is typically a planetary gear set [12]-[14]. Like the parallel architecture, the power-split architecture is characterized by the coexistence of two different power paths reaching the vehicle transmission: a mechanical one and a mechanical/electrical one. Unlike parallel architectures, however, the mechanical power path is not direct, namely the ICE and transmission speeds are decoupled thanks to the action of the planetary gear set. In the mechanical/electric power path, a determined fraction of the ICE power still

undergoes a mechanical-to-electrical energy conversion through EM2 working as a generator, gets stored in an energy storage device, and undergoes a final electrical-to-mechanical energy conversion through EM1, either working as a motor or as a generator, the latter when performing energy recovery. Depending on where the planetary gear set is located in the topology, different types of power-split architectures can be defined [71]. In this work, focus is given on power-split architectures of the output and input types, see Fig. 2.3 and Fig. 2.4, namely where the planetary gear set is located close to the vehicle transmission and close to the ICE, respectively. Like series architectures, power-split architectures allow to decouple the ICE speed and torque from the transmission speed and torque. Additionally, they provide another important advantage: the potentiality of ICE down-sizing. This is enabled thanks to the parallel mechanical/electrical power path, which helps to drive the transmission. Therefore, power-split architectures combine the advantaged of series and parallel architectures.

Chapter 3

Systematic Modeling of Planetary Gear Sets

This chapter deals with the presentation of a systematic approach for the dynamic modeling of complex planetary gear sets [12]-[14], which are a key element of Power-Split HEVs.

The reminder of this chapter is organized as follows. Sec. 3.1 concerns the introduction of the basic rules for the system definition. Next, the general full dynamic model and the POG scheme are introduced and described. In Sec. 3.2, the direct computation of the radii matrix $\mathbf{R}$ and of the relative friction matrix $\mathbf{B}_{\Delta\omega}$ uniquely defining the system are addressed, followed by the derivation of the reduced-order model and by the introduction of the formula for computing the time behavior of the tangential forces in the reduced-order model. In order to show how to use the proposed approach, several case studies have been in considered: the systematic modeling of the Ravigneaux planetary gear set used in [74]-[76] is addressed in Sec. 3.2. With reference to this case study, a comparison with the lever analogy is also performed, in order to highlight pros and cons of the two methods. The systematic modeling of a double stage planetary gear set is addressed in Sec. 3.3. A compound and a coupled epicyclic gear trains are then considered and modeled in Sec. 3.4 and Sec. 3.5. With reference to the coupled epicyclic gear train, the design of a control aiming at minimizing the dissipated power is also carried out and tested.

Finally, the modeling of two examples of single stage planetary gear sets is addressed in Sec. 3.6 and Sec. 3.7, respectively. The latter two planetary gear sets are those employed in the power split architectures described in Sec. 6.1.4 and Sec. 6.1.5.

3.1 Modeling a three-gears system

This section focuses on the modeling of the three-gears system shown in Fig. 3.1. This system is used as a simple case study to introduce the notations adopted for the proposed systematic modeling procedure. The horizontal colored arrows "→" "→" and "→" , shown in Fig. 3.1.a), highlight the orientation of the rotation axes of the three considered gears. The same color coding is used in Fig. 3.2, showing the equivalent 3D representation of Fig. 3.1.a). By relying upon the well-known Right-hand rule and aligning the right thumb with the three colored arrows "→" "→" and "→" , the reader can verify that the positive direction of rotation is clockwise for all the three angular speeds ω_1, ω_2 and ω_3. This is also highlighted by the black dashed arrows in Fig. 3.2. Additionally, the input torques τ_1, τ_2 and τ_3 are assumed to have the same *positive directions* as the respective angular speeds ω_1, ω_2 and ω_3, as denoted in Fig. 3.1. This ensures that the power flowing through the corresponding energetic port (ω_i, τ_i) is positive if it is entering the system. Each gear is characterized by a one-digit subscript "i" and a specific color. The one-digit subscript "i" denotes all the parameters associated with the gear: J_i and b_i are the moment of inertia and the linear friction coefficient of gear "i". If two gears "i" and "j" are arranged in a mechanical configuration causing the presence of some relative friction between them, the symbol b_{ij} will denote the relative friction coefficient between gear "i" and gear "j".

The gears of the considered system interact with each other by means of their teeth, which represent an elastic coupling. This elastic coupling is denoted in Fig. 3.1 by red lines (i.e. "–") representing the tangential springs acting between the gears. Each tangential spring is characterized by a subscript "ij". The term K_{ij} denotes the stiffness coefficient, whereas the variable F_{ij} denotes the tangential force associated with the spring "ij". The presence of these springs is also highlighted in the 3D

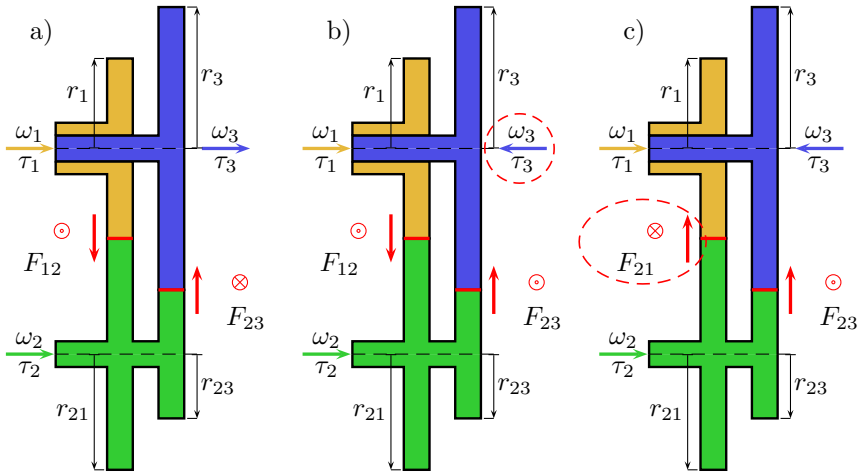

Figure 3.1: Structure of the considered three-gears system.

drawing in Fig. 3.2, where the two tangential springs K_{12} and K_{23} are physically located at the contact points between the gears "1" and "2" and at the contact points between the gears "2" and "3", respectively.

The red vertical arrows " ↓ " " ↑ " shown in Fig. 3.1.a) highlight the *positive orientation* of both the tangential force F_{ij} and the tangential spring K_{ij}, for $ij \in \{12, 23\}$. As far as the system in Fig. 3.1.a) and Fig. 3.2 is concerned, it is possible to see that spring K_{12} has its first terminal connected to gear "1" and its second terminal connected to gear "2". Similarly, spring K_{23} has its first terminal connected to gear "2" and its second terminal connected to gear "3". Fig. 3.2 shows that the forces F_{12} and F_{23} exchanged at the contact points are indeed *tangential* to the gears, which is the reason why the contact springs are referred to as *tangential* springs. With reference to Fig. 3.2, the *positive direction* of forces F_{ij} can be determined as follows. Since the second terminal of spring K_{ij} is connected to gear j, the right thumb has to be aligned with the colored arrow identifying the positive direction of the angular speed ω_j. By applying the Right-hand rule, one finally obtains the *positive direction* of the tangential force F_{ij} associated with spring K_{ij}. With reference to Fig. 3.1, the positive direction of tangential force F_{ij} is:

- entering the page (i.e. "⊗") if force F_{ij} is on the right-hand side of the horizontal arrow identifying the positive direction of angular speed ω_j;

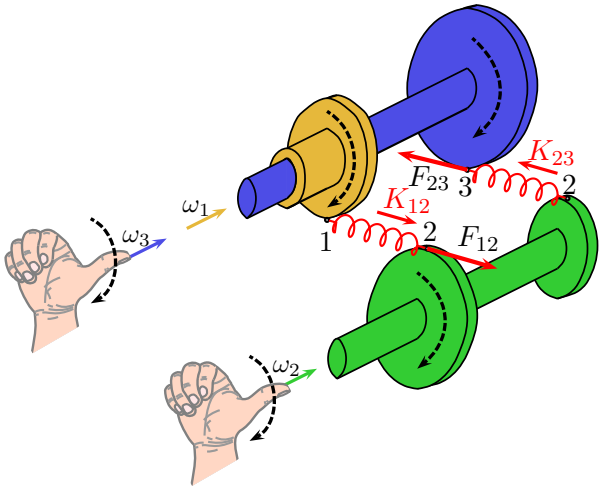

Figure 3.2: Use of the Right-hand rule to compute: the positive direction of rotation of ω_1, ω_2 and ω_3; the positive orientation of F_{12} and F_{23}.

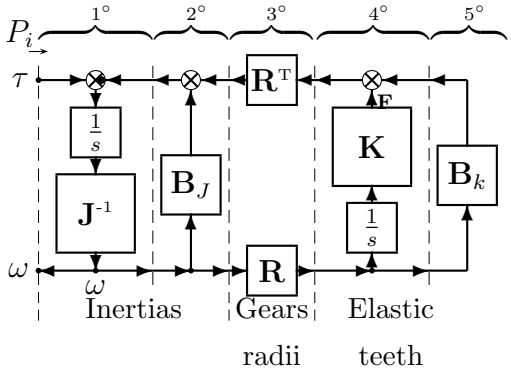

Figure 3.3: General POG scheme of gearing systems.

- exiting the page (i.e. "$\odot$") in the opposite case.

The subscript "ij" also denotes the linear friction coefficient d_{ij} in parallel with the tangential spring "ij".

The proposed systematic modeling approach allows to model any type of complex gear train, planetary or parallel gear set using the general POG scheme shown in Fig. 3.3. Moving from left to right in the POG scheme of Fig. 3.3, the first block is an elaboration block describing the dynamics of the gears inertial elements present within the system. The second block is an elaboration block accounting for the gears viscous and relative friction. The third block is a connection block describing the energy conversion between the mechanical rotational and the mechanical translational energetic domains. The fourth block is an elaboration block accounting for the dynamics of the gears elastic contact points. Finally, the fifth block is an elaboration block describing the friction coefficients associated with the tangential springs. The crossed circles in the upper part of the elaboration blocks are called summation nodes. The presence of a black spot in a summation node means that the considered power variable entering the node has to be subtracted. By reading the POG scheme of Fig. 3.3, the following state space equations of the system can

be directly obtained:

$$\underbrace{\begin{bmatrix}\mathbf{J} & \mathbf{0}\\ \mathbf{0} & \mathbf{K}^{-1}\end{bmatrix}}_{\mathbf{L}}\dot{\mathbf{x}}=\underbrace{\begin{bmatrix}-\mathbf{B}_J-\mathbf{R}^{\mathrm{T}}\mathbf{B}_k\mathbf{R} & -\mathbf{R}^{\mathrm{T}}\\ \mathbf{R} & \mathbf{0}\end{bmatrix}}_{\mathbf{A}}\mathbf{x}+\underbrace{\begin{bmatrix}\mathbf{I}\\ \mathbf{0}\end{bmatrix}}_{\mathbf{B}}\underbrace{\mathbf{u}}_{\boldsymbol{\tau}}, \tag{3.1}$$

where $\mathbf{x}$ is the state vector:

$$\mathbf{x}=\begin{bmatrix}\boldsymbol{\omega}\\ \mathbf{F}\end{bmatrix},\qquad \boldsymbol{\omega}=\begin{bmatrix}\omega_1\\ \omega_2\\ \omega_3\end{bmatrix},\qquad \mathbf{F}=\begin{bmatrix}F_{12}\\ F_{23}\end{bmatrix}, \tag{3.2}$$

$\boldsymbol{\omega}$ is the speed vector, $\mathbf{F}$ is the force vector, $\mathbf{u}=\boldsymbol{\tau}$ is the input torque vector and $\mathbf{y}=\mathbf{B}^{\mathrm{T}}\mathbf{x}=\boldsymbol{\omega}$ is the output vector. The meaning of the matrices within the state space model (3.1) is the following: $\mathbf{L}$, $\mathbf{A}$ and $\mathbf{B}$ are the energy, power and input-power matrices of the system, respectively; $\mathbf{I}$ is an identity matrix of proper dimension; $\mathbf{J}$ and $\mathbf{B}_J$ are the inertia and friction matrices related to the gears; $\mathbf{K}$ and $\mathbf{B}_K$ are the stiffness and friction matrices related to the tangential springs; $\mathbf{R}$ is the radii matrix defining the kinematic relations between the gears and the tangential springs. The friction matrix $\mathbf{B}_J$ is given by the sum of two terms:

$$\mathbf{B}_J=\mathbf{B}_\omega+\mathbf{B}_{\Delta\omega}. \tag{3.3}$$

The matrix $\mathbf{B}_\omega$ is the friction matrix associated with the rotation of the gears around their own rotation axes. The matrix $\mathbf{B}_{\Delta\omega}$ is the relative friction matrix associated with the relative angular speed between two different gears. The structures of matrices $\mathbf{J}$, $\mathbf{B}_\omega$, vector $\boldsymbol{\tau}$ and matrices $\mathbf{K}$, $\mathbf{B}_K$ are:

$$\mathbf{J}=\begin{bmatrix}J_1 & 0 & 0\\ 0 & J_2 & 0\\ 0 & 0 & J_3\end{bmatrix},\ \mathbf{B}_\omega=\begin{bmatrix}b_1 & 0 & 0\\ 0 & b_2 & 0\\ 0 & 0 & b_3\end{bmatrix},\ \boldsymbol{\tau}=\begin{bmatrix}\tau_1\\ \tau_2\\ \tau_3\end{bmatrix},\ \mathbf{K}=\begin{bmatrix}K_{12} & 0\\ 0 & K_{23}\end{bmatrix},\ \mathbf{B}_K=\begin{bmatrix}d_{12} & 0\\ 0 & d_{23}\end{bmatrix}. \tag{3.4}$$

One can easily verify that: a) the structures of matrices $\mathbf{J}$, $\mathbf{B}_\omega$ and vector $\boldsymbol{\tau}$ in (3.4) are completely defined by the order of the angular speeds ω_i within the speed vector $\boldsymbol{\omega}$ defined in (3.2); b) the structures of matrices $\mathbf{K}$ and $\mathbf{B}_K$ in (3.4) are completely defined by the order of the tangential forces F_{ij} within the force vector $\mathbf{F}$ in (3.2).

As the positive direction of the speeds ω_i and the positive orientation of the tangential forces F_{ij} change, only the radii matrix $\mathbf{R}$ and the relative friction matrix $\mathbf{B}_{\Delta\omega}$ vary. By adopting the particular choice of positive directions and orientations as in Fig. 3.1.a), matrices $\mathbf{R}$ and $\mathbf{B}_{\Delta\omega}$ assume the following form:

$$\begin{matrix}12\\23\end{matrix}\ \mathbf{R}=\begin{matrix}\begin{matrix}1&2&3\end{matrix}\\ \begin{bmatrix}-r_1 & -r_{21} & 0\\ 0 & r_{23} & r_3\end{bmatrix}\end{matrix}, \qquad \begin{matrix}1\\2\\3\end{matrix}\ \mathbf{B}_{\Delta\omega}=\begin{matrix}\begin{matrix}1&2&3\end{matrix}\\ \begin{bmatrix}b_{13} & 0 & -b_{13}\\ 0 & 0 & 0\\ -b_{13} & 0 & b_{13}\end{bmatrix}\end{matrix}. \tag{3.5}$$

The green terms in (3.5) denote the subscripts of the state space variables ω_i and F_{ij}. With reference to [2], one can prove that the following two statements hold:

1) *The change of sign for the positive direction of the angular speed ω_i (and of torque τ_i) implies the change of sign for all the coefficients of: a) the i-th column of the radii matrix $\mathbf{R}$; b) the i-th column and the i-th row of the relative friction matrix $\mathbf{B}_{\Delta\omega}$.*

Example. The gearing system in Fig. 3.1.b) differs from the one in Fig. 3.1.a) because the positive direction of the angular speed ω_3 has been changed. Using the Right-hand rule, as described in Fig. 3.2, one can conclude that the positive direction of rotation of the gear J_3 has now changed into counter-clockwise. The new structures of matrices $\mathbf{R}$ and $\mathbf{B}_{\Delta\omega}$ are the following:

$$\begin{matrix}12\\23\end{matrix}\ \mathbf{R}=\begin{matrix}\begin{matrix}1&2&3\end{matrix}\\ \begin{bmatrix}-r_1 & -r_{21} & 0\\ 0 & r_{23} & -r_3\end{bmatrix}\end{matrix}, \qquad \begin{matrix}1\\2\\3\end{matrix}\ \mathbf{B}_{\Delta\omega}=\begin{matrix}\begin{matrix}1&2&3\end{matrix}\\ \begin{bmatrix}b_{13} & 0 & b_{13}\\ 0 & 0 & 0\\ b_{13} & 0 & b_{13}\end{bmatrix}\end{matrix}, \tag{3.6}$$

where the black coefficients have not changed sign with respect to (3.5). The red coefficients in (3.6) have changed their sign, whereas the blue coefficients in (3.6) are those whose sign has not changed because a double sign change has occurred.

According to statement 1), matrices $\mathbf{R}$ and $\mathbf{B}_{\Delta\omega}$ need to be updated as described next. Since the positive direction of ω_3 has changed, the signs of all the coefficients in the third column of matrix $\mathbf{R}$ in (3.5) need to be changed, as shown in (3.6).

Additionally, the signs of all the coefficients in the third column and in the third row of $\mathbf{B}_{\Delta\omega}$ in (3.5) need to be changed, as shown in (3.6). The blue coefficient b_{13} belongs to both the third row and the third column of matrix $\mathbf{B}_{\Delta\omega}$. Consequently, the coefficient b_{13} changes sign twice.

2) *The change of the positive orientation of the tangential forces F_{ij} implies the change of sign for all the coefficients of the ij-th row of the radii matrix* $\mathbf{R}$.

Example. The gearing system in Fig. 3.1.c) differs from the system in Fig. 3.1.b) because the positive orientation of the tangential force F_{12} has been changed. As a consequence, the new structure of matrix $\mathbf{R}$ is the following:

$$\begin{matrix} & \begin{matrix} 1 & 2 & 3 \end{matrix} \\ \begin{matrix} 12 \\ 23 \end{matrix} & \mathbf{R} = \begin{bmatrix} r_1 & r_{21} & 0 \\ 0 & r_{23} & -r_3 \end{bmatrix} \end{matrix}. \tag{3.7}$$

The color coding is the same as in (3.6). According to statement 2), matrix $\mathbf{R}$ needs to be updated as follows. Since the positive orientation of F_{12} has changed, the signs of all the coefficients in the row corresponding to $i = 1$ and $j = 2$ of matrix $\mathbf{R}$ in (3.6), namely the first row, need to be changed, as shown in (3.7).

3.2 Modeling a Ravigneaux planetary gear set

Let us now consider the Ravigneaux planetary gear set shown in Fig. 3.4, for which a possible application is in heavy-duty vehicles [74]. This system has been studied and modeled in [74] using a different approach. Let us introduce the following symbols:

$$\begin{cases} \mathcal{N}_J = \{c,\, p,\, q,\, t,\, s,\, r\}, & n_J = \dim(\mathcal{N}_J) = 6, \\ \mathcal{N}_K = \{pr,\, pt,\, qp,\, qs\}, & n_K = \dim(\mathcal{N}_K) = 4, \\ \mathcal{N}_B = \{cp,\, cq,\, cr,\, st\}, & n_B = \dim(\mathcal{N}_B) = 4, \end{cases} \tag{3.8}$$

where $\mathcal{N}_J$ is the set containing the one-digit subscripts identifying the system gears, n_J is the number of gears, $\mathcal{N}_K$ is the set containing the two-digit subscripts identifying the tangential springs, n_K is the number of tangential springs, $\mathcal{N}_B$ is the set

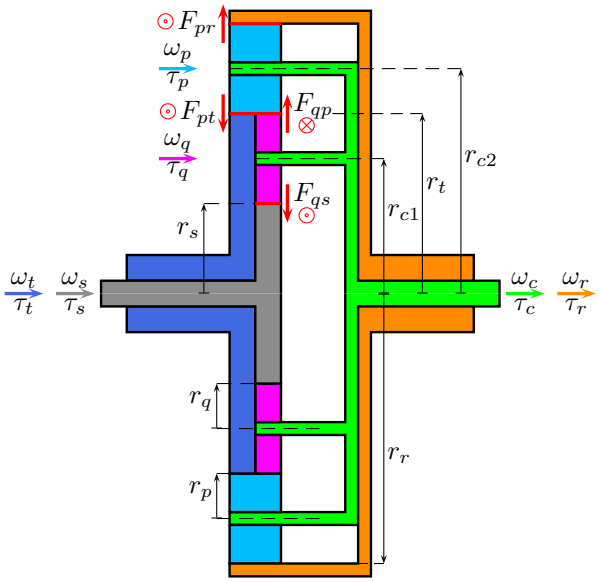

Figure 3.4: Structure of the considered Ravigneaux planetary gear set.

containing all the two-digit subscripts identifying the relative friction coefficients b_{ij} and n_B is the number of relative friction elements present within the system.

The considered system can be modeled using the general POG block scheme shown in Fig. 3.3. The corresponding state space equations are given in (3.1). Let us choose the speed vector $\boldsymbol{\omega}$ and the force vector $\mathbf{F}$ as:

$$\boldsymbol{\omega} = \begin{bmatrix} \omega_c & \omega_p & \omega_q & \omega_t & \omega_s & \omega_r \end{bmatrix}^{\mathrm{T}}, \qquad \mathbf{F} = \begin{bmatrix} F_{pr} & F_{pt} & F_{qp} & F_{qs} \end{bmatrix}^{\mathrm{T}}. \tag{3.9}$$

The order of the speed variables ω_i in $\boldsymbol{\omega}$ completely defines the structures of matrices $\mathbf{J}$, $\mathbf{B}_\omega$ and vector $\boldsymbol{\tau}$:

$$\mathbf{J} = \begin{bmatrix} J_c & 0 & 0 & 0 & 0 & 0 \\ 0 & J_p & 0 & 0 & 0 & 0 \\ 0 & 0 & J_q & 0 & 0 & 0 \\ 0 & 0 & 0 & J_t & 0 & 0 \\ 0 & 0 & 0 & 0 & J_s & 0 \\ 0 & 0 & 0 & 0 & 0 & J_r \end{bmatrix}, \qquad \mathbf{B}_\omega = \begin{bmatrix} b_c & 0 & 0 & 0 & 0 & 0 \\ 0 & b_p & 0 & 0 & 0 & 0 \\ 0 & 0 & b_q & 0 & 0 & 0 \\ 0 & 0 & 0 & b_t & 0 & 0 \\ 0 & 0 & 0 & 0 & b_s & 0 \\ 0 & 0 & 0 & 0 & 0 & b_r \end{bmatrix}, \qquad \boldsymbol{\tau} = \begin{bmatrix} \tau_c \\ \tau_p \\ \tau_q \\ \tau_t \\ \tau_s \\ \tau_r \end{bmatrix}. \tag{3.10}$$

The order of the force variables F_{ij} within vector $\mathbf{F}$ in (3.9) completely defines the

structures of matrices $\mathbf{K}$ and $\mathbf{B}_K$:

$$\mathbf{K}=\begin{bmatrix} K_{pr} & 0 & 0 & 0 \\ 0 & K_{pt} & 0 & 0 \\ 0 & 0 & K_{qp} & 0 \\ 0 & 0 & 0 & K_{qs} \end{bmatrix}, \qquad \mathbf{B}_K=\begin{bmatrix} d_{pr} & 0 & 0 & 0 \\ 0 & d_{pt} & 0 & 0 \\ 0 & 0 & d_{qp} & 0 \\ 0 & 0 & 0 & d_{qs} \end{bmatrix}. \tag{3.11}$$

The only two matrices which are not yet defined in (3.1) are the radii matrix $\mathbf{R}$ and the relative friction matrix $\mathbf{B}_{\Delta\omega}$.

3.2.1 Algorithm 1: calculation of the radii matrix R

Let $r_{ij,h}$ denote the generic coefficient of matrix $\mathbf{R} = [r_{ij,h}]$, where $ij \in \mathcal{N}_K$ and $h \in \mathcal{N}_J$, see (3.8). Coefficient $r_{ij,h}$ links the angular speed ω_h of gear h to the tangential speed of one of the two terminals of the tangential force F_{ij}.

Property 1 The generic coefficient $r_{ij,h}$ of the radii matrix $\mathbf{R}$ can be computed as follows:

$$r_{ij,h} = S_{F_{ij}}\, S_{\omega_h}\, r_h, \tag{3.12}$$

where:

a) r_h is the "*effective radius*" which links the angular speed ω_h to the tangential force F_{ij}. The following two cases can be distinguished: 1) if the angular speed ω_h directly affects the force F_{ij}, see the direct contact of Fig. 3.5.a, then the effective radius r_h coincides with the radius of the gear which links velocity ω_h to force F_{ij}; 2) if the angular speed ω_h affects the force F_{ij} through an intermediate gear "p", see the indirect contacts of Fig. 3.5.b, then the effective radius r_h coincides with the distance between the rotation axes of the two angular speeds ω_h and ω_p.

b) $S_{F_{ij}}$ is the sign of the positive orientation of vector F_{ij}:

$$S_{F_{ij}} = \begin{cases} 1 & \text{if } i = h \text{ (direct) or } i = p \text{ (indirect)}, \\ -1 & \text{if } j = h \text{ (direct) or } j = p \text{ (indirect)}. \end{cases}$$

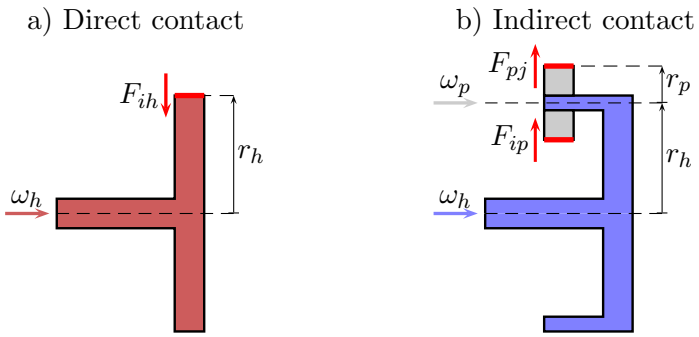

Figure 3.5: *Effective radii* r_h: a) Direct contact; b) Indirect contact.

c) S_{ω_h} is related to the sign of the velocity vector ω_h:

$$S_{\omega_h} = \begin{cases} 1 & \text{if force } F_{ij} \text{ is on the left of vector } \omega_h, \\ -1 & \text{if force } F_{ij} \text{ is on the right of vector } \omega_h. \end{cases}$$

The left and right sides of vector ω_h are determined by moving along the positive direction of vector ω_h.

Example. By applying the previous rules to the gears shown in Fig. 3.5, one obtains: a) the coefficient $r_{ih,h}$ associated with the "direct" contact is $r_{ih,h} = -r_h$ because $S_{F_{ih}} = -1$ and $S_{\omega_h} = 1$; b) the coefficients $r_{pj,h}$ and $r_{ip,h}$ associated with the "indirect" contacts are: $r_{pj,h} = r_h$ because $S_{F_{pj}} = 1$ and $S_{\omega_h} = 1$; $r_{ip,h} = -r_h$ because $S_{F_{ip}} = -1$ and $S_{\omega_h} = 1$.

From (3.1), it can be easily shown that $\dot{x}_{ij} = r_{ij,h}\,\omega_h$ is the tangential speed of one of the two terminals of the spring K_{ij} when the angular speed ω_h moves along its positive direction. Since the sign of $\dot{x}_{ij}$ directly affects the sign of F_{ij}, it results that $\dot{x}_{ij}$ must change sign both when the velocity vector ω_h and the force vector F_{ij} change their positive direction. Fig. 3.6 graphically shows why the *effective radii* are equal to r_h for both the cases a) and b) of direct and indirect contact. In particular, with reference to the indirect contact case b), the tangential speed $\dot{x}_{hp} = r_h\,\omega_h$ is equal to the tangential speeds $\dot{x}_{pj}$ and $\dot{x}_{ip}$ of the two elastic elements K_{pj} and K_{ip}. This holds because the angular speed ω_p is kept equal to zero when ω_h moves along its positive direction.

By applying the systematic rules given in Property 1 to the Ravigneaux planetary gear set of Fig. 3.4, one obtains the following radii matrix $\mathbf{R}$:

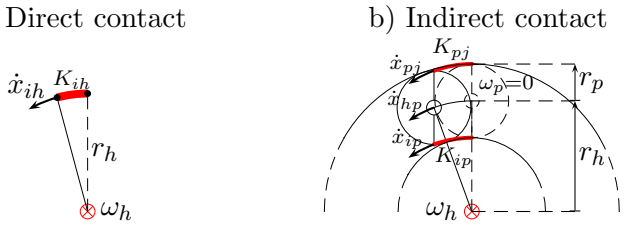

Figure 3.6: Angular speeds ω_h and tangential velocities $\dot{x}_{hj}$.

$$\mathbf{R}=\begin{array}{c} \\ pr \\ pt \\ qp \\ qs \end{array}\begin{array}{c} \begin{array}{cccccc} c & p & q & t & s & r \end{array} \\ \begin{bmatrix} r_{c2} & r_p & 0 & 0 & 0 & -r_r \\ r_{c2} & -r_p & 0 & -r_t & 0 & 0 \\ r_{c1}-r_{c2} & r_p & r_q & 0 & 0 & 0 \\ r_{c1} & 0 & -r_q & 0 & -r_s & 0 \end{bmatrix} \end{array}. \tag{3.13}$$

The coefficient $r_{qp,c}=r_{c1}-r_{c2}$ highlighted in (3.13) describes the interaction between the angular speed ω_c and the tangential force F_{qp}. This coefficient is obtained using the superposition principle: a) the first term $r'_{qp,c}=r_{c1}$ is related to ω_c affecting F_{qp} through gear "q", being r_{c1} the effective radius, for which: $S_{F_{qp}}=1$ and $S_{\omega_c}=1$ hold; b) the second term $r''_{qp,c}=-r_{c2}$ is related to ω_c affecting F_{qp} through gear "p", being r_{c2} the effective radius, for which $S_{F_{qp}}=-1$ and $S_{\omega_c}=1$ hold. The parameters within the radii matrix $\mathbf{R}$ in (3.13) are constrained as follows:

$$r_q=\frac{r_t}{2}-\frac{r_s}{2},\qquad r_p=\frac{r_r}{2}-\frac{r_t}{2},\qquad r_{c1}=\frac{r_s}{2}+\frac{r_t}{2},\qquad r_{c2}=\frac{r_r}{2}+\frac{r_t}{2}. \tag{3.14}$$

The constraints in (3.14) easily follow from Fig. 3.4. Substituting (3.14) in (3.13), one obtains the following equivalent form of the radii matrix $\mathbf{R}$:

$$\mathbf{R}=\begin{array}{c} \\ pr \\ pt \\ qp \\ qs \end{array}\begin{array}{c} \begin{array}{cccccc} c & p & q & t & s & r \end{array} \\ \begin{bmatrix} \frac{r_r}{2}+\frac{r_t}{2} & \frac{r_r}{2}-\frac{r_t}{2} & 0 & 0 & 0 & -r_r \\ \frac{r_r}{2}+\frac{r_t}{2} & \frac{r_t}{2}-\frac{r_r}{2} & 0 & -r_t & 0 & 0 \\ \frac{r_s}{2}-\frac{r_r}{2} & \frac{r_r}{2}-\frac{r_t}{2} & \frac{r_t}{2}-\frac{r_s}{2} & 0 & 0 & 0 \\ \frac{r_s}{2}+\frac{r_t}{2} & 0 & \frac{r_s}{2}-\frac{r_t}{2} & 0 & -r_s & 0 \end{bmatrix} \end{array}. \tag{3.15}$$

Remark 1 *Let us consider all the planetary gear sets that can rotate along a fixed axis when all the gears in the set are locked together. As an example, refer to the case studies shown in Fig. 3.4 and Fig. 3.14. Let* $\mathbf{d}_\omega = \begin{bmatrix} d_1 \; d_2 \; \dots \; d_{n_J} \end{bmatrix}^T$ *denote a vector whose components* d_i *are defined as follows:*

$$d_i = \begin{cases} 1 & \text{if the vectors } \vec{\omega}_i \text{ and } \vec{\omega}_1 \text{ have the same direction,} \\ -1 & \text{otherwise.} \end{cases}$$

One can easily verify that, for the considered planetary gear sets, vector $\mathbf{d}_\omega$ *belongs to the kernel of matrix* $\mathbf{R}$*, that is* $\mathbf{R}\,\mathbf{d}_\omega = 0$*. As far as the Ravigneaux planetary gear set in Fig. 3.4 is concerned,* $d_i = 1$ *holds for* $i = [1,\ 2,\ \dots,\ n_J]$*. Therefore, the relation* $\mathbf{R}\,\mathbf{d}_\omega = 0$ *implies that the sum of all the elements contained within each row of matrix* $\mathbf{R}$ *equals zero.*

This property can be easily proven true by referring to the matrix $\mathbf{R}$ in (3.15) as an example. From a physical point of view, this property means that $d_1\omega_1 = d_2\omega_2 = \dots = d_{n_J}\omega_{n_J} \neq 0$ is a feasible operating condition for the considered system. Note: this property does not apply to the three-gears system in Fig. 3.1.

3.2.2 Algorithm 2: calculation of the relative friction matrix $\mathbf{B}_{\Delta\omega}$

Let B_{ij} denote the generic coefficient of matrix $\mathbf{B}_{\Delta\omega} = [B_{ij}]$ where $i, j \in \mathcal{N}_J$, with the set $\mathcal{N}_J$ is defined in (3.8).

Property 2 The generic coefficient B_{ij} of the relative friction matrix $\mathbf{B}_{\Delta\omega}$ can be computed as:

$$B_{ij} = \begin{cases} \displaystyle\sum_{pq \in \mathcal{N}_i} b_{pq} & \text{if} \quad i = j, \\ S_{ij}\bar{b}_{ij} & \text{if} \quad i \neq j, \end{cases} \tag{3.16}$$

where $\mathcal{N}_i$ is a set of subscripts "pq" defined as follows:

$$\mathcal{N}_i = \{\text{all the subscripts } pq \in \mathcal{N}_B \text{ such that } p = i \text{ or } q = i\}$$

$\mathcal{N}_B$ is defined in (3.8), $\bar{b}_{ij}$ is the relative friction coefficient defined as:

$$\bar{b}_{ij} = \begin{cases} b_{ij} & \text{if} \quad ij \in \mathcal{N}_B, \\ b_{ji} & \text{if} \quad ji \in \mathcal{N}_B, \\ 0 & \text{if} \quad \text{otherwise}, \end{cases}$$

and S_{ij} is a sign function defined as:

$$S_{ij} = \begin{cases} -1 \text{ if } \omega_i \text{ and } \omega_j \text{ have the same positive direction}, \\ 1 \text{ if } \omega_i \text{ and } \omega_j \text{ have different positive direction}, \\ 0 \text{ if } \bar{b}_{ij} = 0. \end{cases}$$

Note: according to (3.16), all the coefficients B_{ii} on the diagonal of matrix $\mathbf{B}_{\Delta\omega}$ are always positive.

Applying the systematic rules given in Property 2, one can build the following relative friction matrix $\mathbf{B}_{\Delta\omega}$ for the considered Ravigneaux planetary gear set:

$$\mathbf{B}_{\Delta\omega} = \begin{array}{c} \\ c \\ p \\ q \\ t \\ s \\ r \end{array} \begin{array}{c} \begin{array}{cccccc} c & p & q & t & s & r \end{array} \\ \begin{bmatrix} b_{cp}+b_{cq}+b_{cr} & -b_{cp} & -b_{cq} & 0 & 0 & -b_{cr} \\ -b_{cp} & b_{cp} & 0 & 0 & 0 & 0 \\ -b_{cq} & 0 & b_{cq} & 0 & 0 & 0 \\ 0 & 0 & 0 & b_{st} & -b_{st} & 0 \\ 0 & 0 & 0 & -b_{st} & b_{st} & 0 \\ -b_{cr} & 0 & 0 & 0 & 0 & b_{cr} \end{bmatrix} \end{array}. \tag{3.17}$$

The generic relative friction coefficient b_{ij} within matrix $\mathbf{B}_{\Delta\omega}$, acting in between gears "i" and "j", can have two different meanings. In fact, it can either be an actual relative friction coefficient within the system or be used to represent a lockup clutch between the two gears. The two limit cases of $b_{ij} \to 0$ and $b_{ij} \to b_{ij}^{\infty}$, where b_{ij}^{∞} has to be sufficiently large, represent the case of open and closed lockup clutch, respectively. This enables the simulation of different operating modes of the transmission system. The proposed model also allows to apply a nonlinear control

to a lockup clutch inserted in between two gears of the system: this can be done by inserting an external control acting on the system input and output vectors $\mathbf{u} = \boldsymbol{\tau}$ and $\mathbf{y} = \boldsymbol{\omega}$.

The vectors and the matrices defined in (3.9), (3.10), (3.11), (3.13) and (3.17) completely define the full elastic model (3.1) of the considered Ravigneaux planetary gear set.

3.2.3 Reduced-order rigid model

Let us assume all the coefficients K_{ij}, for $ij \in \mathcal{N}_K$, within the stiffness matrix $\mathbf{K}$ in (3.11) to tend to infinity. From the state space model (3.1), one obtains the following $n_K = 4$ constraints among the gears angular speeds:

$$\mathbf{R}\,\boldsymbol{\omega} = \mathbf{0} \;\Leftrightarrow\; \begin{cases} r_{c2}\,\omega_c + r_p\,\omega_p - r_r\,\omega_r = 0, \\ r_{c2}\,\omega_c - r_p\,\omega_p - r_t\,\omega_t = 0, \\ r_p\,\omega_p + r_q\,\omega_q + \omega_c(r_{c1} - r_{c2}) = 0, \\ r_{c1}\,\omega_c - r_q\,\omega_q - r_s\,\omega_s = 0. \end{cases} \tag{3.18}$$

These constraints can be used to express n_K angular speeds of the system as a function of the remaining $n_r = n_J - n_K = 2$ angular speeds. The integer n_r also represents the order of the reduced-order rigid model obtained when $\mathbf{K} \to \infty$. Let $\mathbf{x}_1 = \begin{bmatrix} \omega_c & \omega_r \end{bmatrix}^{\mathrm{T}}$ be the state vector of the reduced-order rigid model. Using constraints (3.18) and (3.14), the original state vector $\mathbf{x}$ can be expressed as a function of the new state vector $\mathbf{x}_1$ as:

$$\mathbf{x} = \mathbf{T}_1\,\mathbf{x}_1 \;\Leftrightarrow\; \underbrace{\begin{bmatrix} \boldsymbol{\omega} \\ \mathbf{F} \end{bmatrix}}_{\mathbf{x}} = \underbrace{\begin{bmatrix} \mathbf{Q}_1 \\ \mathbf{0} \end{bmatrix}}_{\mathbf{T}_1} \underbrace{\begin{bmatrix} \omega_c \\ \omega_r \end{bmatrix}}_{\mathbf{x}_1}, \quad \text{where} \quad \mathbf{Q}_1 = \begin{bmatrix} 1 & 0 \\ -\frac{n_1-1}{n_1+1} & \frac{2n_1}{n_1+1} \\ \frac{n_1+n_2-2n_1n_2}{n_1+n_2} & \frac{2n_1n_2}{n_1+n_2} \\ 1-n_1 & n_1 \\ 1-n_2 & n_2 \\ 0 & 1 \end{bmatrix}. \tag{3.19}$$

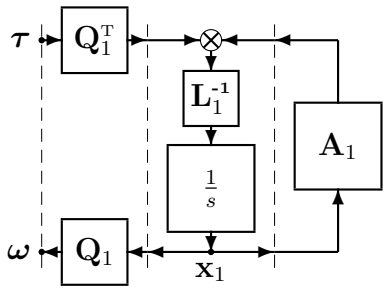

Figure 3.7: Reduced-order rigid POG scheme of gearing systems.

The parameters n_1 and n_2 in (3.19) denote the *ring-over-large sun* and the *ring-over-small sun* gear ratios, respectively:

$$n_1 = -r_r/r_t, \qquad n_2 = r_r/r_s. \tag{3.20}$$

By applying the congruent transformation $\mathbf{x} = \mathbf{T}_1\,\mathbf{x}_1$ to system (3.1), see [2], one obtains the following state space model $\mathbf{L}_1\dot{\mathbf{x}}_1 = \mathbf{A}_1\mathbf{x}_1 + \mathbf{B}_1\mathbf{u}$ of the reduced-order rigid system:

$$\underbrace{\begin{bmatrix} J_{11} & J_{12} \\ J_{12} & J_{22} \end{bmatrix}}_{\mathbf{L}_1} \dot{\mathbf{x}}_1 = \underbrace{\begin{bmatrix} a_{11} & a_{12} \\ a_{12} & a_{22} \end{bmatrix}}_{\mathbf{A}_1} \mathbf{x}_1 + \underbrace{\mathbf{Q}_1^{\mathrm{T}}}_{\mathbf{B}_1} \underbrace{\boldsymbol{\tau}}_{\mathbf{u}}, \tag{3.21}$$

where matrices $\mathbf{L}_1$, $\mathbf{A}_1$ and $\mathbf{B}_1$ have the following structure:

$$\begin{cases} \mathbf{L}_1 = \mathbf{T}_1^{\mathrm{T}}\mathbf{L}\,\mathbf{T}_1 = \mathbf{Q}_1^{\mathrm{T}}\mathbf{J}\,\mathbf{Q}_1, \\ \mathbf{A}_1 = \mathbf{T}_1^{\mathrm{T}}\mathbf{A}\,\mathbf{T}_1 = -\underbrace{\mathbf{Q}_1^{\mathrm{T}}\mathbf{R}^{\mathrm{T}}\mathbf{B}_K\mathbf{R}\,\mathbf{Q}_1}_{\mathbf{0}} - \mathbf{Q}_1^{\mathrm{T}}\mathbf{B}_J\mathbf{Q}_1, \\ \mathbf{B}_1 = \mathbf{T}_1^{\mathrm{T}}\mathbf{B} = \mathbf{Q}_1^{\mathrm{T}}. \end{cases} \tag{3.22}$$

The term $\mathbf{Q}_1^{\mathrm{T}}\mathbf{R}^{\mathrm{T}}\mathbf{B}_K\mathbf{R}\,\mathbf{Q}_1$ in (3.22) is equal to zero because $\mathbf{Q}_1 \in \ker(\mathbf{R})$:

$$\mathbf{R}\,\boldsymbol{\omega} = \mathbf{0} \;\Leftrightarrow\; \mathbf{R}\,\mathbf{Q}_1\,\mathbf{x}_1 = \mathbf{0} \;\Leftrightarrow\; \mathbf{R}\,\mathbf{Q}_1 = \mathbf{0}. \tag{3.23}$$

The full expressions of the elements L_{ij} and a_{ij} within the energy matrix $\mathbf{L}_1$ and the power matrix $\mathbf{A}_1$ are not reported for the sake of brevity, as they can be straightforwardly computed using (3.22). The reduced-order rigid model given in (3.21) can be graphically represented using the POG block scheme in Fig. 3.7.

The constraints among the angular speeds of the Ravigneaux planetary gear set that were derived in [74] using the Willis equation (see Eqs. (3)-(4) in [74]) are the

same as those obtained using the presented systematic approach: see the fourth and fifth rows of system $\boldsymbol{\omega} = \mathbf{Q}_1 \mathbf{x}_1$ in (3.19). Additionally, the static input torques balance given in Eqs. (5)-(6) in [74] is equivalent to the following constraint:

$$\mathbf{B}_1 \boldsymbol{\tau} = \mathbf{Q}_1^{\mathrm{T}} \boldsymbol{\tau} = 0. \tag{3.24}$$

The latter equation can be obtained at steady-state from the first equation of system (3.1) when $\mathbf{B}_J = 0$, that is when the friction terms within the system are neglected.

3.2.4 Calculation of the force vector F

The reduced-order rigid system (3.21) no longer contains any information regarding the force vector $\mathbf{F}$. Nevertheless, vector $\mathbf{F}$ can be obtained from the reduced-order rigid system (3.21), as described by Property 3 illustrated in the following.

Property 3 The time behavior of the force vector $\mathbf{F}$ can be obtained from the state vector $\mathbf{x}_1$ and the input vector $\mathbf{u} = \boldsymbol{\tau}$ of the reduced rigid system (3.21) using the following relation:

$$\mathbf{F} = (\mathbf{R}\mathbf{J}^{-1}\mathbf{R}^{\mathrm{T}})^{-1}\mathbf{R}\mathbf{J}^{-1}(\boldsymbol{\tau} - \mathbf{B}_J\mathbf{Q}_1\mathbf{x}_1). \tag{3.25}$$

Proof. The proof is reported in App. A.

Remark 2 *The relation (3.25) can be very useful because it provides the tangential forces F_{ij} between the gears as a function of the input vector $\boldsymbol{\tau}$ and of the state vector $\mathbf{x}_1$ in the reduced-order rigid model (3.21).*

Note that relation (3.25) can be implemented offline.

3.2.5 Lever Analogy model

A different approach for computing the kinematic relations of a planetary gear set is the Lever Analogy [6]. The considered Ravigneaux planetary gear set can be seen as the combination of two planetary gear sets:

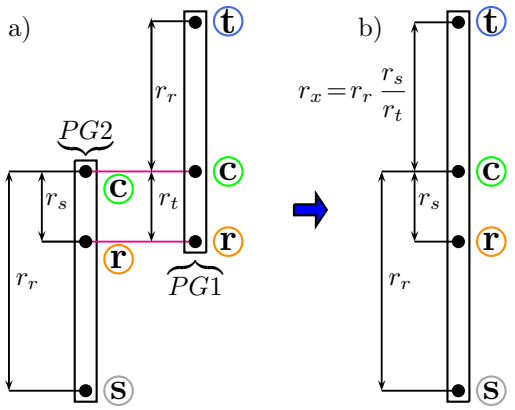

Figure 3.8: Ravigneaux planetary gear set: Lever Diagrams.

i) a single planetary gear set $PG1$, where the sun, the planet pinions, the ring and the carrier are represented by gears "t", "p", "r" and "c", respectively;

ii) a planetary gear set $PG2$ with two sets of planet pinions, where the sun, the outer planet pinions, the inner planet pinions, the ring and the carrier are represented by gears "s", "p", "q", "r" and "c", respectively.

$PG1$ and $PG2$ share the same ring and the same carrier inertial elements. The procedure to follow in order to build a Lever Diagram [6] is the following:

1. replacement of each gear with a vertical lever;
2. rescaling, interconnection and/or combination of levers accordingly;
3. identification of the lever connections, according to the gears connections.

The lever diagrams of the two planetary gear sets $PG1$ and $PG2$ are shown in Fig. 3.8.a). The interconnections between the gears are denoted in Fig. 3.8.a) by horizontal links [6] highlighted in magenta. The whole lever diagram of the Ravigneaux planetary gear set [77] is obtained by rescaling the diagram of $PG1$ with respect to the diagram of $PG2$ according to the following proportion:

$$r_r : r_x = r_t : r_s.$$

The resulting diagram is shown in Fig. 3.8.b). In order to derive the kinematic relations between the angular speeds ω_i, two different scenarios can be considered. In the first scenario, gear "c" is held fixed and gear "r" rotates clockwise. In the second scenario, gear "r" is held fixed and gear "c" rotates clockwise. By applying the superposition principle to these two scenarios, one obtains the following speed equations:

$$\omega_t = \omega_c \left(1 + \frac{r_r}{r_t}\right) - \omega_r \frac{r_r}{r_t}, \qquad \omega_s = \omega_c \left(1 - \frac{r_r}{r_s}\right) + \omega_r \frac{r_r}{r_s},$$

which coincide with those reported in the fourth and fifth rows of system (3.19) using (3.20). In order to derive the torque equations, two torque balances can be applied, considering the ring first and the carrier next as fulcrum, respectively. The obtained torque equations coincide with those given by constraint (3.24). The rotational inertias can finally be included in the diagram by attaching masses to the lever and solving force and moment balance equations [6].

3.2.6 Systematic POG-based approach versus Lever Analogy

The main differences between the POG-based approach and the Lever Analogy approach are listed in the following:

a) *In the POG-based approach, step 1) of the Lever Diagram procedure reported in Sec. 3.2.5 is replaced by the drawing of a simple 2D graphical representation of the considered planetary gear set, such as the one shown in Fig. 3.4.*

b) *In the POG-based approach, step 2) of the Lever Diagram procedure is not required*, since the elements in common to $PG1$ and $PG2$ are not treated as two separated elements, but as a unique inertial element interacting with $PG1$ and $PG2$.

c) *In the POG-based approach, step 3) of the Lever Diagram procedure is automatically incorporated in the definition of set $\mathcal{N}_J$, set $\mathcal{N}_K$ and set $\mathcal{N}_B$.*

d) *The POG-based approach gives both a full dynamic model and a reduced-order rigid model of the considered system.* The reduced-order model allows for faster simulations. Furthermore, the behavior of the forces that are exchanged at the gears

contact points is not lost, as it can be recovered using Property 3.

The POG-based approach proposed in this work of thesis offers the advantages of being systematic, flexible, and of providing a *general model which is directly implementable in the Matlab/Simulink environment*. The systematic property refers to the fact that the procedure for building the model lies on two simple algorithms which can be automatically implemented, once sets $\mathcal{N}_J$, $\mathcal{N}_K$ and $\mathcal{N}_B$ are defined. The flexibility property refers to the fact that the user can very easily choose which relative frictions b_{ij} must be present in the system by defining set $\mathcal{N}_B$. Additionally, the user can freely choose which angular speeds ω_i are to be kept in the state vector of the reduced-order rigid model. The general scheme shown in Fig. 3.3 can be used to model any planetary gear set, and is composed of basic blocks that can be found in the standard Simulink libraries.

In conclusion, the Lever Analogy is mainly suitable for the system kinematic analysis and gives a good understanding of the system thanks to the intuitive comparison with levers. On the other hand, the proposed systematic POG-based approach is suitable for simulation and control purposes. This is thanks to the fact that the system model is general and directly implementable in the Matlab/Simulink environment, and thanks to the fact that the system matrices and vectors are systematically built.

3.2.7 Simulation results with reference to a power-split HEV

The Ravigneaux planetary gear set of Fig. 3.4 has been simulated in order to compare the dynamic behavior and the simulation time of the following two models: the full elastic model given in (3.1) and the reduced-order rigid model given in (3.21). The parameters of the the considered planetary gear set are reported in Tab. 3.1. The simulation results refer to a real case scenario, where the Ravigneaux planetary set gear is exploited as a power-split device in a HEV architecture.

Reference is made to the power-split architecture of a hybrid agricultural vehicle shown in Fig. 3.9. The architecture is composed of three power sources. The first one is an ICE rigidly connected to gear "s". The other two power sources are the electric machines EM1 and EM2, which are rigidly connected to gears "t" and

Table 3.1: Ravigneaux planetary gear set: simulation parameters.

$r_r = 21$ cm	$J_c = 17280$ kg mm^2
$r_s = 7$ cm	$J_p = 3456$ kg mm^2
$r_t = 10.5$ cm	$J_q = 1728$ kg mm^2
$r_q = 1.75$ cm	$J_t = 8640$ kg mm^2
$r_p = 5.25$ cm	$J_s = 5184$ kg mm^2
$r_{c1} = 8.75$ cm	$J_r = 15552$ kg mm^2
$r_{c2} = 15.75$ cm	$b_c = 0.01$ Nm/rpm
$b_p = b_q = b_t = b_c$	$b_s = b_r = b_c$
$b_{st} = 0.01$ Nm/rpm	$b_{cr} = b_{cq} = b_{cp} = b_{st}$
$K_{pt} = K_{pr} = 300000$ N/mm	$K_{qp} = K_{qs} = K_{pt}$
$d_{pt} = 0.1$ N sec/cm	$d_{pr} = d_{qp} = d_{qs} = d_{pt}$

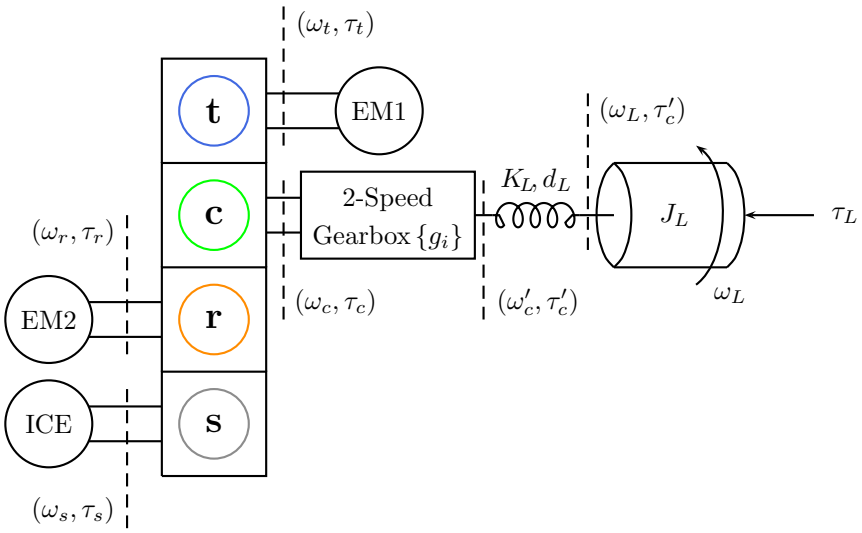

Figure 3.9: Power-split architecture of a hybrid agricultural vehicle.

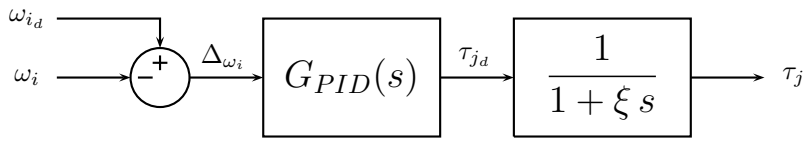

Figure 3.10: Electric machines EM1 and EM2: control and modeling.

"r", respectively. The gear denoted by subscript "c" is rigidly connected to a 2-Speed gearbox, which allows for gear shifting in the considered architecture. The gearbox output shaft is connected to the load inertia J_L through a rotational spring K_L, which accounts for the gearbox elasticity. Furthermore, a friction coefficient d_L is associated with the rotational spring K_L, accounting for the losses occurring during the transients. The overall load inertia J_L includes the inertia of the gearbox output shaft, the inertia of the wheels through the differential, as well as the vehicle mass through the differential and the wheels radius. The external load torque τ_L accounts for the load that the transmission experiences when the agricultural vehicle is operating. Since the objective is to test the full and reduced-order dynamic models of the considered Ravigneaux planetary gear set, a simplified model has been adopted for the three power sources. The ICE is assumed to be a torque generator providing a constant torque $\tau_s = 820\,\text{Nm}$. Since the ICE is rigidly connected to gear "s", its inertia is included in J_s within matrix $\mathbf{J}$ in (3.10). In the considered scenario, the ICE is controlled to maintain a desired constant speed $\omega_{s_d} = 1400\,[\text{rpm}]$. The electric machines EM1 and EM2 are assumed to have a first-order step torque response with a time constant ξ. The considered first-order dynamics only accounts for the electric part of the machines, since EM1 and EM2 are rigidly connected to gears "t" and "r", respectively. A speed control is applied to each electric machine using two PID (Proportional-Integral-Derivative) regulators, as shown in Fig. 3.10. The two PID regulators are characterized by the following transfer function:

$$G_{PID}(s) = C_P\,(C_D\,s + 1) + \frac{C_P}{C_I\,s}, \tag{3.26}$$

where C_P, C_D and C_I are three design parameters. The PID regulator of EM2 determines a desired torque τ_{r_d} in order to keep the ICE speed ω_s equal to the desired speed target ω_{s_d}. Similarly, the PID regulator of EM1 determines a desired

Table 3.2: Architecture in Fig. 3.9 and Fig. 3.10: transmission parameters and initial conditions.

$g_1 = 0.2296$	$g_2 = 0.7273$
$K_L = 50$ kNm/°	$d_L = 42$ Nm/rpm
$J_L = 19.16$ kg m^2	$C_P = 80.75$
$C_D = 0.12 \cdot 10^{-3}$	$C_I = 0.24$
$\xi = 4.7$ ms	$\boldsymbol{\omega}_0$=[0 0 0 0 1400 0]$^{\mathrm{T}}$ rpm, $\mathbf{F}_0$=[0 0 0 0]$^{\mathrm{T}}$ N

torque τ_{t_d} in order to make the gearbox input shaft speed ω_c follow the desired speed profile ω_{c_d}. The gearbox input and output shafts speeds ω_c and ω'_c are related as follows:

$$\omega'_c = \omega_c \, g_i,$$

where $g_i \in \left\{ g_1, \, g_2 \right\}$ is the engaged gear ratio. The angular speed ω'_c is equal to the load angular speed ω_L at steady-state, while they are slightly different during the transients because of the presence of the stiffness K_L. The positive directions of the angular speeds ω_i and of the tangential forces F_{ij} in the Ravigneaux planetary gear set are those given in Fig. 3.4. The parameters of the mechanical transmission connected to the carrier "c" and the initial conditions of the system are reported in Tab. 3.2. The simulation results of the controlled system are shown in Fig. 3.11, Fig. 3.12 and Fig. 3.13. The time behaviors of the load speed ω_L, the gearbox output shaft speed ω'_c, the motive torque τ'_c, the load torque τ_L and of the engaged gear signal are shown in Fig. 3.11. The profile of the load torque τ_L has been chosen to simulate a realistic load torque profile for an agricultural vehicle, which typically travels over an uneven ground. The time behaviors of the angular speeds ω_i of the Ravigneaux planetary gear set, as well as the desired angular speeds ω_{c_d} and ω_{s_d} of the carrier "c" and of the small sun "s", are shown in Fig. 3.12. The figure clearly shows that the objective of the control is achieved: the angular speeds ω_c and ω_s follow the desired speeds ω_{c_d} and ω_{s_d}, respectively. Finally, the time behaviors of the torques τ_i and of the forces F_{ij} of the Ravigneaux planetary gear set are shown in Fig. 3.13.

The simulation results shown in Fig. 3.11, Fig. 3.12 and Fig. 3.13 have been

obtained using the reduced-order model (3.21) of the Ravigneaux planetary gear set, together with Eq. (3.25) in Property 3 for the offline calculation of the contact forces. The same simulation has also been performed using the full model (3.1): the corresponding simulation results are not reported in this work of thesis because they almost coincide with the ones reported in Fig. 3.11, Fig. 3.12 and Fig. 3.13. The resulting simulation times obtained using a "`ode23s (stiff/Mod. Rosenbrock)`" variable-step solver are the following: 57.43 s using the full model and 29.95 s using the reduced-order model. The simulation times could change by employing a different computer and/or a different version of Matlab/Simulink, but still the result clearly shows the saving in terms of simulation time given by the use of the reduced-order model with respect to the full one.

The power-split architecture in Fig. 3.9 has also been simulated using a "`ode4 (Runge/Kutta)`" fixed-step solver with a step size of 10^{-4} s. The obtained simulation time using the reduced-order model of the Ravigneaux planetary gear set in the considered hybrid architecture is 7.24 s. The corresponding simulation results are not reported in this work of thesis because they almost coincide with the ones reported in Fig. 3.11, Fig. 3.12 and Fig. 3.13. The simulation using the full model could not be terminated with the considered step size due to the high-frequency internal dynamics caused by the high stiffness of the planetary gear set contact points, meaning that a lower step size is needed when using the full model.

In conclusion, both the full and the reduced-order dynamic models of the planetary gear set are suitable for being used in the simulation of HEVs, but with different purposes. The full model represents a more detailed modeling of the planetary gear set, because it accounts for the gears elastic contact points as well. On the other hand, the reduced-order model is more suitable for real-time execution, because it allows to use fixed-step solvers with a larger step size.

3.3 Modeling a double-stage planetary gear set

Let us now consider the double-stage planetary gear set shown in Fig. 3.14. For this system, the sets $\mathcal{N}_J$, $\mathcal{N}_K$, $\mathcal{N}_B$ and the parameters n_J, n_K, n_B defined at the

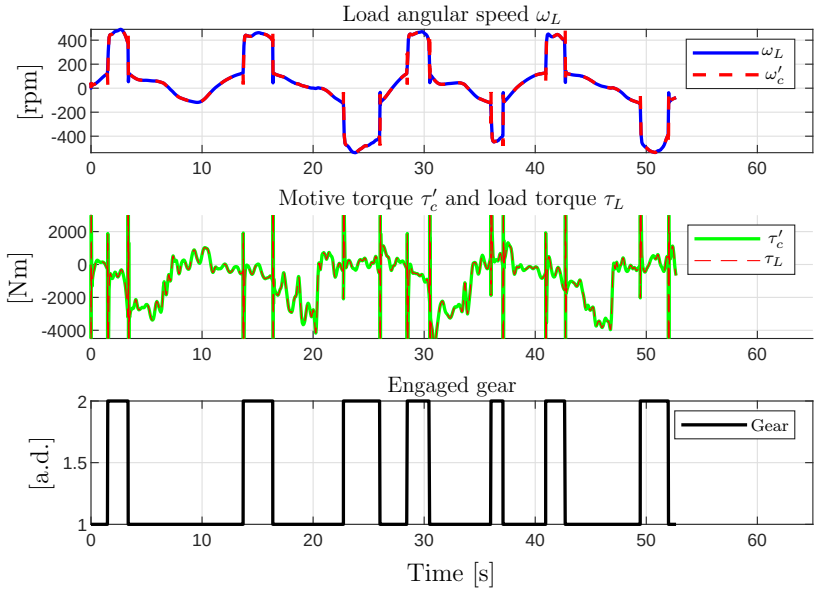

Figure 3.11: Hybrid agricultural vehicle: simulation results from the gearbox to the load.

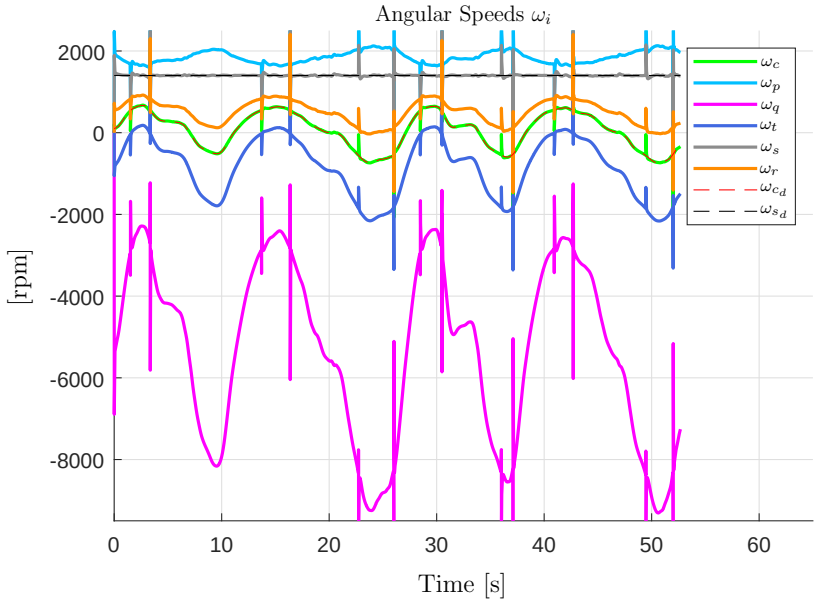

Figure 3.12: Hybrid agricultural vehicle: angular speeds of the Ravigneaux planetary gear set.

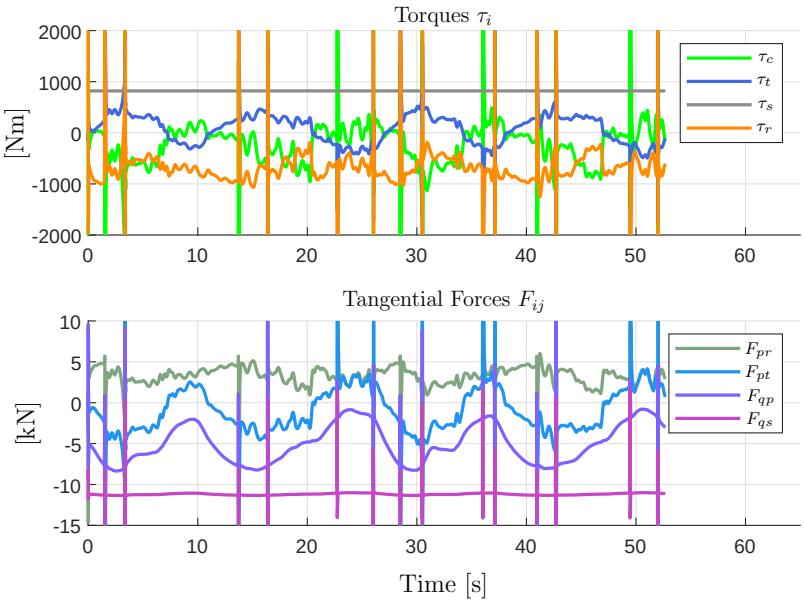

Figure 3.13: Hybrid agricultural vehicle: torques and tangential contact forces of the Ravigneaux planetary gear set.

beginning of Sec. 3.2 are:

$$\begin{cases} \mathcal{N}_J = \{s,\, c,\, p,\, a,\, r,\, b,\, q\}, & n_J = \dim(\mathcal{N}_J) = 7, \\ \mathcal{N}_K = \{sp,\, sa,\, pr,\, ba,\, bq\}, & n_K = \dim(\mathcal{N}_K) = 5, \\ \mathcal{N}_B = \{sr,\, ca,\, cb,\, cp,\, cq\}, & n_B = \dim(\mathcal{N}_B) = 5. \end{cases} \tag{3.27}$$

The considered system can be modeled using the POG scheme shown in Fig. 3.3. Let us choose the speed vector $\boldsymbol{\omega}$, the input torque vector $\boldsymbol{\tau}$ and the force vector $\mathbf{F}$ as follows:

$$\boldsymbol{\omega} = \begin{bmatrix} \omega_s \\ \omega_c \\ \omega_p \\ \omega_a \\ \omega_r \\ \omega_b \\ \omega_q \end{bmatrix}, \qquad \boldsymbol{\tau} = \begin{bmatrix} \tau_s \\ \tau_c \\ \tau_p \\ \tau_a \\ \tau_r \\ \tau_b \\ \tau_q \end{bmatrix}, \qquad \mathbf{F} = \begin{bmatrix} F_{ps} \\ F_{sa} \\ F_{pr} \\ F_{ba} \\ F_{bq} \end{bmatrix}. \tag{3.28}$$

The order of the speed variables ω_i and of the force variables F_{ij} within vectors $\boldsymbol{\omega}$

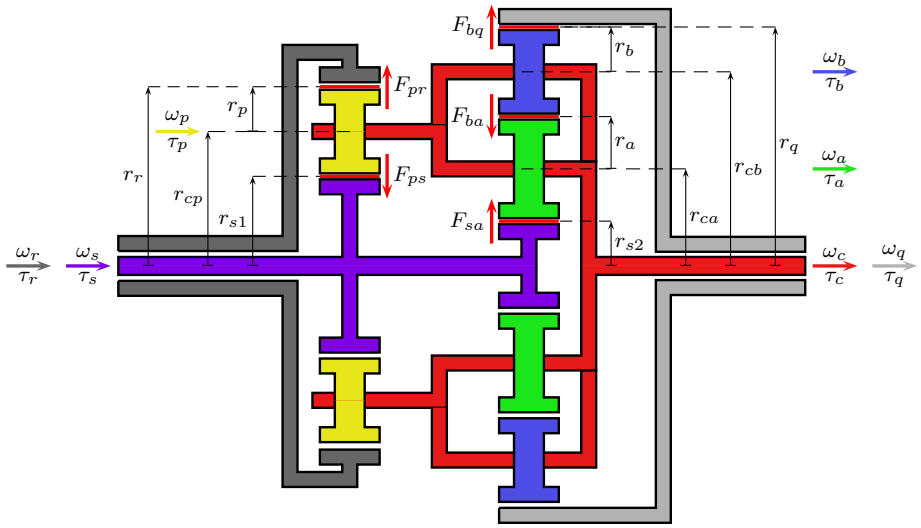

Figure 3.14: Structure of the considered double-stage planetary gear set.

and $\mathbf{F}$ in (3.28) completely defines the structures of the following matrices $\mathbf{J}$, $\mathbf{B}_\omega$, $\mathbf{K}$ and $\mathbf{B}_K$:

$$\mathbf{J} = \mathrm{diag}\,(J_s,\, J_c,\, J_p,\, J_a,\, J_r,\, J_b,\, J_q)\ , \qquad \mathbf{B}_\omega = \mathrm{diag}\,(b_s,\, b_c,\, b_p,\, b_a,\, b_r,\, b_b,\, b_q)\ ,$$
$$\mathbf{K} = \mathrm{diag}\,(K_{ps},\, K_{sa},\, K_{pr},\, K_{ba},\, K_{bq})\ , \qquad \mathbf{B}_K = \mathrm{diag}\,(d_{ps},\, d_{sa},\, d_{pr},\, d_{ba},\, d_{bq})\ .$$

The radii matrix $\mathbf{R}$ can be easily obtained using the rules given in Property 1:

$$\mathbf{R} = \begin{array}{c} \\ ps \\ sa \\ pr \\ ba \\ bq \end{array} \begin{array}{c} \begin{array}{ccccccc} s & c & p & a & r & b & q \end{array} \\ \begin{bmatrix} -r_{s1} & r_{cp} & -r_p & 0 & 0 & 0 & 0 \\ r_{s2} & -r_{ca} & 0 & r_a & 0 & 0 & 0 \\ 0 & r_{cp} & r_p & 0 & -r_r & 0 & 0 \\ 0 & r_{cb}-r_{ca} & 0 & -r_a & 0 & -r_b & 0 \\ 0 & r_{cb} & 0 & 0 & 0 & r_b & -r_q \end{bmatrix} \end{array} . \tag{3.29}$$

The parameters within the radii matrix $\mathbf{R}$ in (3.29) are constrained as follows:

$$r_r = 2r_p + r_{s1}, \qquad r_{cp} = r_p + r_{s1}, \qquad r_{cb} = 2r_a + r_b + r_{s2},$$
$$r_{ca} = r_a + r_{s2}, \qquad r_q = 2r_a + 2r_b + r_{s2},$$

where the constraints can be easily extracted from Fig. 3.14. The relative friction matrix $\mathbf{B}_{\Delta\omega}$ can be obtained using the rules given in Property 2, and results to be the following:

$$\mathbf{B}_{\Delta\omega}=\begin{array}{c} \\ s \\ c \\ p \\ a \\ r \\ b \\ q \end{array}\begin{array}{c}\begin{array}{ccccccc} s & c & p & a & r & b & q \end{array}\\ \begin{bmatrix} b_{sr} & 0 & 0 & 0 & -b_{sr} & 0 & 0 \\ 0 & b_{ca}+b_{cb}+b_{cp}+b_{cq} & -b_{cp} & -b_{ca} & 0 & -b_{cb} & -b_{cq} \\ 0 & -b_{cp} & b_{cp} & 0 & 0 & 0 & 0 \\ 0 & -b_{ca} & 0 & b_{ca} & 0 & 0 & 0 \\ -b_{sr} & 0 & 0 & 0 & b_{sr} & 0 & 0 \\ 0 & -b_{cb} & 0 & 0 & 0 & b_{cb} & 0 \\ 0 & -b_{cq} & 0 & 0 & 0 & 0 & b_{cq} \end{bmatrix}\end{array}. \tag{3.30}$$

When $\mathbf{K} \to \infty$, from the state space model (3.1) one obtains the following constraints on the gears speeds:

$$\mathbf{R}\,\boldsymbol{\omega} = \mathbf{0} \;\Leftrightarrow\; \begin{cases} r_{cp}\,\omega_c - r_p\,\omega_p - r_{s1}\,\omega_s = 0, \\ r_a\,\omega_a - r_{ca}\,\omega_c + r_{s2}\,\omega_s = 0, \\ r_{cp}\,\omega_c + r_p\,\omega_p - r_r\,\omega_r = 0, \\ -r_a\,\omega_a - r_b\,\omega_b - \omega_c(r_{ca} - r_{cb}) = 0, \\ r_b\,\omega_b + r_{cb}\,\omega_c - r_q\,\omega_q = 0. \end{cases} \tag{3.31}$$

These constraints can be used to obtain the reduced-order rigid model for the considered system when $\mathbf{K} \to \infty$. Choosing $\mathbf{x}_1 = \begin{bmatrix} \omega_s & \omega_r \end{bmatrix}^{\mathrm{T}}$ and applying the following state space congruent transformation to system (3.1):

$$\underbrace{\begin{bmatrix} \boldsymbol{\omega} \\ \mathbf{F} \end{bmatrix}}_{\mathbf{x}} = \underbrace{\begin{bmatrix} \mathbf{Q}_1 \\ \mathbf{0} \end{bmatrix}}_{\mathbf{T}_1} \underbrace{\begin{bmatrix} \omega_s \\ \omega_r \end{bmatrix}}_{\mathbf{x}_1}, \quad \text{where} \quad \mathbf{Q}_1 = \begin{bmatrix} 1 & 0 \\ \frac{r_{s1}}{2r_{cp}} & \frac{r_r}{2r_{cp}} \\ -\frac{r_{s1}}{2r_p} & \frac{r_r}{2r_p} \\ \frac{r_{ca}r_{s1}-2r_{cp}r_{s2}}{2r_a r_{cp}} & \frac{r_{ca}r_r}{2r_a r_{cp}} \\ 0 & 1 \\ \frac{r_{cb}r_{s1}-2r_{ca}r_{s1}+2r_{cp}r_{s2}}{2r_b r_{cp}} & -\frac{2r_{ca}r_r-r_{cb}r_r}{2r_b r_{cp}} \\ \frac{r_{cb}r_{s1}-r_{ca}r_{s1}+r_{cp}r_{s2}}{r_{cp}r_q} & -\frac{r_{ca}r_r-r_{cb}r_r}{r_{cp}r_q} \end{bmatrix}, \tag{3.32}$$

one obtains a reduced-order rigid model having the same structure as the model given in (3.21) and (3.22). The analytical expressions of the elements L_{ij} and a_{ij} within matrices $\mathbf{L}_1$ and $\mathbf{A}_1$ are not given for the sake of brevity and can be computed using (3.22).

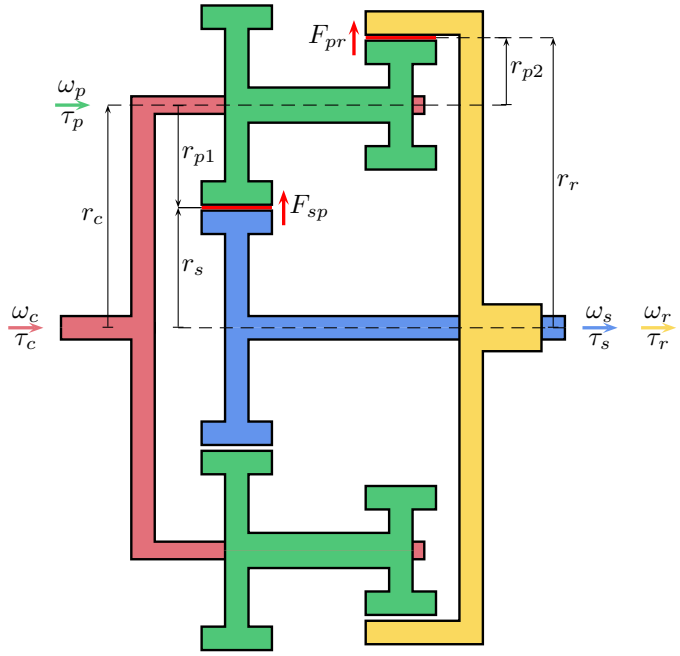

Figure 3.15: Structure of the considered Compound epicyclic gear train.

3.4 Modeling a compound epicyclic gear train

Let us now consider the compound epicyclic gear train shown in Fig. 3.15. For this system, the sets $\mathcal{N}_J$, $\mathcal{N}_K$, $\mathcal{N}_B$ and the parameters n_J, n_K, n_B defined at the beginning of Sec. 3.2 are:

$$\begin{cases} \mathcal{N}_J = \{c,\, p,\, s,\, r\}, & n_J = \dim(\mathcal{N}_J) = 4, \\ \mathcal{N}_K = \{sp,\, pr\}, & n_K = \dim(\mathcal{N}_K) = 2, \\ \mathcal{N}_B = \{\}, & n_B = \dim(\mathcal{N}_B) = 0. \end{cases} \tag{3.33}$$

The considered system can be modeled using the POG scheme shown in Fig. 3.3. Let us choose the speed vector $\boldsymbol{\omega}$, the input torque vector $\boldsymbol{\tau}$ and the force vector $\mathbf{F}$ as follows:

$$\boldsymbol{\omega} = \begin{bmatrix} \omega_c \\ \omega_p \\ \omega_s \\ \omega_r \end{bmatrix}, \qquad \boldsymbol{\tau} = \begin{bmatrix} \tau_c \\ \tau_p \\ \tau_s \\ \tau_r \end{bmatrix}, \qquad \mathbf{F} = \begin{bmatrix} F_{sp} \\ F_{pr} \end{bmatrix}. \tag{3.34}$$

The order of the speed variables ω_i and of the force variables F_{ij} within vectors $\boldsymbol{\omega}$ and $\mathbf{F}$ in (3.34) completely defines the structures of the following matrices $\mathbf{J}$, $\mathbf{B}_\omega$, $\mathbf{K}$ and $\mathbf{B}_K$:

$$\mathbf{J} = \mathrm{diag}\,(J_c,\, J_p,\, J_s,\, J_r)\ , \qquad \mathbf{B}_\omega = \mathrm{diag}\,(b_c,\, b_p,\, b_s,\, b_r)\ ,$$
$$\mathbf{K} = \mathrm{diag}\,(K_{sp},\, K_{pr})\ , \qquad \mathbf{B}_K = \mathrm{diag}\,(d_{sp},\, d_{pr})\ .$$

The radii matrix $\mathbf{R}$ can be easily obtained using the rules given in Property 1:

$$\begin{matrix} sp \\ pr \end{matrix} \mathbf{R} = \begin{matrix} \begin{bmatrix} -r_c & r_{p1} & r_s & 0 \\ r_c & r_{p2} & 0 & -r_r \end{bmatrix}. \end{matrix} \begin{matrix} \\ c \quad p \quad s \quad r \end{matrix} \tag{3.35}$$

Since set $\mathcal{N}_B$ in (3.33) is empty, it is $\mathbf{B}_{\Delta\omega} = \mathbf{0}$. Note that set $\mathcal{N}_B$ *can be defined by the user*, which also allows to simulate different orating modes of the considered planetary gear set. When $\mathbf{K} \to \infty$, from the state space model (3.1) one obtains the following constraints on the gears speeds:

$$\mathbf{R}\,\omega = 0 \quad \Leftrightarrow \quad \begin{cases} r_{p1}\,\omega_p - r_c\,\omega_c + r_s\,\omega_s = 0, \\ r_c\,\omega_c + r_{p2}\,\omega_p - r_r\,\omega_r = 0. \end{cases} \tag{3.36}$$

The constraints in (3.36) can be used to obtain the reduced-order rigid model for the considered system when $\mathbf{K} \to \infty$. Choosing $\mathbf{x}_1 = \begin{bmatrix} \omega_s & \omega_c \end{bmatrix}^{\mathrm{T}}$ and applying the following state space congruent transformation to system (3.1):

$$\underbrace{\begin{bmatrix} \boldsymbol{\omega} \\ \mathbf{F} \end{bmatrix}}_{\mathbf{x}} = \underbrace{\begin{bmatrix} \mathbf{Q}_1 \\ \mathbf{0} \end{bmatrix}}_{\mathbf{T}_1} \underbrace{\begin{bmatrix} \omega_s \\ \omega_c \end{bmatrix}}_{\mathbf{x}_1}, \quad \text{where} \quad \mathbf{Q}_1 = \begin{bmatrix} 0 & 1 \\ -\frac{r_s}{r_{p1}} & \frac{r_c}{r_{p1}} \\ 1 & 0 \\ -\frac{r_{p2} r_s}{r_{p1} r_r} & \frac{r_c r_{p1} + r_c r_{p2}}{r_{p1} r_r} \end{bmatrix}, \tag{3.37}$$

one obtains a reduced-order rigid model having the same structure as the model given in (3.21) and (3.22). The analytical expressions of the elements L_{ij} and a_{ij} within matrices $\mathbf{L}_1$ and $\mathbf{A}_1$ are not given for the sake of brevity and can be computed using (3.22).

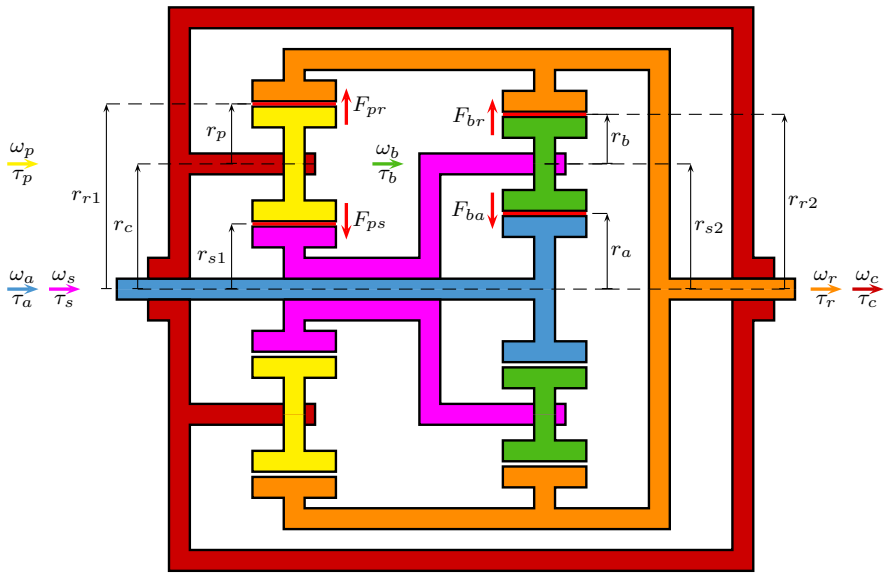

Figure 3.16: Structure of the considered Coupled epicyclic gear train.

3.5 Modeling a coupled epicyclic gear train

Let us now consider the coupled epicyclic gear train shown in Fig. 3.16. For this system, the sets $\mathcal{N}_J, \mathcal{N}_K, \mathcal{N}_B$ and the parameters n_J, n_K, n_B defined at the beginning of Sec. 3.2 are:

$$\begin{cases} \mathcal{N}_J = \{a,\, c,\, p,\, s,\, b,\, r\}, & n_J = \dim(\mathcal{N}_J) = 6, \\ \mathcal{N}_K = \{ps,\, pr,\, br,\, ba\}, & n_K = \dim(\mathcal{N}_K) = 4, \\ \mathcal{N}_B = \{\}, & n_B = \dim(\mathcal{N}_B) = 0. \end{cases} \tag{3.38}$$

The considered system can be modeled using the POG scheme shown in Fig. 3.3. Let us choose the speed vector $\boldsymbol{\omega}$, the input torque vector $\boldsymbol{\tau}$ and the force vector $\mathbf{F}$ as follows:

$$\boldsymbol{\omega}=\begin{bmatrix}\omega_a\\ \omega_c\\ \omega_p\\ \omega_s\\ \omega_b\\ \omega_r\end{bmatrix}, \qquad \boldsymbol{\tau}=\begin{bmatrix}\tau_a\\ \tau_c\\ \tau_p\\ \tau_s\\ \tau_b\\ \tau_r\end{bmatrix}, \qquad \mathbf{F}=\begin{bmatrix}F_{ps}\\ F_{pr}\\ F_{br}\\ F_{ba}\end{bmatrix}. \tag{3.39}$$

The order of the speed variables ω_i and of the force variables F_{ij} within vectors $\boldsymbol{\omega}$ and $\mathbf{F}$ in (3.39) completely defines the structures of the following matrices $\mathbf{J}$, $\mathbf{B}_\omega$, $\mathbf{K}$ and $\mathbf{B}_K$:

$$\mathbf{J}=\operatorname{diag}(J_a,\,J_c,\,J_p,\,J_s,\,J_b,\,J_r)\ , \qquad \mathbf{B}_\omega=\operatorname{diag}(b_a,\,b_c,\,b_p,\,b_s,\,b_b,\,b_r)\ ,$$
$$\mathbf{K}=\operatorname{diag}(K_{ps},\,K_{pr},\,K_{br},\,K_{ba})\ , \qquad \mathbf{B}_K=\operatorname{diag}(d_{ps},\,d_{pr},\,d_{br},\,d_{ba})\ .$$

The radii matrix $\mathbf{R}$ can be easily obtained using the rules given in Property 1:

$$\begin{array}{c} \\ ps \\ pr \\ br \\ ba \end{array} \mathbf{R}= \begin{array}{c} \begin{array}{cccccc} a & c & p & s & b & r \end{array} \\ \begin{bmatrix} 0 & r_c & -r_p & -r_{s1} & 0 & 0 \\ 0 & r_c & r_p & 0 & 0 & -r_{r1} \\ 0 & 0 & 0 & r_{s2} & r_b & -r_{r2} \\ -r_a & 0 & 0 & r_{s2} & -r_b & 0 \end{bmatrix} \end{array}. \tag{3.40}$$

Since set $\mathcal{N}_B$ in (3.38) is empty, it is $\mathbf{B}_{\Delta\omega}=\mathbf{0}$. When $\mathbf{K}\to\infty$, from the state space model (3.1) one obtains the following constraints on the gears speeds:

$$\mathbf{R}\,\boldsymbol{\omega}=\mathbf{0} \quad\Leftrightarrow\quad \begin{cases} r_c\,\omega_c - r_p\,\omega_p - r_{s1}\,\omega_s = 0, \\ r_c\,\omega_c + r_p\,\omega_p - r_{r1}\,\omega_r = 0, \\ r_b\,\omega_b - r_{r2}\,\omega_r + r_{s2}\,\omega_s = 0, \\ r_{s2}\,\omega_s - r_b\,\omega_b - r_a\,\omega_a = 0. \end{cases} \tag{3.41}$$

The constraints in (3.41) can be used to obtain the reduced-order rigid model for the considered system when $\mathbf{K}\to\infty$. Choosing $\mathbf{x}_1=\begin{bmatrix}\omega_a & \omega_r\end{bmatrix}^{\mathrm{T}}$ and applying the

following state space congruent transformation to system (3.1):

$$\underbrace{\begin{bmatrix}\boldsymbol{\omega}\\ \mathbf{F}\end{bmatrix}}_{\mathbf{x}}=\underbrace{\begin{bmatrix}\mathbf{Q}_1\\ \mathbf{0}\end{bmatrix}}_{\mathbf{T}_1}\underbrace{\begin{bmatrix}\omega_s\\ \omega_c\end{bmatrix}}_{\mathbf{x}_1}, \quad \text{where} \quad \mathbf{Q}_1=\begin{bmatrix} 1 & 0 \\ \frac{r_a r_{s1}}{4 r_c r_{s2}} & \frac{2 r_{r1} r_{s2}+r_{r2} r_{s1}}{4 r_c r_{s2}} \\ -\frac{r_a r_{s1}}{4 r_p r_{s2}} & \frac{2 r_{r1} r_{s2}-r_{r2} r_{s1}}{4 r_p r_{s2}} \\ \frac{r_a}{2 r_{s2}} & \frac{r_{r2}}{2 r_{s2}} \\ -\frac{r_a}{2 r_b} & \frac{r_{r2}}{2 r_b} \\ 0 & 1 \end{bmatrix}, \tag{3.42}$$

one obtains a reduced-order rigid model having the same structure as the model given in (3.21) and (3.22). The analytical expressions of the elements L_{ij} and a_{ij} within matrices $\mathbf{L}_1$ and $\mathbf{A}_1$ are not given for the sake of brevity and can be computed using (3.22).

3.5.1 Control design

Let us refer to the reduced rigid model (3.21) obtained using (3.42). Let us use the two velocities ω_a and ω_r in order to obtain a desired value $\bar{\omega}_c$ for the angular velocity ω_c. From (3.42), it follows that:

$$\bar{\omega}_c = q_1\,\omega_a + q_2\,\omega_r = \underbrace{\begin{bmatrix} q_1 & q_2 \end{bmatrix}}_{\mathbf{q}_1^{\mathrm{T}}} \underbrace{\begin{bmatrix}\omega_a\\ \omega_r\end{bmatrix}}_{\mathbf{x}_1} = \mathbf{q}_1^{\mathrm{T}}\,\mathbf{x}_1, \tag{3.43}$$

where:

$$q_1 = \frac{r_a r_{s1}}{4 r_c r_{s2}}, \qquad q_2 = \frac{2 r_{r1} r_{s2} + r_{r2} r_{s1}}{4 r_c r_{s2}}. \tag{3.44}$$

All the solutions $\mathbf{x}_1$ of the linear system (3.43) can be expressed as follows:

$$\mathbf{x}_1 = \bar{\omega}_c\,\mathbf{v}_1 + \alpha\,\mathbf{v}_2, \tag{3.45}$$

where $\mathbf{v}_1$ is any particular solution of equation $1 = \mathbf{q}_1^{\mathrm{T}}\,\mathbf{v}_1$, $\mathbf{v}_2$ is any particular vector such that $\mathbf{v}_2 \in \ker(\mathbf{q}_1^{\mathrm{T}})$, and $\alpha \in \mathcal{R}$. Possible values for vectors $\mathbf{v}_1$ and $\mathbf{v}_2$ are:

$$\mathbf{v}_1 = \begin{bmatrix}\frac{1}{q_1}\\ 0\end{bmatrix}, \qquad \mathbf{v}_1 = \begin{bmatrix}0\\ \frac{1}{q_2}\end{bmatrix}, \qquad \mathbf{v}_2 = \begin{bmatrix} q_2\\ -q_1\end{bmatrix}.$$

The dissipated power P_d of the POG reduced rigid model (3.21) along the solutions (3.45) can be expressed as follows:

$$P_d = \mathbf{x}_1^{\mathrm{T}} \mathbf{A}_1 \mathbf{x}_1 = (\bar{\omega}_c \mathbf{v}_1 + \alpha\, \mathbf{v}_2)^{\mathrm{T}} \mathbf{A}_1 (\bar{\omega}_c \mathbf{v}_1 + \alpha\, \mathbf{v}_2). \tag{3.46}$$

Since matrix $\mathbf{A}_1$ in (3.21) is symmetric, the partial derivative of the dissipated power P_d with respect to α is:

$$\frac{\partial P_d}{\partial \alpha} = 2\, \mathbf{v}_2^{\mathrm{T}} \mathbf{A}_1 (\bar{\omega}_c \mathbf{v}_1 + \alpha\, \mathbf{v}_2). \tag{3.47}$$

The optimal solution in (3.45) minimizing the dissipated power P_d can be obtained from (3.47) as follows:

$$\frac{\partial P_d}{\partial \alpha} = 0 \qquad \Rightarrow \qquad \alpha^* = -\bar{\omega}_c \frac{\mathbf{v}_2^{\mathrm{T}} \mathbf{A}_1 \mathbf{v}_1}{\mathbf{v}_2^{\mathrm{T}} \mathbf{A}_1 \mathbf{v}_2}. \tag{3.48}$$

Substituting α^* in (3.45) one obtains:

$$\overline{\mathbf{x}}_1 = \begin{bmatrix} \bar{\omega}_a \\ \bar{\omega}_r \end{bmatrix} = \bar{\omega}_c \underbrace{\left(\mathbf{v}_1 - \frac{\mathbf{v}_2^{\mathrm{T}} \mathbf{A}_1 \mathbf{v}_1}{\mathbf{v}_2^{\mathrm{T}} \mathbf{A}_1 \mathbf{v}_2} \mathbf{v}_2 \right)}_{\vec{\mathbf{x}}_{1c}} = \bar{\omega}_c\, \vec{\mathbf{x}}_{1c}. \tag{3.49}$$

One can easily prove that vector $\vec{\mathbf{x}}_{1c}$ does not depend on the particular choice of parameter $\bar{\omega}_c$ and of vectors $\mathbf{v}_1$ and $\mathbf{v}_2$. Vector $\mathbf{x}_1 = \overline{\mathbf{x}}_1$ is the solution of equation (3.43) for which the power P_d dissipated in the system is minimum. This optimal condition is shown in Fig. 3.17: the blue lines are the contour ellipses associated with the dissipated power P_d in (3.46) when the parameters reported in Tab. 3.3 are used, the magenta straight line $\mathbf{x}_1$ is the set (3.45) of all the solutions of equation (3.43), vector $\overline{\mathbf{x}}_1$ is the optimal solution minimizing the dissipated power P_d, the red ellipse is the contour line where the dissipated power P_d is minimum with respect to all the possible solutions $\mathbf{x}_1$.

The reduced system $\mathbf{L}_1 \dot{\mathbf{x}}_1 = \mathbf{A}_1 \mathbf{x}_1 + \mathbf{B}_1 \mathbf{u}$ in (3.21) controlled using the input vector $\mathbf{u} = \begin{bmatrix} \tau_a & 0 & 0 & 0 & 0 & \tau_r \end{bmatrix}^{\mathrm{T}}$ simplifies as follows:

$$\mathbf{L}_1 \dot{\mathbf{x}}_1 = \mathbf{A}_1 \mathbf{x}_1 + \boldsymbol{\tau}_1, \qquad \boldsymbol{\tau}_1 = \begin{bmatrix} \tau_a \\ \\ \tau_r \end{bmatrix}. \tag{3.50}$$

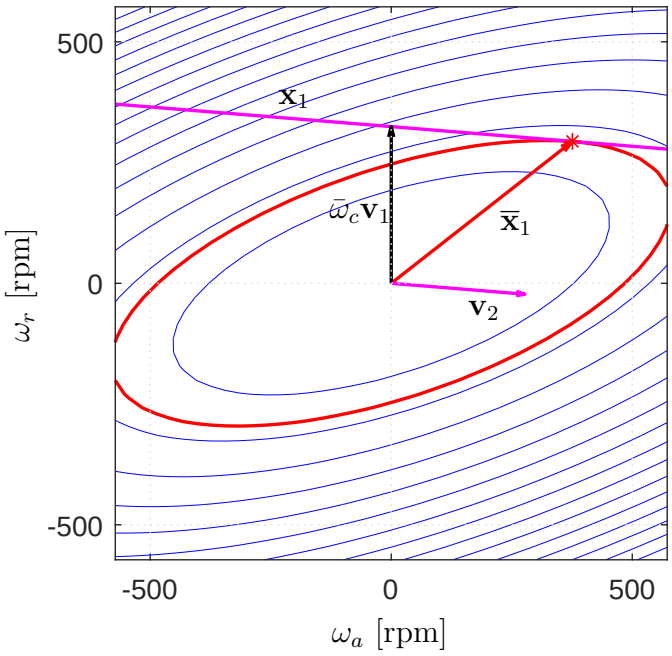

Figure 3.17: Optimal condition $\overline{\mathbf{x}}_1$ minimizing the dissipated power P_d.

One can easily verify that, using the following control law:

$$\boldsymbol{\tau}_1 = -\mathbf{A}_1\mathbf{x}_1 + \mathbf{L}_1[\dot{\overline{\mathbf{x}}}_1 - \mathbf{K}\,(\overline{\mathbf{x}}_1 - \mathbf{x}_1)], \tag{3.51}$$

system (3.50) simplifies as follows:

$$\dot{\overline{\mathbf{x}}}_1 - \dot{\mathbf{x}}_1 = \mathbf{K}\,(\overline{\mathbf{x}}_1 - \mathbf{x}_1), \tag{3.52}$$

where $\mathbf{K} = \mathrm{diag}([k_1 \;\; k_2])$ is a proper constant matrix to be designed. From (3.52), it is easy to see that the two parameters k_l and k_2 of matrix $\mathbf{K}$ are equal to the two eigenvalues λ_1 and λ_2 of system (3.52): $k_1 = \lambda_1$, $k_2 = \lambda_2$.

3.5.2 Simulation results

The Coupled epicyclic gear train shown in Fig. 3.16 has been simulated using the reduced rigid system (3.21), the parameters shown in Tab. 3.3, the initial conditions $\boldsymbol{\omega}_0 = [\ 0\ 0\ 0\ 0\ 0\ 0\ ]$rpm, $\mathbf{F}_0 = [\ 0\ 0\ 0\ 0\ ]$N, the control law given in (3.51), the design parameters $k_1 = \lambda_1 = -10$, $k_2 = \lambda_2 = -10$ and the desired angular velocity

Table 3.3: Coupled epicyclic gear train: simulation parameters.

$r_a = 10.5$ cm	$r_b = 7.5$ cm
$r_p = 9$ cm	$r_{s1} = 9.6$ cm
$r_c = 18.6$ cm	$r_{r1} = 27.6$ cm
$r_{s2} = 18$ cm	$r_{r2} = 25.5$ cm
$J_a = 58081.3$ kg mm^2	$J_c = 2199669.9$ kg mm^2
$J_p = 26527.6$ kg mm^2	$J_s = 501613.4$ kg mm^2
$J_b = 11630$ kg mm^2	$J_r = 3199361.6$ kg mm^2
$b_a = 0.3$ Nm/rpm	$b_c = 0.18$ Nm/rpm
$b_p = 0.28$ Nm/rpm	$b_s = 0.14$ Nm/rpm
$b_b = 0.51$ Nm/rpm	$b_r = 0.12$ Nm/rpm
$K_{ba} = 20$ N/mm	$K_{ps} = 20$ N/mm
$K_{pr} = 20$ N/mm	$K_{br} = 20$ N/mm
$d_{ba} = 1.8$ N s/cm	$d_{ps} = 1.8$ N s/cm
$d_{pr} = 1.8$ N s/cm	$d_{br} = 1.8$ N s/cm

$\bar{\omega}_c = 300$ rpm. According to the definition of vector $\boldsymbol{\tau_1}$ in (3.50), which is employed in the control law in (3.51), one can notice that the two torques applied to the power sections characterized by subscripts "a" and "r" are those employed as control inputs for the considered case study, whereas the inertial elements corresponding to the remaining power sections are disconnected. The numeric values of matrices $\mathbf{L}_1$ are $\mathbf{A}_1$ are the following:

$$\mathbf{L}_1 = \begin{bmatrix} 0.119 & 0.238 \\ 0.238 & 5.401 \end{bmatrix}, \qquad \mathbf{A}_1 = \begin{bmatrix} -5.42 & 5.85 \\ 5.85 & -20.84 \end{bmatrix}.$$

Vector $\mathbf{q}_1$ in (3.43) is characterized by the following parameters: $q_1 = 0.0753$ and $q_2 = 0.9247$. The obtained simulations results are shown in Fig. 3.18: the angular velocities ω_i are reported on the left subplot and the tangential forces F_{ij} are reported on the right subplot. The tangential forces F_{ij} have been computed using Eq. (3.25). From Fig. 3.18, one can appreciate the good control of the desired angular velocity $\bar{\omega}_c = 300$ rpm obtained using the control law (3.51). Note that the transient is

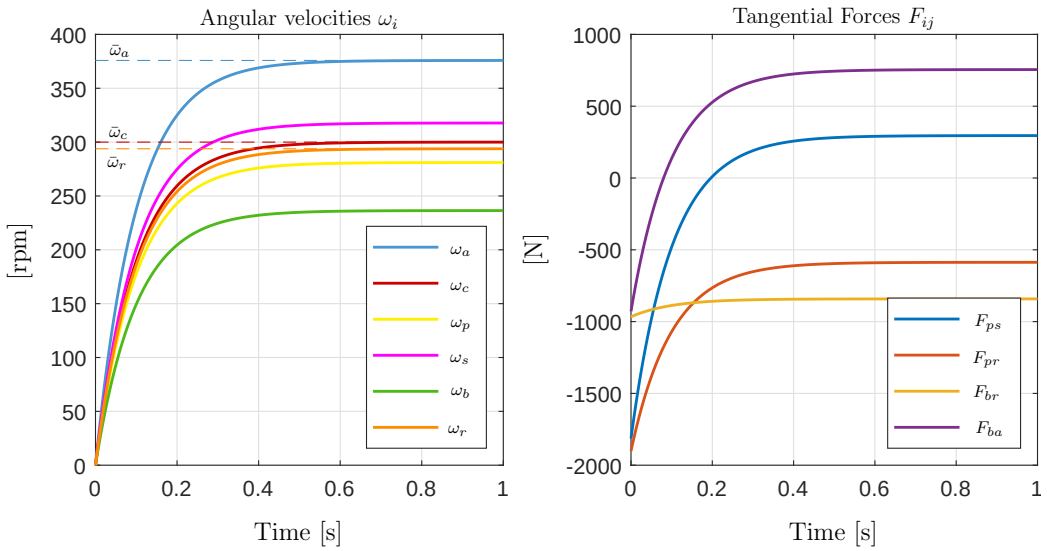

Figure 3.18: Simulation of the Coupled epicyclic gear train: angular velocities ω_i (left subplot) and tangential forces F_{ij} (right subplot).

aperiodic and the settling time $T_s \simeq \frac{3}{\lambda} \simeq 0.34$ is congruent with the choice of the two coincident real eigenvalues in $\lambda_1 = \lambda_2 = -10$.

3.6 Modeling the first single-stage planetary gear set

Let us now consider the single-stage planetary gear set shown in Fig. 3.19, for which a possible application is in power-split architectures for driving agricultural tools in the agricultural field. For this system, the sets $\mathcal{N}_J$, $\mathcal{N}_K$, $\mathcal{N}_B$ and the parameters n_J, n_K, n_B defined at the beginning of Sec. 3.2 are:

$$\begin{cases} \mathcal{N}_J = \{r,\, m,\, s,\, c,\, p,\, g,\, o\}, & n_J = \dim(\mathcal{N}_J) = 7, \\ \mathcal{N}_K = \{rp,\, rg,\, ms,\, sp,\, co\}, & n_K = \dim(\mathcal{N}_K) = 5, \\ \mathcal{N}_B = \{\}, & n_B = \dim(\mathcal{N}_B) = 0. \end{cases} \tag{3.53}$$

The considered system can be modeled using the POG scheme shown in Fig. 3.3. Let us choose the speed vector $\boldsymbol{\omega}$, the input torque vector $\boldsymbol{\tau}$ and the force vector $\mathbf{F}$ as follows:

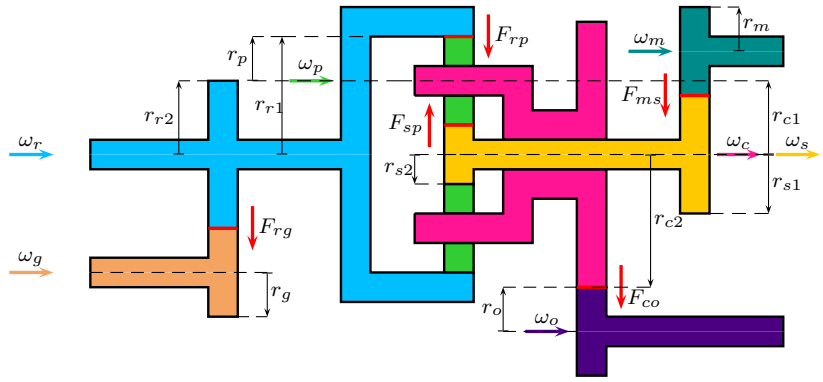

Figure 3.19: Structure of the considered first single-stage planetary gear set.

$$\boldsymbol{\omega} = \begin{bmatrix} \omega_r \\ \omega_m \\ \omega_s \\ \omega_c \\ \omega_p \\ \omega_g \\ \omega_o \end{bmatrix}, \qquad \boldsymbol{\tau} = \begin{bmatrix} \tau_r \\ \tau_m \\ \tau_s \\ \tau_c \\ \tau_p \\ \tau_g \\ \tau_o \end{bmatrix}, \qquad \mathbf{F} = \begin{bmatrix} F_{rp} \\ F_{rg} \\ F_{ms} \\ F_{sp} \\ F_{co} \end{bmatrix}. \tag{3.54}$$

The order of the speed variables ω_i and of the force variables F_{ij} within vectors $\boldsymbol{\omega}$ and $\mathbf{F}$ in (3.54) completely defines the structures of the following matrices $\mathbf{J}$, $\mathbf{B}_\omega$, $\mathbf{K}$ and $\mathbf{B}_K$:

$$\mathbf{J} = \operatorname{diag}(J_r,\, J_m,\, J_s,\, J_c,\, J_p,\, J_g,\, J_o)\ , \qquad \mathbf{B}_\omega = \operatorname{diag}(b_r,\, b_m,\, b_s,\, b_c,\, b_p,\, b_g,\, b_o)\ ,$$
$$\mathbf{K} = \operatorname{diag}(K_{rp},\, K_{rg},\, K_{ms},\, K_{sp},\, K_{co})\ , \qquad \mathbf{B}_K = \operatorname{diag}(d_{rp},\, d_{rg},\, d_{ms},\, d_{sp},\, d_{co})\ .$$

The radii matrix $\mathbf{R}$ can be easily obtained using the rules given in Property 1:

$$\mathbf{R} = \begin{array}{c} \\ rp \\ rg \\ ms \\ sp \\ co \end{array} \begin{array}{c} \begin{array}{ccccccc} r & m & s & c & p & g & o \end{array} \\ \begin{bmatrix} r_{r1} & 0 & 0 & -r_{c1} & -r_p & 0 & 0 \\ -r_{r2} & 0 & 0 & 0 & 0 & -r_g & 0 \\ 0 & -r_m & -r_{s1} & 0 & 0 & 0 & 0 \\ 0 & 0 & r_{s2} & -r_{c1} & r_p & 0 & 0 \\ 0 & 0 & 0 & -r_{c2} & 0 & 0 & -r_o \end{bmatrix} \end{array}. \tag{3.55}$$

The parameters within the radii matrix $\mathbf{R}$ in (3.55) are constrained as follows:

$$r_{c1} = r_p + r_{s2}, \qquad r_{r1} = 2\,r_p + r_{s2}. \tag{3.56}$$

The constraints in (3.56) easily follow from Fig. 3.19. Since set $\mathcal{N}_B$ in (3.53) is empty, it is $\mathbf{B}_{\Delta\omega} = \mathbf{0}$. When $\mathbf{K} \to \infty$, from the state space model (3.1) one obtains the following constraints on the gears speeds:

$$\mathbf{R}\,\boldsymbol{\omega} = \mathbf{0} \quad \Leftrightarrow \quad \begin{cases} r_{r1}\,\omega_r - r_p\,\omega_p - r_{c1}\,\omega_c = 0, \\ -r_g\,\omega_g - r_{r2}\,\omega_r = 0, \\ -r_m\,\omega_m - r_{s1}\,\omega_s = 0, \\ r_p\,\omega_p - r_{c1}\,\omega_c + r_{s2}\,\omega_s = 0, \\ -r_{c2}\,\omega_c - r_o\,\omega_o = 0. \end{cases} \tag{3.57}$$

These constraints can be used to obtain the reduced-order rigid model for the considered system when $\mathbf{K} \to \infty$. Choosing $\mathbf{x}_1 = \begin{bmatrix} \omega_c & \omega_r \end{bmatrix}^{\mathrm{T}}$ and applying the following state space congruent transformation to system (3.1):

$$\underbrace{\begin{bmatrix} \boldsymbol{\omega} \\ \mathbf{F} \end{bmatrix}}_{\mathbf{x}} = \underbrace{\begin{bmatrix} \mathbf{Q}_1 \\ \mathbf{0} \end{bmatrix}}_{\mathbf{T}_1} \underbrace{\begin{bmatrix} \omega_s \\ \omega_c \end{bmatrix}}_{\mathbf{x}_1}, \quad \text{where} \quad \mathbf{Q}_1 = \begin{bmatrix} 0 & 1 \\ -\frac{2r_{c1}r_{s1}}{r_m r_{s2}} & \frac{r_{r1}r_{s1}}{r_m r_{s2}} \\ \frac{2r_{c1}}{r_{s2}} & -\frac{r_{r1}}{r_{s2}} \\ 1 & 0 \\ -\frac{r_{c1}}{r_p} & \frac{r_{r1}}{r_p} \\ 0 & -\frac{r_{r2}}{r_g} \\ -\frac{r_{c2}}{r_o} & 0 \end{bmatrix}, \tag{3.58}$$

one obtains a reduced-order rigid model having the same structure as the model given in (3.21) and (3.22). The analytical expressions of the elements L_{ij} and a_{ij} within matrices $\mathbf{L}_1$ and $\mathbf{A}_1$ are not given for the sake of brevity and can be computed using (3.22).

3.7 Modeling the second single-stage planetary gear set

Let us now consider the single-stage planetary gear set shown in Fig. 3.20, for which a possible application is in power-split architectures for driving vehicles in

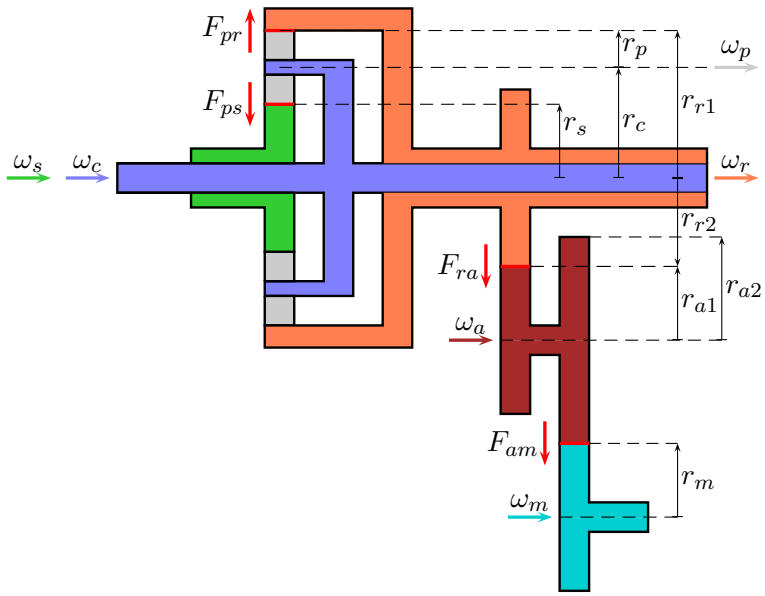

Figure 3.20: Structure of the considered second single-stage planetary gear set.

the construction field such as Wheel Loaders. For this system, the sets $\mathcal{N}_J$, $\mathcal{N}_K$, $\mathcal{N}_B$ and the parameters n_J, n_K, n_B defined at the beginning of Sec. 3.2 are:

$$\begin{cases} \mathcal{N}_J = \{c,\, p,\, s,\, r,\, a,\, m\}, & n_J = \dim(\mathcal{N}_J) = 6, \\ \mathcal{N}_K = \{ps,\, pr,\, ra,\, am\}, & n_K = \dim(\mathcal{N}_K) = 4, \\ \mathcal{N}_B = \{\}, & n_B = \dim(\mathcal{N}_B) = 0. \end{cases} \tag{3.59}$$

The considered system can be modeled using the POG scheme shown in Fig. 3.3. Let us choose the speed vector $\boldsymbol{\omega}$, the input torque vector $\boldsymbol{\tau}$ and the force vector $\mathbf{F}$ as follows:

$$\boldsymbol{\omega} = \begin{bmatrix} \omega_c \\ \omega_p \\ \omega_s \\ \omega_r \\ \omega_a \\ \omega_m \end{bmatrix}, \qquad \boldsymbol{\tau} = \begin{bmatrix} \tau_c \\ \tau_p \\ \tau_s \\ \tau_r \\ \tau_a \\ \tau_m \end{bmatrix}, \qquad \mathbf{F} = \begin{bmatrix} F_{ps} \\ F_{pr} \\ F_{ra} \\ F_{am} \end{bmatrix}. \tag{3.60}$$

The order of the speed variables ω_i and of the force variables F_{ij} within vectors $\boldsymbol{\omega}$ and $\mathbf{F}$ in (3.60) completely defines the structures of the following matrices $\mathbf{J}$, $\mathbf{B}_\omega$,

$\mathbf{K}$ and $\mathbf{B}_K$:

$$\mathbf{J} = \mathrm{diag}\,(J_c,\, J_p,\, J_s,\, J_r,\, J_a,\, J_m)\ , \qquad \mathbf{B}_\omega = \mathrm{diag}\,(b_c,\, b_p,\, b_s,\, b_r,\, b_a,\, b_m)\ ,$$
$$\mathbf{K} = \mathrm{diag}\,(K_{ps},\, K_{pr},\, K_{ra},\, K_{am})\ , \qquad \mathbf{B}_K = \mathrm{diag}\,(d_{ps},\, d_{pr},\, d_{ra},\, d_{am})\ .$$

The radii matrix $\mathbf{R}$ can be easily obtained using the rules given in Property 1:

$$\mathbf{R} = \begin{array}{c} \\ ps \\ pr \\ ra \\ am \end{array} \begin{array}{c} \begin{array}{cccccc} c & p & s & r & a & m \end{array} \\ \begin{bmatrix} r_c & -r_p & -r_s & 0 & 0 & 0 \\ r_c & r_p & 0 & -r_{r1} & 0 & 0 \\ 0 & 0 & 0 & -r_{r2} & -r_{a1} & 0 \\ 0 & 0 & 0 & 0 & -r_{a2} & -r_m \end{bmatrix} \end{array} \tag{3.61}$$

The parameters within the radii matrix $\mathbf{R}$ in (3.61) are constrained as follows:

$$r_c = r_p + r_s, \qquad r_{r1} = 2\,r_p + r_s. \tag{3.62}$$

The constraints in (3.62) easily follow from Fig. 3.20. Since set $\mathcal{N}_B$ in (3.59) is empty, it is $\mathbf{B}_{\Delta\omega} = \mathbf{0}$. When $\mathbf{K} \to \infty$, from the state space model (3.1) one obtains the following constraints on the gears speeds:

$$\mathbf{R}\,\boldsymbol{\omega} = \mathbf{0} \quad \Leftrightarrow \quad \begin{cases} r_c\,\omega_c - r_p\,\omega_p - r_s\,\omega_s = 0, \\ r_c\,\omega_c + r_p\,\omega_p - r_{r1}\,\omega_r = 0, \\ -r_{a1}\,\omega_a - r_{r2}\,\omega_r = 0, \\ -r_{a2}\,\omega_a - r_m\,\omega_m = 0. \end{cases} \tag{3.63}$$

These constraints can be used to obtain the reduced-order rigid model for the considered system when $\mathbf{K} \to \infty$. Choosing $\mathbf{x}_1 = \begin{bmatrix} \omega_c & \omega_r \end{bmatrix}^{\mathrm{T}}$ and applying the following state space congruent transformation to system (3.1):

$$\underbrace{\begin{bmatrix} \boldsymbol{\omega} \\ \mathbf{F} \end{bmatrix}}_{\mathbf{x}} = \underbrace{\begin{bmatrix} \mathbf{Q}_1 \\ \mathbf{0} \end{bmatrix}}_{\mathbf{T}_1} \underbrace{\begin{bmatrix} \omega_s \\ \omega_c \end{bmatrix}}_{\mathbf{x}_1}, \quad \text{where} \quad \mathbf{Q}_1 = \begin{bmatrix} 1 & 0 \\ -\frac{r_c}{r_p} & \frac{r_{r1}}{r_p} \\ \frac{2r_c}{r_s} & -\frac{r_{r1}}{r_s} \\ 0 & 1 \\ 0 & -\frac{r_{r2}}{r_{a1}} \\ 0 & \frac{r_{a2}r_{r2}}{r_{a1}r_m} \end{bmatrix}, \tag{3.64}$$

one obtains a reduced-order rigid model having the same structure as the model given in (3.21) and (3.22). The analytical expressions of the elements L_{ij} and a_{ij} within matrices $\mathbf{L}_1$ and $\mathbf{A}_1$ are not given for the sake of brevity and can be computed using (3.22).

Note that, by neglecting the dissipative terms within matrix $\mathbf{A}_1$ in (3.21) and assuming the system at steady-state, one obtains $\mathbf{Q}_1^{\mathrm{T}}\boldsymbol{\tau} = 0 \leftrightarrow \boldsymbol{\tau} \in \ker(\mathbf{Q}_1^{\mathrm{T}})$. If no input torque is applied to gear p and to gear a in Fig. 3.20, it follows that $\tau_p = \tau_a = 0$, which means that $\mathbf{Q}_1^{\mathrm{T}}\boldsymbol{\tau} = 0$ leads to the following steady-state torque constraints:

$$\tau_c + \frac{2\,r_c}{r_s}\,\tau_s = 0, \qquad -\frac{r_{r1}}{r_s}\,\tau_s + \tau_r + \frac{r_{a2}\,r_{r2}}{r_{a1}\,r_m}\,\tau_m = 0. \tag{3.65}$$

3.8 Conclusions

In this chapter, a systematic methodology for modeling planetary gear sets has been presented. The proposed approach relies upon a general model, which can be used to model any planetary gear set and is directly implementable in the Matlab/Simulink environment. All the system matrices and vectors are either automatically defined or directly computable using the two presented algorithms. The potentiality of inserting some relative friction between any two of the system gears allows to insert lockup clutches in the planetary gear set, thus allowing to simulate different operating modes of the transmission system. The proposed approach allows to obtain two dynamic models of the system: a full elastic model accounting for the gears elastic interaction and a reduced-order rigid model. The first one is suitable for accurately simulating the system, whereas the second one is suitable for fixed-step simulations which are needed for real-time execution. In the reduced-order model, the time behavior of the tangential forces can still be recovered, even if they are no longer present in the system. Furthermore, the kinematic speed and torque equations automatically turn out when the reduced-order model is computed. The proposed modeling approach has been applied to several studies implemented in the Matlab/Simulink environment. Furthermore, the design of a suitable control law

allowing to achieve the desired velocity while minimizing the system dissipations has been presented with reference to one of the case studies.

Chapter 4

Modeling of Multilevel Flying-Capacitor Converters

This chapter deals with the modeling, control and robustness assessment of a type of multilevel converters, namely multilevel flying-capacitor converters [27], using the POG modeling technique [2]-[3], extending the modeling approach that was proposed in [28].

The remainder of this chapter is organized as follows. Sec. 4.1, and the included subsections, address the dynamic modeling of the multilevel flying-capacitor converter. The main matrices and vectors of the model are introduced and described, together with some interesting properties that they exhibit. The model verification against the PLECS simulator is addressed in Sec. 4.1.4. Sec. 4.2 deals with the control of the multilevel flying-capacitor converter. In particular, Sec. 4.2.1 addresses the minimum distance algorithm, whereas Sec. 4.2.2 defines the basic configuration of the multilevel flying-capacitor converter. Sec. 4.2.3 describes the robustness assessment of the considered converter in extended mode using a minimum distance algorithm, whereas Sec. 4.2.4 proposes the new variable-step control algorithm. The converter simulation in extended mode with different dynamic loads is addressed in Sec. 4.3.

4.1 Modeling of the n-Dimensional Converter

4.1.1 Physical System and Configuration Vectors

Let us consider the electric scheme of an n-dimensional Multilevel Flying-Capacitor Converter that is shown in Fig. 4.1. The output voltage V_{out} is a function of the IGBTs activation signals $T_i \in \{0,\ 1\}$, for $i \in \{1\ ,2\ ,\dots\ ,n\}$. Let $\mathbf{V}_c$ and $\mathbf{T}_j$ denote the capacitors voltage column vector and the IGBTs signal row vectors, defined as follows:

$$\mathbf{V}_c = \begin{bmatrix} V_1 \\ V_2 \\ V_3 \\ \vdots \\ V_n \end{bmatrix}, \quad \begin{bmatrix} \mathbf{T}_0 \\ \mathbf{T}_1 \\ \mathbf{T}_2 \\ \mathbf{T}_3 \\ \vdots \\ \mathbf{T}_{m_c-2} \\ \mathbf{T}_{m_c-1} \end{bmatrix} = \begin{bmatrix} 0 & \dots & 0 & 0 & 0 \\ 0 & \dots & 0 & 0 & 1 \\ 0 & \dots & 0 & 1 & 0 \\ 0 & \dots & 0 & 1 & 1 \\ \vdots & \ddots & \vdots & \vdots & \vdots \\ 1 & \dots & 1 & 1 & 0 \\ 1 & \dots & 1 & 1 & 1 \end{bmatrix} \quad \begin{matrix} n=3 \\ \Rightarrow \end{matrix} \quad \begin{bmatrix} \mathbf{T}_0 \\ \mathbf{T}_1 \\ \mathbf{T}_2 \\ \mathbf{T}_3 \\ \mathbf{T}_4 \\ \mathbf{T}_5 \\ \mathbf{T}_6 \\ \mathbf{T}_7 \end{bmatrix} = \begin{bmatrix} 0 & 0 & 0 \\ 0 & 0 & 1 \\ 0 & 1 & 0 \\ 0 & 1 & 1 \\ 1 & 0 & 0 \\ 1 & 0 & 1 \\ 1 & 1 & 0 \\ 1 & 1 & 1 \end{bmatrix}, \quad (4.1)$$

where $j \in \{0\ ,1\ ,\dots\ ,m_c-1\}$, $m_c = 2^n$, and V_i are the voltages across the capacitors C_i. The electrical schemes that are reported in Fig. 4.2 show how, for the case $n = 3$, the output voltage V_{out} is a function of the IGBTs signal vectors $\mathbf{T}_j$ in the two cases $\mathbf{T}_j = \mathbf{T}_2 = [\ 0\ 1\ 0\ ]$ and $\mathbf{T}_j = \mathbf{T}_6 = [\ 1\ 1\ 0\ ]$.
One can easily verify that the output voltage V_{out} can always be expressed as follows:

$$V_{out} = \mathbf{S}_j\, \mathbf{V}_c, \quad (4.2)$$

where $\mathbf{S}_j = [s_1\ s_2\ \cdots\ s_n]$, for $j \in \{0\ ,1\ ,\dots\ ,m_c-1\}$, are proper configuration vectors. In the two cases of Fig. 4.2, for example, the output voltage V_{out} can be expressed as in (4.2) by using the following two configuration vectors: $\mathbf{S}_2 = [\ 0\ \ 1\ \ -1\ ]$ and $\mathbf{S}_6 = [\ 1\ \ 0\ \ -1\ ]$. Tab. 4.1 shows the relations between the IGBTs signal vectors $\mathbf{T}_j$, the output voltage V_{out} and the configuration vectors $\mathbf{S}_j$ for the case $n = 3$, highlighting the connection between vectors $\mathbf{T}_j$ and $\mathbf{S}_j$. One can verify that the following property holds.

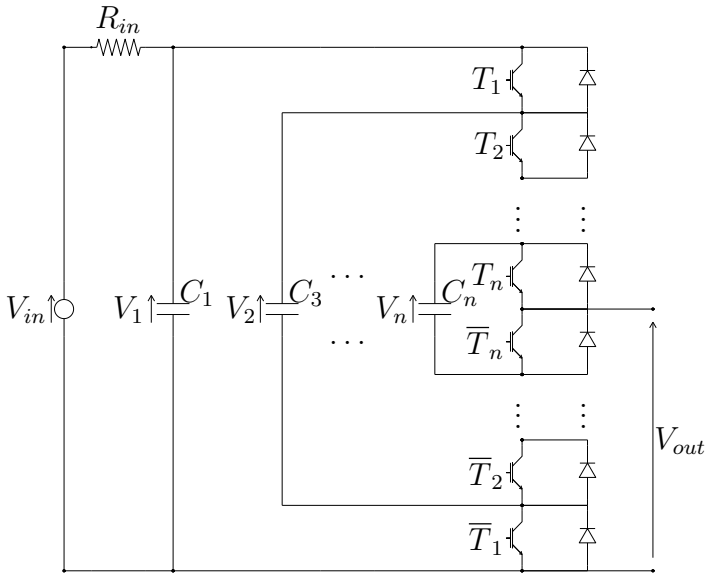

Figure 4.1: Electrical scheme of the n-dimensional Multilevel Flying-Capacitor Converter.

$\mathbf{T}_j$	$[\,T_1\ T_2\ T_3\,]$	V_{out}	$[\,s_1\ \ s_2\ \ s_3\,]$	$\mathbf{S}_j$	V_{out} (4.5)	α_i
$\mathbf{T}_0$	$[\ 0\ \ 0\ \ 0\ ]$	$\mathbf{S}_0\mathbf{V}_c = 0$	$[\ 0\ \ 0\ \ 0\ ]$	$\mathbf{S}_0$	0	0
$\mathbf{T}_1$	$[\ 0\ \ 0\ \ 1\ ]$	$\mathbf{S}_1\mathbf{V}_c = V_3$	$[\ 0\ \ 0\ \ 1\ ]$	$\mathbf{S}_1$	$V_{in}/3$	1
$\mathbf{T}_2$	$[\ 0\ \ 1\ \ 0\ ]$	$\mathbf{S}_2\mathbf{V}_c = V_2 - V_3$	$[\ 0\ \ 1\ -1\ ]$	$\mathbf{S}_2$	$V_{in}/3$	1
$\mathbf{T}_3$	$[\ 0\ \ 1\ \ 1\ ]$	$\mathbf{S}_3\mathbf{V}_c = V_2$	$[\ 0\ \ 1\ \ 0\ ]$	$\mathbf{S}_3$	$2V_{in}/3$	2
$\mathbf{T}_4$	$[\ 1\ \ 0\ \ 0\ ]$	$\mathbf{S}_4\mathbf{V}_c = V_1 - V_2$	$[\ 1\ -1\ \ 0\ ]$	$\mathbf{S}_4$	$V_{in}/3$	1
$\mathbf{T}_5$	$[\ 1\ \ 0\ \ 1\ ]$	$\mathbf{S}_5\mathbf{V}_c = V_1 - V_2 + V_3$	$[\ 1\ -1\ \ 1\ ]$	$\mathbf{S}_5$	$2V_{in}/3$	2
$\mathbf{T}_6$	$[\ 1\ \ 1\ \ 0\ ]$	$\mathbf{S}_6\mathbf{V}_c = V_1 - V_3$	$[\ 1\ \ 0\ -1\ ]$	$\mathbf{S}_6$	$2V_{in}/3$	2
$\mathbf{T}_7$	$[\ 1\ \ 1\ \ 1\ ]$	$\mathbf{S}_7\mathbf{V}_c = V_1$	$[\ 1\ \ 0\ \ 0\ ]$	$\mathbf{S}_7$	V_{in}	3

Table 4.1: Relations between the IGBTs signal vectors $\mathbf{T}_j$, the output voltage V_{out} and the configuration vectors $\mathbf{S}_j$ when $n = 3$.

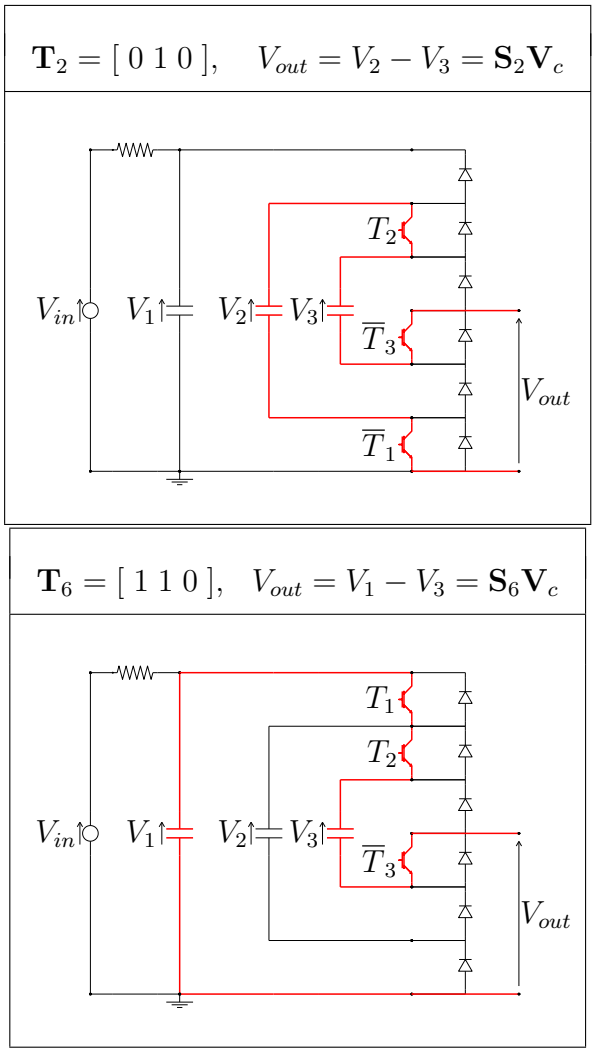

Figure 4.2: Electrical schemes showing how the output voltage V_{out} is obtained as a function of the Insulated Gate Bipolar Transistors (IGBTs) signal vectors $\mathbf{T}_i$ in the two cases $\mathbf{T}_j = \mathbf{T}_2 = [\,0\;1\;0\,]$ and $\mathbf{T}_j = \mathbf{T}_6 = [\,1\;1\;0\,]$.

Property 4 *For $j \in \{0\ ,1\ ,\dots\ ,m_c-1\}$, the components $s_i \in \{-1,\ 0,\ 1\}$ of the configuration vectors $\mathbf{S}_j = [s_1\ s_2\ \cdots\ s_n]$ can be obtained from the components $T_i \in \{0,\ 1\}$ of the IGBTs signal vectors $\mathbf{T}_j = [T_1\ T_2\ \cdots\ T_n]$, as follows:*

$$s_i = \begin{cases} T_1 & \text{if} \quad i = 1, \\ \overline{T}_{i-1}\, T_i - T_{i-1}\, \overline{T}_i & \text{if} \quad i \in \{2, \cdots, n\}, \end{cases} \tag{4.3}$$

or, equivalently, as follows:

$$s_i = \begin{cases} 1 & \text{if} \quad T_i > T_{i-1}, \\ 0 & \text{if} \quad T_i = T_{i-1}, \\ -1 & \text{if} \quad T_i < T_{i-1}, \end{cases} \tag{4.4}$$

for $i \in \{1,\ 2,\ \cdots,\ n\}$ and $T_0 = 0$.

As an example, the Reader can verify that Property 4 holds for all the configuration vectors $\mathbf{S}_j$ that are reported in Tab. 4.1 for the case $n = 3$. The second last column of Tab. 4.1 shows the values of the output voltage V_{out} corresponding to the following capacitors voltages V_i:

$$V_1 = V_{in}, \qquad V_2 = \frac{2V_{in}}{3}, \qquad V_3 = \frac{V_{in}}{3} \qquad \Rightarrow \qquad \mathbf{V}_c = \begin{bmatrix} V_{in} \\ \frac{2V_{in}}{3} \\ \frac{V_{in}}{3} \end{bmatrix}. \tag{4.5}$$

The last column of Tab. 4.1 shows the normalized values α_i, as defined in Sec. 4.1.3, used for representing the equally spaced values of the output voltage V_{out} in the case of $n = 3$ capacitors and $m = 4$ output voltage levels.

Let $\mathbf{S}_M$ denote the matrix containing all the possible configuration vectors $\mathbf{S}_j$,

for $j \in \{0\,, 1\,, \ldots\,, m_c - 1\}$:

$$\mathbf{S}_M = \begin{bmatrix} \mathbf{S}_0 \\ \mathbf{S}_1 \\ \vdots \\ \mathbf{S}_{m_c-1} \end{bmatrix}, \qquad \begin{matrix} \text{if } n = 3 \\ \rightarrow \end{matrix} \qquad \mathbf{S}_M = \begin{bmatrix} \mathbf{S}_0 \\ \mathbf{S}_1 \\ \mathbf{S}_2 \\ \mathbf{S}_3 \\ \mathbf{S}_4 \\ \mathbf{S}_5 \\ \mathbf{S}_6 \\ \mathbf{S}_7 \end{bmatrix} = \begin{bmatrix} 0 & 0 & 0 \\ 0 & 0 & 1 \\ 0 & 1 & -1 \\ 0 & 1 & 0 \\ 1 & -1 & 0 \\ 1 & -1 & 1 \\ 1 & 0 & -1 \\ 1 & 0 & 0 \end{bmatrix}. \tag{4.6}$$

Matrix $\mathbf{S}_M$ can always be rewritten in block matrix form as follows:

$$\mathbf{S}_M = \left[\begin{array}{c|c} \mathbf{0} & \mathbf{S}_{M0} \\ \hline \mathbf{1} & \mathbf{S}_{M1} \end{array}\right], \qquad \begin{matrix} \text{if } n = 3 \\ \rightarrow \end{matrix} \qquad \mathbf{S}_M = \left[\begin{array}{c|cc} 0 & 0 & 0 \\ 0 & 0 & 1 \\ 0 & 1 & -1 \\ 0 & 1 & 0 \\ \hline 1 & -1 & 0 \\ 1 & -1 & 1 \\ 1 & 0 & -1 \\ 1 & 0 & 0 \end{array}\right]. \tag{4.7}$$

One can verify that the block matrices $\mathbf{S}_{M0},\ \mathbf{S}_{M1} \in \mathbf{R}^{2^{n-1}\times(n-1)}$ satisfy the following property.

Property 5 *Let $\mathbf{S}^j_{M0}$ and $\mathbf{S}^j_{M1}$ denote the j-th row of the block matrices $\mathbf{S}_{M0},\ \mathbf{S}_{M1} \in \mathbf{R}^{2^{n-1}\times(n-1)}$ defined in (4.7). Matrix $\mathbf{S}_{M1}$ can be obtained from matrix $\mathbf{S}_{M0}$, as follows:*

$$\mathbf{S}^j_{M1} = -\mathbf{S}^{2^{n-1}+1-j}_{M0} \qquad \textit{for} \qquad j \in \left\{1,\, 2,\, \cdots,\, 2^{n-1}\right\}. \tag{4.8}$$

Eq. (4.8) means that the rows of matrix $\mathbf{S}_{M1}$ are equal, with opposite sign, to the rows of matrix $\mathbf{S}_{M0}$ considered in reverse order.

From Property (5) and Eqs (4.2) and (4.7), one can verify that the following property holds.

Property 6 *If the output value* $V_{out1} = \mathbf{S}_j\,\mathbf{V}_c$ *is obtained using the configuration vector* $\mathbf{S}_j$*, then the following conjugate output value*

$$V_{out2} = V_{in} - V_{out1} = \mathbf{S}_{m_c-j}\,\mathbf{V}_c$$

is obtained by employing the configuration vector $\mathbf{S}_{m_c-j}$*, for* $j \in \{0,\,1,\,\cdots,\,m_c-1\}$ *and* $m_c = 2^n$*.*

4.1.2 Dynamic model

The dynamic model of the Multilevel Flying-Capacitor Converter shown in Fig. 4.1 can be given by using the POG scheme reported in Fig. 4.3. The corresponding POG state-space equations are the following:

$$\begin{cases} \mathbf{C}\,\dot{\mathbf{V}}_c = \mathbf{A}\,\mathbf{V}_c - \mathbf{S}_j^{\mathrm{T}}\,I_{out} + \mathbf{B}\,V_{in}, \\ V_{out} = \mathbf{S}_j\,\mathbf{V}_c. \end{cases} \tag{4.9}$$

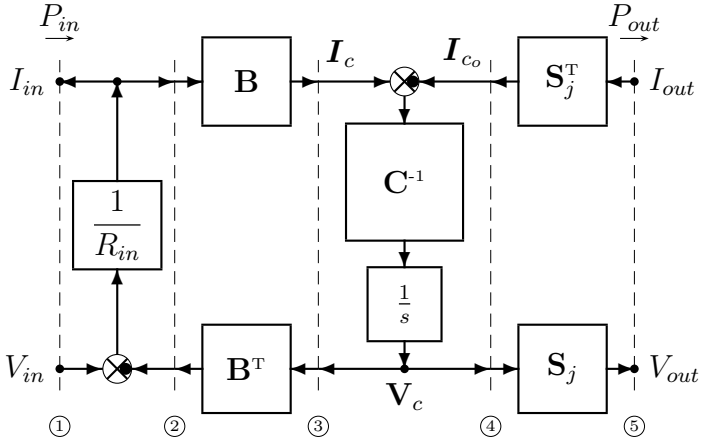

Figure 4.3: POG model of the Multilevel Flying-Capacitor Converter.

Matrices $\mathbf{C}$, $\mathbf{A}$ and vectors $\mathbf{V}_c$, $\mathbf{S}_j^{\mathrm{T}}$ and $\mathbf{B}$ are defined as follows:

$$\mathbf{C}=\left[\begin{array}{c|ccc} C_1 & 0 & \cdots & 0 \\ \hline 0 & C_2 & \cdots & 0 \\ \vdots & \vdots & \ddots & \vdots \\ 0 & 0 & \cdots & C_n \end{array}\right],\ \mathbf{A}=\left[\begin{array}{c|ccc} \frac{-1}{R_{in}} & 0 & \cdots & 0 \\ \hline 0 & 0 & \cdots & 0 \\ \vdots & \vdots & \ddots & \vdots \\ 0 & 0 & \cdots & 0 \end{array}\right],\ \mathbf{V}_c=\left[\begin{array}{c} V_1 \\ \hline V_2 \\ \vdots \\ V_n \end{array}\right],\ \mathbf{S}_j^{\mathrm{T}}=\left[\begin{array}{c} s_1 \\ \hline s_2 \\ \vdots \\ s_n \end{array}\right],\ \mathbf{B}=\left[\begin{array}{c} \frac{1}{R_{in}} \\ \hline 0 \\ \vdots \\ 0 \end{array}\right]. \tag{4.10}$$

A representation such as the one that is shown in (4.9) and (4.10) highlights the following interesting features of the system:

- The energy matrix $\mathbf{C}$ groups together the dynamic physical parameters C_i for $i \in \{1, 2, \ldots, n\}$, namely the system capacitors.
- The power matrix $\mathbf{A}$ and the input matrix $\mathbf{B}$ contain the static physical parameter R_{in}, which is the system input resistance.
- The *configuration vector* $\mathbf{S}_j$ contains the control signals that directly determine how the output current I_{out} is going to charge/discharge the capacitors through $\mathbf{I}_{c_0} = \mathbf{S}_j^{\mathrm{T}} I_{out}$ and, at the same time, how the output voltage V_{out} is going to be generated from the capacitors voltages through (4.2).

Therefore, the proposed POG state-space model allows the parameters within the system matrices to maintain their physical meaning, and also allows to emphasize the presence of the configuration vector $\mathbf{S}_j$, representing the output of the two control algorithms that are addressed in Sec. 4.2.1 and Sec. 4.2.4. The POG block scheme that is shown in Fig. 4.3 presents a graphical representation of the dynamic model of the considered system. The vertical dashed lines ①, ②, …, ⑤ present in the POG scheme describe the system power sections: the product of the two power variables characterizing the power section has the physical meaning of "power flowing through the considered power section". The input power $P_{in} = V_{in}\, I_{in}$ flows through power section ① and the output power $P_{out} = V_{out}\, I_{out}$ flows through power section ⑤. The block scheme in between sections ① and ② describes the static equation of the input resistance R_{in}, the block scheme in between sections ② and ③ describes the interaction between the input resistance R_{in} and the capacitors C_i, and the block scheme in between sections ③ and ④ describes the dynamic equations of the capacitors C_i. Finally, the block scheme in between sections ④ and ⑤, which is characterized by the configuration vector $\mathbf{S}_j$, describes the interaction between the capacitors C_i and the output power section ⑤.

Remark 3 *The first vectorial equation of system* (4.9) *can be rewritten as follows:*

$$\dot{\mathbf{V}}_c = \mathbf{C}^{-1}\mathbf{A}\mathbf{V}_c \underbrace{-\mathbf{C}^{-1}\mathbf{S}_j^T I_{out}}_{\dot{\mathbf{V}}_c^{out}} + \mathbf{C}^{-1}\mathbf{B}\, V_{in}.$$

Vector $\dot{\mathbf{V}}_c^{out} = -\mathbf{C}^{-1}\mathbf{S}_j^T I_{out}$ *is the component of the velocity vector* $\dot{\mathbf{V}}_c$ *which is due to the presence of the output current* I_{out}*. The direction of vector* $\dot{\mathbf{V}}_c^{out}$ *is completely defined by the configuration vector* $\mathbf{S}_j$ *and by the values of the capacitors* C_i*.*

Remark 4 *The first scalar equation of system* (4.9) *can be rewritten as follows:*

$$R_{in}C_1\dot{V}_1 = V_{in} - V_1 - R_{in}\, s_1\, I_{out}. \tag{4.11}$$

Because the value of the input resistance R_{in} *is typically very low, from (4.11) it follows that* $V_1 \simeq V_{in}$*, that is the value of voltage* V_1 *tends to remain close to the input voltage value* V_{in}*. Hereinafter, the condition* $V_1 = V_{in}$ *will be assumed. This condition holds exactly if* $R_{in} \to 0$*, or if capacitor* C_1 *is replaced with a battery providing a constant voltage* V_{in}*.*

4.1.3 Calculation of all the Configuration Voltage Vectors

An m-level Multilevel Converter is characterized by m different equally spaced values V_{oi} of the output voltage V_{out}:

$$V_{oi} = \frac{i\, V_{in}}{m-1} \qquad \text{for} \qquad i = \{0,\ 1,\ \ldots,\ m-1\}. \tag{4.12}$$

In the following, the values V_{oi} in (4.12) will often be referred to by using the symbolic integer values α_i, defined as follows:

$$\alpha_i = \frac{V_{oi}}{K_m} = i \qquad \text{where} \qquad K_m = \frac{V_{in}}{m-1}, \tag{4.13}$$

for $i = \{0,\ 1,\ \ldots,\ m-1\}$. From (4.13), it follows that the product $\alpha_i\, K_m$ directly gives the values of the corresponding equally spaced values V_{oi} of the output voltage V_{out}. All of the possible values V_{oi} of the output voltage V_{out} that can be obtained using a particular voltage vector $\mathbf{V}_c$ can be expressed as follows:

$$\mathbf{V}_o = \mathbf{S}_M \mathbf{V}_c, \tag{4.14}$$

where $\mathbf{S}_M$ is the matrix defined in (4.6). The considered Flying-Capacitor system acts properly as a Multilevel Converter only if vector $\mathbf{V}_o = [\ V_{o1},\ V_{o2},\ \ldots,\ V_{om_c}]^{\mathrm{T}}$

contains, among its components V_{oj}, all the m different equally spaced values V_{oi} given in (4.12):

$$\forall i \in \{0,\ 1,\ \ldots,\ m-1\},\ \ \exists\, V_{oj} \in \{V_{o1},\ V_{o2},\ \ldots,\ V_{om_c}\}\ \mid\ V_{oj} = \frac{i\, V_{in}}{m-1}. \quad (4.15)$$

Definition 1 *Any voltage vector $\mathbf{V}_c$ satisfying (4.14) and (4.15) will be called a "Configuration Voltage Vector of order m" for the Multilevel Flying-Capacitor Converter.*

The problem of finding all the Configuration Voltage Vectors $\mathbf{V}_c$ of order m for the considered Multilevel Flying-Capacitor Converter can be solved as follows. Dividing (4.14) by constant K_m, one obtains the following symbolic integer relation:

$$\mathbf{V}_L = \mathbf{S}_M \mathbf{V}_m \qquad \text{where} \qquad \mathbf{V}_L = \frac{\mathbf{V}_o}{K_m} \quad \text{and} \quad \mathbf{V}_m = \frac{\mathbf{V}_c}{K_m}. \quad (4.16)$$

A vector $\mathbf{V}_m$ in (4.16) is a Configuration Voltage Vector of order m only if all the components V_{Lj} of vector $\mathbf{V}_L = [V_{L1},\ V_{L2},\ \ldots,\ V_{Lm_c}]$, for $j \in \{1,\ 2,\ \ldots,\ m_c\}$, are integer values $V_{Lj} \in \{0,\ 1,\ \ldots,\ m-1\}$ that satisfy the following relation:

$$\text{unique}(\{V_{L1},\ V_{L2},\ \ldots,\ V_{Lm_c}\}) = \{0,\ 1,\ \ldots,\ m-1\}, \quad (4.17)$$

where "unique($\mathcal{S}$)" is a function providing a new set containing all the elements of set $\mathcal{S}$ which are different from each other.

Property 7 *In (4.16), all the components β_i of a Configuration Voltage Vector $\mathbf{V}_m$, for $i \in \{1,\ \ldots,\ n\}$, are integer values satisfying $\beta_i \in \{0,\ 1,\ \ldots,\ m-1\}$:*

$$\mathbf{V}_m = \begin{bmatrix} \beta_n \\ \beta_{n-1} \\ \vdots \\ \beta_1 \end{bmatrix} = \begin{bmatrix} m-1 \\ \beta_{n-1} \\ \vdots \\ \beta_1 \end{bmatrix}, \quad (4.18)$$

where $\beta_{i+1} \geq \beta_i$ for $i \in \{1,\ 2,\ \ldots,\ n-2\}$. Furthermore, note that the top component β_n of vector $\mathbf{V}_m$ is always given by $\beta_n = m-1$.

The first statement of Property 7 holds true because: 1) all the components V_{Lj} of vector $\mathbf{V}_L$ in (4.16) are integer values, see (4.17); 2) the configuration vectors $\mathbf{S}_1 = [0\ \ldots,\ 0,\ 0,\ 1]$, $\mathbf{S}_2 = [0\ \ldots,\ 0,\ 1,\ 0]$, $\mathbf{S}_3 = [0\ \ldots,\ 1,\ 0,\ 0]$, ..., $\mathbf{S}_{m_c} = [1,\ 0\ \ldots,\ 0,\ 0]$ are always present among the rows of matrix $\mathbf{S}_M$. The second statement of Property 7 holds true because the top component β_n of vector $\mathbf{V}_m$ is always equal to the first component V_1 of vector $\mathbf{V}_c$ expressed in symbolic integer form: $\beta_n = V_1/K_m = V_{in}/K_m = m-1$, see (4.13). This relation holds thanks to the assumption $V_1 = V_{in}$ made in Remark 4.

Thanks to Property 7, all the Configuration Voltage Vectors $\mathbf{V}_m$ of order m for the considered Multilevel Flying-Capacitor Converter can be found by making an exhaustive research in (4.18) for $\beta_i \in \{0,\ 1,\ \ldots,\ m-1\}$, and keeping all the solutions $\mathbf{V}_m$ that satisfy (4.16) and (4.18). Tab. 4.2 reports all the Configuration Voltage Vectors $\mathbf{V}_m$ for the case $n = 3$ and for $m \in \{4,\ 5,\ \ldots,\ 8\}$. The total number N_c of Configuration Voltage Vectors for the case $n = 3$ is $N_c = 24$. Fig. 4.4 shows a graphical representation of the normalized form $\overline{\overline{\mathbf{V}}}_m$ of all the Configuration Voltage Vectors $\mathbf{V}_m$ for the case $n = 3$. The normalized form $\overline{\overline{\mathbf{V}}}_m$ of the Voltage Vectors $\mathbf{V}_m$ defined in (4.18) is obtained as follows:

$$\overline{\overline{\mathbf{V}}}_m = \frac{\mathbf{V}_m(2:\text{end})}{m-1} = \begin{bmatrix} \frac{\beta_{n-1}}{m-1} \\ \vdots \\ \frac{\beta_1}{m-1} \end{bmatrix} = \begin{bmatrix} \overline{\overline{V}}_2 \\ \vdots \\ \overline{\overline{V}}_n \end{bmatrix} \quad \begin{matrix} \text{if } n=3 \\ \rightarrow \end{matrix} \quad \overline{\overline{\mathbf{V}}}_m = \begin{bmatrix} \overline{\overline{V}}_2 \\ \overline{\overline{V}}_3 \end{bmatrix}, \tag{4.19}$$

meaning that the last $n-1$ components of vector $\mathbf{V}_m$, from the second to the last one, are normalized by $m-1$. Fig. 4.4 clearly shows a symmetry with respect to the red straight line $\overline{\overline{V}}_3 = 1 - \overline{\overline{V}}_2$. This symmetry is strictly connected to Property 8 and Property 9, introduced in the following.

Property 8 *For every Configuration Voltage Vector* $\mathbf{V}_m$*, there exists a* Conjugate

m	4	4	4	5	5	5	6	6	6	6	6	6	7	7	7	7	7	7	8	8	8	8	8	8
$\mathbf{V}_m$	3	3	3	4	4	4	5	5	5	5	5	5	6	6	6	6	6	6	7	7	7	7	7	7
	1	2	2	2	3	3	2	3	3	4	4	4	3	3	4	4	5	5	3	3	5	6	5	6
	1	1	2	1	1	2	1	1	2	1	2	3	1	2	1	3	2	3	1	2	1	2	4	4
N_β	2	3	4	3	4	5	3	4	5	5	6	7	4	5	5	7	7	8	4	5	6	8	9	10

Table 4.2: All the Configuration Voltage Vectors $\mathbf{V}_m$ for the case $n = 3$ and $m \in \{4, 5, \ldots, 8\}$.

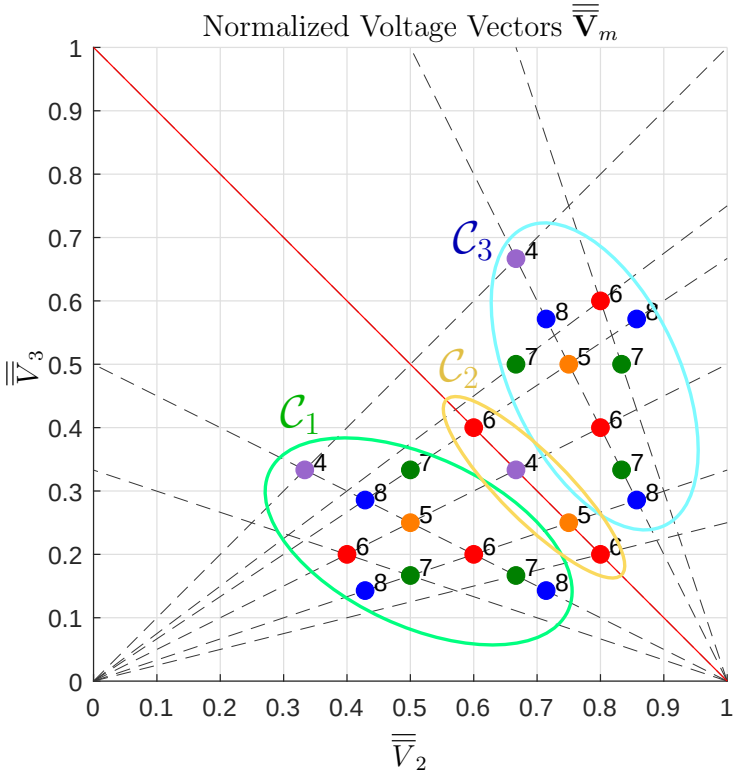

Figure 4.4: All the Configuration Voltage Vectors $\mathbf{V}_m$, in normalized form $\overline{\overline{\mathbf{V}}}_m$, for the case $n = 3$.

Configuration Voltage Vector $\mathbf{V}_m^\star$, *defined as follows:*

$$\mathbf{V}_m = \begin{bmatrix} m-1 \\ \beta_{n-1} \\ \vdots \\ \beta_2 \\ \beta_1 \end{bmatrix} \quad \Rightarrow \quad \mathbf{V}_m^\star = \begin{bmatrix} m-1 \\ m-1-\beta_1 \\ m-1-\beta_2 \\ \vdots \\ m-1-\beta_{n-1} \end{bmatrix}. \tag{4.20}$$

Furthermore, one can easily verify that $(\mathbf{V}_m^\star)^\star = \mathbf{V}_m$. *This property directly follows from Property 6.*

Property 9 *Every Configuration Voltage Vector* $\mathbf{V}_m$, *see (4.20), is characterized by a configuration number* N_β, *defined as follows:*

$$N_\beta = \sum_{i=1}^{n-1} \beta_i.$$

The set $\mathcal{C}$ *of all the Configuration Voltage Vectors* $\mathbf{V}_m$ *can be divided into three different subsets, which are denoted by* $\mathcal{C}_1$, $\mathcal{C}_2$, *and* $\mathcal{C}_3$, *defined as follows:*

$$\begin{gathered} \mathcal{C}_1 = \{\mathbf{V}_m \in \mathcal{C} | N_\beta < m-1\}, \qquad \mathcal{C}_2 = \{\mathbf{V}_m \in \mathcal{C} | N_\beta = m-1\}, \\ \mathcal{C}_3 = \{\mathbf{V}_m \in \mathcal{C} | N_\beta > m-1\}. \end{gathered} \tag{4.21}$$

The sets $\mathcal{C}_1$ *and* $\mathcal{C}_3$ *are conjugate to one another: if* $\mathbf{V}_m \in \mathcal{C}_1$, *then* $\mathbf{V}_m^\star \in \mathcal{C}_3$ *and vice versa. Furthermore, set* $\mathcal{C}_2$ *is conjugate to itself: if* $\mathbf{V}_m \in \mathcal{C}_2$, *then* $\mathbf{V}_m^\star = \mathbf{V}_m$.

Note: Tab. 4.2 has been given, for each number of output voltage levels m, in ascending order from left to right with respect to the configuration number N_β. Additionally, the colors that are present in Tab. 4.2 denote the subsets to which the Configuration Voltage Vectors $\mathbf{V}_m$ belong: green color if $\mathbf{V}_m \in \mathcal{C}_1$, yellow color if $\mathbf{V}_m \in \mathcal{C}_2$, and blue color if $\mathbf{V}_m \in \mathcal{C}_3$. The same color notation has been adopted in Fig. 4.4 to identify the subsets to which the normalized forms $\overline{\overline{\mathbf{V}}}_m$ of the Configuration Voltage Vectors $\mathbf{V}_m$ belong, which are highlighted by the colored ellipses.

The number N_c of Configuration Voltage Vectors $\mathbf{V}_m$ for the case $n = 4$ is $N_c = 407$. Fig. 4.5 shows a graphical representation of the normalized form $\overline{\overline{\mathbf{V}}}_m$ of

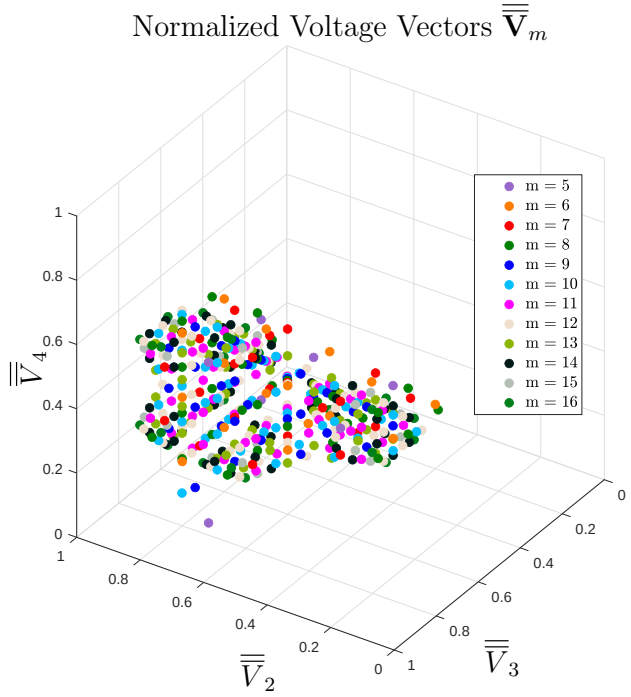

Figure 4.5: All the Configuration Voltage Vectors $\mathbf{V}_m$, in normalized form $\overline{\overline{\mathbf{V}}}_m$, for the case $n = 4$.

all the Configuration Voltage Vectors $\mathbf{V}_m$ for the case $n = 4$. The considerations that are introduced in Property 8 and Property 9 also apply to the set of all the Configuration Voltage Vectors $\mathbf{V}_m$ for the cases $n = 4$, $n = 5$, etc.

The number N_c of the Configuration Voltage Vectors $\mathbf{V}_m$ increases very rapidly by increasing n, with a rate faster than exponential: $N_c = 24$ for $n = 3$, $N_c = 407$ for $n = 4$, $N_c = 14252$ for $n = 5$, $N_c = 1044305$ for $n = 6$, etc.

4.1.4 Model verification

The model of the multilevel flying-capacitor converter proposed in Fig. 4.3 has been tested in simulation against one of the most well-known platforms for the simulation of power electronics systems, namely PLECS, in order to perform a model verification. For this comparative simulations, the case $n = 4$ and $\mathbf{V}_m = [4\ 3\ 2\ 1]^{\mathrm{T}}$ has been considered as a case study. Fig. 4.6 reports the PLECS model and the system parameters. The initial and desired voltages for the multilevel converter capacitors can be

determined by computing the voltage vector $\mathbf{V}_c$ starting from the configuration voltage vector $\mathbf{V}_m$ and using (4.13) and (4.16), namely $\mathbf{V}_c = [100\ 75\ 50\ 25]^{\mathrm{T}}$. The initial conditions of the RLC load are assumed to be equal to zero. The desired voltage V_d is assumed to be sinusoidal with an offset equal to $V_{in}/2$, a peak-to-peak amplitude equal to V_{in} and a frequency equal to 50 Hz. The simulation performed using the PLECS model in Fig. 4.6 and the simulation performed using the Matlab/Simulink POG model in Fig. 4.3 have both been performed applying the Minimum Distance Control described in Sec. 4.2.1.

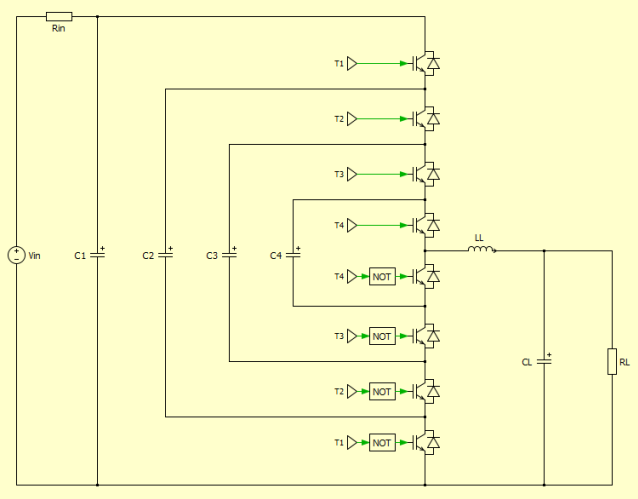

V_{in}	100 [V]
R_{in}	0.1 [mΩ]
C_1	25 [mF]
C_2	33 [mF]
C_3	50 [mF]
C_4	100 [mF]
L_L	19 [mH]
C_L	50 [μF]
R_L	10 [Ω]

Figure 4.6: PLECS implementation and parameters of the $n = 4$ multilevel flying-capacitor converter.

The results that are given by the PLECS model are shown in Fig. 4.7. The comparison of these results with those given by the Matlab/Simulink POG model is reported in Fig. 4.8.

The very good matching between the output voltage characteristics that are given by PLECS and by Matlab/Simulink in Fig. 4.8 verifies the correctness of the proposed model of the multilevel flying-capacitor converter.

Figure 4.7: Simulation results given by the PLECS model: output voltage V_{out} (upper subplot) and filtered voltage across C_L (lower subplot).

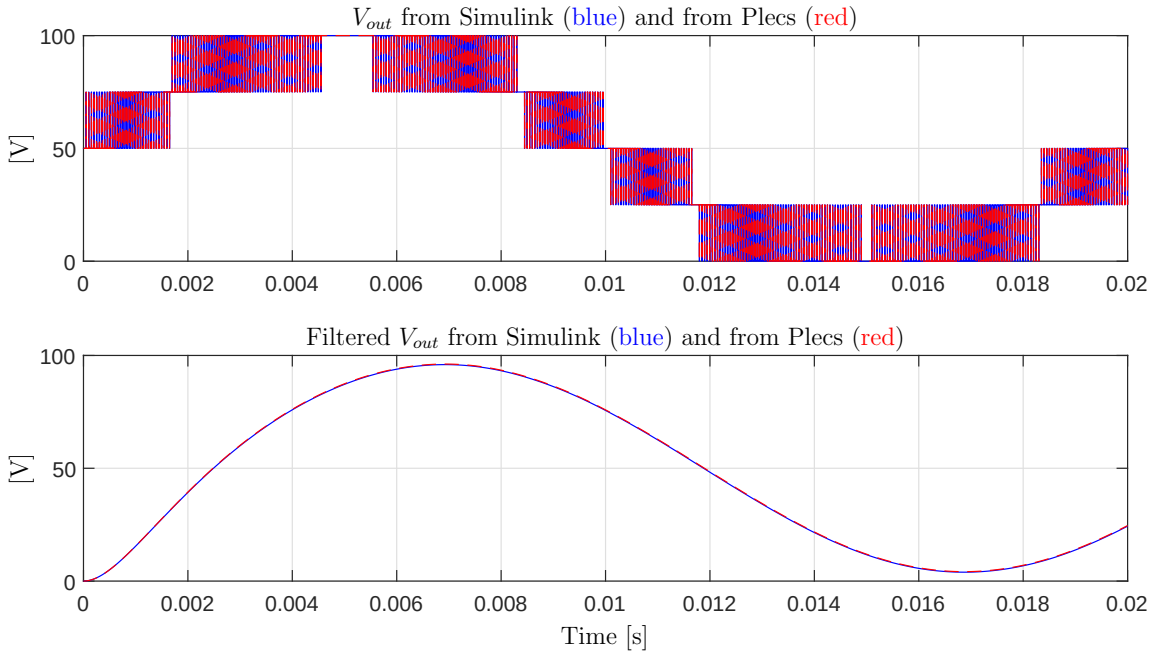

Figure 4.8: Comparison of the results given by PLECS and Matlab/Simulink: output voltage V_{out} (upper subplot) and filtered voltage across C_L (lower subplot).

4.2 Control of the Converter

4.2.1 Minimum Distance Control

Fig. 4.9 shows the typical scheme of a closed-loop Minimum Distance Control of a Multilevel Flying-Capacitor Converter. The first block of the scheme is the Output Level Generator. Let us consider the case of $m = 6$ output voltage levels, which will, therefore, be equally spaced between level "0" and level "$m - 1 = 5$". The black characteristic in Fig. 4.10 shows the desired normalized voltage $\tilde{V}_d$ multiplied by $m - 1$, in order to see it superimposed to the blue characteristic, namely the *desired output voltage level* α.

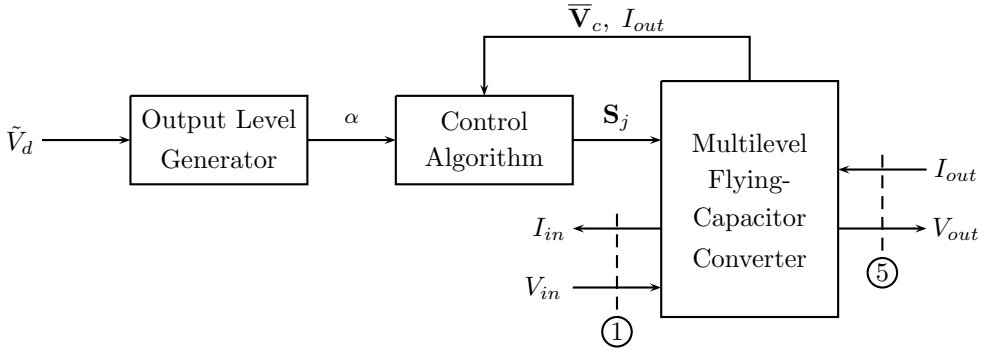

Figure 4.9: Typical scheme of a closed-loop Minimum Distance Control of a Multilevel Flying-Capacitor Converter.

The Output Level Generator generates an integer value $\alpha \in \{0,\ 1,\ \ldots,\ m-1\}$, which defines the desired output level to be applied at a certain time instant t_k:

$$\alpha = \sum_{h=0}^{m-1} (V_d \geq V_{cr_h}),$$

where $(V_d \geq V_{cr_h}) = 1$ if $V_d \geq V_{cr_h}$ and $(V_d \geq V_{cr_h}) = 0$ if $V_d < V_{cr_h}$. The second and third blocks in the scheme of Fig. 4.9 are the Control Algorithm and the Multilevel Flying-Capacitor Converter. The latter is modeled using the POG block scheme that is shown in Fig. 4.3. Indeed, it is possible to notice the correspondence between the power sections ① and ⑤ in Fig. 4.3 and Fig. 4.9. The purpose of the Control Algorithm is to properly generate the Configuration Voltage Vector $\mathbf{S}_j$, which has

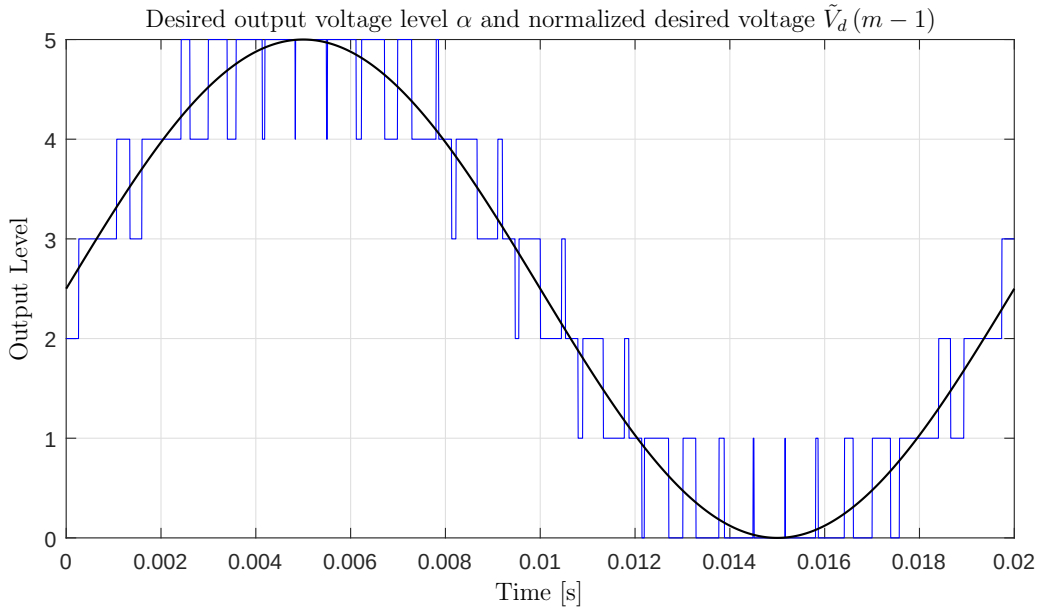

Figure 4.10: Desired output voltage level α superimposed to normalized desired voltage $\tilde{V}_d\,(m-1)$.

a one-to-one correspondence with the IGBTs signal vector $\mathbf{T}_j$ through Property 4, giving the desired output level α. This will be accomplished by exploiting the redundance of Configuration Voltage Vectors $\mathbf{S}_j$ generating the same desired output level α when available, as described in the remainder of this section. The Control Algorithm shown in Fig. 4.9 is typically a "Minimum Distance Algorithm". Thanks to the assumption $V_1 = V_{in}$ made in Remark 4, the Minimum Distance algorithm only applies to the components V_2, V_3, ..., V_n of the capacitors voltage vector $\mathbf{V}_c$. Let us denote as $\overline{\mathbf{V}}_c = \mathbf{V}_c(2\!:\!n)$, $\overline{\mathbf{V}}_{m0} = K_m\mathbf{V}_m(2\!:\!n) = V_{in}\overline{\overline{\mathbf{V}}}_m$ and $\overline{\mathbf{S}}_{Cj} = -\mathbf{S}_j(2\!:\!n)./\mathbf{C}(2\!:\!n)$ the following reduced vectors:

$$\overline{\mathbf{V}}_c = \begin{bmatrix} V_2 \\ V_3 \\ \vdots \\ V_n \end{bmatrix}, \qquad \overline{\mathbf{V}}_{m0} = \begin{bmatrix} \frac{V_{in}\beta_{n-1}}{m-1} \\ \frac{V_{in}\beta_{n-2}}{m-1} \\ \vdots \\ \frac{V_{in}\beta_1}{m-1} \end{bmatrix}, \qquad \overline{\mathbf{S}}_{Cj} = \begin{bmatrix} -\frac{s_{2j}}{C_2} \\ -\frac{s_{3j}}{C_3} \\ \vdots \\ -\frac{s_{nj}}{C_n} \end{bmatrix}, \tag{4.22}$$

where $\mathbf{V}_m$ is the considered Configuration Voltage Vector that is introduced in (4.16) and $\mathbf{S}_j$ is the j-th configuration vector defined in (4.10). The minimum distance algorithm tries to keep the reduced voltage vector $\overline{\mathbf{V}}_c$ as close as possible

to the desired reduced voltage vector $\overline{\mathbf{V}}_{m0}$. Let α be the desired output level to be applied at time t_k and let

$$\mathcal{S}_\alpha = \left\{ j \;\mid\; j \in [0,\ 1,\ \ldots,\ m_c - 1] \wedge \mathbf{S}_j \mathbf{V}_c = \frac{\alpha V_{in}}{m-1} \right\} \tag{4.23}$$

be the set of the indexes j of all the configuration vectors $\mathbf{S}_j$, which, for the considered Configuration Voltage Vector $\mathbf{V}_m$, provide the output level α. The Minimum Distance algorithm acts as follows:

1. At instant t_k, read the value of the reduced voltage vector $\overline{\mathbf{V}}_c(t_k)$;

2. For any $j \in \mathcal{S}_\alpha$, compute the new position $\overline{\mathbf{V}}_{cj}(t_k + T_W)$ of the reduced voltage vector $\overline{\mathbf{V}}_c$ at instant $t_k + T_W$, which is due to the application of the configuration vector $\mathbf{S}_j$:

$$\overline{\mathbf{V}}_{cj}(t_k + T_W) = \overline{\mathbf{V}}_c(t_k) + \underbrace{\overline{\mathbf{S}}_{Cj}\, I_{out}\, T_W}_{\Delta\overline{\mathbf{S}}_{Cj}} = \overline{\mathbf{V}}_c(t_k) + \Delta\overline{\mathbf{S}}_{Cj}, \tag{4.24}$$

   where I_{out} is the value of the output current at instant t_k and T_W is the time for which the configuration vector $\mathbf{S}_j$ is applied.

3. For any $j \in \mathcal{S}_\alpha$, compute the following distance vectors:

$$\Delta\overline{\mathbf{V}}_{cj} = \overline{\mathbf{V}}_{cj}(t_k + T_W) - \overline{\mathbf{V}}_{m0} \tag{4.25}$$

   between points $\overline{\mathbf{V}}_{cj}(t_k + T_W)$ and the desired reduced Voltage Vector $\overline{\mathbf{V}}_{m0}$.

4. At instant t_k, apply the configuration vector $\mathbf{S}_{j^*}$, with $j^* \in \mathcal{S}_\alpha$, for which the norm of vectors $\Delta\overline{\mathbf{V}}_{cj}$ is minimized:

$$\mathbf{S}_{j^*} \quad \text{such that} \quad |\Delta\overline{\mathbf{V}}_{cj^*}| \leq |\Delta\overline{\mathbf{V}}_{cj}| \quad \text{for} \quad j \in \mathcal{S}_\alpha. \tag{4.26}$$

Fig. 4.11 shows a graphical example of how the Minimum Distance algorithm works in the case of $n = 3$, $m = 4$, $\mathbf{V}_m = [\ 3\ \ 2\ \ 1\ ]^{\mathrm{T}}$ when the desired output level is $\alpha = 1$. In this case, the distance vector $\Delta\overline{\mathbf{V}}_{cj}$ in (4.25) having the minimum norm is $|\Delta\mathbf{V}_{c4}|$, highlighted in magenta in the figure.

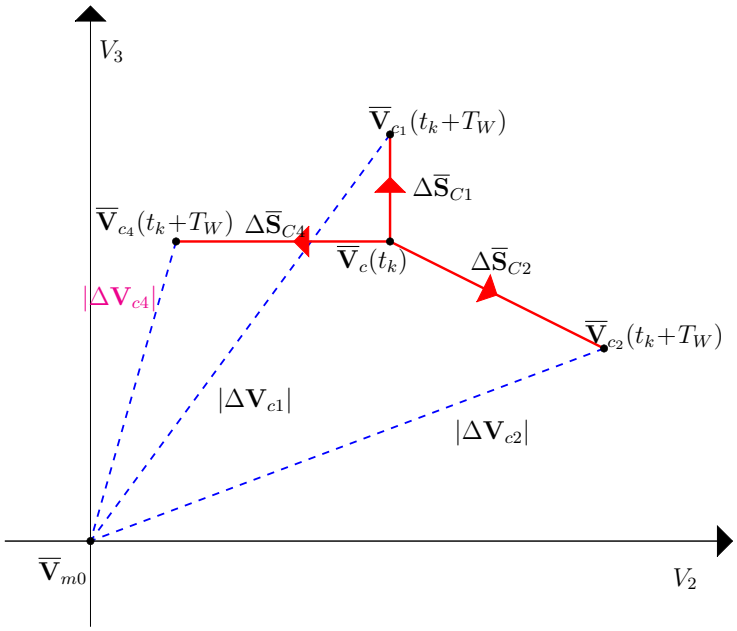

Figure 4.11: Calculations of the Minimum Distance algorithm in the case of $n = 3$, $m = 4$, $\mathbf{V}_m = [\,3\;\;2\;\;1\,]^{\mathrm{T}}$ when the desired output level is $\alpha = 1$.

4.2.2 Basic Configurations

For any n-dimensional multilevel flying-capacitor converter, let us denote, as *Basic Configuration Voltage Vector*, the following Configuration Voltage Vector:

$$\mathbf{V}_m^* = \Big[\, m{-}1 \quad m{-}2 \quad \ldots \quad 2 \quad 1 \,\Big]^{\mathrm{T}}, \tag{4.27}$$

occurring when $m = n + 1$.

Property 10 *For any given n, the basic configuration voltage vector $\mathbf{V}_m^*$ is the only configuration voltage vector for which the Minimum Distance algorithm is able to keep the reduced voltage vector $\overline{\mathbf{V}}_c$ in the neighborhood of the desired reduced voltage vector $\overline{\mathbf{V}}_{m0}^*$, for any value of the normalized desired voltage $\tilde{V}_d$ and the output current I_{out}.*

This property holds because the Basic Configuration Voltage Vector $\mathbf{V}_m^*$ is the only one for which the number of possible configurations $\mathbf{S}_j$ that are associated to the two adjacent levels of any desired voltage V_d are sufficient to guarantee that, at each

PWM step, the distance between the reduced vector $\mathbf{V}_c$ and the desired reduced voltage vector $\mathbf{V}^*_{m0}$ is decreased for any value of the output current I_{out}. For any other Configuration Voltage Vector $\mathbf{V}_m$, it is always possible to find values for V_d and I_{out} causing the reduced vector $\mathbf{V}_c$ to indefinitely diverge from the desired reduced voltage vector $\mathbf{V}_{m0}$.

Fig. 4.12 shows a first example of the validity of Property 10, for the case $n = 3$ and $\mathbf{V}^*_m = [\ 3\ \ 2\ \ 1\ ]^{\mathrm{T}}$. In this figure, a certain number of trajectories in the space (V_2, V_3) starting from initial conditions that are distant from the desired reduced voltage vector $\overline{\mathbf{V}}_{m0}$ are shown. Red asterisks in the figure denote the considered initial conditions. The trajectories have been obtained using the Minimum Distance algorithm and using the following input signals:

$$V_d = \frac{V_{in}}{2} + \frac{V_{in}}{2}\sin(800\pi t), \qquad I_{out} = 10\,A, \qquad V_{in} = 1\,V. \tag{4.28}$$

The figure clearly shows that all the trajectories asymptotically tend to the desired reduced voltage vector $\overline{\mathbf{V}}_{m0} = [\ 0.66\ \ 0.33\ ]^{\mathrm{T}}$.

A second similar example is given in Fig. 4.13 for the case $n = 4$ and $\mathbf{V}^*_m = [\ 4\ \ 3\ \ 2\ \ 1\ ]^{\mathrm{T}}$. The three-dimensional trajectories in the space (V_2, V_3, V_4) have been obtained using the same input signals (4.28) that were used for the previous example. Even in this case, one can notice that all the trajectories asymptotically tend to the desired reduced voltage vector $\overline{\mathbf{V}}_{m0} = [\ 0.75\ \ 0.5\ \ 0.25\ ]^{\mathrm{T}}$.

4.2.3 Robustness Assessment of the Configuration Voltage Vectors

All of the Configuration Voltage Vectors $\mathbf{V}_m$ different from the basic one $\mathbf{V}^*_m$ are characterized by divergent voltage trajectories under particularly unfavorable operating conditions, as stated in Property 10. In Fig. 4.14 and Fig. 4.15, for example, the voltage trajectories that are associated with two different Configuration Voltage Vectors $\mathbf{V}_m$ in the space (V_2, V_3) for the case $n = 3$ are reported, starting from different initial conditions that are distant from the desired reduced voltage vector $\overline{\mathbf{V}}_{m0}$. The considered initial conditions are denoted by red asterisks in the figures. The trajectories shown in Fig. 4.14 have been obtained using $\mathbf{V}_m = [5\ 4\ 3]^{\mathrm{T}}$,

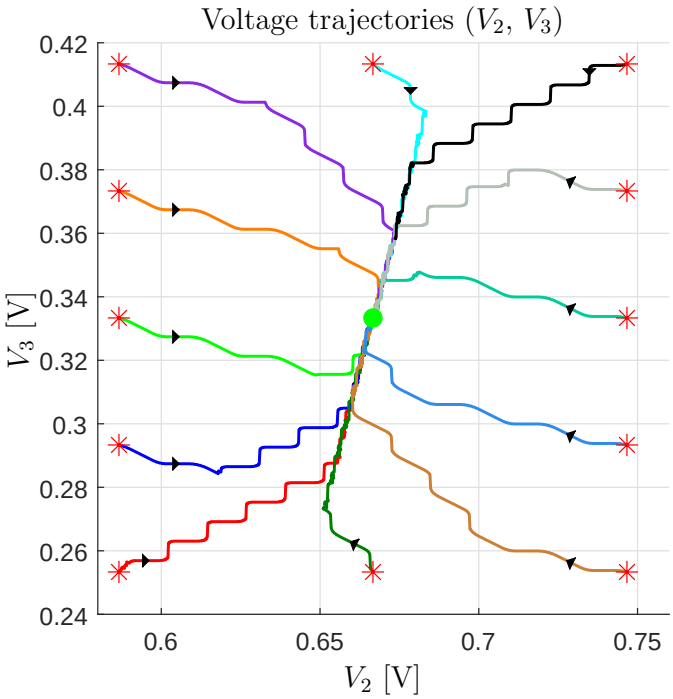

Figure 4.12: Stability of the Basic Configuration Voltage Vector $\mathbf{V}_m^* = [3\ \ 2\ \ 1]^{\mathrm{T}}$ for $n = 3$.

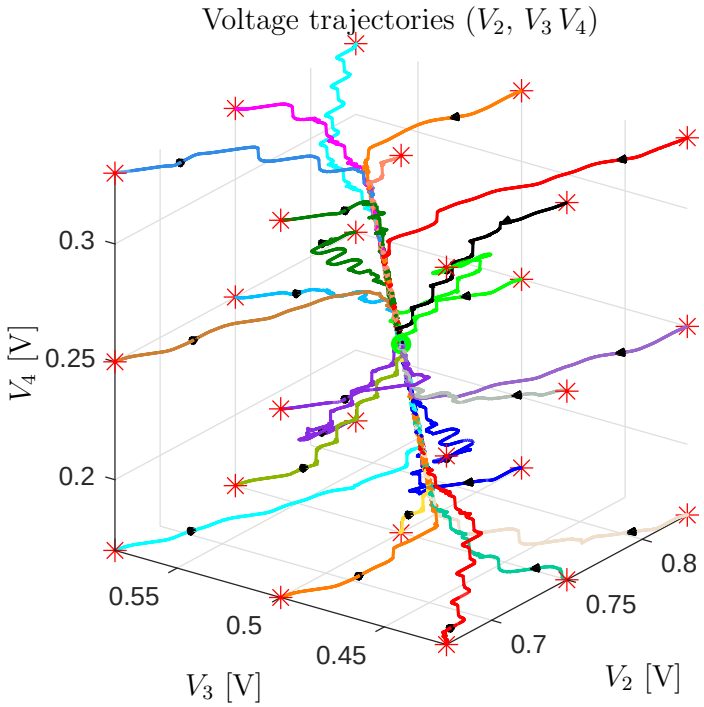

Figure 4.13: Stability of the Basic Configuration Voltage Vector $\mathbf{V}_m^* = [4\ \ 3\ \ 2\ \ 1]^{\mathrm{T}}$ for $n = 4$.

$\overline{\mathbf{V}}_{m0} = [\ 0.8 \quad 0.6\ ]^{\mathrm{T}}$, $V_d = 0.3\,V$ and $I_{out} = 10\,A$. The trajectories in Fig. 4.15 have been obtained using $\mathbf{V}_m = [5\ 3\ 2]^{\mathrm{T}}$, $\overline{\mathbf{V}}_{m0} = [\ 0.6 \quad 0.4\ ]^{\mathrm{T}}$, $V_d = 0.7\,V$ and $I_{out} = 10\,A$. In both cases, after a transient, all the trajectories tend to diverge along a particular direction, which is characteristic of the considered Configuration Voltage Vectors $\mathbf{V}_m$. One can verify that the same qualitative behavior is obtained for any $\mathbf{V}_m$ different from the Basic Configuration Voltage Vector $\mathbf{V}_m^*$.

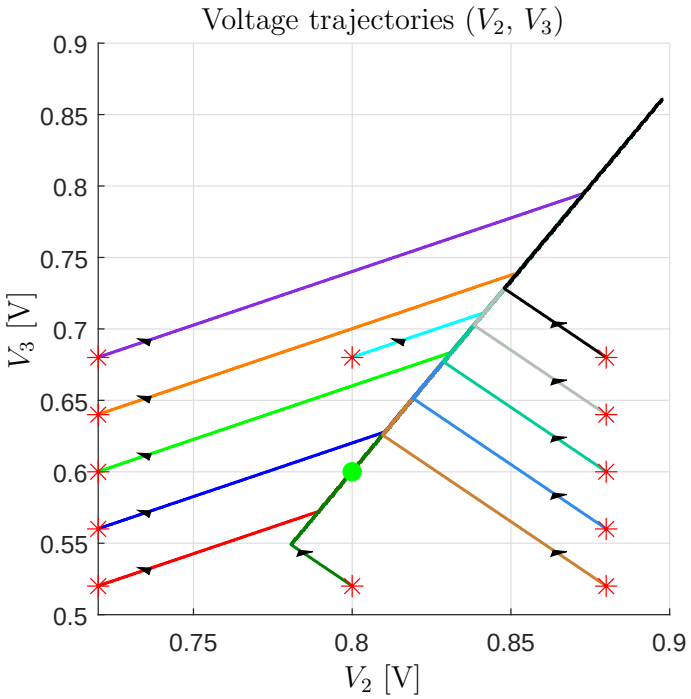

Figure 4.14: Instability of the Configuration Voltage Vector $\mathbf{V}_m = [5\ 4\ 3]^{\mathrm{T}}$ when $V_d = 0.3$ and $I_{out} = 10\,[A]$.

From the previous considerations, the need to find a criterion to evaluate the degree of divergence of the different Configuration Voltage Vectors $\mathbf{V}_m$ arises. For this purpose, a *Vectorial Divergence Function* $\overrightarrow{\mathbf{V}}_m(\tilde{V}_d)$ can be defined for each $\mathbf{V}_m$. Before giving the definition of this function, the following preliminary material needs to be introduced.

- Given the Configuration Voltage Vectors $\mathbf{V}_m = [\ m-1 \quad \beta_{n-1} \quad \dots \quad \beta_2 \quad \beta_1\ ]^{\mathrm{T}}$ and the value of the last n-th capacitor C_n, let us choose the values of the

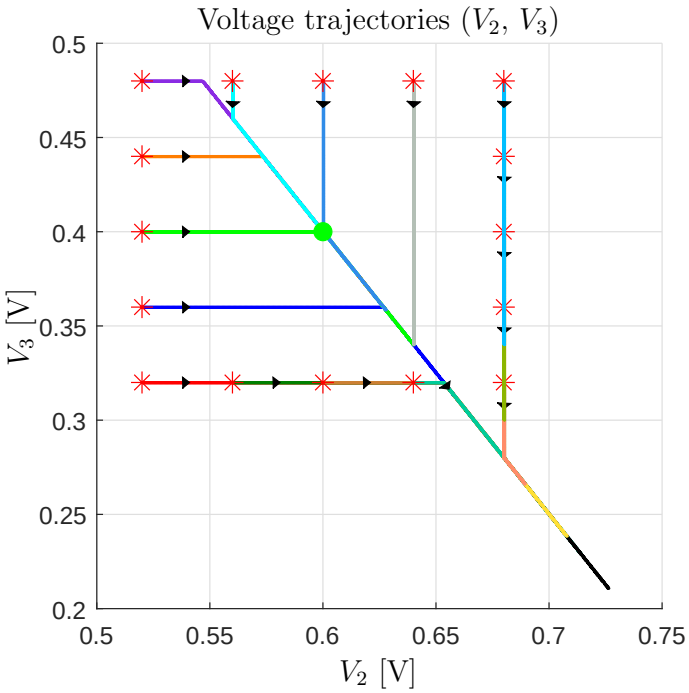

Figure 4.15: Instability of the Configuration Voltage Vector $\mathbf{V}_m = [5\ 3\ 2]^{\mathrm{T}}$ when $V_d = 0.7$ and $I_{out} = 10\,[A]$.

remaining $n-1$ capacitors C_1, C_2, …, C_{n-1}, as follows:

$$C_1 = \frac{\beta_1 C_n}{m-1}, \quad C_2 = \frac{\beta_1 C_n}{\beta_{n-1}}, \quad \ldots, \quad C_{n-2} = \frac{\beta_1 C_n}{\beta_3}, \quad C_{n-1} = \frac{\beta_1 C_n}{\beta_2}, \tag{4.29}$$

namely, each capacitor C_i is chosen inversely proportional to the components of vector $\mathbf{V}_m$.

- The Minimum-Distance Algorithm that is given in Sec. 4.2.1 can be rewritten in an equivalent form by using the following Matlab-like function "$[\mathbf{S}_j,\ \Delta\overline{\mathbf{V}}] = \mathbf{MDA}(\Delta\overline{\mathbf{V}}, \alpha, I_{out}, T_W)$", which must be called providing $\Delta\overline{\mathbf{V}} = \overline{\mathbf{V}}_c(t_k) - \overline{\mathbf{V}}_{m0}$:

---

function $[\mathbf{S}_j,\ \Delta\overline{\mathbf{V}}] = \mathbf{MDA}(\Delta\overline{\mathbf{V}}, \alpha, I_{out}, T_W)$
Compute set $\mathcal{S}_\alpha$ in (4.23); Compute vectors $\overline{\mathbf{S}}_{Cj}$ in (4.22) using (4.29);
for $j \in \mathcal{S}_\alpha$
    Compute $\Delta\overline{\mathbf{V}}_{cj}$ as follows, see (4.25): $\Delta\overline{\mathbf{V}}_{cj} = \Delta\overline{\mathbf{V}} + \overline{\mathbf{S}}_{Cj}\, I_{out}\, T_W$;
end
Find $j^* \in \mathcal{S}_\alpha$ for which the norm of vectors $\Delta\overline{\mathbf{V}}_{cj}$ is minimized, as in (4.26);
Set $\mathbf{S}_j = \mathbf{S}_j^*$; Set $\Delta\overline{\mathbf{V}} = \Delta\overline{\mathbf{V}}_{cj}^*$;

Definition 2 *Given a Configuration Voltage Vector* $\mathbf{V}_m$*, the corresponding* Vectorial Divergence Function $\overrightarrow{\mathbf{V}}_m(\tilde{V}_d)$ *is defined, by employing a Matlab-like notation, as follows:*

$I_{out} = 1$; % *Function normalized with respect to* I_{out}
$T_{PWM} = 1$; % *Function normalized with respect to time*
$C_n = 1$; % *Function normalized with respect to* C_n
for $\tilde{V}_d = (0 : 1/N_{Points} : 1)$ % N_{Points} *of variable* $\tilde{V}_d \in [0,\ 1]$
    $V_D = \tilde{V}_d(m-1)$; % N_{Points} *of variable* $V_D \in [0,\ m-1]$
    $\alpha_H = ceil(V_D)$; % *Upper adjacent level*
    $\alpha_L = floor(V_D)$; % *Lower adjacent level*
    $d_c = V_D - \alpha_L$; % *Duty cycle of the upper level*
    $\Delta\overline{\mathbf{V}} = 0$; % *Zero initial condition*
    for $h = 1 : N_{Steps}$ % *Repeat* N_{Steps} *times*
        $T_W = d_c T_{PWM}$ % *Time interval of the upper level*
        $[\sim, \Delta\overline{\mathbf{V}}] = \mathbf{MDA}(\Delta\overline{\mathbf{V}}, \alpha_H, I_{out}, T_W)$; % *Upper level Minimum Distance Algorithm*
        $T_W = (1 - d_c) T\_PWM$ % *Time interval of the lower level*
        $[\sim, \Delta\overline{\mathbf{V}}] = \mathbf{MDA}(\Delta\overline{\mathbf{V}}, \alpha_L, I_{out}, T_W)$; % *Lower level Minimum Distance Algorithm*
    end
    $\overrightarrow{\mathbf{V}}_m(\tilde{V}_d) = \Delta\overline{\mathbf{V}}/N_{Steps}$; % *Function* $\overrightarrow{\mathbf{V}}_m$ *is defined in point* $\tilde{V}_d$
end

The precision of calculation of function $\overrightarrow{\mathbf{V}}_m(\tilde{V}_d)$ increases if the values of parameters

N_{Points} and N_{Steps} increase. The Vectorial Divergence Function $\overrightarrow{\mathbf{V}}_m(\tilde{V}_d)$ satisfies the following properties.

Property 11 *The Vectorial Divergence Function $\overrightarrow{\mathbf{V}}_m(\tilde{V}_d)$ of all the Basic Configuration Voltage Vectors $\mathbf{V}_m^*$ is zero for any value of variable $\tilde{V}_d = [0\ \ 1]$:*

$$\overrightarrow{\mathbf{V}}_m(\tilde{V}_d) = 0 \qquad for \qquad \tilde{V}_d = [0,\ \ 1].$$

This property holds as a direct consequence of Property 10.

Property 12 *The Vectorial Divergence Function $\overrightarrow{\mathbf{V}}_m(\tilde{V}_d)$ satisfies the following symmetry with respect to the value $\tilde{V}_d = 0.5$:*

$$\overrightarrow{\mathbf{V}}_m(\tilde{V}_d) = -\overrightarrow{\mathbf{V}}_m(1 - \tilde{V}_d), \qquad for \qquad \tilde{V}_d \in [0,\ 0.5].$$

This property holds as a direct consequence of Property 6. Property 12 implies the symmetry of the Vectorial Divergence Function $\overrightarrow{\mathbf{V}}_m(\tilde{V}_d)$ with respect to the origin. Fig. 4.16 gives an example showing two different graphical representations of the Vectorial Divergence Function $\overrightarrow{\mathbf{V}}_m(\tilde{V}_d)$ that is associated with all the Configuration Voltage Vectors $\mathbf{V}_m$ for the case $n = 3$, $N_{Points} = 400$ and $N_{Steps} = 200$. The left subplot shows the norm $|\overrightarrow{\mathbf{V}}_m(\tilde{V}_d)|$ of the Vectorial Divergence Function versus $\tilde{V}_d \in [0,\ 0.5]$. The function $|\overrightarrow{\mathbf{V}}_m(\tilde{V}_d)|$ has not been plotted for $\tilde{V}_d \in [0.5,\ 1]$ because of the symmetry defined in Property 12. The right subplot of Fig. 4.16 shows the Vectorial Divergence Function $\overrightarrow{\mathbf{V}}_m(\tilde{V}_d)$ on plane $(V_2,\ V_3)$. This subplot clearly shows the symmetry of function $\overrightarrow{\mathbf{V}}_m(\tilde{V}_d)$ with respect to the origin, as stated in Property 12. The two digit numbers "$m.i$", which are present for each characteristic in the two subplots of Fig. 4.16, denote the number m of output levels and the order i of the Configuration Voltage Vector $\mathbf{V}_m$ of the nearby colored line, according to the order and the colors reported in Fig. 4.17. The two subplots of Fig. 4.16 clearly show that the norm $|\overrightarrow{\mathbf{V}}_m(\tilde{V}_d)|$ of the Vectorial Divergence Function $\overrightarrow{\mathbf{V}}_m(\tilde{V}_d)$ tends to increase with the number m of the output levels and, therefore, it can be used as a starting point to estimate the degree of divergence and, thus, the degradation of the voltage balancing capability associated to the corresponding Configuration Voltage Vector $\mathbf{V}_m$. For this purpose, let us define the following Divergence Index.

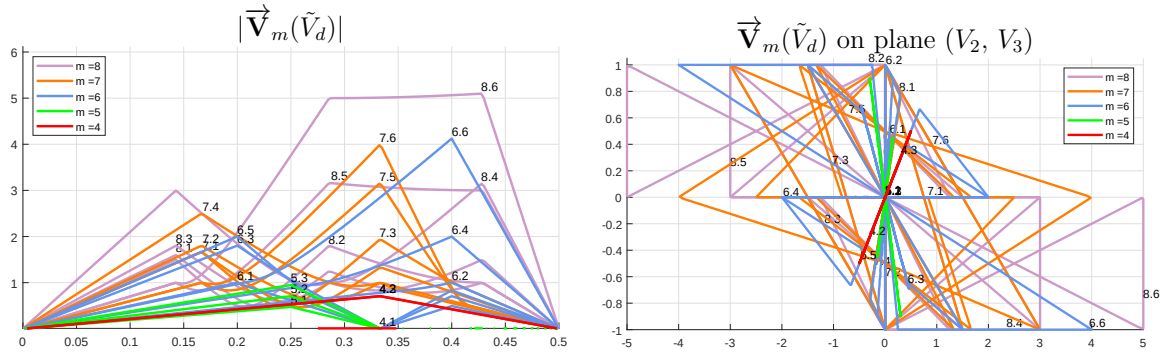

Figure 4.16: Left subplot: Norm $|\overrightarrow{\mathbf{V}}_m(\tilde{V}_d)|$ of the Vectorial Divergence Function vs $\tilde{V}_d \in [0, 0.5]$; **Right** subplot: Vectorial Divergence Function $\overrightarrow{\mathbf{V}}_m(\tilde{V}_d)$ on the plane (V_2, V_3) for all the Configuration Voltage Vectors $\mathbf{V}_m$ in the case $n = 3$.

Definition 3 *The* Divergence Index I_M *of a Configuration Voltage Vector* $\mathbf{V}_m$ *is defined as follows:*

$$I_M = \max\left(|\overrightarrow{\mathbf{V}}_m(\tilde{V}_d)|\right),$$

namely as the maximum value of the norm $|\overrightarrow{\mathbf{V}}_m(\tilde{V}_d)|$ *of the Vectorial Divergence Function* $\overrightarrow{\mathbf{V}}_m(\tilde{V}_d)$.

The larger the Divergence Index I_M, the less robust is the corresponding Configuration Voltage Vector $\mathbf{V}_m$. *Therefore, the Divergence Index* I_M *is inversely proportional to the degree of robustness of the corresponding Configuration Voltage Vector* $\mathbf{V}_m$. For all the Basic Configuration Voltage Vectors $\mathbf{V}_m^*$, the Divergence Index I_M is zero, according to Property 11. Index I_M can also be used to provide a new sorting for the Configuration Voltage Vectors $\mathbf{V}_m$ having the same number m of output levels. Fig. 4.17 shows the new sorting, in ascending order of the Divergence Index I_M for each vector $\mathbf{V}_m$ having the same number m of output voltage levels. Therefore, the different Configuration Voltage Vectors $\mathbf{V}_m$ having the same number m of output levels are sorted in decreasing degree of robustness when moving from left to right in Fig. 4.17. The magenta line that is reported in Fig. 4.17 is the *Mean Index* I_m of the Configuration Voltage Vectors $\mathbf{V}_m$. The *Mean Index* I_m is defined as the mean value of the norm $|\overrightarrow{\mathbf{V}}_m(\tilde{V}_d)|$ of the Vectorial Divergence Function $\overrightarrow{\mathbf{V}}_m(\tilde{V}_d)$: $I_m = \text{mean}\left(|\overrightarrow{\mathbf{V}}_m(\tilde{V}_d)|\right)$. Fig. 4.17 clearly shows a strong correlation between the *Divergence Index* I_M and *Mean Index* I_m.

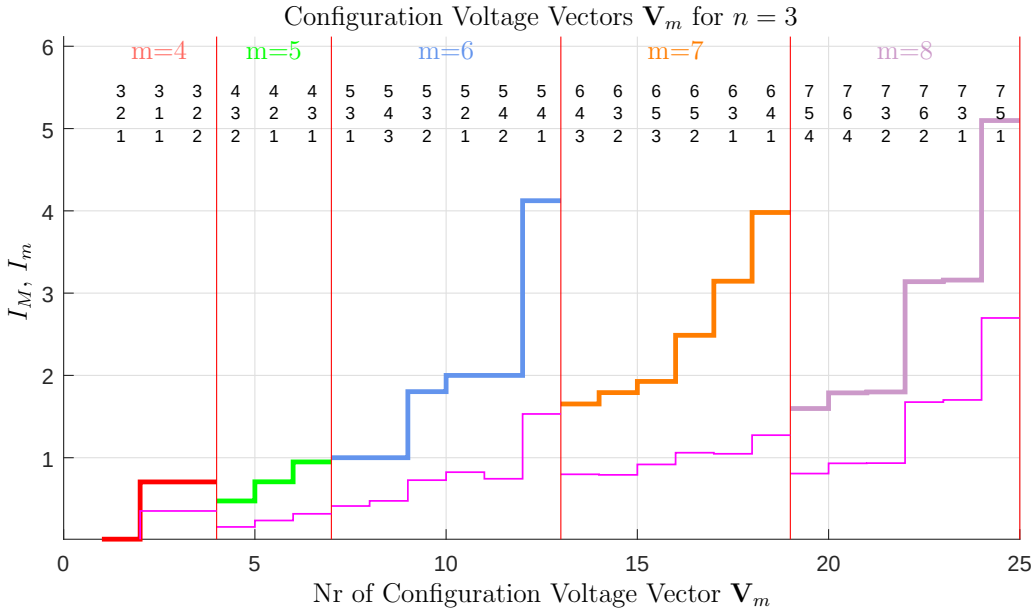

Figure 4.17: Configuration Voltage Vectors $\mathbf{V}_m$, for $n = 3$, sorted in ascending order with respect to the Divergence Index I_M.

In order to verify the correctness of the sorting proposed in Fig. 4.17, all the Configuration Voltage Vectors $\mathbf{V}_m$, for $n = 3$, have been tested in simulation using the three types of voltage signals V_d that are shown in Fig. 4.18 (sinusoidal, triangular, and sawtooth) with $V_{in} = 1\,\mathrm{V}$, an offset equal to $V_{in}/2$, a peak-to-peak amplitude equal to V_{in}, a frequency equal to 50 Hz, an output current equal to $I_{out} = 1\,\mathrm{A}$, and capacitors C_i chosen as in (4.29) with $C_n = 1\,\mathrm{F}$. Fig. 4.19 shows the results of these simulations, where the Divergence Index I_M (red characteristic, left vertical axis) is compared with the maximum norm $\max(|\Delta\overline{\mathbf{V}}|)$ of vectors $\Delta\overline{\mathbf{V}} = \overline{\mathbf{V}}_c(t) - \overline{\mathbf{V}}_{m0}$ obtained in simulation for the three types of the considered periodical signals (colored characteristics, right vertical axis). Two different reference axes have been used in Fig. 4.19, because the Vectorial Divergence Function $\overrightarrow{\overline{\mathbf{V}}}_m(\tilde{V}_d)$ and corresponding Divergence Index I_M have been computed using a constant normalized voltage $\tilde{V}_d \in [0,\, 1]$, whereas the maximum norms $\max(|\Delta\overline{\mathbf{V}}|)$ have been obtained in simulation using different signals, i.e. periodical normalized signals $\tilde{V}_d$ with a non-zero frequency of 50 Hz. It can be shown that the two quantities I_M and $\max(|\Delta\overline{\mathbf{V}}|)$ would tend to be comparable only if the frequency of the periodical normalized signals $\tilde{V}_d$

became equal to zero. Consequently, *the Divergence Index I_M represents an upper boundary for the maximum norm index* $\max(|\Delta\overline{\mathbf{V}}|)$*, for each Configuration Voltage Vector* $\mathbf{V}_m$. Furthermore, Fig. 4.19 shows the good direct proportionality existing between the Divergence Index I_M and the maximum norm indices $\max(|\Delta\overline{\mathbf{V}}|)$ of the three considered signals. This good proportionality shows the effectiveness of using the Divergence Index I_M for evaluating the divergence characteristics of the different Configuration Voltage Vectors $\mathbf{V}_m$, which gives a direct measurement of their degree of robustness. Even for the case $n = 4$, all the Configuration Voltage Vectors

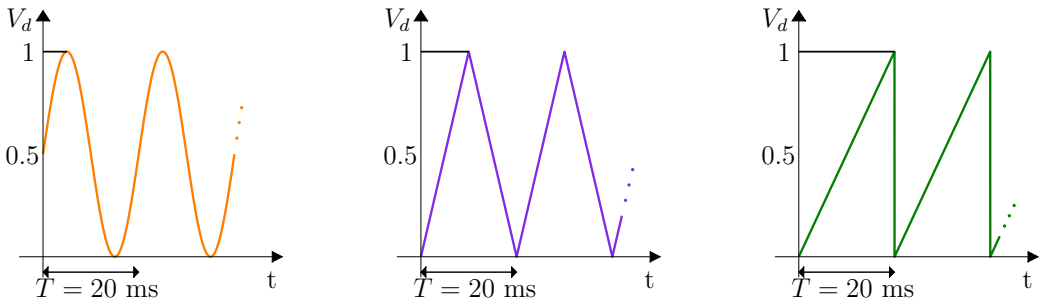

Figure 4.18: Desired voltage signals V_d for the comparisons in Fig. 4.19 and Fig. 4.20.

$\mathbf{V}_m$ have been tested in simulation by employing the same normalized periodical signals $\tilde{V}_d$ used for the case $n = 3$, which are shown in Fig. 4.18. Fig. 4.20 reports the results of these simulations and the comparison between the Divergence Index I_M (red characteristic, left vertical axis) and the maximum norm indices $\max(|\Delta\overline{\mathbf{V}}|)$ (colored lines, right vertical axis). In this figure, the 407 Configuration Voltage Vectors $\mathbf{V}_m$ of case $n = 4$ have been sorted with respect to the Divergence Index I_M. The upper part of the figure shows, for each $m \in [5,\ 6,\ \ldots,\ 16]$, the Configuration Voltage Vector $\mathbf{V}_m$ having the minimum Divergence Index I_M. The simulation results that are reported in Fig. 4.20 show the good direct proportionality existing between the Divergence Index I_M and the maximum norm indices $\max(|\Delta\overline{\mathbf{V}}|)$ even in the case $n = 4$, and, therefore, the effectiveness of using the Divergence Index I_M for evaluating the divergence characteristics, i.e. the degree of robustness, of the different Configuration Voltage Vectors $\mathbf{V}_m$.

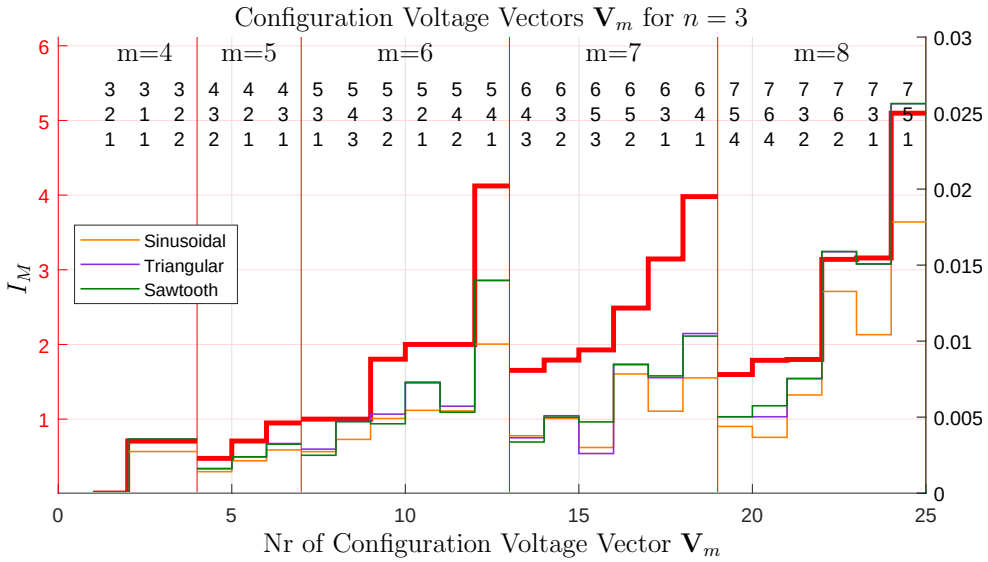

Figure 4.19: Comparison between the Divergence Index I_M and metric $\max(\Delta\overline{\mathbf{V}})$, computed from simulation using three different $\tilde{V}_d$ signals, for the Configuration Voltage Vectors $\mathbf{V}_m$ in the case $n = 3$.

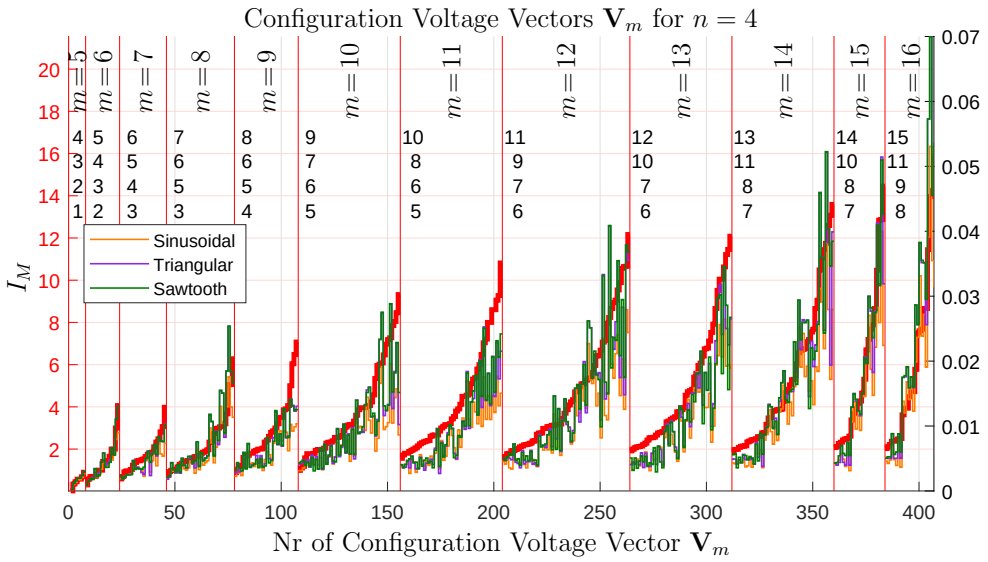

Figure 4.20: Comparison between the Divergence Index I_M and metric $\max(\Delta\overline{\mathbf{V}})$, computed from simulation using three different $\tilde{V}_d$ signals, for the Configuration Voltage Vectors $\mathbf{V}_m$ in the case $n = 4$.

Minimum Distance Control: Stability Issues in Extended Operation

The analysis performed on the basis of the Vectorial Divergence Function $\overrightarrow{\mathbf{V}}_m(\tilde{V}_d)$ has shown that all the Configuration Voltage Vectors $\mathbf{V}_m$, other than the basic one $\mathbf{V}_m^*$, are unstable with different degrees of divergence in some unfavorable conditions, such as constant desired voltage $\tilde{V}_d$, while using the Minimum Distance algorithm. Moreover, Fig. 4.19 and Fig. 4.20 have shown that, for some periodical desired signal $\tilde{V}_d$ with an average value equal to 0.5, the maximum distance $\max(\Delta\overline{\mathbf{V}})$ of the voltage vector $\overline{\mathbf{V}}_c$ from the desired voltage vector $\overline{\mathbf{V}}_{m0}$ remains bounded. The amplitude of the maximum distance $\max(\Delta\overline{\mathbf{V}})$ increases if the output current I_{out} increases, and it decreases if capacitor C_n or the frequency of the periodical signal $\tilde{V}_d$ increase.

If $\overline{\mathbf{V}}_c$ remains in the vicinity of the desired voltage vector $\overline{\mathbf{V}}_{m0}$, then the multilevel converter works properly, providing an output signal V_{out} switching between equally spaced voltage values. On the contrary, if the maximum distance $\max(\Delta\overline{\mathbf{V}})$ increases excessively, then the output values $\mathbf{S}_M\mathbf{V}_c$ of the multilevel converter will no longer be equally spaced and the average value of the output switching signal V_{out} will no longer be equal to the desired signal $V_{in}\tilde{V}_d$. If this situation occurs, the multilevel converter cannot work properly, because it provides output signals that are not equal to the desired ones. The output voltage error $V_{err} = V_{out} - V_{in}\tilde{V}_d$ remains low and, therefore, acceptable, only if the maximum distance $\max(\Delta\overline{\mathbf{V}})$ remains sufficiently low. Unfortunately, in practical applications, such as the electric motors control, it can happen that the desired voltage vector $\tilde{V}_d$ does not have an average value equal to 0.5. In this condition, vector $\overline{\mathbf{V}}_c$ diverges from the desired voltage vector $\overline{\mathbf{V}}_{m0}$, which means that the output voltage error V_{err} increases excessively and the multilevel converter can no longer work correctly. Another destabilizing condition can be identified in a sudden load change. These two scenarios are considered in the following two simulation case studies:

(A) Let us consider the case of a constant output current $I_{out} = 1.1$ A and a sinusoidal desired voltage with an average value that is equal to 0.5: $\tilde{V}_d = 0.5 + 0.5\sin(393\,t)$. Furthermore, the voltage signal is supposed to remain constant at the

value $\tilde{V}_d = 0.43$ for a short time interval $t \in [t_1 \;\; t_2]$, where $t_1 \simeq 32\,\text{ms}$ and $t_2 \simeq 72\,\text{ms}$. Fig. 4.21 shows the simulation results. The red characteristic in Fig. 4.21 is the desired signal $\tilde{V}_d$, the gray characteristic is the output switching signal V_{out}, whereas the blue characteristic is the average value of the output signal V_{out}. From the figure, it is evident that: 1) in the first part of the simulation, i.e. $t < t_1$, the multilevel converter works correctly, since the output switching levels are equally spaced and, thus, the output voltage error V_{err} is very low; 2) during the second part of the simulation, i.e. $t \in [t_1 \;\; t_2]$, the values of the output switching levels change considerably with respect to the desired ones, and they are no longer equally spaced. Therefore, the average value of the output signal V_{out} (blue characteristic) is no longer equal to the desired value $\tilde{V}_d$ (red characteristic); 3) in the third part of the simulation, i.e. $t > t_2$, the multilevel converter no longer works correctly, since the output signals (the gray and blue characteristics) are no longer equal to the desired one (the red characteristic). This is due to the fact that the trajectories of the reduced voltage vector $\overline{\mathbf{V}}_c$ have diverged from the desired value $\overline{\mathbf{V}}_{m0}$ because of the constant voltage $\tilde{V}_d$. Moreover, the Minimum Distance algorithm is not able to force the reduced voltage vector $\overline{\mathbf{V}}_c$ to move back towards the desired voltage vector $\overline{\mathbf{V}}_{m0}$ after the divergence has occurred.

(B) Let us consider the case of a sinusoidal desired voltage with an average value that is equal to 0.5: $\tilde{V}_d = 0.5 + 0.5\sin(393\,t)$. The load current is supposed to be constant and equal to $I_{out} = 1\,\text{A}$ for $t < t_1 = 0.04\,\text{s}$. Next, a sudden load change causing a current step is supposed to occur, causing I_{out} to jump from 1 A to 10.5 A for $t_1 \leq t < t_2 = 0.1\,\text{s}$. The load operating condition giving $I_{out} = 1\,\text{A}$ is supposed to be reestablished for $t \geq t_2$. Fig. 4.22 shows the simulation results. The characteristics color notation is the same as the one adopted in Fig. 4.21. From Fig. 4.22, it is evident that: 1) in the first part of the simulation, i.e. $t < t_1$, the multilevel converter works correctly, since the output switching levels are equally spaced, which means that the output voltage error V_{err} is very low; 2) for $t \in [t_1 \;\; t_2)$, the values of the output switching levels change with respect to the desired ones, and they are no longer equally spaced; 3) for $t \geq t_2$, the output voltage levels remain

unequally spaced, due to the divergence of the trajectories of the reduced voltage vector $\overline{\mathbf{V}}_c$ from the desired value $\overline{\mathbf{V}}_{m0}$ caused by the sudden load change. Moreover, the Minimum Distance algorithm is not able to force the reduced voltage vector $\overline{\mathbf{V}}_c$ to move back towards the desired voltage vector $\overline{\mathbf{V}}_{m0}$ after the divergence has occurred.

Unfortunately, situations such as those that are shown in Fig. 4.21 and Fig. 4.22 can happen for all of the Configuration Voltage Vectors $\mathbf{V}_m$, except for the basic one $\mathbf{V}_m^*$. This poses quite a limitation on the operation of the converter in the so-called "Extended Operation", namely for $\mathbf{V}_m \neq \mathbf{V}_m^*$ allowing to generate a number of output voltage levels $m > n + 1$ for the given n, since unpredictable undesired conditions may compromise the correct functioning of the multilevel converter.

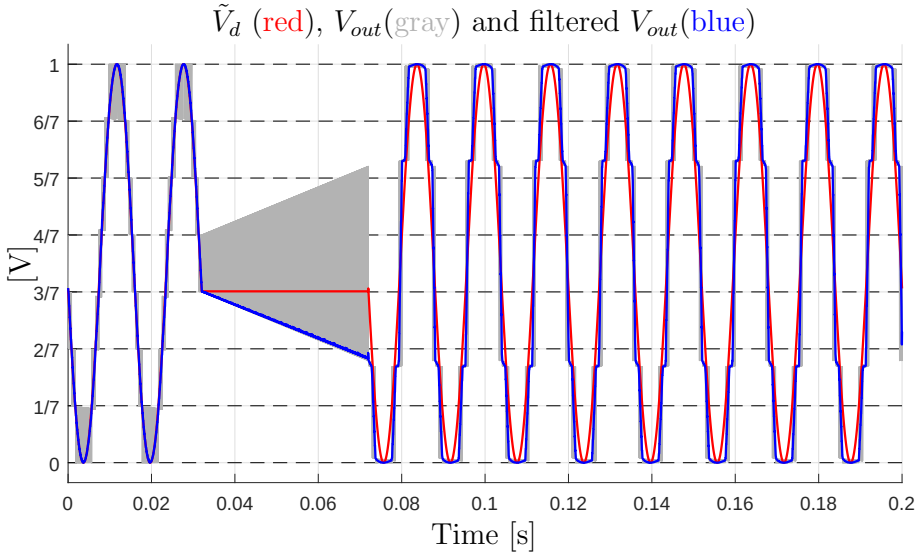

Figure 4.21: Deformation of the output voltage waveform in the extended operation of the converter with the Configuration Voltage Vector $\mathbf{V}_m = [7\ 6\ 2]^{\mathrm{T}}$ caused by the voltage trajectory divergence in presence of a constant output voltage.

4.2.4 Variable-Step Control

To cope with the divergence problem described in the previous section, the use of a new solution based on the PWM physical scheme that is shown in Fig. 4.23 is proposed.

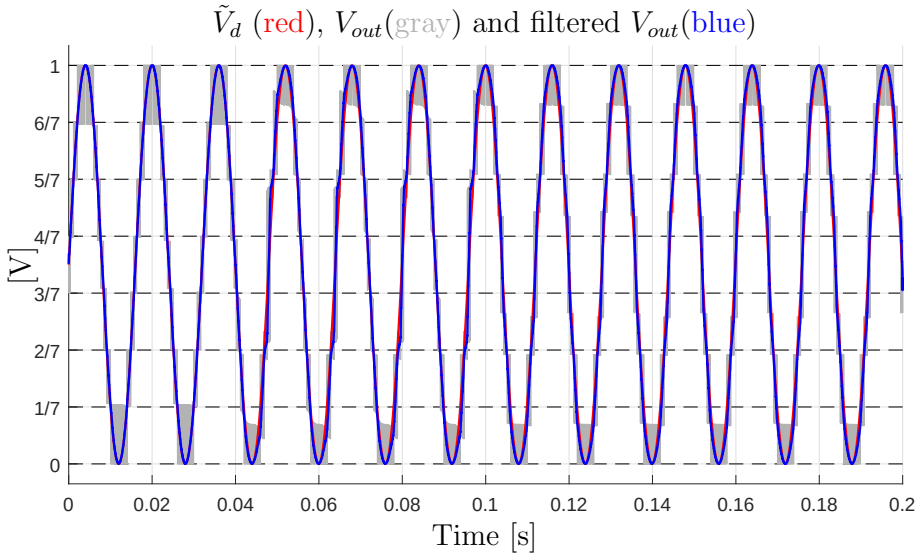

Figure 4.22: Deformation of the output voltage waveform in the extended operation of the converter with the Configuration Voltage Vector $\mathbf{V}_m = [7\ 6\ 2]^{\mathrm{T}}$ caused by the voltage trajectory divergence in presence of a sudden load change.

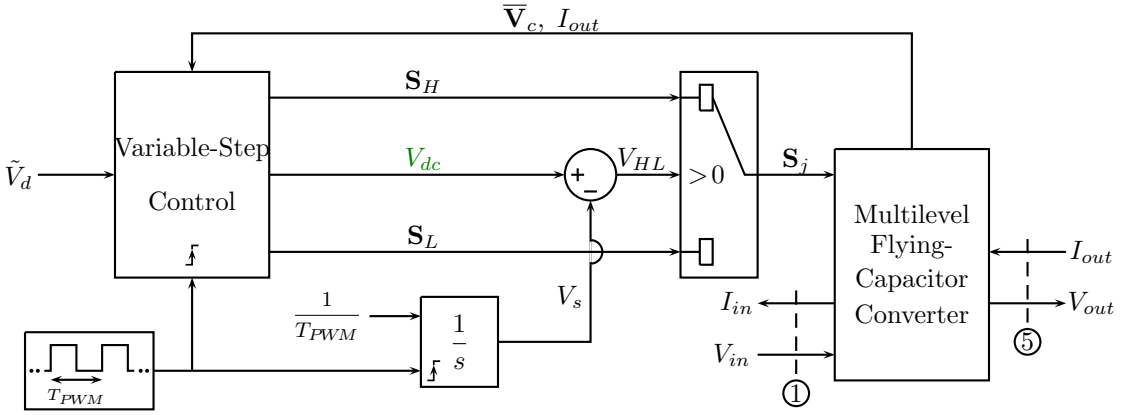

Figure 4.23: PWM physical scheme and Variable-Step Control of the Multilevel Flying-Capacitor Converter.

The basic elements of the new PWM scheme are the following:

(a) a square wave signal having period T_{PWM} acting as a clock, which activates the Variable-Step Control and resets the integrator to the zero initial condition when the rising edge occurs;

(b) an integrator with a constant input $\frac{1}{T_{PWM}}$ and a reset signal that is timed by the square clock. The output V_s of the integrator is a sawtooth signal which ranges from 0 to 1 within a time interval $t \in [t_r,\, t_r + T_{PWM}]$, where t_r is the reset time instant, see the black line in Fig. 4.24;

(c) the voltage V_{dc} that is provided by the Variable-Step Control block, defining the duty cycle of the high level of the PWM signal, namely the time interval T_H, see the green line in Fig. 4.24;

(d) the value of the signal $V_{HL} = V_{dc} - V_s$ determines the output of the selector and, thus, the configuration vector $\mathbf{S}_j$ which is going to be applied to the multilevel converter during the next time interval: $\mathbf{S}_j = \mathbf{S}_H$ for a time interval T_H if $V_{HL} > 0$ and $\mathbf{S}_j = \mathbf{S}_L$ for a time interval $T_{PWM} - T_H$ if $V_{HL} < 0$;

(e) at each activation time, the Variable-Step Control reads the input signal $\tilde{V}_d$ and generates three output signals: $\mathbf{S}_H$, V_{dc} and $\mathbf{S}_L$. Using these signals, the Variable-Step Algorithm can decide the duty cycle d_c and the two levels $\mathbf{S}_H\mathbf{V}_c$ and $\mathbf{S}_L\mathbf{V}_c$ of the next PWM period;

(f) let $V_H > V_d$ denote the voltage corresponding to configuration vector $\mathbf{S}_H$ and $V_L < V_d$ denote the voltage corresponding to configuration vector $\mathbf{S}_L$. The duty cycle $d_c = T_H/T_{PWM}$ of the next PWM period, that is the ratio between the duration T_H of the higher level and the duration of the PWM period T_{PWM}, can be computed as follows:

$$V_d = V_H\, d_c + V_L(1 - d_c) \qquad \leftrightarrow \qquad d_c = \frac{V_d - V_L}{V_H - V_L}. \tag{4.30}$$

Using (4.30), the duty cycle d_c always guarantees that the average value of the PWM output voltage in the next period T_{PWM} is equal to the desired value V_d.

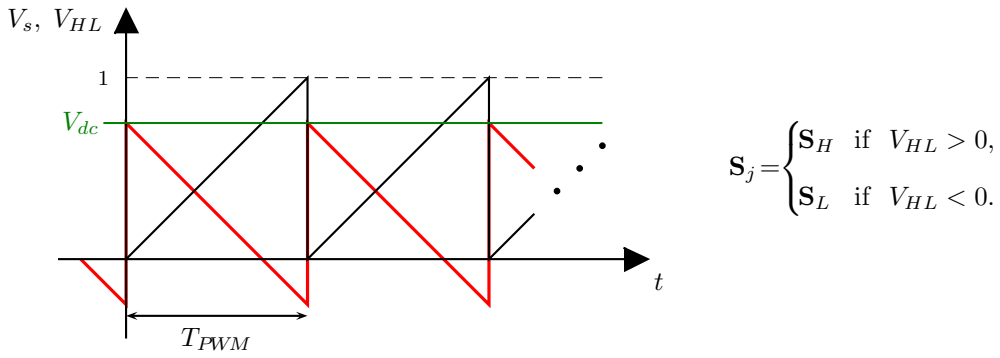

Figure 4.24: Scheme for the application of the configuration vectors $\mathbf{S}_{j_H}$ and $\mathbf{S}_{j_L}$ associated with the higher and lower level time intervals T_H and $T_{PWM} - T_H$.

Fig. 4.25 provides the basic structure of the Variable-Step Control algorithm by means of a Matlab-like function called "**Multi_Step_Algorithm**$(\cdots)$". This function is called at each activation time providing the following input parameters: $\Delta\overline{\mathbf{V}}$, $\tilde{V}_d$, I_{out}, T_{PWM}, N_s, V_{r0}. The "Multi_Step_Algorithm" attempts to keep the reduced voltage vector $\overline{\mathbf{V}}_c$ as close as possible to the desired reduced voltage vector $\overline{\mathbf{V}}_{m0}$, see (4.22). The main features of the "Multi_Step_Algorithm" are the following:

- At each activation time t_k, the "Multi_Step_Algorithm" computes the two configuration vectors $\mathbf{S}_H$, $\mathbf{S}_L$ and the duty cycle V_{dc} to be applied in the following PWM time interval $[t_k \quad t_k + T_{PWM}]$: configuration $\mathbf{S}_H$ will be applied in the first part of the PWM period when $V_{HL} = V_{dc} - V_s > 0$, while configuration $\mathbf{S}_L$ will be applied in the second part of the PWM period when $V_{HL} < 0$, see Fig. 4.24.

- The input N_s defines the maximum amplitude of the Step to be used in the algorithm, which is the *maximum level-to-level distance*. The **for** cycle at line 5 in Fig. 4.25 defines the current value $N_{si} \in [1,\ 2,\ \ldots,\ N_s]$ of the amplitude of the Step, i.e. the current level-to-level distance. The **for** cycle at line 6 defines the current value k of the up and down shift to be considered for the current amplitude N_{si} of the Step.

- At lines 7 and 8, the current values of the upper level α_H, the lower level

function $[\mathbf{S}_H,\ V_{dc},\ \mathbf{S}_L] = \mathbf{Multi\_Step\_Algorithm}(\Delta\overline{\mathbf{V}},\ \tilde{V}_d,\ I_{out},\ T_{PWM},\ N_s,\ V_{r0})$

1. $V_D = \tilde{V}_d(m-1)$;
2. $\alpha_{H0} = \text{ceil}(V_D)$;
3. $V_{dc} = V_D - \text{floor}(V_D)$;
4. $N_m = \infty$;
5. **for** $N_{si} = 1 : N_s$
6. **for** $k = 0 : N_{si} - 1$
7. $\alpha_H = \alpha_{H0} + k; \quad \alpha_L = \alpha_H - N_{si}$;
8. Compute the new duty cycle d_c;
9. **if** $(\alpha_H < m)\&\&(\alpha_L \geq 0)$
10. Compute sets $\mathcal{S}_{\alpha_H}$ and $\mathcal{S}_{\alpha_L}$;
11. Compute vectors $\overline{\mathbf{S}}_{CHi}$ and $\overline{\mathbf{S}}_{CLj}$;
12. **for** $i \in \mathcal{S}_{\alpha_H}$
13. **for** $j \in \mathcal{S}_{\alpha_L}$
14. $\Delta\overline{\mathbf{V}}_{cij} = \Delta\overline{\mathbf{V}} + [\overline{\mathbf{S}}_{CHi}\, d_c + \overline{\mathbf{S}}_{CLj}(1-d_c)] I_{out} T_{PWM}$;
15. **if** $\text{norm}(\Delta\overline{\mathbf{V}}_{cij}) < N_m$
16. $N_m = \text{norm}(\Delta\overline{\mathbf{V}}_{cij})$;
17. Set: $\mathbf{S}_H = \mathbf{S}_i; \quad \mathbf{S}_L = \mathbf{S}_j; \quad V_{dc} = d_c$;
18. **end**
19. **end**
20. **end**
21. **end**
22. **end**
23. **if** $(N_m < \text{norm}(\Delta\overline{\mathbf{V}}))||(N_m < V_{r0} N_{si})$
24. **return**
25. **end**
26. **end**

Figure 4.25: Matlab-like form of the Variable-Step Control algorithm.

α_L, and the duty cycle d_c are computed. If the current values of α_H and α_L are admissible, see condition at line 9, then the sets $\mathcal{S}_{\alpha_H}$ and $\mathcal{S}_{\alpha_L}$ of the admissible configuration vectors $\mathbf{S}_{Hi}$ and $\mathbf{S}_{Lj}$ and the corresponding vectors $\overline{\mathbf{S}}_{CHi}$ and $\overline{\mathbf{S}}_{CLj}$ are computed at lines 10 and 11.

- The two **for** cycles at lines 12 and 13 are used to compute the distance vector $\Delta\overline{\mathbf{V}}_{cij}$ for each possible combination of the configuration vectors $\mathbf{S}_i$ and $\mathbf{S}_j$ belonging to the two sets $\mathcal{S}_{\alpha_H}$ and $\mathcal{S}_{\alpha_L}$. At line 14, the distance vector $\Delta\overline{\mathbf{V}}_{cij}$ is computed starting from the initial condition $\Delta\overline{\mathbf{V}}$ and adding the two terms $\overline{\mathbf{S}}_{CHi}\, d_c I_{out} T_{PWM}$ and $\overline{\mathbf{S}}_{CLj}(1-d_c) I_{out} T_{PWM}$, due to the application of the configuration vectors $\mathbf{S}_{Hi}$ and $\mathbf{S}_{Li}$ in the first part $d_c T_{PWM}$ and in the second part $(1-d_c)T_{PWM}$ of the PWM period T_{PWM}, respectively.

- If the norm of the distance vector $\Delta\overline{\mathbf{V}}_{cij}$ is smaller than the current minimum norm N_m, see line 15, then the algorithm updates the value of parameter N_m, see line 16, and it sets the values of the output variables $\mathbf{S}_H$, $\mathbf{S}_L$ and V_{dc} equal to the values $\mathbf{S}_i$, $\mathbf{S}_j$ and d_c of the current solution, see line 17.

- The "Multi_Step_Algorithm" ends its minimum distance vector search, see line 24, when one of the conditions at line 23 is verified, or when the maximum level-to-level distance N_s has been achieved. At line 23, the algorithm exits the search if the current minimum distance N_m is lower than the initial one, or if N_m is lower than radius $V_{r0}\, N_{si}$, where V_{r0} is the input basic radius and N_{si} is the current level-to-level distance. Radius $V_{r0}\, N_{si}$ represents the varying radius of an hypersphere in the $(n-1)$-dimensional space. Fig. 4.26 shows the resulting circumferences with varying radius $V_{r0}\, N_{si}$ for the case $n = 3$.

- The "Multi_Step_Algorithm" introduces and uses the new concept of "*variable level-to-level distance*". This concept means that the algorithm can choose a higher level α_H and a lower level α_L *that are not adjacent*, see line 7 of the algorithm. The current level-to-level distance is denoted by variable $N_{si} \in [1,\, N_s]$. The new duty cycle d_c associated with the two levels α_H and α_L, computed in line 8, guarantees that the average value of the PWM output voltage in the next PWM period T_{PWM} will be equal to the desired value V_d.

- The ability to change the level-to-level distance allows the "Multi_Step_Algorithm" to keep the reduced voltage vector $\overline{\mathbf{V}}_c$ in the vicinity of the desired voltage vector $\overline{\mathbf{V}}_{m0}$ even in extended operation and in presence of some particularly unfavorable operating conditions, such as normalized desired voltage $\tilde{V}_d$ having an average value different from 0.5.

- If the unfavorable conditions persist, the algorithm can enlarge the level-to-level distance N_{si} up to its upper boundary $N_s = m - 1$. This enlargement increases the number of the configuration vectors $\mathbf{S}_j$ that the algorithm can use to keep vector $\overline{\mathbf{V}}_c$ in the vicinity of the desired vector $\overline{\mathbf{V}}_{m0}$, and to maintain the correct functioning of the multilevel converter. Furthermore, when the unfavorable conditions no longer occur, the "Multi_Step_Algorithm" has the ability to force the converter to go back to work as a normal multilevel converter switching between adjacent levels only, i.e. with a current level-to-level distance N_{si} equal to one.

- The example reported in Fig. 4.27 shows all the possible combinations of levels α_H and α_L that can be obtained when $m = 6$, $N_{si} \in \{1, 2, 3, 4, 5\}$ and the desired voltage $V_D = (m-1)\tilde{V}_d$ is in between levels "2" and "3".

- The main advantage offered by the proposed Variable-Step Control with respect to the classical Minimum-Distance Control is the fact that it is able to ensure the correct functioning of the multilevel converter even under particularly unfavorable operating conditions, such as a constant desired output voltage or a sudden load change for example, by effectively preventing the capacitors voltage trajectories divergence.

Variable-Step Control: Solution of the Stability Issues in Extended Operation

Sec. 4.2.3 has shown that the Minimum Distance Control is not capable of ensuring the correct operation of the multilevel flying-capacitor converter, in extended mode, under particularly unfavorable operating conditions, such as a desired voltage $\tilde{V}_d$

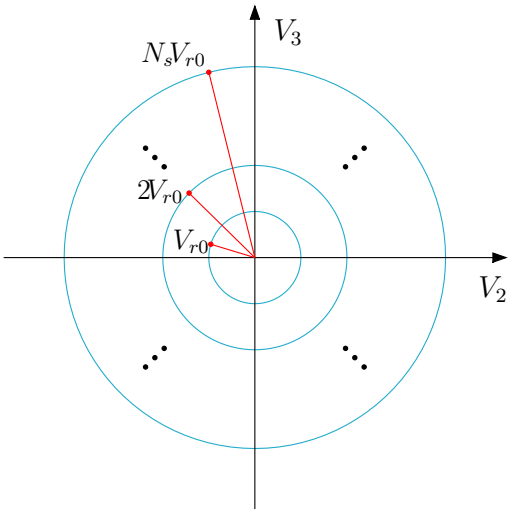

Figure 4.26: Circumference with varying radius $N_{si}\,V_{r0}$ in the two-dimensional space for the case $n = 3$.

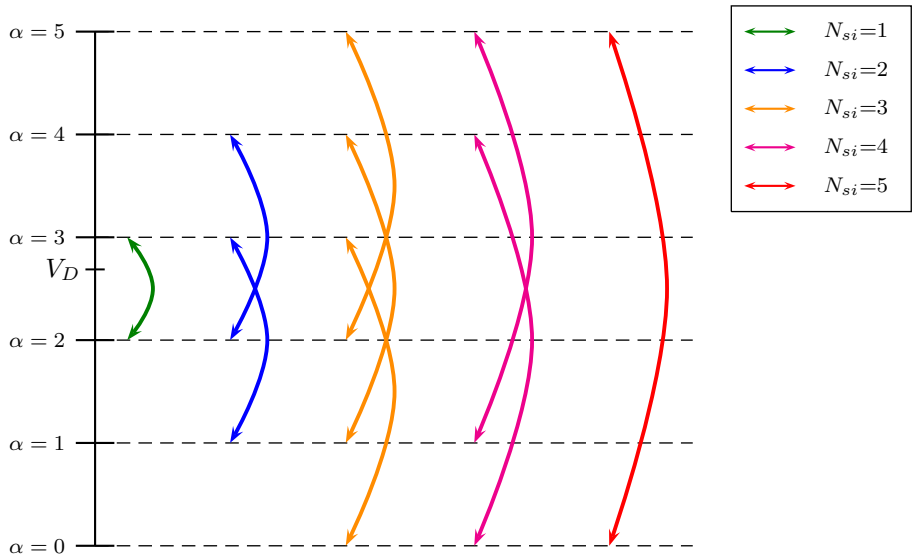

Figure 4.27: Possible combinations of higher and lower output voltage levels α_H and α_L as a function of the current level-to-level distance N_{si} for the case $m = 6$ and a desired voltage V_D in between "2" and "3".

with an average value that is different from 0.5 or a sudden load change. Examples of this type are shown in Fig. 4.21 and Fig. 4.22, respectively. On the contrary, the Variable-Step Control that was presented in the previous section is able to ensure the correct functioning of the multilevel converter, even under unfavorable operating conditions. To give some examples, reference is made to Fig. 4.28 and Fig. 4.29, showing the simulation results obtained using the Variable-Step Control under the same operating conditions as those of the simulations in Fig. 4.21 and Fig. 4.22, respectively, when the Minimum Distance Control was used instead. In Fig. 4.28 and Fig. 4.29, the red characteristic is the desired signal $\tilde{V}_d$, the gray characteristic is the switching output signal V_{out}, and the green characteristic is the average value of the output signal V_{out}.

With reference to Fig. 4.28, it is evident that: 1) in the first part of the simulation, for $t < t_1$, the multilevel converter works correctly in extended operation using the minimum level-to-level distance $N_{si} = 1$ and the output voltage error $V_{err} = V_{out} - V_{in}\tilde{V}_d$ remains low; 2) during the second part of the simulation, for $t \in [t_1 \quad t_2]$, the current level-to-level distance N_{si} increases from 1 to 2, and the gray output variable V_{out} switches between levels $V_L = 2/7$ and $V_H = 4/7$. In this part of the simulation, the effectiveness of the Variable-Step Control comes into play, which prevents vector $\overline{\mathbf{V}}_c$ from diverging excessively from the desired reduced vector $\overline{\mathbf{V}}_{m0}$, even in the presence of the unfavorable condition of a signal $\tilde{V}_d$ constant and different from 0.5. On the other hand, in the simulation of Fig. 4.21, the Minimum Distance Algorithm was not able to prevent the divergence of the vector $\overline{\mathbf{V}}_c$, therefore compromising the correct functioning of the converter; 3) in the third part of the simulation, for $t > t_2$, the operating condition $N_{si} = 2$ is maintained until the distance between vectors $\overline{\mathbf{V}}_c$ and $\overline{\mathbf{V}}_{m0}$ is sufficiently reduced, namely until time instant $t_3 \simeq 176\,\text{ms}$; 4) in the fourth part of the simulation, for $t > t_3$, the converter starts operating as a classical multilevel flying-capacitor converter in extended mode once again, setting the current level-to-level distance N_{si} back to 1. On the other hand, in the simulation of Fig. 4.21, the Minimum Distance Algorithm was not able to force the vector $\overline{\mathbf{V}}_c$ to move back towards the desired vector $\overline{\mathbf{V}}_{m0}$ after the divergence occurred.

With reference to Fig. 4.29, it is evident that: 1) in the first part of the simulation, for $t < t_1$, the multilevel converter works correctly in extended operation using the minimum level-to-level distance $N_{si} = 1$ and the output voltage error $V_{err} = V_{out} - V_{in}\tilde{V}_d$ remains low; 2) for $t \in [t_1 \;\; t_2)$, the current level-to-level distance N_{si} increases from 1 to 2, in order to prevent vector $\overline{\mathbf{V}}_c$ from diverging excessively from the desired reduced vector $\overline{\mathbf{V}}_{m0}$ as a consequence of the undesired sudden load change. On the other hand, in the simulation of Fig. 4.22, the Minimum Distance Algorithm was not able to prevent the divergence of the vector $\overline{\mathbf{V}}_c$, therefore compromising the correct functioning of the converter; 3) for $t \geq t_2$, the operating condition $N_{si} = 2$ is maintained until $t = t_3 \simeq 0.1039\,\mathrm{s}$, namely for the very short time interval that it takes for the distance between vectors $\overline{\mathbf{V}}_c$ and $\overline{\mathbf{V}}_{m0}$ to be sufficiently reduced; 4) for $t \geq t_3$, the converter starts operating as a classical multilevel flying-capacitor converter in extended mode once again, setting the current level-to-level distance N_{si} back to 1. On the other hand, in the simulation of Fig. 4.22, the Minimum Distance Algorithm was not able to force the vector $\overline{\mathbf{V}}_c$ to move back towards the desired vector $\overline{\mathbf{V}}_{m0}$ after the divergence occurred.

The simulation results that are reported in Fig. 4.28 and Fig. 4.29 clearly highlight the effectiveness of the proposed Variable-Step Control as compared with the classical Minimum Distance Control. This especially holds in those applications, such as the electric motors control, where it can happen that the desired voltage vector $\tilde{V}_d$ does not have an average value equal to 0.5, or that an undesired sudden load change occurs. At the same time, it is desirable to have the converter operating in extended mode, because of all the advantages in the output voltage quality coming from a larger number of output voltage levels without increasing the number of capacitors. The proposed Variable-Step Control aims at enabling the multilevel flying-capacitor converter operation in extended mode any time the operating conditions allow it, and it enlarges the level-to-level distance N_{si} only when strictly necessary to prevent the divergence of the flying capacitors voltages.

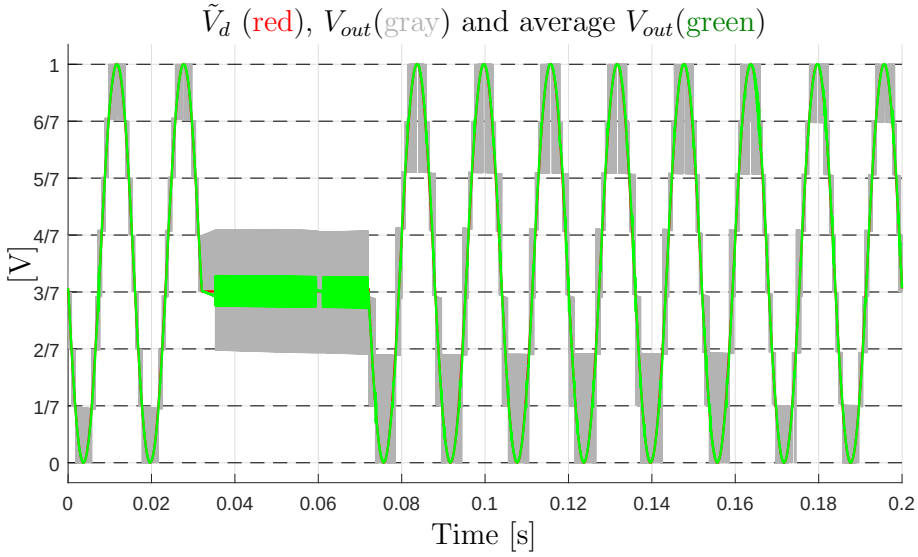

Figure 4.28: Non-Deformation of the output voltage waveform in the extended operation of the converter with the Configuration Voltage Vector $\mathbf{V}_m = [7\ 6\ 2]^{\mathrm{T}}$, in the presence of a constant output voltage, thanks to the Variable-Step Control.

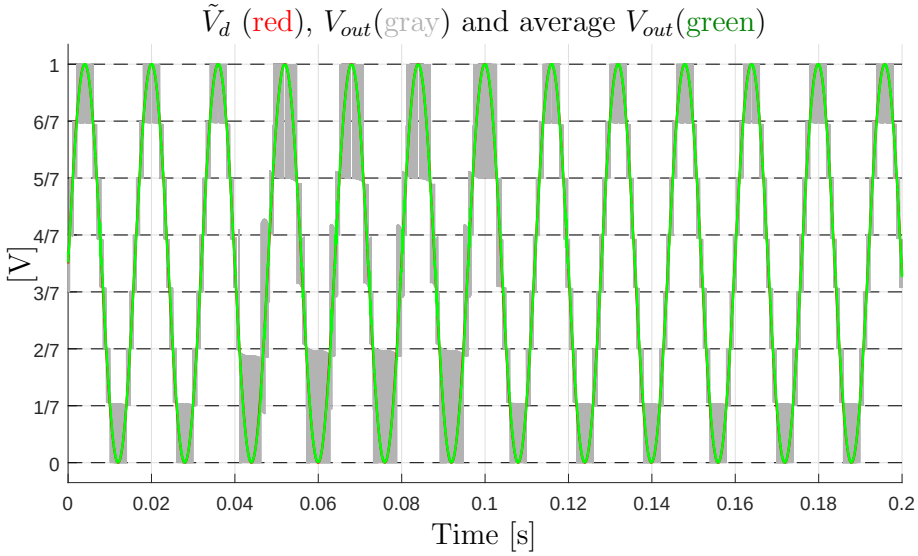

Figure 4.29: Non-Deformation of the output voltage waveform in the extended operation of the converter with the Configuration Voltage Vector $\mathbf{V}_m = [7\ 6\ 2]^{\mathrm{T}}$, in the presence of a sudden load change, thanks to the Variable-Step Control.

4.3 Converter testing with dynamic loads

This section deals with the simulation of the multilevel flying-capacitor converter with $n = 3$ in extended operation, while using the Configuration Voltage Vector $\mathbf{V}_m = [5\ 4\ 1]^{\mathrm{T}}$, with several proposed load case studies. The considered load configuration is an RLC circuit, where a capacitor C_L and a resistor R_L are connected in parallel, and their parallel configuration is connected in series to an inductor L_L. The described load can be modeled using the POG block scheme that is shown in Fig. 4.30 on the left. The transfer function $H(s)$ relating the output power variable I_{out} to the input power variable V_{out} is the following:

$$H(s) = \frac{I_{out}(s)}{V_{out}(s)} = \frac{sR_LC_L+1}{s^2R_LC_LL_L+sL_L+R_L}. \tag{4.31}$$

The parameters values for the considered load case studies are shown in Fig. 4.30 on the right, together with the converter parameters. As far as loads 1, 2 and 3 are concerned, the desired voltage V_d is assumed to be sinusoidal with an offset that is equal to $V_{in}/2$, a peak-to-peak amplitude equal to V_{in} and a frequency equal to 50 Hz. As far as load 4 is concerned, the desired voltage V_d is assumed to be constant and equal to 4.5 V. By focusing on the loads 1, 2, and 3, and using the parameters L_L, C_L, and R_L given in Fig. 4.30, one can notice that they represent the cases of voltage V_{out} delayed by $\pi/4$ with respect to current I_{out}, current I_{out} delayed by $\pi/4$ with respect to voltage V_{out}, and current I_{out} in phase with voltage V_{out}, respectively. The initial conditions of the RLC load are assumed to be equal to zero. Fig. 4.31 shows the simulation results in terms of output voltages V_{out}. The first three rows of subplots show the simulation results after the transient when the loads 1, 2 and 3 are considered. From the first three rows of subplots on the left-hand side, obtained using the Minimum Distance Control, it is possible to see that the average V_{out} characteristic exhibits different degrees of deviation from the desired voltage V_d. This is due to the fact that the distance between vectors $\overline{\mathbf{V}}_c$ and $\overline{\mathbf{V}}_{m0}$ tends to increase, even if the average value of $\tilde{V}_d$ is equal to 0.5, i.e. the average value of V_d is equal to $V_{in}/2$. This can be explained by recalling that the output current I_{out} *is not constant*, as the load is dynamic, which means that the *strength* of the control action applied by the Configuration Vector $\mathbf{S}_j$ in (4.24) *changes in*

time through I_{out}, which is a function of V_{out}. Without a loss of generality, it is possible to state that this makes the Voltage Configuration Vectors $\mathbf{V}_m$ different from the basic one $\mathbf{V}_m^*$ loose the full flying capacitors voltage balancing capability, i.e. to become unstable, *even when the average value of the desired voltage* V_d *is equal to* $V_{in}/2$. It follows that the distance between vectors $\overline{\mathbf{V}}_c$ and $\overline{\mathbf{V}}_{m0}$ will keep increasing, thus causing the output voltage levels to be increasingly unequally spaced. On the other hand, the subplots on the right-hand side show the very good matching between the average V_{out} characteristic and the desired voltage V_d when the converter is controlled using the Variable-Step Control. It follows that the Variable-Step Control is capable of handling the cases of non-constant output current I_{out} in extended operation as well, by increasing the current level-to-level distance N_{si} when necessary in order to prevent the divergence of vector $\overline{\mathbf{V}}_c$ from vector $\overline{\mathbf{V}}_{m0}$. As an example of this, the voltage trajectories of the flying capacitors, namely the components of vector $\overline{\mathbf{V}}_c$, are shown in Fig. 4.32 for the case "Load 2" when the two different controls are used. From the figure, it is clearly possible to see that the Minimum Distance Control causes the divergence of vector $\overline{\mathbf{V}}_c$ (blue characteristic) from the desired vector $\overline{\mathbf{V}}_{m0}$, which is highlighted by the red spot in the figure. Furthermore, the blue characteristic also shows that the strength of the control action applied by the Configuration Vector $\mathbf{S}_j$ in (4.24) is indeed not constant during the simulation, but it is a function of the output current I_{out}, since the length of the blue voltage trajectories in Fig. 4.32 is not constant. On the other hand, the Variable-Step Control is indeed capable of ensuring the convergence of vector $\overline{\mathbf{V}}_c$ to the desired vector $\overline{\mathbf{V}}_{m0}$. The fourth row of subplots presented in Fig. 4.31 shows the case of constant desired voltage V_d with the load parameters identified by "Load 4" in Fig. 4.30 on the right. The bottom-left subplot shows that the case of constant desired voltage $V_d \neq V_{in}/2$, namely $\tilde{V}_d \neq 0.5$, is still the most severe one. This can be seen from the fact that the output voltage levels quickly become unequally spaced because of the divergence of vector $\overline{\mathbf{V}}_c$ from vector $\overline{\mathbf{V}}_{m0}$. Furthermore, note that the average output voltage in the bottom-left subplot of Fig. 4.31 tends to decrease, as a consequence of the divergence of the vector $\overline{\mathbf{V}}_c$ trajectories. Consequently, the output current I_{out} will also tend to decrease. This

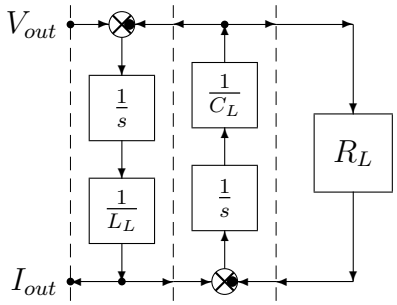

	Load 1	Load 2	Load 3	Load 4
L_L	84.06 [μH]	31.7 [mH]	316.8 [μH]	31.7 [mH]
C_L	320 [μF]	320 [μF]	320 [μF]	320 [μF]
R_L	10 [Ω]	10 [Ω]	1 [Ω]	10 [Ω]

V_{in}	10 [V]	10 [V]	10 [V]	10 [V]
R_{in}	0.1 [mΩ]	0.1 [mΩ]	0.1 [mΩ]	0.1 [mΩ]
C_1	2 [mF]	2 [mF]	2 [mF]	4 [mF]
C_2	2.5 [mF]	2.5 [mF]	2.5 [mF]	5 [mF]
C_3	10 [mF]	10 [mF]	10 [mF]	20 [mF]

Figure 4.30: On the left: RLC load POG scheme; On the right: RLC load and converter parameters.

situation gives rise to an unstable loop: the more V_{out} decreases with respect to the desired value V_d, the lower the output current I_{out}, the weaker the control action applied by the Configuration Vector $\mathbf{S}_j$ in (4.24), the more severe the divergence of the $\overline{\mathbf{V}}_c$ trajectories from $\overline{\mathbf{V}}_{m0}$. However, the bottom-right subplot of Fig. 4.31 shows how the divergence of the $\overline{\mathbf{V}}_c$ trajectories from $\overline{\mathbf{V}}_{m0}$ is prevented by the Variable-Step Control, thanks to the increase of the current level-to-level distance N_{si} from 1 to 2, showing the effectiveness of the proposed Variable-Step Control.

4.4 Conclusions

In this chapter, the modeling, the control, and the robustness assessment of the multilevel flying-capacitor converter have been addressed. The main contributions of this chapter are summarized in the following:

- the Power-Oriented Graphs modeling technique has been exploited to derive the system dynamic model of the n-dimensional converter, generating a POG model that can be directly implemented in Matlab/Simulink by employing standard Simulink libraries;

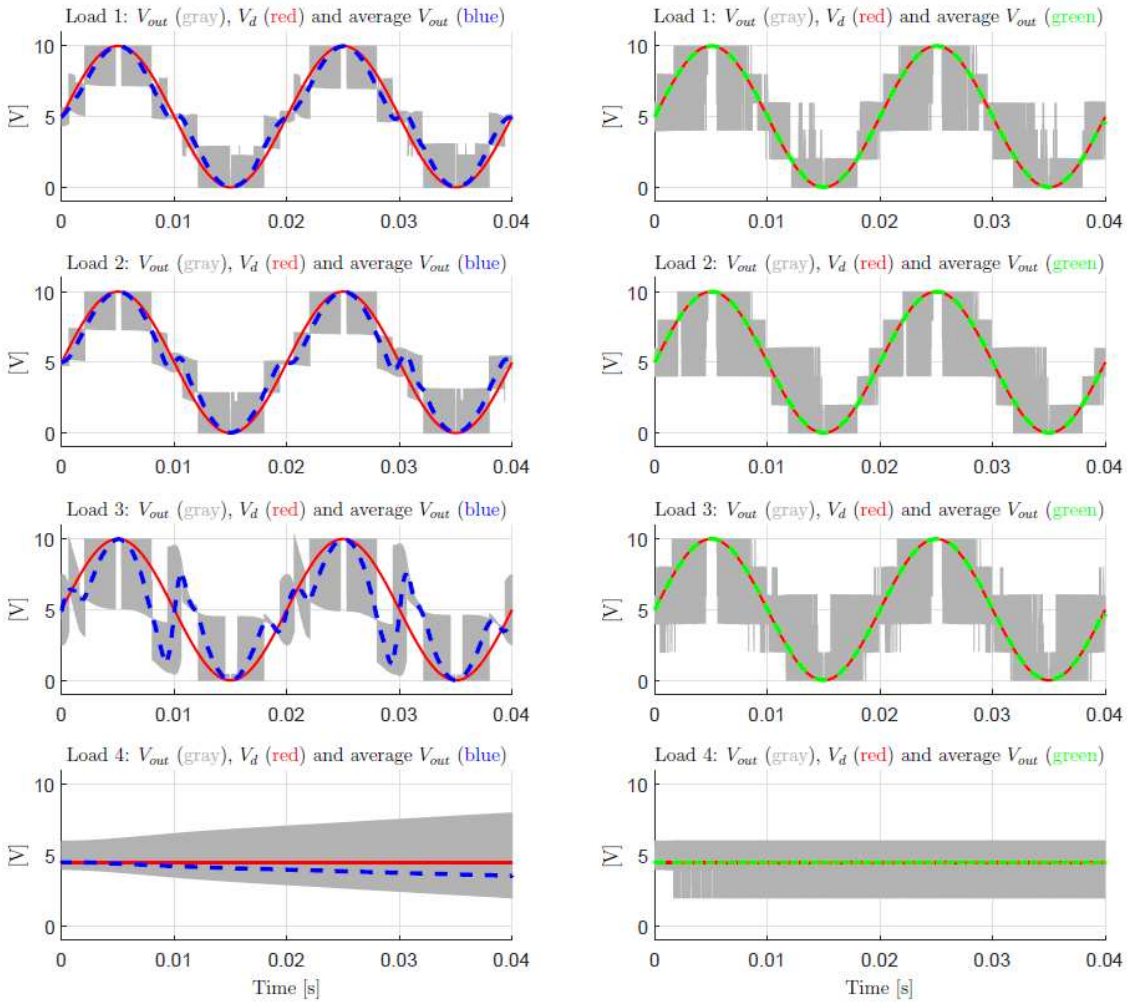

Figure 4.31: Left subplots: simulations using the Minimum Distance Control for $\mathbf{V}_m = [5\ 4\ 1]^{\mathrm{T}}$; Right subplot: simulations using the Variable-Step Control for $\mathbf{V}_m = [5\ 4\ 1]^{\mathrm{T}}$.

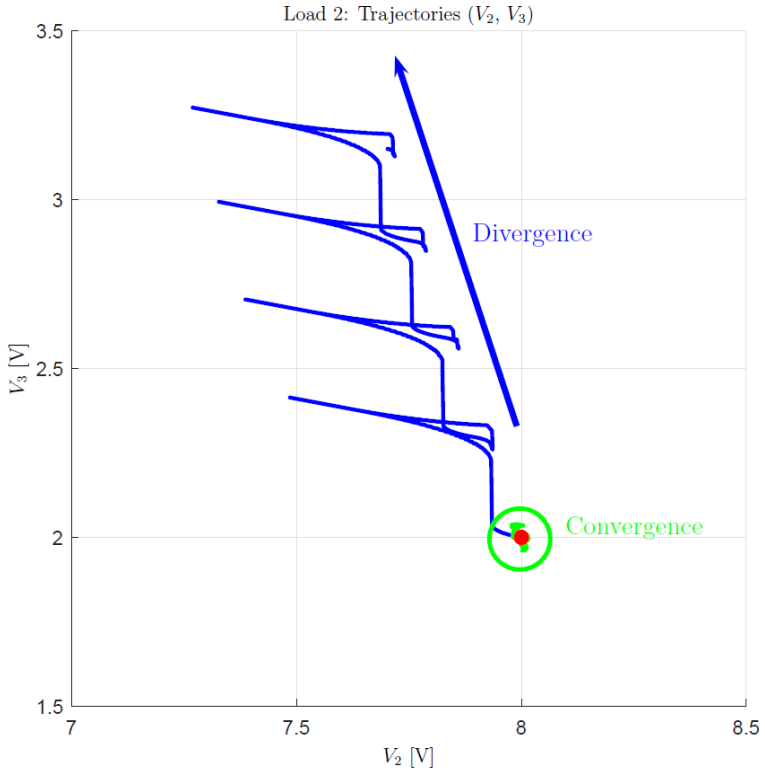

Figure 4.32: Voltage trajectories for the "Load 2" case using the Minimum Distance Control (blue) and the Variable-Step Control (green).

- a procedure for computing all the possible voltage vector configurations $\mathbf{V}_m$ providing equally spaced levels of the output voltage V_{out} has been given;
- the robustness assessment of the converter operating in extended mode when using a Minimum Distance Control has been performed;
- a Divergence Index I_M has been introduced, which can be used as a metric for properly ordering the different Configuration Voltage Vectors on the basis of their voltage balancing capability in extended operation;
- a new Variable-Step Control algorithm has been proposed, allowing for the safe extended operation of the converter even under particularly destabilizing operating conditions, such as a constant desired output voltage or a sudden load change.

The good performances of the proposed control algorithm have finally been tested in simulation and compared with the results that are given by the classical Minimum Distance Control. The next steps of the research work presented in this chapter include the code optimization of the Variable-Step Control, in order to study and address its real-time implementation, as well as the investigation of the other potential benefits that the Variable-Step Control can bring. Additionally, the closed-loop stability analysis through the load can provide important criteria that the load must satisfy in order to ensure closed-loop stability. As far as the modeling part is concerned, the presented modeling procedure can be extended in order to show that it can also be easily applied to other converter topologies, such as the diode-clamped topology. Furthermore, the analysis and the modeling of other multilevel converters can be addressed, in order to perform their stability analysis and investigate the properties they exhibit, following the outlines introduced in this chapter for multilevel flying-capacitor converters.

Chapter 5

Modeling of Permanent Magnet Synchronous Electric Motors

This chapter deals with the theoretical analysis, modeling and parameters estimation of three-phase Permanent Magnet Synchronous Motors (PMSMs) [34]-[41]. The modeling is performed by means of the POG technique [2]-[3]. The structure of the chapter is as follows. The dynamics of the three-phase PMSM is presented both in the static reference frame, see Sec. 5.1, and in a transformed rotating reference frame, see Sec. 5.2. The state-space transformations to be applied in order to turn the system into the rotating reference frame are illustrated and both the POG model in the static reference frame and the POG model in the rotating reference frame are reported and commented in detail. The torque vector analysis is then performed, together with the description of the simplified motor dynamics in the case of star-connected phases and with the description of the optimal way of generating the desired torque. A procedure for the estimation of the motor parameters is finally illustrated in Sec 5.3, which is based on the efficiency analysis of physical systems using a unified approach presented in [41]-[42].

5.1 Modeling in the static frame

The schematic view of a three-phase PMSM is reported in Fig. 5.1.

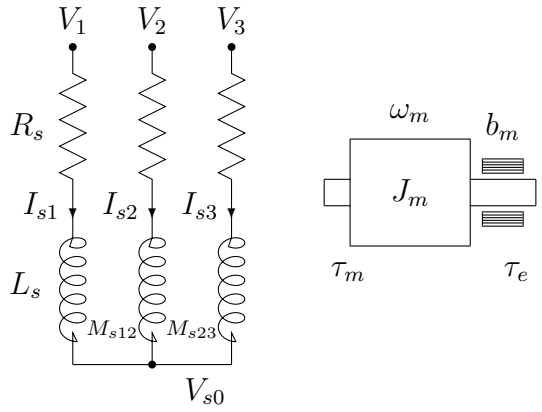

Figure 5.1: Schematic view of a three-phase PMSM.

For a three-phase PMSM, the number of stator phases m_s is equal to 3. A summary and description of the motor parameters can be found in Tab. 5.1. Fluxes $\phi(\theta)$ and $\phi_c(\theta)$ are related through the following relations:

$$\phi(\theta) = \varphi_r\,\bar{\phi}(\theta), \qquad\qquad \phi_c(\theta) = p\,N_c\,\phi(\theta) = p\,N_c\,\varphi_r\,\bar{\phi}(\theta) = \varphi_c\,\bar{\phi}(\theta),$$

where φ_r and φ_c are the maximum values of functions $\phi(\theta)$ and $\phi_c(\theta)$ respectively, $\varphi_c = p\,N_c\,\varphi_r$ and $\bar{\phi}(\theta)$ is the rotor flux normalized with respect to its maximum value. The basic angular displacement γ_s, in the case of electric motors with $m_s = 3$ phases, is $\gamma_s = 2\pi/m_s = 2\pi/3$. The following hypotheses are made:
H1) Function $\phi(\theta)$ is periodic with period 2π;
H2) Function $\phi(\theta)$ is an even function of θ;
H3) Function $\phi(\theta + \frac{\pi}{2})$ is an odd function of θ;
H4) For $\theta = 0$, the rotor flux $\phi_c(\theta)$ chained with phase 1 is maximum;
H5) The electric motor is homogeneous in its electric characteristics:

$$\begin{cases} M_{ij} = M_{s0}\cos((i-j)\gamma_s) \\ L_{si} = L_s = L_{s0} + M_{s0} \\ R_{si} = R_s \end{cases}, \qquad i,j \in \{1,2,3\}. \tag{5.1}$$

Note that the parameters L_{si} and R_{si} have been defined for $p = 1$, meaning that they represent the $i-th$ stator phase self induction coefficient and the i$-th$ stator phase resistance of a single polar expansion.

$m_s = 3$	number of motor phases;
p	number of polar expansions;
θ, θ_m	electric and rotor angular positions: $\theta = p\,\theta_m$;
ω, ω_m	electric and rotor angular velocities: $\omega = p\,\omega_m$;
N_c	number of coils for each phase;
R_{si}	i-th stator phase resistance ($p = 1$);
L_{si}	i-th stator phase self induction coefficient ($p = 1$);
M_{s0}	maximum value of mutual inductance between stator phases;
$\phi(\theta)$	rotor permanent magnet flux;
$\phi_c(\theta)$	total rotor flux chained with stator phase 1;
φ_r	maximum value of function $\phi(\theta)$;
φ_c	maximum value of function $\phi_c(\theta)$;
J_m	rotor moment of inertia;
b_m	rotor linear friction coefficient;
τ_m	electromotive torque working on the rotor;
τ_e	external load torque working on the rotor;
γ_s	basic angular displacement ($\gamma_s = 2\pi/m_s = 2\pi/3$)

Table 5.1: Parameters of the three-phase PMSM.

Additionally, the angular displacement of the three chained fluxes is given by:

$$\phi_{ci}(\theta) = \phi_c\left(\theta - (i-1)\gamma_s\right), \qquad i \in \{1,2,3\}. \tag{5.2}$$

Function $\phi_c(\theta)$, like function $\phi(\theta)$, is an even function (H2) and periodic with period 2π (H1), therefore it can be developed in Fourier series of cosines. Additionally, function $\phi_c(\theta + \frac{\pi}{2})$ is odd with respect to θ (H3), meaning that its Fourier series development is composed of odd harmonics only.

$$\phi_c(\theta) = \varphi_c\,\bar{\phi}(\theta) = \varphi_c \sum_{n=1:2}^{\infty} a_n \cos(n\theta). \tag{5.3}$$

Remark 5 *in the following, index n of coefficients a_n can also assume negative or null values, in these cases $a_n = 0$ will be assumed for $n \leq 0$.*

Let us introduce the following vectors:

$$ {}^t\mathbf{I}_s = \begin{bmatrix} I_{s1} \\ I_{s2} \\ I_{s3} \end{bmatrix}, \qquad {}^t\mathbf{V}_s = \begin{bmatrix} V_{s1} \\ V_{s2} \\ V_{s3} \end{bmatrix} = \begin{bmatrix} V_1 - V_{s0} \\ V_2 - V_{s0} \\ V_3 - V_{s0} \end{bmatrix}, \qquad {}^t\mathbf{V} = \begin{bmatrix} {}^t\mathbf{V}_s \\ -\tau_e \end{bmatrix}, \tag{5.4} $$

where ${}^t\mathbf{I}_s$, ${}^t\mathbf{V}_s$ are the stator current and voltage vectors and ${}^t\mathbf{V}$ is the input vector of the global system, i.e. electric plus mechanical parts.

Let ${}^t\mathbf{L}_s$ denote the self and mutual inductance coefficients matrix; according to hypothesis H5, the latter matrix is:

$$ \begin{aligned} {}^t\mathbf{L}_s &= p\, L_{s0}\, \mathbf{I}_{m_s} + p\, M_{s0} \underset{1:3}{\overset{i}{\underset{}{[\![}}} \cos((i-j)\gamma_s) \underset{1:3}{\overset{j}{\underset{}{]\!]}}} \\ &= p \begin{bmatrix} L_{s0} + M_{s0} & M_{s0}\cos(\gamma_s) & M_{s0}\cos(2\gamma_s) \\ M_{s0}\cos(\gamma_s) & L_{s0} + M_{s0} & M_{s0}\cos(\gamma_s) \\ M_{s0}\cos(2\gamma_s) & M_{s0}\cos(\gamma_s) & L_{s0} + M_{s0} \end{bmatrix} \\ &= p \begin{bmatrix} L_{s0} + M_{s0} & -\frac{M_{s0}}{2} & -\frac{M_{s0}}{2} \\ -\frac{M_{s0}}{2} & L_{s0} + M_{s0} & -\frac{M_{s0}}{2} \\ -\frac{M_{s0}}{2} & -\frac{M_{s0}}{2} & L_{s0} + M_{s0} \end{bmatrix}. \end{aligned} $$

The last result has been obtained by recalling that $\cos(\gamma_s) = \cos(2\gamma_s) = -0.5$. Matrix ${}^t\mathbf{L}_s$ is constant, symmetric and positive definite. Matrix ${}^t\mathbf{R}_s$ is the stator resistances matrix:

$$ {}^t\mathbf{R}_s = p\, R_s\, \mathbf{I}_{m_s} = p \begin{bmatrix} R_s & 0 & 0 \\ 0 & R_s & 0 \\ 0 & 0 & R_s \end{bmatrix}. $$

Vector ${}^t\mathbf{\Phi}_c(\theta)$, containing the rotor fluxes chained with the stator phases, is denoted by:

$$ {}^t\mathbf{\Phi}_c(\theta) = \begin{bmatrix} \phi_{c1}(\theta) \\ \phi_{c2}(\theta) \\ \phi_{c3}(\theta) \end{bmatrix} = \begin{bmatrix} \phi_c(\theta) \\ \phi_c(\theta - \gamma_s) \\ \phi_c(\theta - 2\gamma_s) \end{bmatrix}. \tag{5.5} $$

The particular structure of vector ${}^t\mathbf{\Phi}_c(\theta)$ directly comes from hypothesis H5, i.e. magnetic symmetry of the electric motor. From relations (5.3) and (5.5), the following representation of vector ${}^t\mathbf{\Phi}_c(\theta)$ can be derived:

$$ {}^t\mathbf{\Phi}_c(\theta) = \varphi_c \left\| \left[\sum_{n=1:2}^{\infty} a_n \cos[n(\theta - h\,\gamma_s)] \right] \right\|_{0:2}^{h}. \tag{5.6} $$

Symbol ${}^t\mathbf{K}_\tau(\theta)$ denotes a new vector defined as:

$$ {}^t\mathbf{K}_\tau(\theta) = \frac{\partial\, {}^t\mathbf{\Phi}_c(p\,\theta_m)}{\partial \theta_m} = p\,\frac{\partial\, {}^t\mathbf{\Phi}_c(\theta)}{\partial \theta}. \tag{5.7} $$

From relations (5.6) and (5.7), the following expression of vector ${}^t\mathbf{K}_\tau(\theta)$ is obtained:

$$ {}^t\mathbf{K}_\tau(\theta) = p\ \varphi_c \left\| \left[-\sum_{n=1:2}^{\infty} n\, a_n \sin[n(\theta - h\,\gamma_s)] \right] \right\|_{0:2}^{h}. \tag{5.8} $$

The superscript "t" denotes that symbols are defined in the static reference frame Σ_t.

5.2 Modeling in the rotating frame

In the static reference frame, the dynamic equations of the PMSM can be written in a POG state-space representation as follows [35]:

$$ \underbrace{\left[\begin{array}{c|c} {}^t\mathbf{L}_s & 0 \\ \hline 0 & J_m \end{array}\right]}_{{}^t\mathbf{L}} \underbrace{\left[\begin{array}{c} {}^t\dot{\mathbf{I}}_s \\ \hline \dot{\omega}_m \end{array}\right]}_{{}^t\dot{\mathbf{x}}} = -\underbrace{\left[\begin{array}{c|c} {}^t\mathbf{R}_s & {}^t\mathbf{K}_\tau(\theta) \\ \hline -{}^t\mathbf{K}_\tau^{\mathrm{T}}(\theta) & b_m \end{array}\right]}_{{}^t\mathbf{R} + {}^t\mathbf{W}} \underbrace{\left[\begin{array}{c} {}^t\mathbf{I}_s \\ \hline \omega_m \end{array}\right]}_{{}^t\mathbf{x}} + \underbrace{\left[\begin{array}{c} {}^t\mathbf{V}_s \\ \hline -\tau_e \end{array}\right]}_{{}^t\mathbf{V}}. \tag{5.9} $$

Let us now consider the following orthonormal coordinate transformations ${}^{t}\mathbf{T}_{b}$ and ${}^{b}\mathbf{T}_{\omega}$:

$$ {}^{t}\mathbf{T}_{b} = \sqrt{\frac{2}{3}} \begin{bmatrix} \cos(0) & \sin(0) & \frac{1}{\sqrt{2}} \\ \cos(\gamma_s) & \sin(\gamma_s) & \frac{1}{\sqrt{2}} \\ \cos(2\gamma_s) & \sin(2\gamma_s) & \frac{1}{\sqrt{2}} \end{bmatrix} = \sqrt{\frac{2}{3}} \begin{bmatrix} 1 & 0 & \frac{1}{\sqrt{2}} \\ -\frac{1}{2} & \frac{\sqrt{3}}{2} & \frac{1}{\sqrt{2}} \\ -\frac{1}{2} & -\frac{\sqrt{3}}{2} & \frac{1}{\sqrt{2}} \end{bmatrix}, $$

$$ {}^{b}\mathbf{T}_{\omega} = \begin{bmatrix} \cos(\theta) & -\sin(\theta) & 0 \\ \sin(\theta) & \cos(\theta) & 0 \\ 0 & 0 & 1 \end{bmatrix} = \begin{bmatrix} e^{\mathbf{j}\theta} & 0 \\ 0 & 1 \end{bmatrix}. $$

Matrix ${}^{t}\mathbf{T}_{b}$ is similar to the generalized Concordia transformation, the difference is that a permutation on columns has been added. This matrix transforms the system variables from the original reference frame Σ_t into an intermediate reference frame Σ_b. Matrix ${}^{b}\mathbf{T}_{\omega}$ represents a multiple rotation in the state space as a function of the electric angle θ. This matrix transforms the system from the intermediate reference frame Σ_b into the final rotating reference frame Σ_ω. Multiplying the two matrices ${}^{t}\mathbf{T}_{b}$ and ${}^{b}\mathbf{T}_{\omega}$, the final transformation matrix ${}^{t}\mathbf{T}_{\omega}$ is obtained, having the following structure:

$$ \begin{aligned} {}^{t}\mathbf{T}_{\omega} = {}^{t}\mathbf{T}_{b}\,{}^{b}\mathbf{T}_{\omega} &= \sqrt{\tfrac{2}{3}} \begin{bmatrix} \cos(\theta) & -\sin(\theta) & \frac{1}{\sqrt{2}} \\ \cos(\gamma_s - \theta) & \sin(\gamma_s - \theta) & \frac{1}{\sqrt{2}} \\ \cos(2\gamma_s - \theta) & \sin(2\gamma_s - \theta) & \frac{1}{\sqrt{2}} \end{bmatrix} \\ &= \sqrt{\tfrac{2}{3}} \begin{bmatrix} \cos(\theta) & -\sin(\theta) & \frac{1}{\sqrt{2}} \\ \cos(\frac{2}{3}\pi - \theta) & \sin(\frac{2}{3}\pi - \theta) & \frac{1}{\sqrt{2}} \\ \cos(\frac{4}{3}\pi - \theta) & \sin(\frac{4}{3}\pi - \theta) & \frac{1}{\sqrt{2}} \end{bmatrix}. \end{aligned} $$

Matrix ${}^{t}\mathbf{T}_{\omega} = {}^{t}\mathbf{T}_{b}\,{}^{b}\mathbf{T}_{\omega}$ is an orthonormal matrix allowing to write the equations of the electric part of the motor with respect to the rotating reference frame Σ_ω. Let ${}^{t}\overline{\mathbf{T}}_{\omega} \in \mathbb{R}^{(m_s+1)\times(m_s+1)}$, i.e. ${}^{t}\overline{\mathbf{T}}_{\omega} \in \mathbb{R}^{4\times4}$, denote the transformation matrix defined as:

$$ {}^{t}\overline{\mathbf{T}}_{\omega} = \begin{bmatrix} {}^{t}\mathbf{T}_{\omega} & 0 \\ 0 & 1 \end{bmatrix}. $$

When using transformation ${}^{t}\mathbf{x} = {}^{t}\overline{\mathbf{T}}_{\omega}\,{}^{\omega}\mathbf{x}$, it is necessary to recall that matrix ${}^{t}\overline{\mathbf{T}}_{\omega}$ is time varying, meaning that:

$$ {}^{t}\dot{\mathbf{x}} = {}^{t}\overline{\mathbf{T}}_{\omega}\,{}^{\omega}\dot{\mathbf{x}} + {}^{t}\dot{\overline{\mathbf{T}}}_{\omega}\,{}^{\omega}\mathbf{x} = \begin{bmatrix} {}^{t}\mathbf{T}_{\omega} & 0 \\ 0 & 1 \end{bmatrix} {}^{\omega}\dot{\mathbf{x}} + \begin{bmatrix} {}^{t}\dot{\mathbf{T}}_{\omega} & 0 \\ 0 & 0 \end{bmatrix} {}^{\omega}\mathbf{x}. $$

Applying this transformation to system (5.9), one obtains:

$$ {}^{t}\overline{\mathbf{T}}_{\omega}^{\mathrm{T}}\,{}^{t}\mathbf{L}({}^{t}\overline{\mathbf{T}}_{\omega}\,{}^{\omega}\dot{\mathbf{x}} + {}^{t}\dot{\overline{\mathbf{T}}}_{\omega}\,{}^{\omega}\mathbf{x}) = -\,{}^{t}\overline{\mathbf{T}}_{\omega}^{\mathrm{T}}({}^{t}\mathbf{R} + {}^{t}\mathbf{W})\,{}^{t}\overline{\mathbf{T}}_{\omega}\,{}^{\omega}\mathbf{x} + {}^{t}\overline{\mathbf{T}}_{\omega}^{\mathrm{T}}\,{}^{t}\mathbf{V}, \tag{5.10} $$

which can be rewritten as:

$$ \underbrace{{}^{t}\overline{\mathbf{T}}_{\omega}^{\mathrm{T}}\,{}^{t}\mathbf{L}\,{}^{t}\overline{\mathbf{T}}_{\omega}}_{{}^{\omega}\mathbf{L}}\,{}^{\omega}\dot{\mathbf{x}} = -(\underbrace{{}^{t}\overline{\mathbf{T}}_{\omega}^{\mathrm{T}}\,{}^{t}\mathbf{R}\,{}^{t}\overline{\mathbf{T}}_{\omega}}_{{}^{\omega}\mathbf{R}} + \underbrace{{}^{t}\overline{\mathbf{T}}_{\omega}^{\mathrm{T}}\,{}^{t}\mathbf{W}\,{}^{t}\overline{\mathbf{T}}_{\omega} + {}^{t}\overline{\mathbf{T}}_{\omega}^{\mathrm{T}}\,{}^{t}\mathbf{L}\,{}^{t}\dot{\overline{\mathbf{T}}}_{\omega}}_{{}^{\omega}\mathbf{W}})\,{}^{\omega}\mathbf{x} + \underbrace{{}^{t}\overline{\mathbf{T}}_{\omega}^{\mathrm{T}}\,{}^{t}\mathbf{V}}_{{}^{\omega}\mathbf{V}}. \tag{5.11} $$

In the transformed rotating frame Σ_{ω}, the dynamic equations of the electric motor (both electric and mechanical parts) assume the following structure:

$$ \underbrace{\left[\begin{array}{c|c} {}^{\omega}\mathbf{L}_s & 0 \\ \hline 0 & J_m \end{array}\right]}_{{}^{\omega}\mathbf{L}} \underbrace{\left[\begin{array}{c} {}^{\omega}\dot{\mathbf{I}}_s \\ \hline \dot{\omega}_m \end{array}\right]}_{{}^{\omega}\dot{\mathbf{x}}} = -\underbrace{\left[\begin{array}{c|c} {}^{\omega}\mathbf{R}_s + {}^{\omega}\mathbf{L}_s\,{}^{\omega}\mathbf{J}_s & {}^{\omega}\mathbf{K}_{\tau}(\theta) \\ \hline -\,{}^{\omega}\mathbf{K}_{\tau}^{\mathrm{T}}(\theta) & b_m \end{array}\right]}_{{}^{\omega}\mathbf{R} + {}^{\omega}\mathbf{W}} \underbrace{\left[\begin{array}{c} {}^{\omega}\mathbf{I}_s \\ \hline \omega_m \end{array}\right]}_{{}^{\omega}\mathbf{x}} + \underbrace{\left[\begin{array}{c} {}^{\omega}\mathbf{V}_s \\ \hline -\tau_e \end{array}\right]}_{{}^{\omega}\mathbf{V}}, \tag{5.12} $$

where:

$$ {}^{\omega}\mathbf{W} = {}^{t}\overline{\mathbf{T}}_{\omega}^{\mathrm{T}}\,{}^{t}\mathbf{W}\,{}^{t}\overline{\mathbf{T}}_{\omega} + {}^{t}\overline{\mathbf{T}}_{\omega}^{\mathrm{T}}\,{}^{t}\mathbf{L}\,{}^{t}\dot{\overline{\mathbf{T}}}_{\omega} = \left[\begin{array}{c|c} {}^{\omega}\mathbf{L}_s\,{}^{\omega}\mathbf{J}_s & {}^{\omega}\mathbf{K}_{\tau}(\theta) \\ \hline -\,{}^{\omega}\mathbf{K}_{\tau}^{\mathrm{T}}(\theta) & 0 \end{array}\right], \tag{5.13} $$

${}^{\omega}\mathbf{I}_s = {}^{t}\mathbf{T}_{\omega}^{\mathrm{T}}\,{}^{t}\mathbf{I}_s$, ${}^{\omega}\mathbf{L}_s = {}^{t}\mathbf{T}_{\omega}^{\mathrm{T}}\,{}^{t}\mathbf{L}_s\,{}^{t}\mathbf{T}_{\omega}$, ${}^{\omega}\mathbf{R}_s = {}^{t}\mathbf{T}_{\omega}^{\mathrm{T}}\,{}^{t}\mathbf{R}_s\,{}^{t}\mathbf{T}_{\omega}$, ${}^{\omega}\mathbf{J}_s = {}^{t}\mathbf{T}_{\omega}^{\mathrm{T}}\,{}^{t}\dot{\mathbf{T}}_{\omega}$, ${}^{\omega}\mathbf{K}_{\tau} = {}^{t}\mathbf{T}_{\omega}^{\mathrm{T}}\,{}^{t}\mathbf{K}_{\tau}$ and ${}^{\omega}\mathbf{V}_s = {}^{t}\mathbf{T}_{\omega}^{\mathrm{T}}\,{}^{t}\mathbf{V}_s$. System (5.12) can be written in a compact form as:

$$ {}^{\omega}\mathbf{L}\,{}^{\omega}\dot{\mathbf{x}} = -({}^{\omega}\mathbf{R} + {}^{\omega}\mathbf{W})\,{}^{\omega}\mathbf{x} + {}^{\omega}\mathbf{V}. \tag{5.14} $$

The POG block scheme corresponding to the dynamic system (5.12) in the reference frame Σ_{ω} is reported in Fig. 5.2.

It can be proven that the transformed matrices and vectors assume the following form [35]:

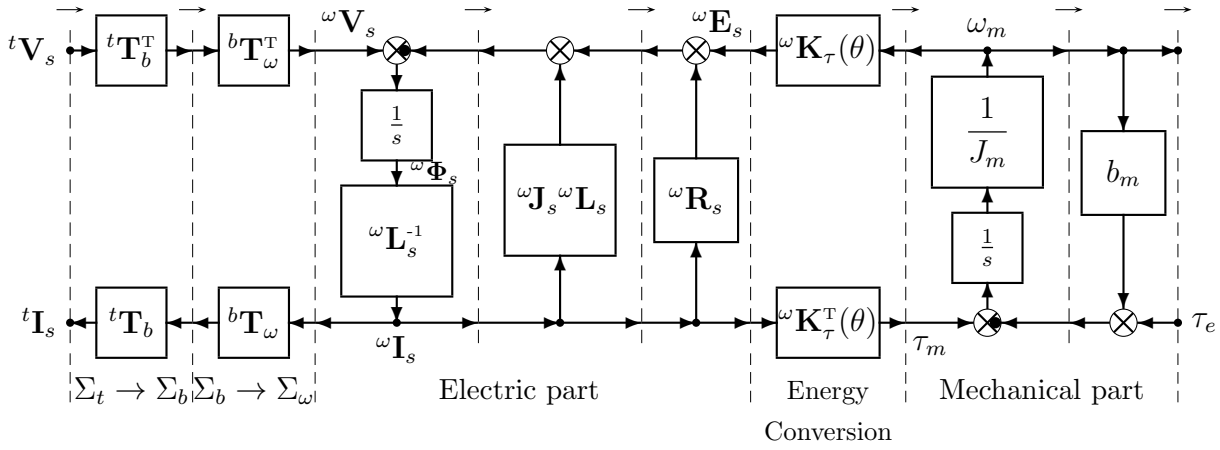

Figure 5.2: POG block scheme of the three-phase synchronous electric motor in the transformed reference frame Σ_ω.

$$ {}^\omega\mathbf{J}_s = \begin{bmatrix} 0 & -p\omega_m & 0 \\ p\omega_m & 0 & 0 \\ 0 & 0 & 0 \end{bmatrix}, \quad {}^\omega\mathbf{L}_s = p \begin{bmatrix} L_{se} & 0 & 0 \\ 0 & L_{se} & 0 \\ 0 & 0 & L_{s0} \end{bmatrix}, \text{ with } L_{se} = L_{s0} + \frac{3}{2} M_{s0}, \tag{5.15} $$

$$ {}^\omega\mathbf{R}_s = {}^t\mathbf{R}_s, \quad {}^\omega\mathbf{K}_\tau(\theta) = \begin{bmatrix} {}^\omega K_d \\ {}^\omega K_q \\ {}^\omega K_{s3} \end{bmatrix}, \quad {}^\omega\mathbf{I}_s = \begin{bmatrix} {}^\omega I_d \\ {}^\omega I_q \\ {}^\omega I_{s3} \end{bmatrix}, \quad {}^\omega\mathbf{V}_s = \begin{bmatrix} {}^\omega V_d \\ {}^\omega V_q \\ {}^\omega V_{s3} \end{bmatrix}. \tag{5.16} $$

It can be shown [35] that the last component of vector ${}^\omega\mathbf{I}_s$, ${}^\omega I_{s3}$, is proportional to the sum of currents I_{sh}, for $h = \{1, 2, 3\}$, circulating in the three stator phases, and that the last component of vector ${}^\omega\mathbf{V}_s$, ${}^\omega V_{s3}$, is proportional to the sum of voltages V_{sh}, for $h = \{1, 2, 3\}$, on the three stator phases:

$$ {}^\omega I_{s3} = \sqrt{\frac{1}{3}} \sum_{h=1}^{3} I_{sh}, \quad {}^\omega V_{s3} = \sqrt{\frac{1}{3}} \sum_{h=1}^{3} V_{sh} = \sqrt{\frac{1}{3}} \sum_{h=1}^{3} (V_h - V_{s0}). \tag{5.17} $$

From (5.13), (5.15) and (5.16), system (5.12) can be rewritten in an expanded

form as follows:

$$\underbrace{\left[\begin{array}{ccc|c} p\,L_{se} & 0 & 0 & 0 \\ 0 & p\,L_{se} & 0 & 0 \\ 0 & 0 & p\,L_{s0} & 0 \\ \hline 0 & 0 & 0 & J_m \end{array}\right]}_{^{\omega}\mathbf{L}} \underbrace{\left[\begin{array}{c} {}^{\omega}\dot{I}_d \\ {}^{\omega}\dot{I}_q \\ {}^{\omega}\dot{I}_{s3} \\ \hline \dot{\omega}_m \end{array}\right]}_{^{\omega}\dot{\mathbf{x}}} =$$

$$-\underbrace{\left[\begin{array}{ccc|c} p\,R_s & -p^2\,\omega_m\,L_{se} & 0 & {}^{\omega}K_d \\ p^2\,\omega_m\,L_{se} & p\,R_s & 0 & {}^{\omega}K_q \\ 0 & 0 & p\,R_s & {}^{\omega}K_{s3} \\ \hline -{}^{\omega}K_d & -{}^{\omega}K_q & -{}^{\omega}K_{s3} & b_m \end{array}\right]}_{^{\omega}\mathbf{R}+{}^{\omega}\mathbf{W}} \underbrace{\left[\begin{array}{c} {}^{\omega}I_d \\ {}^{\omega}I_q \\ {}^{\omega}I_{s3} \\ \hline \omega_m \end{array}\right]}_{^{\omega}\mathbf{x}} + \underbrace{\left[\begin{array}{c} {}^{\omega}V_d \\ {}^{\omega}V_q \\ {}^{\omega}V_{s3} \\ \hline -\tau_e \end{array}\right]}_{^{\omega}\mathbf{V}} . \tag{5.18}$$

It can be proven [35] that the following proposition holds:

Proposition: the torque vector ${}^{\omega}\mathbf{K}_{\tau}$ can be constant (namely not function of the electric angle θ) only for those flux functions $\bar{\phi}(\theta)$ which can be expressed in Fourier series development as follows:

$$\bar{\phi}(\theta) = \sum_{i=1:2}^{m_s-2} a_i \cos(i\,\theta)\,. \tag{5.19}$$

Since the present electric motor is three-phase, expression (5.19) becomes:

$$\bar{\phi}(\theta) = a_1 \cos(\theta)\,. \tag{5.20}$$

If the rotor flux is defined by function $\bar{\phi}(\theta)$, i.e. sinusoidal for a three-phase motor, then the electric motor is able to generate a constant motor torque τ_m , as long as current vector ${}^{\omega}\mathbf{I}_s$ is constant. All the constant components of the torque vector ${}^{\omega}\mathbf{K}_{\tau}$ can be obtained by replacing $n = 0$ within vector ${}^{\omega}\mathbf{K}_{\tau}(\theta)$ in Eq. (5.16):

$${}^{\omega}\mathbf{K}_{\tau}(\theta)^{\mathrm{T}}|_{n=0} = \varphi_c\,p\sqrt{\frac{3}{2}}\left[\begin{array}{ccc} 0 & a_1 & 0 \end{array}\right]. \tag{5.21}$$

Since the desired rotor flux is sinusoidal, expression (5.21) becomes:

$${}^{\omega}\mathbf{K}_{\tau}^{\mathrm{T}}|_{n=0} = \varphi_c\,p\sqrt{\frac{3}{2}}\left[\begin{array}{ccc} 0 & 1 & 0 \end{array}\right]. \tag{5.22}$$

From Eq. (5.21), one can also rewrite the system reporting the dynamic equations of the electric motor, both electric and mechanical parts, in the rotating frame Σ_ω (system (5.12)) in the case of sinusoidal rotor flux, that is when the torque vector is constant:

$$\underbrace{\left[\begin{array}{ccc|c} p\,L_{se} & 0 & 0 & 0 \\ 0 & p\,L_{se} & 0 & 0 \\ 0 & 0 & p\,L_{s0} & 0 \\ \hline 0 & 0 & 0 & J_m \end{array}\right]}_{{}^{\omega}\mathbf{L}} \underbrace{\left[\begin{array}{c} {}^{\omega}\dot{I}_d \\ {}^{\omega}\dot{I}_q \\ {}^{\omega}\dot{I}_{s3} \\ \hline \dot{\omega}_m \end{array}\right]}_{{}^{\omega}\dot{\mathbf{x}}} = \\ -\underbrace{\left[\begin{array}{ccc|c} p\,R_s & -p^2\,\omega_m\,L_{se} & 0 & 0 \\ p^2\,\omega_m\,L_{se} & p\,R_s & 0 & {}^{\omega}K_q \\ 0 & 0 & p\,R_s & 0 \\ \hline 0 & -{}^{\omega}K_q & 0 & b_m \end{array}\right]}_{{}^{\omega}\mathbf{R}+{}^{\omega}\mathbf{W}} \underbrace{\left[\begin{array}{c} {}^{\omega}I_d \\ {}^{\omega}I_q \\ {}^{\omega}I_{s3} \\ \hline \omega_m \end{array}\right]}_{{}^{\omega}\mathbf{x}} + \underbrace{\left[\begin{array}{c} {}^{\omega}V_d \\ {}^{\omega}V_q \\ {}^{\omega}V_{s3} \\ \hline -\tau_e \end{array}\right]}_{{}^{\omega}\mathbf{V}} . \tag{5.23}$$

Under the hypothesis of star-connected phases, a static constraint between the stator currents originates, see (5.17). Therefore, the electric part of the PMSM is described by a system having dynamic dimension equal to $m_s - 1 = 2$.

The dynamic equations of the motor with star-connected phases become [35]:

$$\left[\begin{array}{c|c} p\begin{bmatrix} L_{se} & 0 \\ 0 & L_{se} \end{bmatrix} & 0 \\ \hline 0 & J_m \end{array}\right] \left[\begin{array}{c} {}^{\omega}\dot{I}_d \\ {}^{\omega}\dot{I}_q \\ \hline \dot{\omega}_m \end{array}\right] = -\left[\begin{array}{c|c} p\begin{bmatrix} R_s & -p\omega_m L_{se} \\ p\omega_m L_{se} & R_s \end{bmatrix} & \begin{bmatrix} {}^{\omega}K_d \\ {}^{\omega}K_q \end{bmatrix} \\ \hline -\begin{bmatrix} {}^{\omega}K_d & {}^{\omega}K_q \end{bmatrix} & b_m \end{array}\right] \left[\begin{array}{c} {}^{\omega}I_d \\ {}^{\omega}I_q \\ \hline \omega_m \end{array}\right] + \left[\begin{array}{c} {}^{\omega}V_d \\ {}^{\omega}V_q \\ \hline -\tau_e \end{array}\right] . \tag{5.24}$$

5.2.1 Optimal generation of the desired torque τ_{ref}

The desired torque τ_{ref}, generated by current vector ${}^{\omega}\mathbf{I}_{ref}$, is given by:

$$\tau_{ref} = {}^{\omega}\mathbf{K}_{\tau}^{\mathrm{T}}\,{}^{\omega}\mathbf{I}_{ref} . \tag{5.25}$$

The set of all the current vectors ${}^{\omega}\mathbf{I}_{ref}$ satisfying relation (5.25) is:

$${}^{\omega}\mathbf{I}_{ref} = {}^{\omega}\mathbf{I}_0 + \mathrm{Ker}[{}^{\omega}\mathbf{K}_{\tau}^{\mathrm{T}}], \tag{5.26}$$

where ${}^{\omega}\mathbf{I}_0$ is a particular solution of system (5.25) and $\mathrm{Ker}[{}^{\omega}\mathbf{K}_{\tau}^{\mathrm{T}}]$ is the kernel of row matrix ${}^{\omega}\mathbf{K}_{\tau}^{\mathrm{T}}$. Among all the vectors ${}^{\omega}\mathbf{I}_{ref}$ given by (5.26), the one having the minimum modulus is the current vector ${}^{\omega}\mathbf{I}_{ref}$ which is parallel to vector ${}^{\omega}\mathbf{K}_{\tau}$:

$$ {}^{\omega}\mathbf{I}_{ref} = \frac{\tau_{ref}}{|{}^{\omega}\mathbf{K}_{\tau}|}\, {}^{\omega}\vec{\mathbf{K}}_{\tau}, \tag{5.27} $$

where ${}^{\omega}\vec{\mathbf{K}}_{\tau}$ denotes the unit vector corresponding to vector ${}^{\omega}\mathbf{K}_{\tau}$. Note that the modulus of current ${}^{\omega}\mathbf{I}_{ref}$ is inversely proportional to the modulus of vector ${}^{\omega}\mathbf{K}_{\tau}$. The latter consideration implies that, among all the fluxes given by (5.19), the one minimizing the modulus of the current ${}^{\omega}\mathbf{I}_{ref}$ is exactly the one maximizing the modulus $|{}^{\omega}\mathbf{K}_{\tau}|$ of the torque vector ${}^{\omega}\mathbf{K}_{\tau}$. From (5.21), remembering that coefficient a_1 is the amplitude coefficient in the expression of the rotor flux $\bar{\phi}(\theta)$ normalized with respect to its maximum value, it follows that $a_1 = 1$ is the correct value in order to maximize the modulus of the torque vector and therefore minimize the modulus of the stator currents vector ${}^{\omega}\mathbf{I}_{ref}$.

Eq. (5.21) clearly shows that, when the torque vector ${}^{\omega}\mathbf{K}_{\tau}$ is constant, its odd component is equal to zero: ${}^{\omega}K_d = 0$. Since from (5.27) it is known that the minimum current vector ${}^{\omega}\mathbf{I}_{ref}$ generating the desired torque τ_{ref} is parallel to the torque vector ${}^{\omega}\mathbf{K}_{\tau}$, one can conclude that the best way of generating the desired torque τ_{ref} requires the *direct* component ${}^{\omega}I_d$ of vector ${}^{\omega}\mathbf{I}_{ref}$ to be equal to zero, a result which well agrees with one of the typical controls employed in the literature [78].

5.3 Efficiency and parameters estimation

5.3.1 Efficiency analysis

Under the hypothesis of sinusoidal rotor flux, see (5.23), and of star connected phases, see (5.24), the steady-state equations of a PMSM in the rotating frame Σ_{ω},

see [36], have the following structure:

$$\underbrace{\left[\begin{array}{cc|c} pR_s & -p^2\omega_m L_{se} & 0 \\ p^2\omega_m L_{se} & p\,R_s & {}^{\omega}K_q \\ \hline 0 & -{}^{\omega}K_q & b_m \end{array}\right]\left[\begin{array}{c} {}^{\omega}I_d \\ {}^{\omega}I_q \\ \hline \omega_m \end{array}\right]-\left[\begin{array}{c} {}^{\omega}V_d \\ {}^{\omega}V_q \\ \hline -\tau_e \end{array}\right]=\left[\begin{array}{c} 0 \\ 0 \\ \hline 0 \end{array}\right]}_{\mathbf{f}(\mathbf{x}_{ss},\mathbf{u})=\mathbf{0}}. \tag{5.28}$$

Controlled PMSM

If voltage ${}^{\omega}V_d$ is chosen in order to impose the condition ${}^{\omega}I_d = 0$, see Sec. 5.2.1, the nonlinear static equations (5.28) simplify as follows:

$$\left[\begin{array}{c} {}^{\omega}V_d \\ {}^{\omega}V_q \\ \hline -\tau_e \end{array}\right]=\left[\begin{array}{cc|c} -p^2\,\omega_m\,L_{se} & & 0 \\ p\,R_s & & {}^{\omega}K_q \\ \hline -{}^{\omega}K_q & & b_m \end{array}\right]\left[\begin{array}{c} {}^{\omega}I_q \\ \hline \omega_m \end{array}\right]. \tag{5.29}$$

By solving with respect to ${}^{\omega}I_q$, ${}^{\omega}V_d$ and ${}^{\omega}V_q$, one obtains:

$$\left[\begin{array}{c} {}^{\omega}I_q \\ {}^{\omega}V_d \\ {}^{\omega}V_q \end{array}\right]=\left[\begin{array}{c} \dfrac{b_m\,\omega_m+\tau_e}{{}^{\omega}K_q} \\ -\dfrac{p^2\,\omega_m\,L_{se}(b_m\,\omega_m+\tau_e)}{{}^{\omega}K_q} \\ \dfrac{\omega_m\,{}^{\omega}K_q^2+R_s\,\tau_e\,p+R_s\,b_m\,p\,\omega_m}{{}^{\omega}K_q} \end{array}\right]. \tag{5.30}$$

Without the first equation, system (5.29) can be rewritten as:

$$\left[\begin{array}{c} u_1 \\ u_2 \end{array}\right]=\underbrace{\left[\begin{array}{c} {}^{\omega}V_q \\ \tau_e \end{array}\right]}_{\mathbf{u}}=\left[\begin{array}{cc} p\,R_s & {}^{\omega}K_q \\ {}^{\omega}K_q & -b_m \end{array}\right]\underbrace{\left[\begin{array}{c} {}^{\omega}I_q \\ \omega_m \end{array}\right]}_{\mathbf{y}}.$$

By solving with respect to $\mathbf{y}$, it results:

$$\left[\begin{array}{c} y_1 \\ y_2 \end{array}\right]=\underbrace{\left[\begin{array}{c} {}^{\omega}I_q \\ \omega_m \end{array}\right]}_{\mathbf{y}}=\underbrace{\left[\begin{array}{cc} \dfrac{b_m}{pR_sb_m+{}^{\omega}K_q^2} & \dfrac{{}^{\omega}K_q}{pR_sb_m+{}^{\omega}K_q^2} \\ \dfrac{{}^{\omega}K_q}{pR_sb_m+{}^{\omega}K_q^2} & -\dfrac{p\,R_s}{pR_sb_m+{}^{\omega}K_q^2} \end{array}\right]}_{\mathbf{H}_0}\underbrace{\left[\begin{array}{c} {}^{\omega}V_q \\ \tau_e \end{array}\right]}_{\mathbf{u}}.$$

The obtained matrix $\mathbf{H}_0$ has the structure defined in [41]-(2), where parameters a, b, c, d are:

$$a = \frac{b_m}{\Delta}, \qquad b = \frac{{}^{\omega}K_q}{\Delta} = c, \qquad d = \frac{p\,R_s}{\Delta}, \tag{5.31}$$

and where $\Delta = pR_s b_m + {}^{\omega}K_q^2$. For the considered PMSM, the maximum efficiency value E^*, see [41]-(18), is:

$$E^* = \frac{\left(\sqrt{1+q}-1\right)}{\left(\sqrt{1+q}+1\right)} \quad \text{where} \quad q = \frac{{}^{\omega}K_q^2}{p\,R_s\,b_m}. \tag{5.32}$$

The general case

If the electric motor is not controlled, both currents ${}^{\omega}I_d$ and ${}^{\omega}I_q$ are different from zero. In this case, system (5.28) can be rewritten as follows:

$$\underbrace{\begin{bmatrix} 0 \\ {}^{\omega}K_q\,\omega_m \\ b_m\omega_m + \tau_e \end{bmatrix}}_{\mathbf{b}} = \underbrace{\begin{bmatrix} -pR_s & p^2\omega_m L_{se} & 1 & 0 \\ -p^2\omega_m L_{se} & -pR_s & 0 & 1 \\ 0 & {}^{\omega}K_q & 0 & 0 \end{bmatrix}}_{\mathbf{A}} \underbrace{\begin{bmatrix} {}^{\omega}I_d \\ {}^{\omega}I_q \\ {}^{\omega}V_d \\ {}^{\omega}V_q \end{bmatrix}}_{\mathbf{x}}. \tag{5.33}$$

The solution of system (5.33) is:

$$\mathbf{x} = \underbrace{\begin{bmatrix} \frac{p\,\omega_m\,L_{se}(b_m\,\omega_m+\tau_e)}{{}^{\omega}K_q\,R_s} \\ \frac{b_m\,\omega_m+\tau_e}{{}^{\omega}K_q} \\ 0 \\ \frac{p(p^2\omega_m^2 L_{se}^2+R_s^2)(b_m\omega_m+\tau_e)+{}^{\omega}K_q^2 R_s\,\omega_m}{{}^{\omega}K_q\,R_s} \end{bmatrix}}_{\mathbf{x}_0} + \underbrace{\begin{bmatrix} \alpha \\ 0 \\ \alpha p R_s \\ \alpha p^2 \omega_m L_{se} \end{bmatrix}}_{\ker(\mathbf{A})}, \tag{5.34}$$

where $\alpha \in \mathbf{R}$ is an arbitrary real parameter. Solution (5.34) can also be expressed as follows:

$$\mathbf{x} = \begin{bmatrix} I_{d0}+\alpha \\ I_{q0} \\ \alpha\,p\,R_s \\ V_{q0}+\alpha p^2\omega_m L_{se} \end{bmatrix} \quad \text{where} \quad \begin{bmatrix} I_{d0} \\ I_{q0} \\ 0 \\ V_{q0} \end{bmatrix} = \mathbf{x}_0. \tag{5.35}$$

The power $P_1 = {}^{\omega}V_d\,{}^{\omega}I_d + {}^{\omega}V_q\,{}^{\omega}I_q$ entering the system is given by:

$$P_1 = \alpha\,p\,R_s(I_{d0}+\alpha) + I_{q0}(V_{q0}+\alpha\,p^2\,\omega_m\,L_{se}).$$

The efficiency $E(\omega_m,\, \tau_e) = \frac{P_2}{P_1}$ of the PMSM on the output plane can be expressed as follows:

$$E(\omega_m, \tau_e) = \frac{\omega_m\, \tau_e}{\alpha p R_s (I_{d0}+\alpha) + I_{q0}(V_{q0}+\alpha p^2 \omega_m L_{se})}, \tag{5.36}$$

where $P_2 = \omega_m\, \tau_e$ is the power exiting the system. Efficiency $E(\omega_m,\, \tau_e)$ is a function of parameter α. The maximum efficiency is obtained when the partial derivative of function $E(\omega_m,\, \tau_e)$ with respect to α is equal to zero:

$$\frac{\partial E(\omega_m, \tau_e)}{\partial \alpha} = \frac{-\omega_m \tau_e (p R_s (I_{d0}+2\alpha) + I_{q0} p^2 \omega_m L_{se})}{(p R_s (\alpha I_{d0}+\alpha^2) + I_{q0}(V_{q0}+\alpha p^2 \omega_m L_{se}))^2} = 0.$$

By solving with respect to α, one obtains:

$$\alpha^* = \frac{-R_s\, I_{d0} - I_{q0}\, p\, \omega_m\, L_{se}}{2\, R_s}. \tag{5.37}$$

By substituting (5.34) in (5.37), it results:

$$\alpha^* = -\frac{p\, \omega_m\, L_{se}(b_m\, \omega_m + \tau_e)}{{}^{\omega}K_q\, R_s} = -I_{d0}. \tag{5.38}$$

By substituting (5.38) in (5.35), one obtains:

$$\mathbf{x}^* = \begin{bmatrix} 0 \\ \dfrac{b_m\, \omega_m + \tau_e}{{}^{\omega}K_q} \\ -\dfrac{p^2\, \omega_m\, L_{se}(b_m\, \omega_m + \tau_e)}{{}^{\omega}K_q} \\ \dfrac{\omega_m\, {}^{\omega}K_q^2 + R_s\, \tau_e\, p + R_s\, b_m\, p\, \omega_m}{{}^{\omega}K_q} \end{bmatrix}. \tag{5.39}$$

Note that the obtained solution $\mathbf{x}^*$ is equal to the solution obtained in (5.30) when the control strategy imposes the condition ${}^{\omega}I_d = 0$.

5.3.2 Parameters estimation

The analysis presented in Sec. 5.3.1 can be used, for example, to estimate the parameters of a PMSM. The efficiency map of electric PMSM is typically given on the output plane $(y_2,\, u_2) = (\omega_m,\, \tau_e)$. For these systems, Eq. [41]-(20) can be rewritten as follows:

$$\begin{bmatrix} \bar{u}_1 \\ {}^{\omega}I_q \end{bmatrix} = \begin{bmatrix} \frac{d}{c} & \frac{1}{c} \\ \frac{a\,d+b\,c}{c} & \frac{a}{c} \end{bmatrix} \begin{bmatrix} \bar{u}_2 \\ \omega_m \end{bmatrix},$$

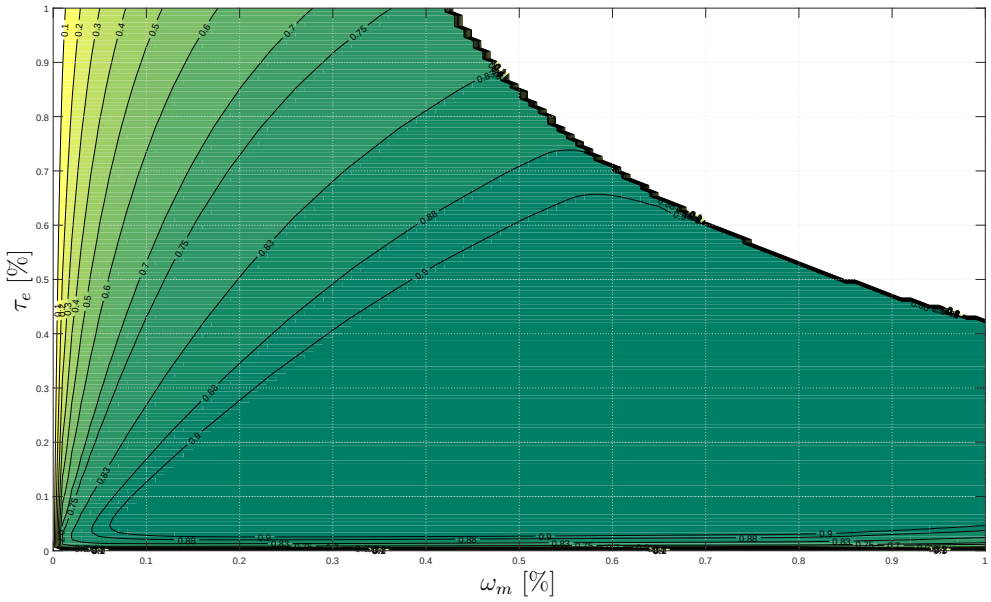

Figure 5.3: Normalized efficiency map of an industrial electric motor on plane (ω_m, τ_e).

where a, b, c, d are the coefficients of matrix $\mathbf{H}_0$ defined in (5.31) and inputs u_1 and u_2 are defined as follows:

$$\begin{cases} u_2 = \tau_e = \bar{u}_2 - b_c \operatorname{sign}(\omega_m) \\ u_1 = {}^{\omega}V_q = \bar{u}_1 + R_{sq}\, {}^{\omega}I_q^2 \end{cases} . \tag{5.40}$$

Parameters b_c and R_{sq} in (5.40) are, respectively, the amplitude of the Coulomb friction acting on the rotor, and the dissipative coefficient accounting for the Joule losses of the motor. The efficiency of the PMSM depends on the values of the dissipative parameters b_m, b_c, R_s, R_{sq}, which are usually unknown. Nevertheless, their values can be estimated if the efficiency map of the system on the output plane (ω_m, τ_e) in given. Let us consider, for example, the normalized efficiency map of an industrial three-phase synchronous electric motor shown in Fig. 5.3. From this figure, one can read the efficiency of the system on a properly chosen set of points. Then, a least square algorithm can be used to minimize the mean squared error between the real efficiency on the selected points and the efficiency of the PMSM model on the same points. By applying this procedure to the normalized efficiency map shown in Fig. 5.3, one obtains the following estimated parameters for the considered industrial PMSM: $b_m = 6.46\,10^{-3}$ [Nm/(rad/s)], $b_c = 1.97$ [Nm],

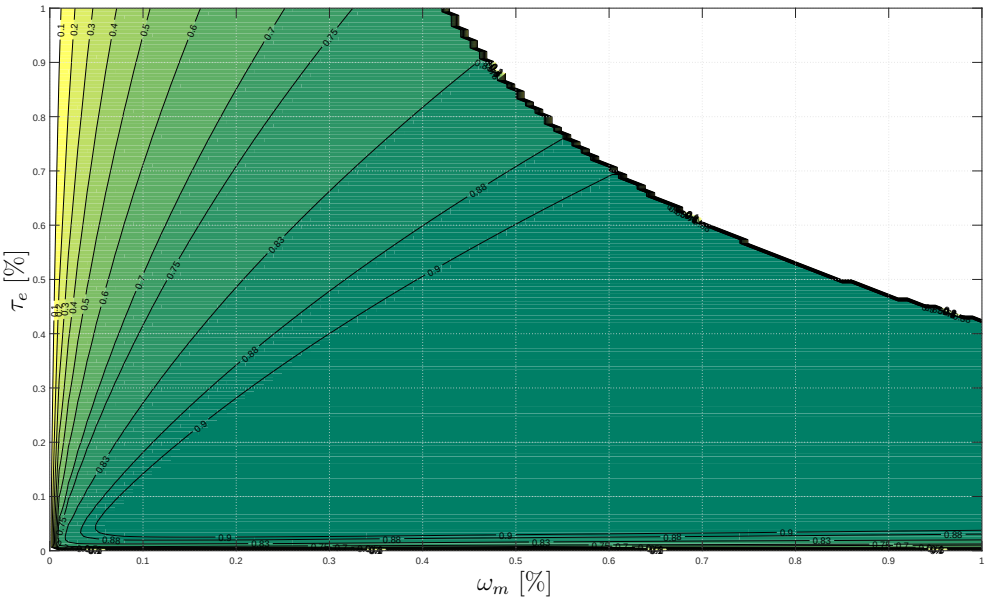

Figure 5.4: Estimated efficiency map of an industrial electric motor on plane (ω_m, τ_e).

$R_s = 2.8$ [mΩ], $R_{sq} = 3.52$ [$\mu V/A^2$]. Fig. 5.4 shows the obtained estimated efficiency maps of the considered industrial electric motor. Comparing Fig. 5.4 with Fig. 5.3 one can see a very good matching between the estimated and the actual efficiency maps, denoting the effectiveness of the presented procedure.

5.4 Conclusions

The dynamics of the Permanent Magnet Synchronous Motors has been analyzed and studied in detail in this chapter, and the state-space transformations allowing to turn the system into a rotating transformed reference frame have been presented. The torque vector analysis has been performed next, followed by the description of the simplified motor dynamics in the case of star-connected phases and with the description of the optimal way of generating the desired torque. Finally, the Permanent Magnet Synchronous Motors efficiency analysis has been performed, based on which the machine parameters estimation has been addressed starting from the system efficiency map.

Chapter 6

Modeling and Control of Hybrid Electric Vehicles

This chapter addresses the modeling, control and simulation of the four HEV categories analyzed in Sec. 2, reported in Fig. 2.1, Fig. 2.2, Fig.2.3 and Fig. 2.4. The control of an HEV architecture is an essential part both for series HEVs [43]-[45], parallel HEVs [46]-[51] and power-split HEVs [52]-[58], and essentially consists in providing an answer to the following question: "how is the energy management problem addressed?". The remainder of this chapter is organized as follows. Sec. 6.1 and the following subsections address the control of power-split HEV architectures. Next, the modeling, control and simulation of two power-split HEV architecture case studies are addressed. Sec. 6.2 and the following subsections address the control of series HEV architectures. Next, the modeling, control and simulation of a series HEV architecture case study are addressed. Finally, the control of parallel HEV architectures is addressed in Sec. 6.3 and the following subsections, together with the modeling, control and simulation of a parallel HEV architecture case study.

6.1 Control of a Power-Split HEV architecture

Let us consider the power-split architectures shown in Fig. 2.3 and Fig. 2.4. For the considered architectures, the energy storage device is a supercapacitor. The

power demand coming from the load is satisfied thanks to the joint work of the three power sources present within the considered architecture: the ICE, EM1 and EM2. Therefore, the answer to the above question can be provided by describing the control applied to each of the three different power sources and the interactions among them. In the following subsections, a new approach for the control of Power-Split HEVs is presented and described.

6.1.1 Control of the ICE

The presence of a power-split device such as a planetary gear set allows to decouple the ICE speed from the transmission speed, thus allowing to choose the most suitable ICE speed according to the ICE power demand. A speed control is therefore applied to the ICE, which can be implemented by a properly designed PID (Proportional-Integral-Derivative) regulator.

The objective of the control strategy is to make the ICE work in the most efficient operating regions for as long as possible, in order to minimize the specific fuel consumption. For this endothermic power source, namely the ICE, the most efficient operating regions correspond to those where the ICE specific consumption is minimized. A piece of information which is typically made available by the provider is the ICE *specific consumption map* reported on a two-dimensional operating plane (ω_{ice}, τ_{ice}), having the ICE speed ω_{ice} on the x axis and the ICE torque τ_{ice} on the y-axis, see the colored map in Fig. 6.1. The map is characterized by different colored areas, whose meaning is the following: the closer the operating point gets to the inner green area, the lower the ICE specific fuel consumption associated with that operating point. In order to minimize the consumption, it is useful to use a tool such as the *minimum specific consumption path*. The latter is defined on the operating plane (ω_{ice}, τ_{ice}) by following these steps:

1. Trace the constant power curves from zero to the maximum ICE power $P_{ice_{max}}$ on plane (ω_{ice}, τ_{ice}), see the blue lines in Fig. 6.1;

2. By using the ICE specific consumption map, determine the most suitable operating point on each constant power curve, that is the point minimizing

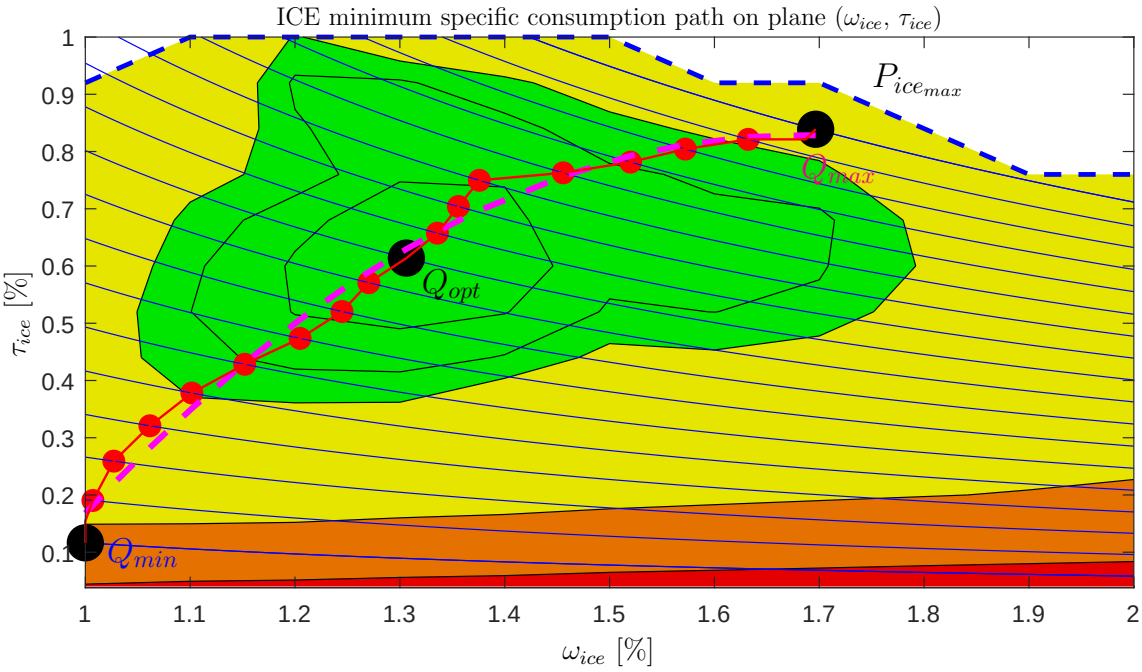

Figure 6.1: ICE minimum specific consumption path on the operating plane (ω_{ice}, τ_{ice}).

the ICE specific fuel consumption;

3. Approximate the obtained suitable operating points by using a proper smooth mathematical function, in order to ensure smooth transitions from an operating point to another when the power demand changes;

The different constant power curves have been traced with a certain precision $\Delta_{P_{ice}}$ which, in the ICE of Fig. 6.1, is $\Delta_{P_{ice}} = 10$ kW. For the employed ICE, the computed points on each constant power curve are marked by the red and black dots reported in Fig. 6.1. In order to derive a smoother characteristic, the path drawn in red in Fig. 6.1 has been approximated by using the following second order polynomial function:

$$\tau_{ice} = a_0 + \omega_{ice} a_1 + \omega_{ice}^2 a_2, \qquad \text{where} \qquad a_0 = -4.01 \cdot 10^3, \quad a_1 = 57.41, \quad a_2 = -0.16. \tag{6.1}$$

The smooth path (6.1) represents the chosen *minimum specific consumption path* on the ICE specific consumption map and is reported in magenta in Fig. 6.1.

Once the *minimum specific consumption path* is computed, the most suitable point on such path is determined as a non-linear function of the voltage V_c across

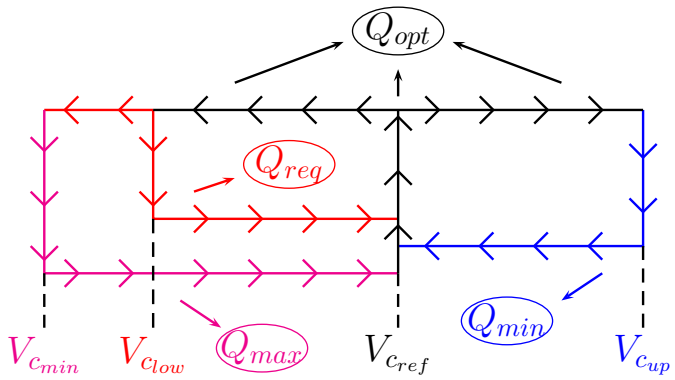

Figure 6.2: Hysteresis control of the ICE.

the supercapacitor, which gives an indication about the state of charge of the supercapacitor itself. The adopted non-linear function generating an hysteresis control for the ICE is graphically described in Fig. 6.2 and logically described as follows:

$$(\omega_{ice_{des}}, \tau_{ice_{des}}) = \begin{cases} Q_{opt} & \text{if} \quad V_{c_{low}} < V_c < V_{c_{up}} \\ Q_{req} & \text{if} \quad V_c \leq V_{c_{low}} \text{ until } V_c = V_{c_{ref}} \\ Q_{max} & \text{if} \quad V_c \leq V_{c_{min}} \text{ until } V_c = V_{c_{ref}} \\ Q_{min} & \text{if} \quad V_c \geq V_{c_{up}} \text{ until } V_c = V_{c_{ref}} \end{cases}, \tag{6.2}$$

where Q_{opt}, Q_{req}, Q_{max} and Q_{min} are defined as follows:

$$Q_{opt} = \left(\omega_{ice_{opt}}, \tau_{ice_{opt}}\right), \quad Q_{req} = \left(\omega_{ice_{req}}, \tau_{ice_{req}}\right),$$

$$Q_{max} = \left(\omega_{ice_{max}}, \tau_{ice_{max}}\right), \quad Q_{min} = \left(\omega_{ice_{min}}, \tau_{ice_{min}}\right).$$

The operating points Q_{opt}, Q_{max} and Q_{min} are shown in Fig. 6.1 and belong to the *minimum specific consumption path*. Voltages $V_{c_{min}}$, $V_{c_{low}}$ and $V_{c_{up}}$ are the minimum, the lower and the upper thresholds for the supercapacitor voltage V_c. These voltages satisfy the following inequalities: $V_{c_{min}} < V_{c_{low}} < V_{c_{up}}$. The reference voltage $V_{c_{ref}} = (V_{c_{up}} + V_{c_{low}})/2$ is the mean value between the two voltages $V_{c_{up}}$ and $V_{c_{low}}$. As a safety measure, whenever the condition $V_c \leq V_{c_{min}}$ is verified, the desired ICE operating point is set as follows $(\omega_{ice_{des}}, \tau_{ice_{des}}) = Q_{max}$, until $V_c = V_{c_{ref}}$ is once again verified,

in order to avoid excessive discharge of the supercapacitor because of possible peaks from the load external disturbance torque.

The ICE operating points Q_{opt}, Q_{max} and Q_{min} are chosen on the *minimum specific consumption path* as described in the following. The *optimal operating point* Q_{opt} is the closest to the minimum consumption point in the center of the inner green area of the specific consumption map shown in Fig. 6.1. The *minimum operating point* Q_{min} is the minimum point on the *minimum specific consumption path*: $\omega_{ice_{min}} = \min(\omega_{ice})$ and $\tau_{ice_{min}} = \min(\tau_{ice})$. The *maximum operating point* Q_{max} is the maximum point on the *minimum specific consumption path*: $\omega_{ice_{max}} = \max(\omega_{ice})$ and $\tau_{ice_{max}} = \max(\tau_{ice})$.

The use of a *required operating point* Q_{req}, instead of using the *maximum operating point* Q_{max}, when $V_c \leq V_{c_{low}}$, allows to keep the operating point as close to the green area in Fig. 6.1 as possible, unless it is strictly necessary to move it, that is if condition $V_c \leq V_{c_{min}}$ occurs. The philosophy behind this reasoning is indeed the one specified at the beginning of this section: the minimization of the ICE specific consumption whenever possible. The *required operating point* $Q_{req} = \left(\omega_{ice_{req}}, \tau_{ice_{req}}\right)$ when $V_c \leq V_{c_{low}}$ is computed as follows:

$$1)\ \Delta_P = \frac{\Delta_E}{\Delta_T} = \frac{\frac{1}{2} C_s V_{c_{ref}}^2 - \frac{1}{2} C_s V_{c_{low}}^2}{\Delta_T},\quad 2)\ P_{ice_{req}} = P_{ice_{opt}} + \Delta_P = \omega_{ice_{opt}} \tau_{ice_{opt}} + \Delta_P,$$

$$3)\ \omega_{ice_{req}} = k_1 P_{ice_{req}} + k_2 = 0.43 \cdot 10^{-3} P_{ice_{req}} + 93.16,\quad 4)\ \tau_{ice_{req}} = a_0 + \omega_{ice_{req}} a_1 + \omega_{ice_{req}}^2 a_2,$$

where Δ_P is the ICE required additional power, $\Delta_T = t_{low} - t_{ref}$ is the time interval between the instant t_{low} when $V_c = V_{c_{low}}$ and the instant t_{ref} when $V_c = V_{c_{ref}}$, k_1 and k_2 describe a linear dependence between $\omega_{ice_{req}}$ and $P_{ice_{req}}$, and the polynomial used in step 4) is the one defined in (6.1). The increasing of the ICE power by the required Δ_P has two consequences:

1) The reduction of the power that EM1 provides to the transmission, thus the reduction of the power absorbed from the supercapacitor;

2) The increase of the power flowing through EM2 and entering the supercapacitor.

Both consequences contribute to the recharge of the supercapacitor itself. In addition, note that the relation reported in step 3), where the *required ICE speed* $\omega_{ice_{req}}$ is chosen as a linear dependence of the ICE demanded power $P_{ice_{req}}$, well highlights the *speed control* applied to the ICE.

An important observation has to be made: the dimensioning of the supercapacitor affects the frequency of variation of the ICE operating point. This can be evinced by looking at the relation $\Delta_P = \Delta_E/\Delta_T$ appearing in the first step of the computation of the ICE required operating point when $V_c \leq V_{c_{low}}$ reported above. The quantity Δ_E, representing the difference between the energy stored within the supercapacitor when $V_c = V_{c_{ref}}$ and the energy stored within the supercapacitor when $V_c = V_{c_{low}}$, is directly proportional to the capacitance value C_s. By assuming that the difference between the power exiting and entering the supercapacitor, $P_{out} - P_{in}$, is positive and constant over a certain time interval, the supercapacitor voltage V_c starts decreasing with a constant slope, and the time it takes for V_c to decrease by a certain Δ_{V_c} is directly proportional to the capacitance C_s. This means that the capacitance value C_s has to be chosen properly, according to these considerations, as a function of the average power absorbed by the load for a given application, in order not to cause excessive variations of the ICE operating point, thus improving the end user driving/working experience.

6.1.2 Control of Electric Machine EM2

A torque control is applied to EM2. The goal of this control is to ensure that the ICE torque is always equal to the desired torque $\tau_{ice_{des}}$ provided by the hysteresis control described in (6.2) as a function of the desired ICE speed $\omega_{ice_{des}}$, in order to confine the ICE operating point on the *minimum specific consumption path*. Therefore, the desired torque $\tau_{m2_{des}}$ for the Electric Machine EM2 is chosen as follows:

$$\tau_{EM2_{des}} = f_{EM2}(\Delta_{\tau_{ice}}), \tag{6.3}$$

where $f_{EM2}(\Delta_{\tau_{ice}})$ is a proper function of the ICE torque error. The desired torque $\tau_{EM2_{des}}$ is then demanded to EM2 by means of an inverter, which has been inserted within subsystem "EM2 Drive" in Fig. 2.3 and Fig. 2.4.

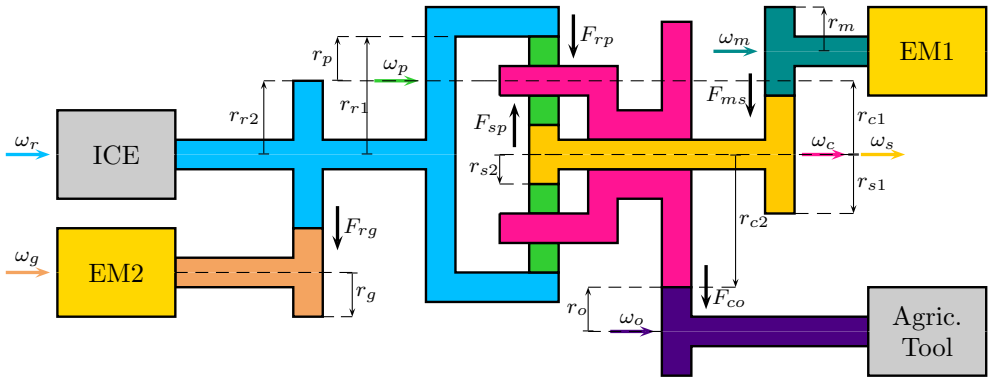

Figure 6.3: Structure of the considered power-split hybrid propulsion system.

6.1.3 Control of Electric Machine EM1

The electric machine EM1 is the one responsible for driving the transmission by providing the fraction of transmission power which is not given by the ICE. A speed control is therefore applied to EM1, in order to make it follow the desired speed profile $\omega_{EM1_{des}}$, which will be a function of the transmission speed ω_t, the ICE speed ω_{ICE} and the EM2 speed ω_{EM2}.

The torque demanded to EM1 will therefore be equal to

$$\tau_{EM1_{des}} = f_{EM1}(\Delta_{\omega_{EM1}}), \tag{6.4}$$

where $f_{EM1}(\Delta_{\omega_{EM1}})$ is a proper function of the EM1 speed error.

The desired torque $\tau_{EM1_{des}}$ is then demanded to EM1 by means of an inverter, which has been inserted within subsystem "EM1 Drive" in Fig. 2.3 and Fig. 2.4.

6.1.4 Output power-split case study

Let us consider the architecture which is shown in Fig. 6.3, which is power split of the output type, see Fig. 2.3.

Modeling

In this architecture, the ICE is connected to the ring planetary gear set port, the electric machine EM2 is still connected to the ring planetary gear set port through

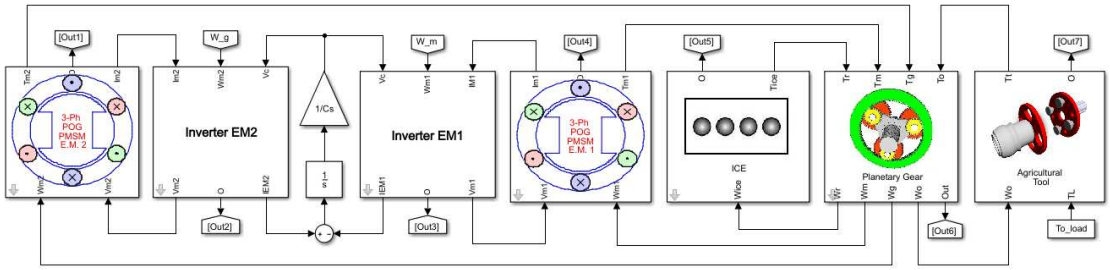

Figure 6.4: Simulink implementation of the power-split hybrid propulsion system shown in Fig. 6.3.

an additional ratio, the electric machine EM1 is connected to the sun planetary gear set port through an additional ratio. In this case, the considered architecture was not intended to drive a transmission system, but was intended to generate a power port to drive an agricultural tool. The agricultural tool is connected to the carrier planetary gear set port through an additional ratio. The corresponding Simulink block scheme is shown in Fig. 6.4.

The elements composing the hybrid architecture in Fig. 6.4 are, from left to right, the electric machine denoted by EM2, the inverter controlling this latter element (i.e. the block "EM2 Drive" in Fig. 2.3), the energy storage device (i.e. the supercapacitor C_s), the inverter controlling the electric machine EM1 (i.e. the block "EM1 Drive" in Fig. 2.3), the electric machine EM1, the ICE, the planetary gear set acting as a power-split device and, finally, the agricultural tool representing the load of the system.

The electric machines used in this architecture are PMSMs and have been modeled by using the POG technique, see Chap.5. Two industrial PMSMs have been used for this project; the actual parameters values used in the machines models have been estimated from the machines datasheet by applying an estimation procedure based on a least square algorithm, as described in Sec. 5.3. The inverters employed to control the two PMSMs apply a vectorial control based on the POG state space equations, see [37]. The vectorial control aims at minimizing the power dissipated because of the direct current component, see Sec. 5.2.1. The dynamic model of the supercapacitor has been obtained by using the POG modeling technique. The internal combustion engine has been modeled within the subsystem named "ICE" in

Fig. 6.4. The shaft of the agricultural tool has been modeled as an inertia equipped with a linear friction coefficient accounting for the friction losses; an external torque profile can then be applied in order to simulate the presence of a disturbance coming from a real case scenario on the field. The planetary gear set is the one modeled in Sec. 3.6. The rigid model (3.21)-(3.22), obtained applying (3.58), is the one used in the next subsection for the simulation of the presented hybrid propulsion system.

Simulation

The architecture shown in Fig. 6.4 has been tested in simulation referring to an industrial case study: the objective of the simulation is to keep the angular speed ω_o of the load shaft equal to a constant value $\omega_{o_{des}}$ in presence of an external disturbance, namely a resistive torque $\tau_{o_{load}}$ applied to the load. In this case, Eq. (6.3) and Eq. (6.4) are, respectively:

$$\tau_{EM2_{des}} = K_{EM2} \underbrace{\Delta_{\tau_{ice}}}_{\tau_{ice_{des}} - \tau_{ice}},$$

$$\tau_{EM1_{des}} = \frac{K_{EM1_P} K_{EM1_I} K_{EM1_D} s^2 + K_{EM1_P} K_{EM1_I} s + K_{EM1_P}}{K_{EM1_I} s} \underbrace{\Delta_{\omega_{EM1}}}_{\omega_{EM1_{des}} - \omega_{EM1}}.$$

The desired electric machine EM1 speed $\omega_{EM1_{des}}$ is related to the desired load speed $\omega_{o_{des}}$ and to the desired ICE speed $\omega_{ice_{des}}$ as follows:

$$\omega_{EM1_{des}} = -\frac{r_{s1}}{r_m} \left[\frac{-\frac{2\, r_{c1}\, r_o}{r_{c2}}\, \omega_{o_{des}} - r_{r1}\, \omega_{ice_{des}}}{r_{s2}} \right],$$

where the different radii are defined in Fig. 6.3. The obtained simulation results are shown in Fig. 6.5, Fig. 6.6, Fig. 6.7, Fig. 6.8 and Fig. 6.9. The plots reported in the figures have been normalized for trade secret reasons, however the reader can still appreciate the results from the characteristics behavior.

The upper subplot in Fig. 6.5 shows the external torque disturbance $\tau_{o_{load}}$ applied to the load (blue dashed curve) and the torque τ_t made available by the joint contribution of the ICE and EM1 (red curve). The lower subplot in Fig. 6.5 shows the desired load speed $\omega_{o_{des}}$ (blue dashed line) and the actual load speed ω_o (red

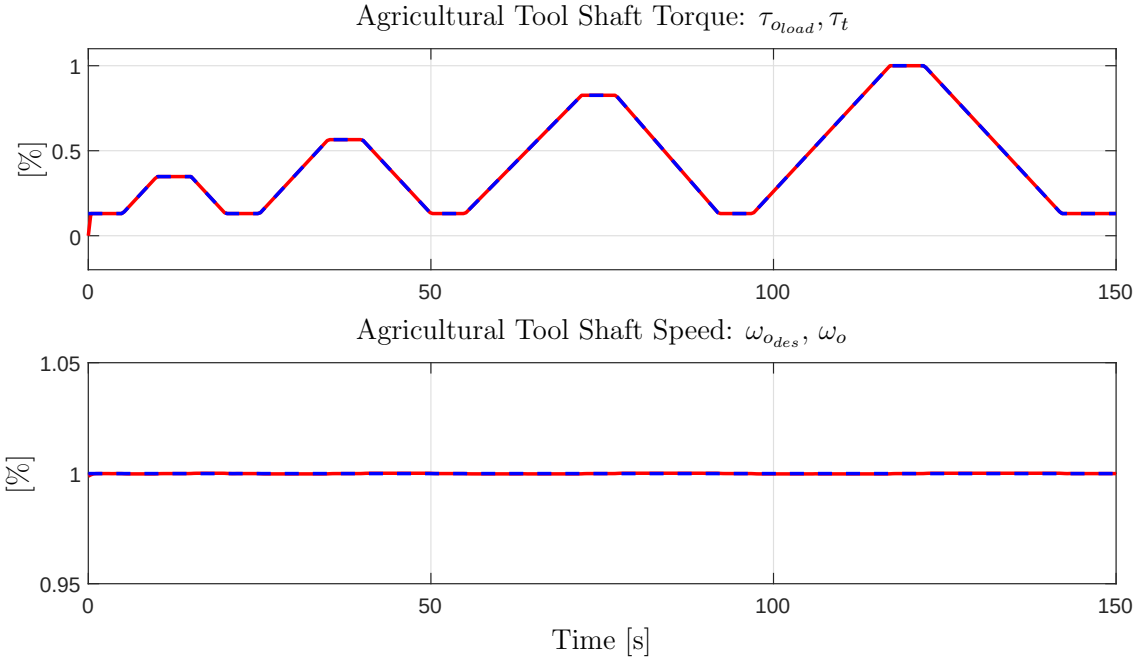

Figure 6.5: Resistive and motive agricultural tool shaft torque; Desired and actual agricultural tool shaft speed.

line). The good tracking of the desired signals shows the effectiveness of the speed control applied to EM1.

The upper subplot in Fig. 6.6 shows: the torque τ_{ice_D} demanded by the ICE speed control (blue dashed characteristic), the ICE desired torque $\tau_{ice_{des}}$ (green dashed line), and the ICE actual torque τ_{ice} (red characteristic). The green and red characteristics are very close, denoting the effectiveness of the torque control applied to EM2. The lower subplot in Fig. 6.6 shows the ICE desired speed $\omega_{ice_{des}}$ (blue dashed curve) and the ICE actual speed ω_{ice} (red curve). The good tracking of the desired signal shows the effectiveness of the speed control applied to the ICE.

The ICE operating points on the ICE consumption map are shown in red in Fig. 6.7. This figure clearly shows that the ICE operating points are always very close to the minimum specific consumption path (dashed magenta curve), denoting the effectiveness of the proposed control strategy. In particular, in this simulation there are three different zones along the *minimum specific consumption path* where the ICE operating points are grouped: 1) the minimum power zone corresponding to *minimum operating point* Q_{min} (zone delimited by the blue ellipse in Fig. 6.7, 2) the

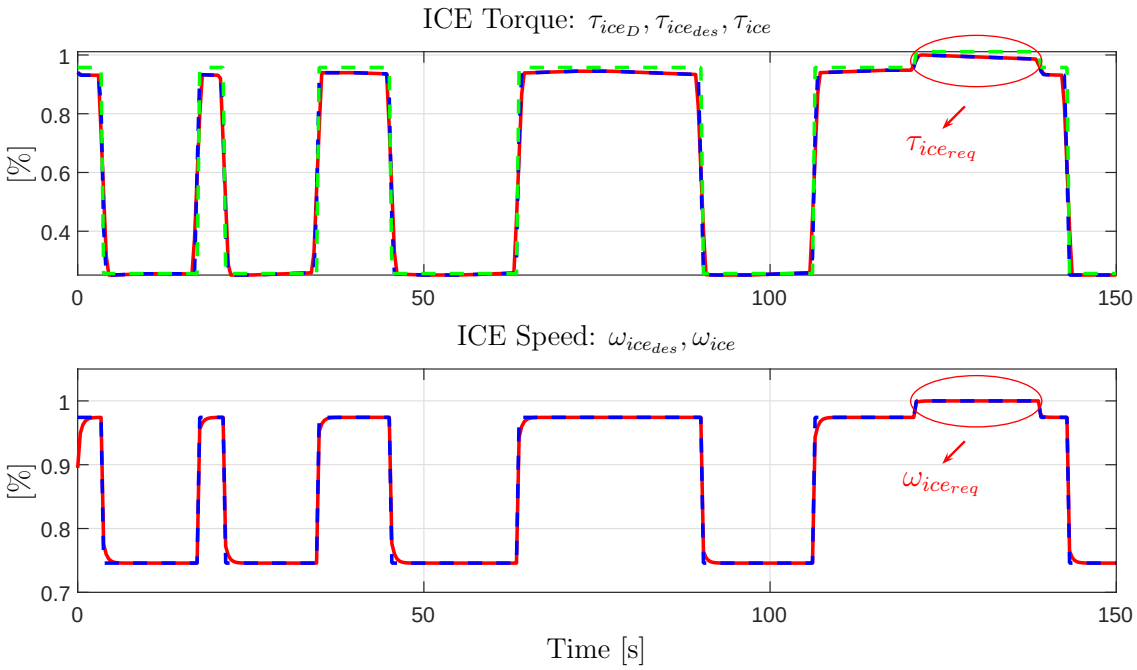

Figure 6.6: Demanded, desired and actual ICE torque; Desired and actual ICE speed.

lowest consumption zone corresponding to the *optimal operating point* Q_{opt} (zone delimited by the black ellipse in Fig. 6.7, and 3) the zone of the path corresponding to the *required operating point* Q_{req} in correspondence of a time interval where V_c needs to be increased from $V_c \leq V_{c_{low}}$ to $V_c = V_{c_{ref}}$ (zone delimited by the red circle in Fig. 6.7, very close to the middle of the inner green area). The time intervals in which the ICE operates in the required operating point Q_{req} are also highlighted in Fig. 6.6 by two red ellipses: the one in the upper subplot highlights when $\tau_{ice} = \tau_{ice_{req}}$, the one in the lower subplot highlights when $\omega_{ice} = \omega_{ice_{req}}$.

The blue curve in the upper subplot of Fig. 6.8 shows the supercapacitor voltage V_c and the thresholds used in the hysteresis control law (6.2): $V_{c_{low}}$ (lower magenta dashed line), $V_{c_{up}}$ (upper magenta dashed line), $V_{c_{min}}$ (lowest red dashed line) and $V_{c_{ref}}$ (green dashed line). The red dot present in this subplot highlights the time instant when voltage V_c becomes lower than threshold $V_{c_{low}}$, in which the procedure for computing the ICE required operating point Q_{req} on the *minimum specific consumption path* described in Sec. 6.1.1 is activated. Then, the speed control applied

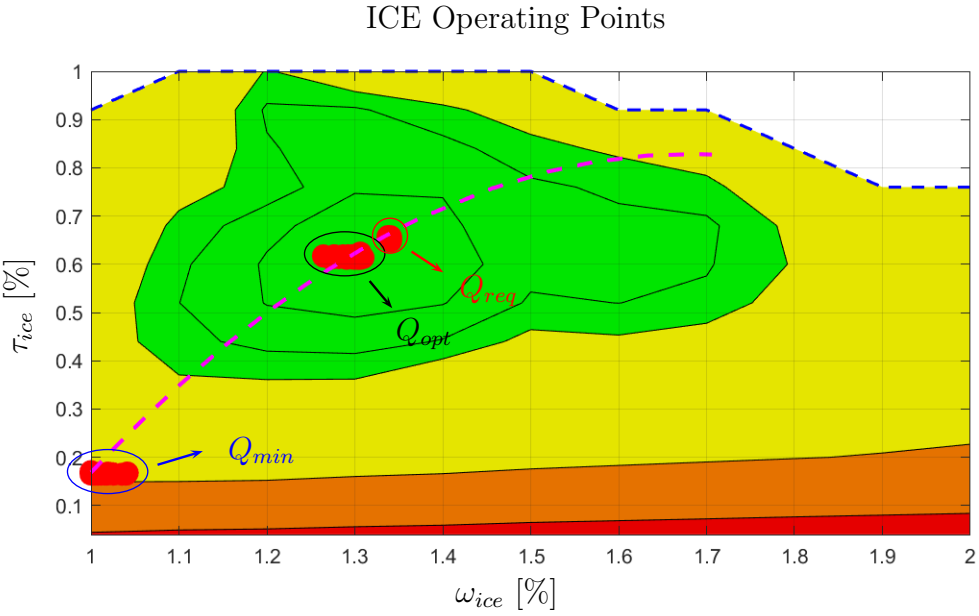

Figure 6.7: ICE operating points and ICE minimum specific consumption path on the specific consumption map.

to the ICE and the torque control applied to EM2 act in order to take the ICE to the required operating point: $(\omega_{ice_{req}}, \tau_{ice_{req}}) = Q_{req}$ as it can be seen from Fig. 6.6 and Fig. 6.7.

The lower subplot of Fig. 6.8 shows the current I_{EM2} flowing through EM2 and entering the supercapacitor (blue curve), and the current I_{EM1} exiting the supercapacitor and flowing through EM1 (red curve).

The desired and actual torques of EM1 and EM2, $\tau_{EM1_{des}}$, $\tau_{EM2_{des}}$, τ_{EM1} and τ_{EM2}, are shown in Fig. 6.9 in blue dashed line and in red line, respectively. The desired torque $\tau_{EM2_{des}}$ has been designed to minimize the ICE torque error $\Delta_{\tau_{ice}}$, and the desired torque $\tau_{EM1_{des}}$ has been designed to compensate for the external disturbance $\tau_{o_{load}}$ of the load.

6.1.5 Input power-split case study

Let us consider the architecture which is shown in Fig. 6.10, which is structured in Fig. 6.11. This architecture is power split of the input type, see Fig. 2.4.

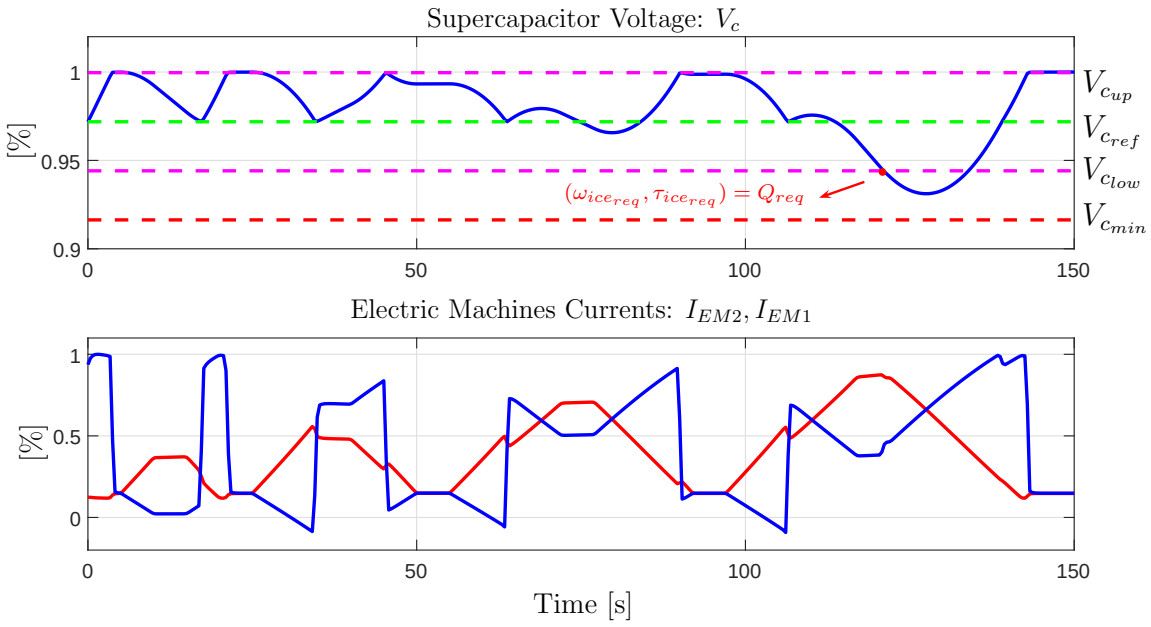

Figure 6.8: Voltage across the supercapacitor; Currents from the inverters.

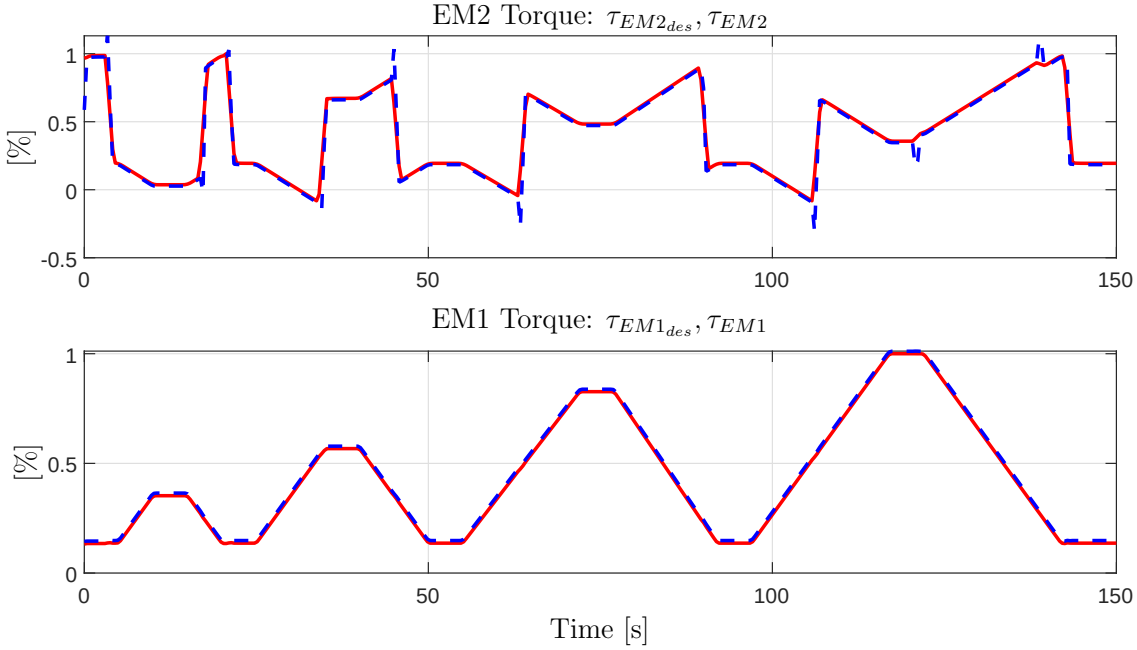

Figure 6.9: Desired and actual EM2 torques; Desired and actual EM1 torques.

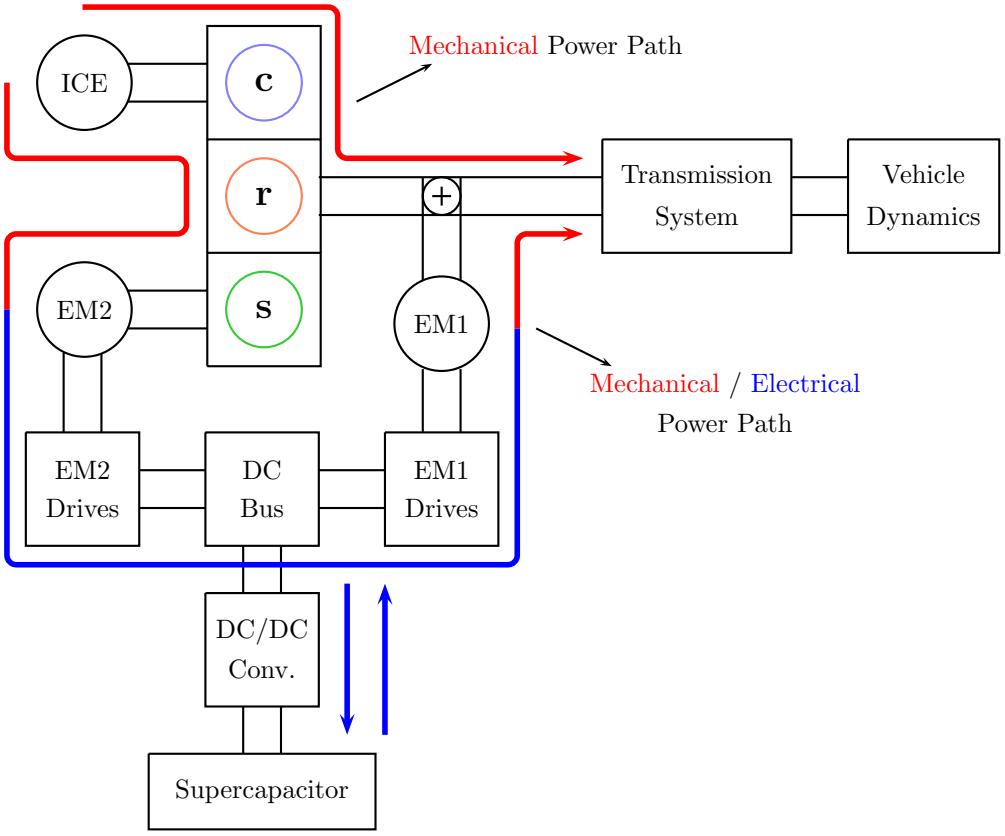

Figure 6.10: Schematic view of the considered power-split HEWL architecture.

Modeling

In this architecture, the ICE is connected to the carrier planetary gear set port, the electric machine EM2 is connected to the sun planetary gear set port, and the transmission system is connected to the ring planetary gear set port. The electric machine EM1 is also connected to the ring planetary gear set port through an additional ratio, in order to help drive the transmission system of the considered vehicle which, in this case, is a wheel loader. The considered vehicle is therefore a Hybrid Electric Wheel Loader (HEWL). The corresponding Simulink block scheme is shown in Fig. 6.12.

Moving from left to right, the physical elements present within the subsystems of Fig. 6.12 are: the electric machine EM2, the drives of EM2 (i.e. the block "EM2 Drive" in Fig. 2.4), the supercapacitor acting as energy storage device, the DC/DC converter, the DC bus, the drives of EM1 (i.e. the block "EM1 Drive" in Fig. 2.4),

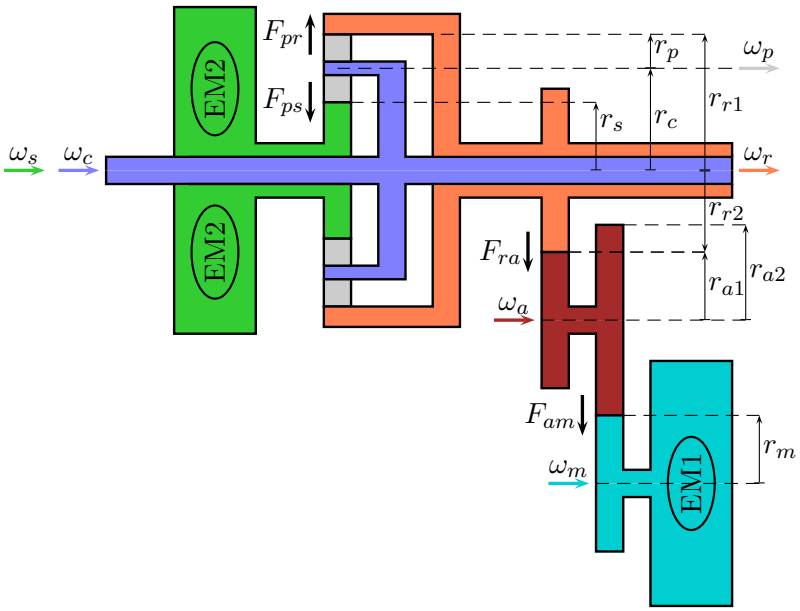

Figure 6.11: Structure of the considered power-split HEWL architecture.

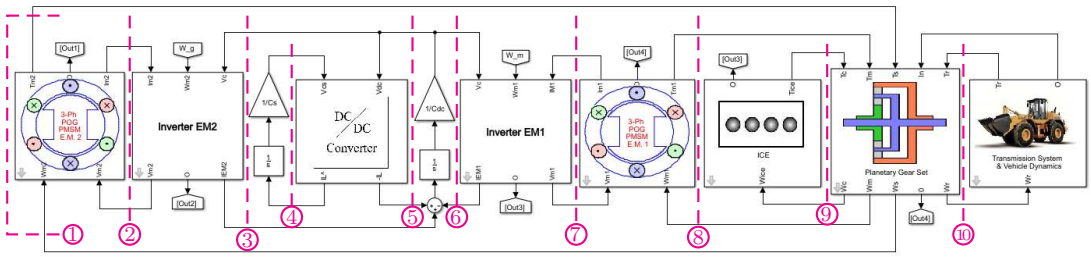

Figure 6.12: Simulink implementation of the power-split HEWL shown in Fig. 6.11.

the electric machine EM1, the ICE, the planetary gear set, the transmission system and the vehicle dynamics. The magenta dashed lines in Fig. 6.12 highlight the *power sections* of the system, see Chap. 1. The considered electric machines EM1 and EM2 are PMSMs and have been modeled using the POG technique, see Chap. 5. The machine model parameters have been estimated as in Sec. 5.3. The drives of EM1 and EM2 have been implemented using a vectorial control [37]. The vectorial control aims at minimizing the power dissipated because of the direct current component, see Sec. 5.2.1. The supercapacitor and the DC bus have been modeled as two capacitors C_s and C_{dc}, characterized by the following first-order differential equations:

$$C_s \dot{V}_s = \hat{I}_L, \qquad C_{dc} \dot{V}_{dc} = I_{EM2} - I_{EM1} + (-I_L), \tag{6.5}$$

where V_s and V_{dc} are the voltages across C_s and C_{dc}, $\hat{I}_L$ is the load current I_{EM2}–I_{EM1} up-converted, I_{EM2} and I_{EM1} are the EM2 and EM1 currents after AC/DC conversion and $-I_L = -(I_{EM2} - I_{EM1})$. The DC/DC converter is supposed to be lossless and is modeled as a logical Matlab function that down-converts voltage V_{dc} to voltage $V_s < V_{dc}$ and up-converts the load current $I_{EM2} - I_{EM1}$ to the load current $\hat{I}_L > I_{EM2} - I_{EM1}$. The planetary gear set is the one modeled in Sec. 3.7. The rigid model (3.21)-(3.22), obtained applying (3.58), is the one used in the next subsection for the simulation of the presented hybrid propulsion system. The Simulink implementation of the vehicle transmission system is reported inside the subsystem called "Transmission System & Vehicle Dynamics" in Fig. 6.12. The structure of the considered transmission system is schematized in Fig. 6.13, whereas the corresponding POG model [59] is reported in Fig. 6.14. Indeed, the input section in the POG

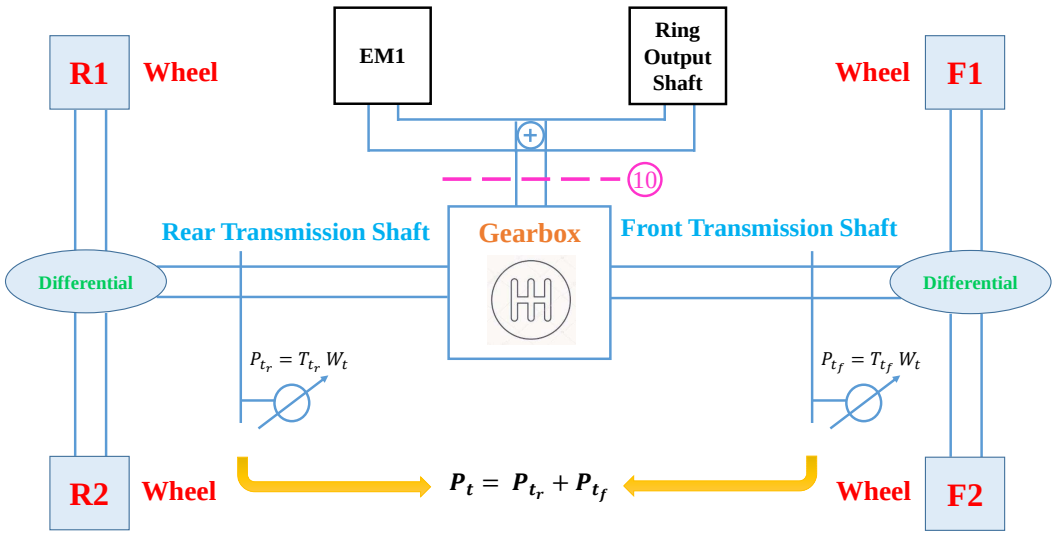

Figure 6.13: Structure of the transmission system of the considered power-split HEWL.

model of Fig. 6.14, denoted as section 10, coincides with the corresponding sections in Fig. 6.12 and Fig. 6.13. The two power variables characterizing section 10 are the ring load torque τ_r and the ring speed ω_r. The part highlighted in orange in Fig. 6.13 and Fig. 6.14 is the Gearbox, where the time-variant connection block characterized by parameters $R_g \in \{1/r_{1b};\ 1/r_{2b};\ 1/r_{3b}; 1/r_{1f};\ 1/r_{2f};\ 1/r_{3f};\ 1/r_{4f}\}$ models the

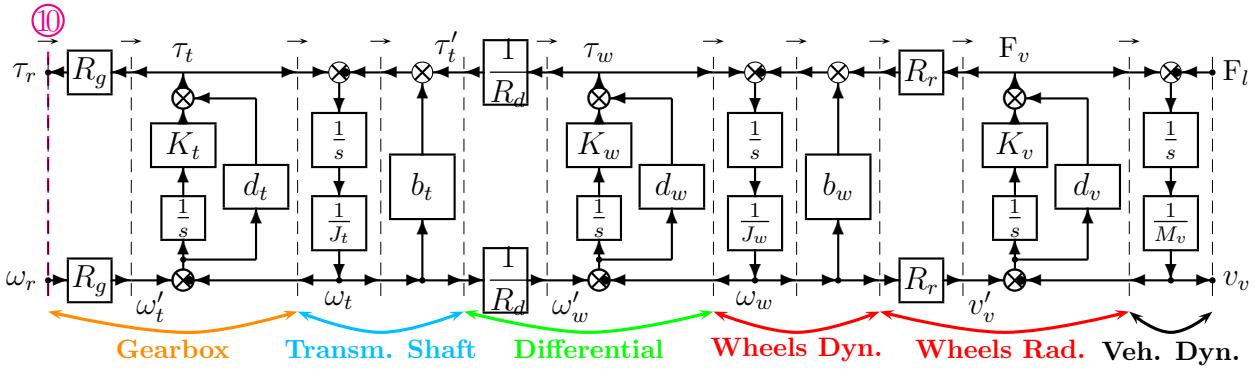

Figure 6.14: POG block scheme of the transmission system of the considered power-split HEWL.

gearshifting mechanism, being r_{1b}, r_{2b}, r_{3b} the first, second and third backward gear ratios and r_{1f}, r_{2f}, r_{3f}, r_{4f} the first, second, third and fourth forward gear ratios. The torsional spring characterized by stiffness coefficient K_t accounts for the gearbox elasticity, whereas the dissipative element d_t accounts for the energy loss occurring during the transient. The Transmission Shaft part highlighted in lightblue accounts for the rear and front transmission shafts: J_t is the moment of inertia and b_t is a linear friction coefficient. The part highlighted in green is the Differential; its contribution is accounted for by parameter R_d, together with a rotational spring K_w accounting for the intrinsic elasticity and its friction coefficient d_w. The two parts highlighted in red account for the Wheels Dynamics, where J_w is the equivalent moment of inertia of the four wheels and b_w is a linear friction coefficient, and for the Wheels Radius R_r, with the rotational spring K_v and the friction coefficient d_v accounting for the intrinsic wheels elasticity and for the transient losses. The final part describes the Vehicle Dynamics, where parameter M_v is the vehicle mass. The external force F_l accounts for the load force that the vehicle is subject to during its operation.

Simulation

The architecture of the HEWL reported in Fig. 6.12 has been simulated in Matlab/Simulink with reference to a typical driving cycle for this type of vehicle. The simulation has been performed using the architecture parameters shown in Tab. 6.1 and starting from zero initial conditions, expect for the initial carrier and ICE speed

PMSMs	
p	4
L_{se}	32.68 [μH]
J_M	0.22 [kg m^2]
R_s	0.95 [m Ω]
K_q	0.65 [Nm/A]
b_M	$1 \cdot 10^{-3}$ [(Nm s)/rad]
R_{sq}	2.64 [nV/A^2]
b_c	0.83 [μNm]
b_{Mq}	$3.4 \cdot 10^{-9}$ [Nm s^2/rad^2]

Planetary Gear Set	
J_c	0.047 [kg m^2]
J_p	0.63·10^{-3} [kg m^2]
J_s	0.67·10^{-3} [kg m^2]+J_M
J_r	0.06 [kg m^2]
J_a	8.6·10^{-3} [kg m^2]
J_m	0.45·10^{-3} [kg m^2]+J_M
$b_c \ldots b_m$	1.4·10^{-3} [(Nm s)/rad]
r_c	7.5 [cm]
r_p	3.4 [cm]
r_s	4.2 [cm]
r_{r1}	11 [cm]
r_{r2}	4.6 [cm]
r_{a1}	2.64 [cm]
r_{a2}	4.6 [cm]
r_m	2.4 [cm]

ICE Control	
$K_{P_{ice}}$	220
$K_{I_{ice}}$	1.87

PMSM: Vectorial Control	
τ_s	3 [ms]

Transmission and Vehicle	
r_{1b}	3.251
r_{2b}	1.822
r_{3b}	0.945
r_{1f}	3.145
r_{2f}	1.984
r_{3f}	1.272
r_{4f}	0.936
K_t	4.01·10^7 [Nm/rad]
d_t	305.6 [Nm s/rad]
J_t	1.5·10^{-3} [kg m^2]
b_t	2.4 [(Nm s)/rad]
R_d	21.22
K_w	$= K_t$
d_w	$= d_t$
J_w	4.25·10^3 [kg m^2]
b_w	24 [(Nm s)/rad]
R_r	0.58 [m]
K_v	6.2·10^6 [N/m]
d_v	284.5 · 10^3 [N s/m]
M_v	14.4·10^3 $\rightarrow$ 18.4·10^3 [kg]

EM2 Control	
K_{EM2_P}	35
K_{EM2_I}	0.17

EM1 Control	
K_{EM1_P}	80.75
K_{EM1_I}	0.49

Supercapacitor	
C_s	50 [F]

DC Link	
C_{dc}	10 [mF]

Table 6.1: Parameters of the considered architecture.

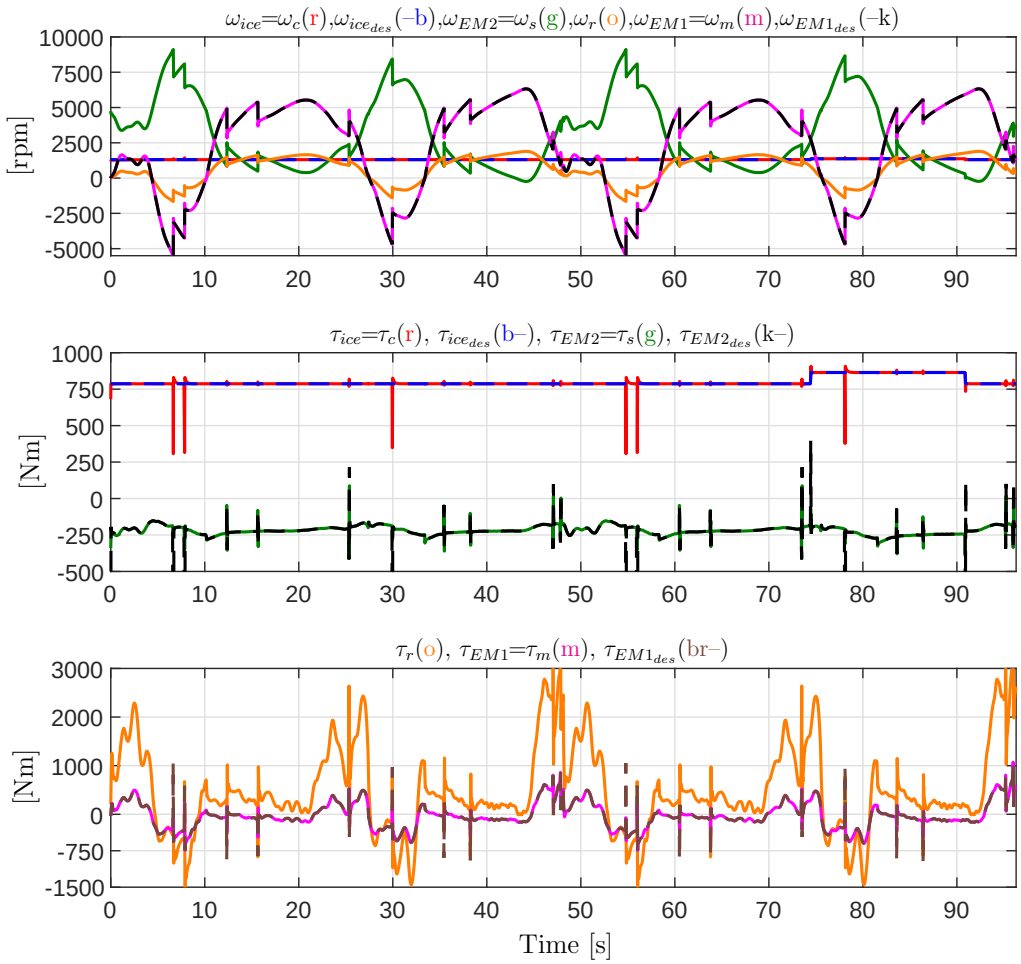

Figure 6.15: Planetary gear set angular velocities and torques.

$\omega_{ice_0} = \omega_{ice_{opt}} = 1306\,[\text{rpm}]$ and the initial supercapacitor and DC bus voltages $V_{s_0} = 700\,[\text{V}]$ and $V_{dc_0} = 750\,[\text{V}]$. In this case, Eq. 6.3 and Eq. 6.4 are, respectively:

$$\tau_{EM2_{des}} = \left(\frac{K_{EM2_P} + K_{EM2_P} K_{EM2_I} s}{K_{EM2_I} s} \right) \underbrace{\Delta_{\tau_{ice}}}_{\tau_{ice} - \tau_{ice_{des}}},$$

$$\tau_{EM1_{des}} = \left(\frac{K_{EM1_P} + K_{EM1_P} K_{EM1_I} s}{K_{EM1_I} s} \right) \underbrace{\Delta_{\omega_{EM1}}}_{w_{EM1_{des}} - w_{EM1}}.$$

The desired electric machine EM1 speed $\omega_{EM1_{des}}$ is related to the desired trans-

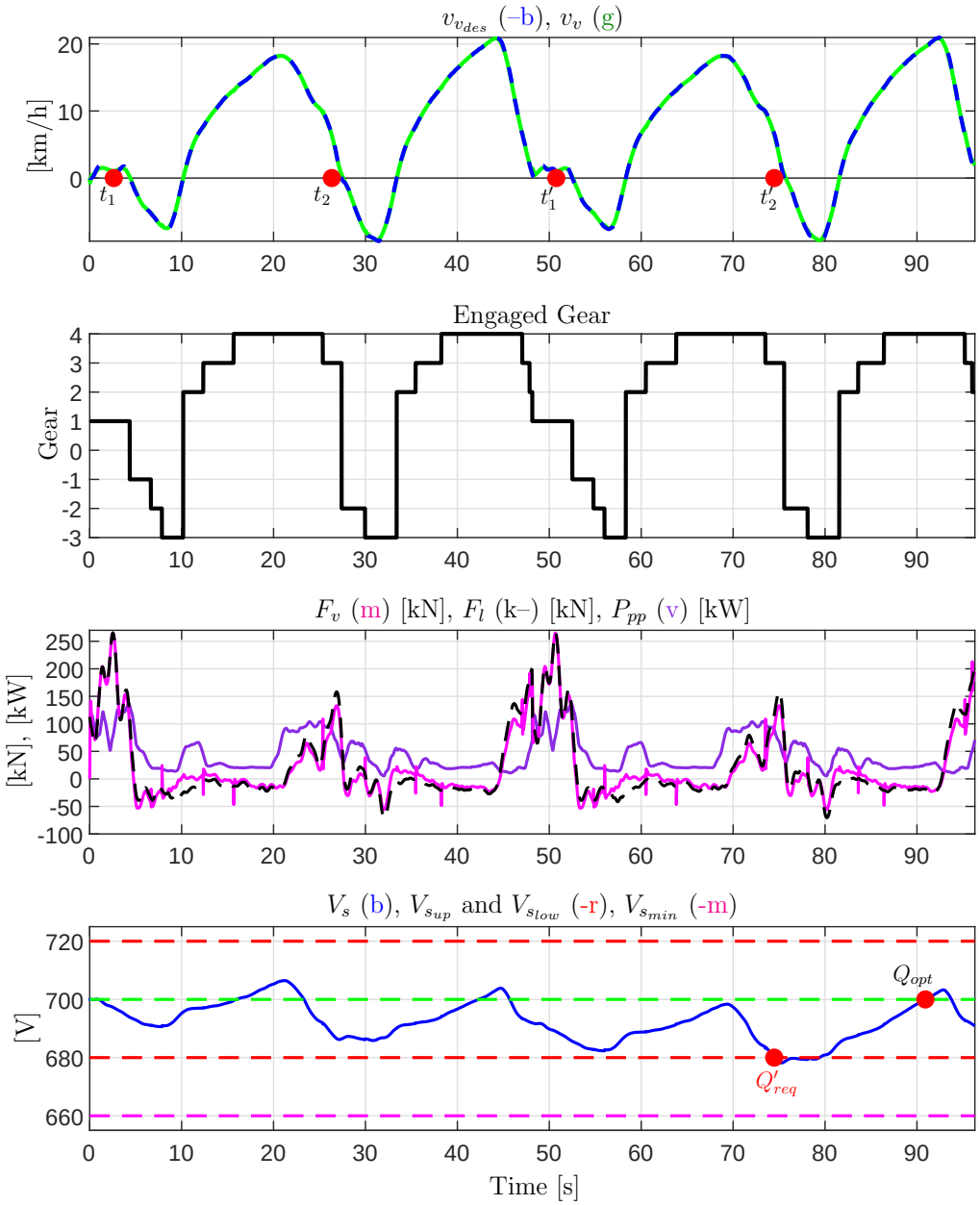

Figure 6.16: Vehicle Speed; Engaged Gear; Wheels Force and Pumps Power; Supercapacitor Voltage.

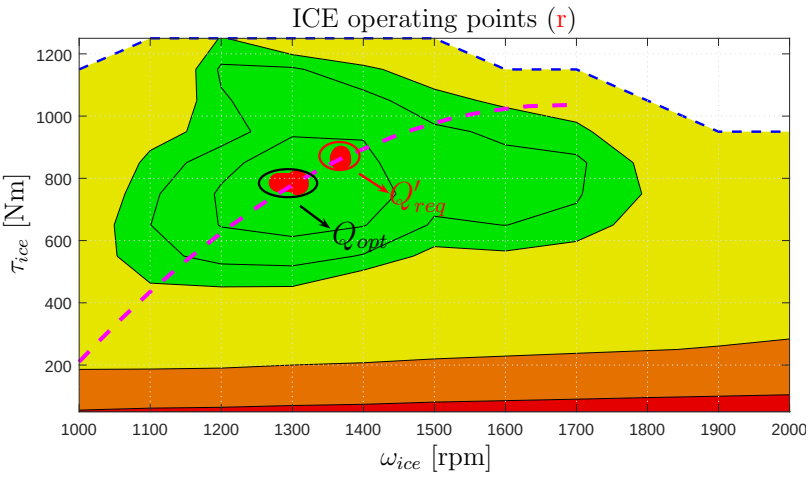

Figure 6.17: ICE operating points on ICE specific consumption map.

mission speed $\omega_{r_{des}}$ and to the desired ICE speed $\omega_{ice_{des}}$ as follows:

$$\omega_{EM1_{des}} = \omega_{r_{des}} \left(\frac{r_{a2}\, r_{r2}}{r_{a1}\, r_m} \right),$$

where the different radii are defined in Fig. 6.11. The desired vehicle speed profile is shown in blue dashed line in the first subplot of Fig. 6.16. The load force profile that the vehicle experiences during its operation, applied as a signal F_l in the transmission system POG block scheme in Fig. 6.14, is shown in black dashed line in the third subplot of Fig. 6.16. During the considered driving cycle, the Wheel Loader starts digging to load the bucket before time instant t_1 and starts unloading the bucket at time instant t_2. The same operation is repeated at time instants t'_1 and t'_2. The time instants t_1, t_2, t'_1 and t'_2 are highlighted in the first subplot of Fig. 6.16 by four red spots. The change of mass following the Wheel Loader loading and unloading the bucket at the considered time instants is accounted for by making the vehicle mass M_v change from $14.4 \cdot 10^3$ [kg] (empty bucked) to $18.4 \cdot 10^3$ [kg] (full bucked) when $t \in (t_1,\, t_2) \bigvee t \in (t'_1,\, t'_2)$ and viceversa, as reported in Tab. 6.1. The hydraulic load that the Wheel Loader is subject to during the considered driving cycle, which includes the power needed to power the mechanical arm loading the bucket, is given by the power profile P_{pp} shown in violet in the third subplot of Fig. 6.16. The power profile P_{pp} is divided by the DC bus voltage V_{dc} in order to originate an "equivalent load current" to be added to I_{EM1} in (6.5), thus accounting for the additional power

from the supercapacitor requested by the hydraulic load. Note that all the main load contributions that one might encounter on the field have been accounted for in the simulation: the external load force profile F_l experienced by the vehicle, the vehicle mass change caused by the Wheel Loader loading and unloading the bucket, and the "equivalent load current" accounting for the additional power required to power the mechanical arm moving the bucket. The simulation results are shown in Fig. 6.15, Fig. 6.16 and Fig. 6.17. The first subplot of Fig. 6.15 shows the angular velocities of the planetary gear set inertial elements. From the good matching between the desired and actual ICE and EM1 speeds $\omega_{ice_{des}}$, $\omega_{ice} = \omega_c$, $\omega_{EM1_{des}}$, $\omega_{EM1} = \omega_m$, it is possible to notice the effectiveness of the speed control applied to the two elements ICE and EM1. The second and third subplots of Fig. 6.15 show the input torques of the planetary gear set inertial elements. The good matching between the desired and actual EM1 torques $\tau_{EM1_{des}}$, $\tau_{EM1} = \tau_m$ highlights the effectiveness of the speed and vectorial control applied to EM1, whereas the good matching between the desired and actual ICE and EM2 torques $\tau_{ice_{des}}$, $\tau_{ice} = \tau_c$, $\tau_{EM2_{des}}$, $\tau_{EM2} = \tau_s$ highlights the effectiveness of the torque and vectorial control applied to EM2. The subplots of Fig. 6.16 show, from top to bottom, the desired and actual vehicle speeds, the engaged gear, the vehicle motive and load forces, the pumps power profile and the supercapacitor voltage. The DC bus voltage V_{dc} is not shown since it remains constant as required, whereas the pumps load current and the EM1 and EM2 load/generated currents are eventually absorbed from the supercapacitor. From the first subplot, it is indeed possible to see that the Wheel Loader follows the desired speed profile. From the third subplot, one can notice a peak in the load force F_l before time instants t_1 and t_1', which are due to the Wheel Loader digging to load the bucket. Fig. 6.17 shows the ICE operating points at steady-state on the 2D operating plane (ω_{ice}, τ_{ice}) showing the ICE specific fuel consumption map. The fourth subplot of Fig. 6.16 shows that the behavior of the supercapacitor voltage V_s during the simulation causes two changes of the ICE operating point according to (6.2) (note that, in this case, the supercapacitor voltage is denoted by V_s instead of V_c): Q'_{req} is a required operating points on the ICE *minimum specific consumption path* called by the condition $V_s < V_{s_{low}}$ when occurring, whereas Q_{opt}

is indeed the optimal operating point in the middle of the least consumption area in Fig. 6.17. The ICE operating point is equal to Q_{opt} at the beginning of the simulation as initial condition and at steady state when condition $V_s = V_{s_{ref}}$ is verified once again after the operating point Q'_{req} was called. From Fig. 6.15 and Fig. 6.17, it is possible to see that the ring load torque τ_r fluctuations due to the operation of the considered heavy-duty vehicle, such as the peaks of load torque when digging for example, are now compensated by the joint contribution of the EM1 torque $\tau_{EM1} = \tau_m$ and of the ICE torque $\tau_{ice} = \tau_c$, the latter always confined on the ICE *minimum specific consumption path* thanks to the action of EM2. This allows to reduce the fluctuations of the ICE operating point during the considered driving cycle, leading to a more comfortable driving experience. Metrics providing the comparison of the ICE specific fuel consumption with respect to the one given by the traditional non-hybrid Wheel Loader could not be reported in this chapter because of industrial secret reasons. Nevertheless, Fig. 6.17 shows that the ICE operating point coincides with the optimal one Q_{opt} for as long as possible and, in any case, it never leaves the ICE *minimum specific consumption path* at steady state. Furthermore, note that the calculations required by the presented control strategy are contained, which makes it interesting for real-time implementation.

6.2 Control of a Series HEV architecture

Let us consider the series architecture shown in Fig. 2.1. For the considered architecture, the energy storage device is a supercapacitor. In order to satisfy the power demand coming from the load, a solution to the energy management problem to coordinate the joint work of the three power sources present within the considered architecture, i.e. the ICE, EM1 and EM2, must be provided. The latter is based on the *minimum specific consumption path* concept illustrated in Sec. 6.1.1.

6.2.1 Control of the ICE

Series HEVs are characterized by the absence of a direct mechanical power path between the ICE and the transmission. Therefore, the ICE speed and torques are

still degrees of freedom, see Chap. 2. This means that the same *minimum specific consumption path* concept illustrated in Sec. 6.1.1 can be applied for series HEVs as well.

6.2.2 Control of Electric Machine EM2

A torque control is applied to EM2. The goal of this control is to ensure that the ICE torque is always equal to the desired torque $\tau_{ice_{des}}$ provided by the hysteresis control described in (6.2) as a function of the desired ICE speed $\omega_{ice_{des}}$, in order to confine the ICE operating point on the *minimum specific consumption path*. Since the ICE and EM2 are directly coupled through a "Gear Mesh" block, relation (6.3) turns into:

$$\tau_{EM2_{des}} = f_{EM2}(\tau_{ice_{des}}), \tag{6.6}$$

where $f_{EM2}(\tau_{ice_{des}})$ actually describes a proportional relation between $\tau_{EM2_{des}}$ and $\tau_{ice_{des}}$ according to the first "Gear Mesh" block on the left in Fig. 2.1. The desired torque $\tau_{EM2_{des}}$ is then demanded to EM2 by means of an inverter, which has been inserted within subsystem "EM2 Drive" in Fig. 2.1.

6.2.3 Control of Electric Machine EM1

The electric machine EM1 is the one responsible for driving the transmission by providing the full transmission power request. A speed control is therefore applied to EM1, in order to make it follow the desired speed profile $\omega_{EM1_{des}}$, which will be a function of the desired transmission speed $\omega_{t_{des}}$ which in turn is a function of the desired vehicle speed $v_{v_{des}}$. The torque demanded to EM1 will therefore be equal to

$$\tau_{EM1_{des}} = f_{EM1}(\Delta_{\omega_{EM1}}), \tag{6.7}$$

where $f_{EM1}(\Delta_{\omega_{EM1}})$ is a proper function of the EM1 speed error. The desired torque $\tau_{EM1_{des}}$ is then demanded to EM1 by means of an inverter, which has been inserted within subsystem "EM1 Drive" in Fig. 2.1.

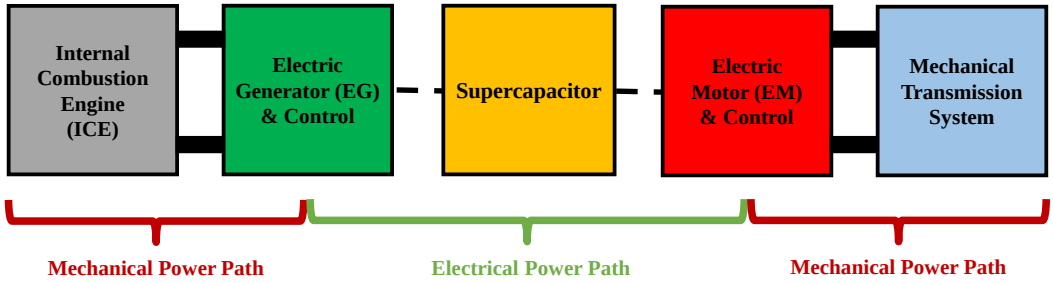

Figure 6.18: Structure of the considered series HEWL architecture.

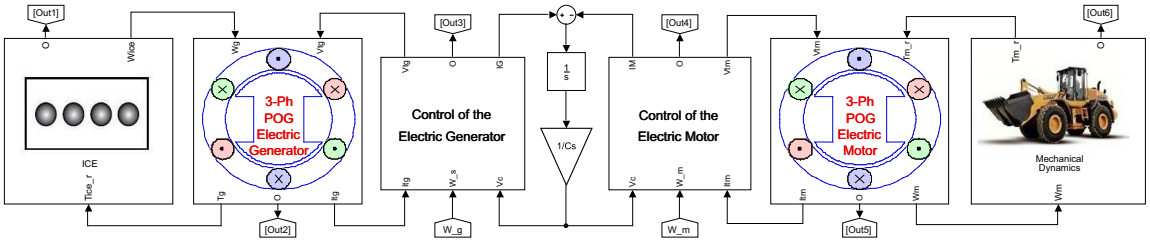

Figure 6.19: Simulink implementation of the series HEWL shown in Fig. 6.18.

6.2.4 Series case study

Let us consider the architecture shown in Fig. 6.18, which is of the series type (see Fig. 2.1) modeling a series HEWL.

Modeling

The Simulink block scheme of the architecture reported in Fig. 6.18 is shown in Fig. 6.19. From Fig. 6.18 and Fig. 6.19, it is possible to appreciate the one-to-one correspondence between the conceptual scheme of the architecture and its Simulink implementation. The elements composing the hybrid architecture in Fig. 6.19 are, from left to right, the ICE, the EG (EM2 in Fig. 2.1), the inverter controlling this machine, the supercapacitor playing the role of energy storage device, the inverter controlling the EM, the EM (EM1 in Fig. 2.1) and the mechanical transmission system of the vehicle, i.e. the Wheel Loader, from the gearbox all the way down to the wheels. The considered electric machines EM1 and EM2 are PMSMs, and have been modeled using the POG technique, see Chap. 5. The machine model

parameters have been estimated as in Sec. 5.3. The drives of EM1 and EM2 have been implemented using a vectorial control [37]. The vectorial control aims at minimizing the power dissipated because of the direct current component, see Sec. 5.2.1.

The Simulink implementation of the vehicle transmission system is reported inside the subsystem called "Mechanical Transmission System" in Fig. 6.18. The structure of the considered transmission system is schematized in Fig. 6.20, whereas the corresponding POG model from the gearbox all the way down to the vehicle wheels is still the one reported in Fig. 6.14. In this case, the time-variant connec-

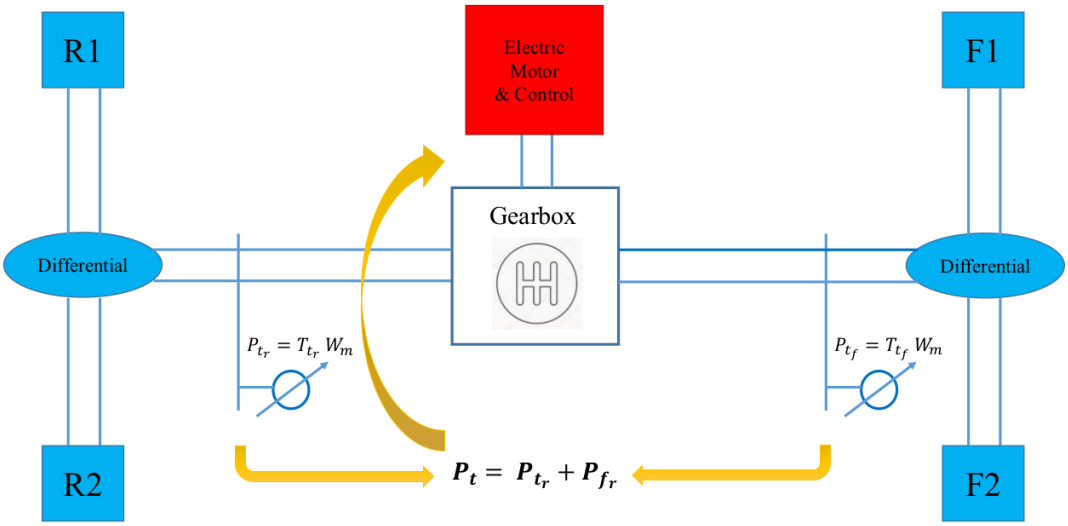

Figure 6.20: Structure of the transmission system of the considered series HEWL.

tion block R_g is characterized by two gear ratios: parameter $R_g \in \{1/r_1; 1/r_2\}$. Let us analyze in detail the contributions to the external force F_l, which are modeled by the POG block scheme in Fig. 6.21. These contributions are, from left to right, the Coulomb friction, the route slope action and the air friction. As far as the Coulomb friction is concerned, the classical modeling as a sign function $F_{a0}\,\mathrm{sign}(v_v)$, where F_{a0} is the modulus of the Coulomb friction and v_v is the vehicle speed, has been replaced by an arctan function: $F_c = \frac{2\,F_{a0}}{\pi}\,\mathrm{atan}(k\,v_v)$. By choosing a rate of change

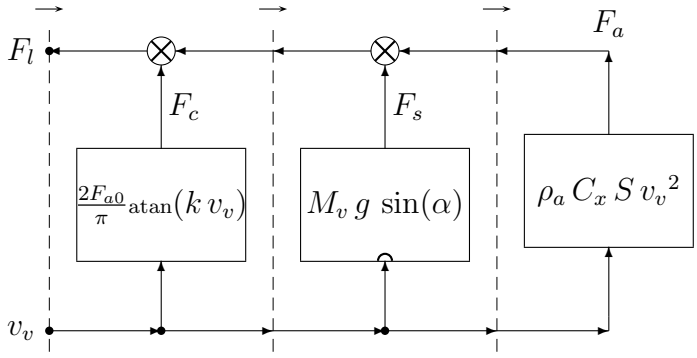

Figure 6.21: Modeling of the external force contributions for the architecture in Fig. 6.18 and Fig. 6.19.

k which is sufficiently high, it is possible to obtain a good approximation of the Coulomb friction with a smoother transition from $-F_{a_0}$ to F_{a_0} and viceversa when the vehicle direction reverses, i.e. when the sign of v_v changes, thus reducing the risk of causing system oscillations. As for the route slope action, the corresponding force is given by $F_s = M_v\,g\sin(\alpha)$, where M_v is the vehicle mass, g is the gravitational acceleration, α is the route slope and the resulting F_s is the projection of the vehicle weight force along the vehicle path direction. The air friction is accounted for by formula $F_a = \rho_a\,C_x\,S\,{v_v}^2$, where ρ_a is the air density, C_x is the air penetration coefficient and S is the transverse section of the vehicle. It is worth highlighting that the air friction impact is going to be quite limited in an application such as the one under consideration, as Wheel Loaders are vehicles which are not supposed to travel at high speed.

Simulation

The considered architecture reported in Fig. 6.19 has been simulated with reference to an industrial case study: the goal of the simulation is to make the vehicle follow a desired speed profile $v_{v_{des}}$ when the most significant friction contributions acting on the system are: 1) the Coulomb friction; 2) an external resistive force profile. In

this case, Eq. (6.6) and Eq. (6.7) are, respectively:

$$\tau_{EM2_{des}} = \tau_{ice_{des}},$$

$$\tau_{EM1_{des}} = \frac{K_{EM1_P} K_{EM1_I} s + K_{EM1_P}}{K_{EM1_I} s} \underbrace{\Delta_{\omega_{EM1}}}_{\omega_{EM1_{des}} - \omega_{EM1}}.$$

where the first one holds because there is no reduction ratio between ICE and EM2. The desired electric machine EM1 speed $\omega_{EM1_{des}}$ is related to the desired vehicle speed $v_{v_{des}}$ as follows:

$$\omega_{EM1_{des}} = \frac{R_d}{R_r\, R_g}\, v_{v_{des}}.$$

The actual values of the model parameters could not be reported because of industrial secret reasons. The external resistive force profile is responsible for simulating the resistive force that the transmission system is subject to when the Wheel Loader is either digging (i.e. loading the bucket) or unloading the bucket. The total resistive force applied to the vehicle $F_{t_{exp}}$ is therefore given by the two contributions 1) and 2) reported above and has been acquired by experimental measurements performed on the field for the analyzed cycle. The corresponding load power $P_{t_{exp}}$ is absorbed by the rear and front transmission shafts in order to make the vehicle follow the desired speed profile $v_{v_{des}}$ when the total experimental resistive force $F_{t_{exp}}$ is applied to the vehicle. In the considered hybrid architecture, such power $P_{t_{exp}}$ must be fully provided by EM1, see Chap. 2. In this simulation, the vehicle is supposed to be working on a plane route, meaning that the route slope external force contribution has no impact. Additionally, the air friction is neglected because of the low traveling speed of the Wheel Loader.

The obtained simulation results are shown in Fig. 6.22, Fig. 6.23, Fig. 6.24, Fig. 6.25 and Fig. 6.26. The upper subplot of Fig. 6.22 shows the desired speed profile $v_{v_{des}}$ that the vehicle is required to follow (blue dashed curve) and the actual vehicle speed v_v (green curve). The middle subplot of Fig. 6.22 shows the currently engaged gear, which upshifts from $R_g = 1/r_1$ to $R_g = 1/r_2$ when the absolute value of the vehicle speed overtakes the threshold of 8 [km/h] and viceversa. The lower subplot of Fig. 6.22 shows the total transmission power $P_{t_{exp}}$ acquired from

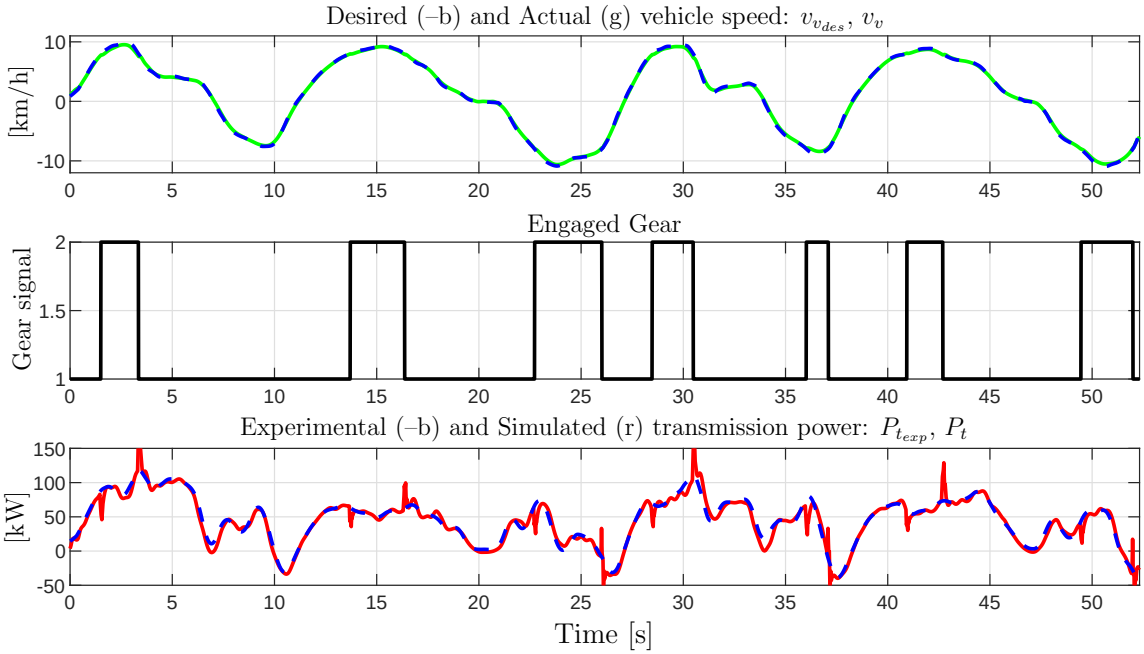

Figure 6.22: Desired and Actual Vehicle Speed; Gear; Transmission power.

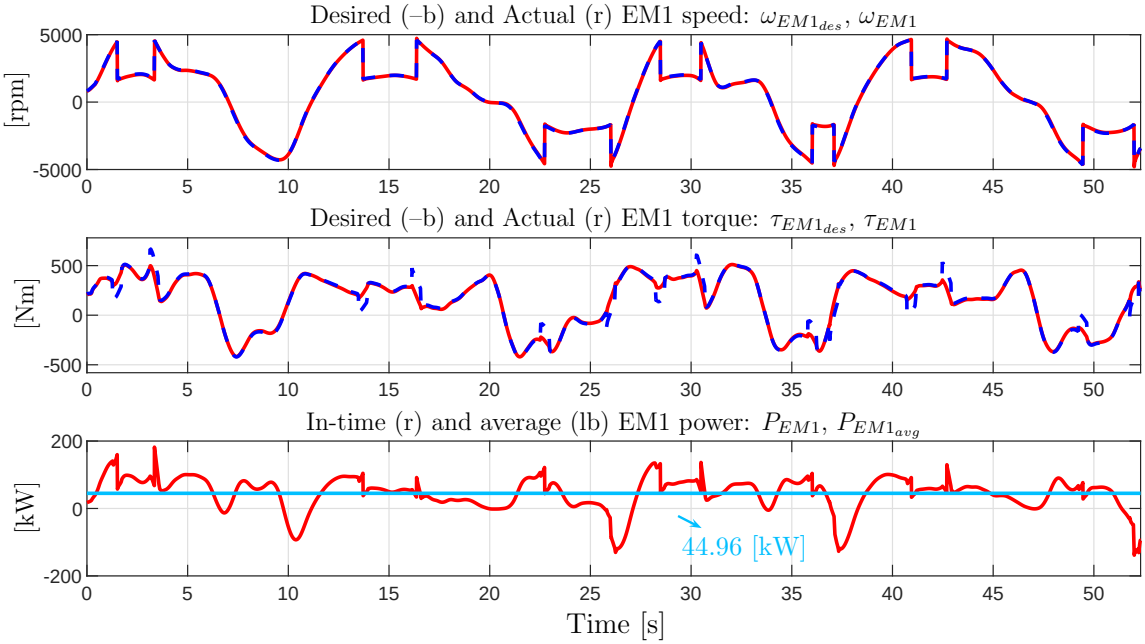

Figure 6.23: EM1: Desired and Actual Speed; Desired and Actual torque; In-time and average power.

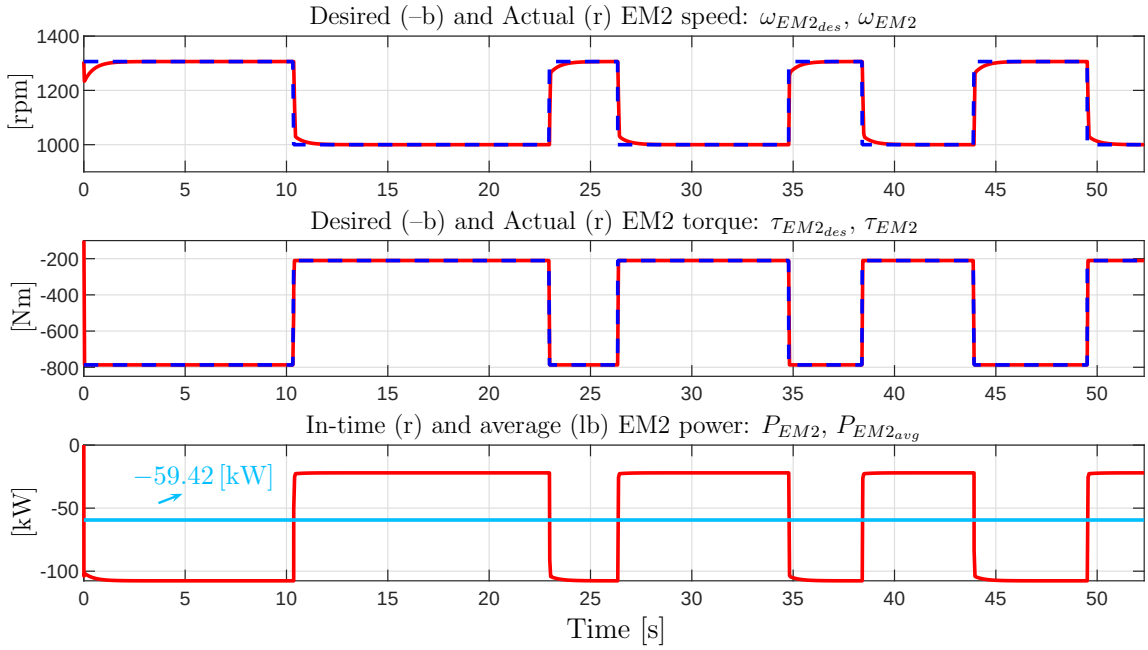

Figure 6.24: EM2: Desired and Actual Speed; Desired and Actual torque; In-time and average power.

experimental data on the field during the given cycle (blue dashed curve) and the transmission power P_t from the simulation (red curve): the good matching between $P_{t_{exp}}$ and P_t denotes the effectiveness of the control applied on EM1, allowing to fully satisfy the power demand from the transmission.

Fig. 6.23 shows the desired EM1 speed profile $\omega_{EM1_{des}}$ (blue dashed curve) and the actual EM1 speed ω_{EM1} (red curve) in the upper subplot. From the middle subplot of Fig. 6.23, it is possible to see the desired torque $\tau_{EM1_{des}}$ for EM1 in order to follow the desired speed profile $\omega_{EM1_{des}}$ and the actual EM1 torque τ_{EM1}. The good matching between the desired and actual speed and torque characteristics furthermore denotes the effectiveness of the speed control applied to EM1, allowing to satisfy the power demand coming from the load, i.e. the transmission. The lower subplot of Fig. 6.23 shows the power profile P_{EM1} generated by EM1 (red curve) and the average value of such power $P_{EM1_{avg}}$ (light blue line).

The upper subplot of Fig. 6.24 shows the EM2 desired speed, which coincides with the ICE desired speed $\omega_{EM2_{des}} = \omega_{ice_{des}}$, and the actual EM2 and ICE speed

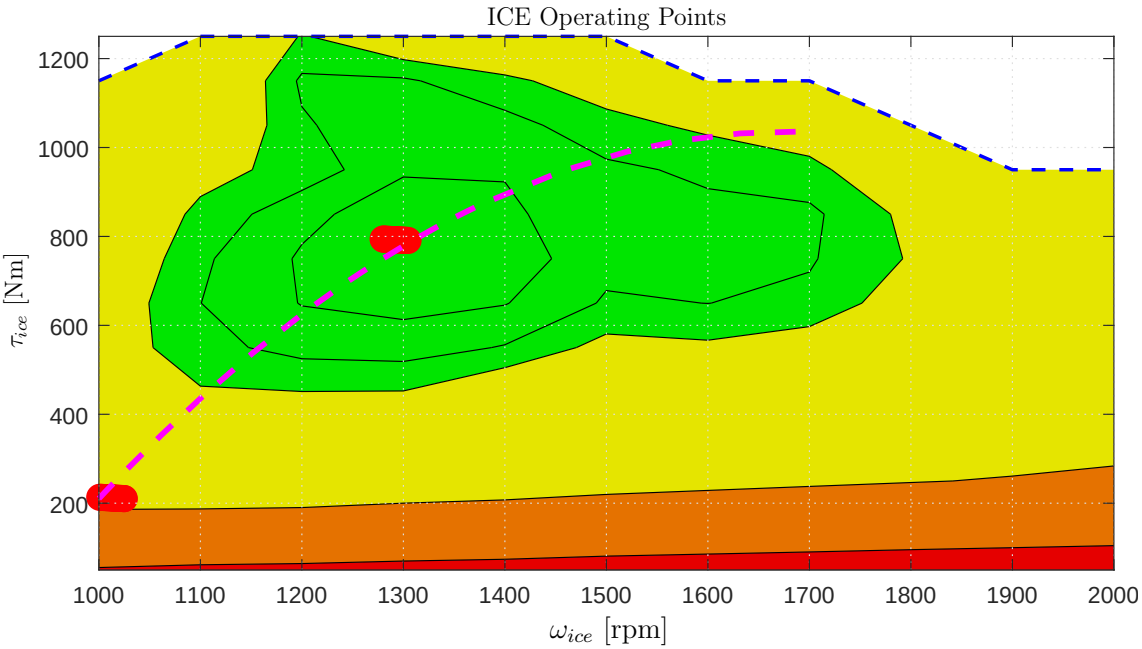

Figure 6.25: ICE operating points and ICE minimum specific consumption path on the specific consumption map.

$\omega_{EM2} = \omega_{ice}$: the good matching between the two characteristics highlights the effectiveness of the speed control applied to the ICE. The points in which a variation of ω_{EM2} occurs are those in which the supercapacitor voltage becomes greater than the upper threshold $V_c > V_{c_{up}}$, in correspondence of which the EM2 and ICE speed is set from the initial optimal value $\omega_{EM2} = \omega_{ice} = \omega_{ice_{opt}}$ down to the minimum value $\omega_{EM2} = \omega_{ice} = \omega_{ice_{min}}$ in order not to overcharge the supercapacitor according to (6.2), and those in which the decreasing supercapacitor voltage V_c reaches the reference value $V_{c_{ref}}$, in correspondence of which the EM2 and ICE speed is newly set to the optimal one $\omega_{EM2} = \omega_{ice} = \omega_{ice_{opt}}$. The middle subplot of Fig. 6.24 shows the EM2 desired torque $\tau_{EM2_{des}}$ (blue dashed curve), given by (6.2) and (6.6), and the actual EM2 torque τ_{EM2} (red curve). The latter τ_{EM2} also represents the load torque τ_{ice_l} applied to the ICE, see Fig. 6.19, which has to be counteracted by the ICE motive torque τ_{ice} in order to maintain the desired ICE speed $\omega_{ice_{des}}$. The good matching between the two desired and actual torque characteristics $\tau_{EM2_{des}}$ and τ_{EM2} shows the effectiveness of the torque control applied to EM2, whose purpose is

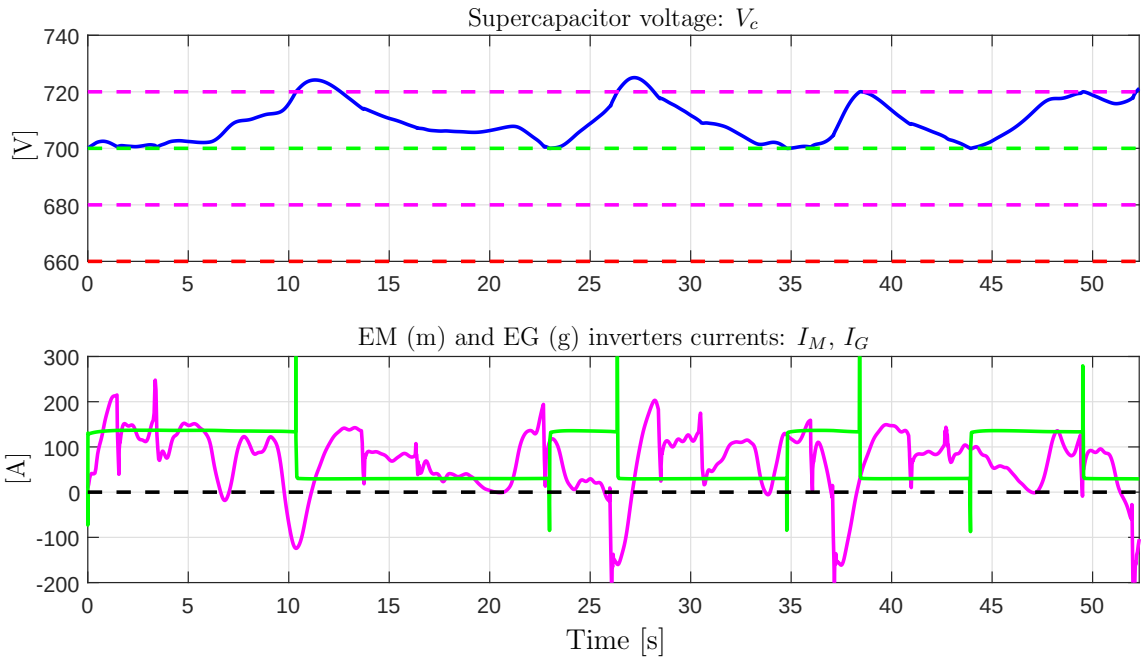

Figure 6.26: Supercapacitor voltage; Currents from the inverters.

to ensure that the condition $\tau_{ice} = \tau_{ice_{des}}$ is always verified, thus confining the ICE operating point on the *minimum specific consumption path*. The lower subplot of Fig. 6.24 shows the power profile P_{EM2} of EM2 (red curve), which is negative because the machine acts as a generator, and the average value of such power $P_{EM2_{avg}}$ (light blue line).

The ICE operating points are marked by the red dots in Fig. 6.25, showing the ICE specific consumption map on the operating plane (ω_{ice}, τ_{ice}). From this figure one can notice that, under the current simulation conditions, the ICE operating point is either equal to the optimal one $Q_{ice} = Q_{opt}$ or to the minimum one $Q_{ice} = Q_{min}$. This well agrees with the following observation: with reference to the third subplots of Fig. 6.23 and Fig. 6.24, it is possible to verify that the average EM1 power $P_{EM1_{avg}}$, and thus the average transmission power $P_{t_{avg}}$, are lower than the modulus of the average ICE and EM2 power $P_{EM2_{avg}}$ in the considered operating points $Q_{EM2} = Q_{ice} \in \{Q_{min}, Q_{opt}\}$. This explains why, *under the considered simulation conditions*, there is no need for the ICE to work in the operating points $\{Q_{req}, Q_{max}\}$, since the generated power would be much higher than the one absorbed by the

transmission. Metrics providing the reduction of the ICE specific fuel consumption with respect to the traditional non-hybrid Wheel Loader could not be provided because of industrial secret reasons.

Fig. 6.26 shows the voltage drop across the supercapacitor in the upper subplot (blue curve) and the considered thresholds $V_{c_{min}}$, $V_{c_{low}}$,$V_{c_{ref}}$ and $V_{c_{up}}$ introduced in (6.2) in red, magenta, green and magenta dashed lines, respectively.

The lower subplot of Fig. 6.26 shows the EM2 inverter current I_{EM2} (green curve) always recharging the supercapacitor ($I_{EM2} > 0$), and the EM1 inverter current I_{EM1} (magenta curve), either discharging ($I_{EM1} > 0$) or recharging ($I_{EM1} < 0$) the supercapacitor depending on the Wheel Loader operating conditions. The discrimination about whether EM1 and EM2 are recharging or discharging the supercapacitor can be made on the basis of the EM2 and EM1 inverter currents I_{EM2} and I_{EM1} by carefully looking at the summation node at the input of the supercapacitor shown in Fig. 6.19. Since the EM2 inverter current I_{EM2} enters the supercapacitor input summation node with a "+" sign, whereas the EM1 inverter current I_{EM1} enters the supercapacitor input summation node with a "-" sign, it follows that:

$$\begin{cases} I_{EM1} > 0 \quad \Rightarrow \quad \text{EM1 discharging the supercapacitor } \checkmark \\ I_{EM1} < 0 \quad \Rightarrow \quad \text{EM1 recharging the supercapacitor } \checkmark \\ I_{EM2} > 0 \quad \Rightarrow \quad \text{EM2 recharging the supercapacitor } \checkmark \\ I_{EM2} < 0 \quad \Rightarrow \quad \text{EM2 discharging the supercapacitor } \otimes \end{cases}$$

Note that the last case ($I_{EM2} < 0$) can never happen, as in the considered architecture EM2 cannot work as a motor, since the ICE cannot absorb power. As regards the condition $I_{EM1} < 0$, the time frames in which EM1 does contribute to *recharge* the supercapacitor are those in which the vehicle is required to decelerate: the braking action is performed with the aid of EM1 and energy recovery takes place. The potentiality of performing this latter operation is one of the main advantages of Hybrid Electric Vehicles.

6.3 Control of a Parallel HEV architecture

Let us consider the parallel architecture shown in Fig. 2.2. For the considered architecture, the energy storage device is a supercapacitor. The power demand coming from the load is satisfied thanks to the joint work of the three power sources present within the considered architecture: the ICE, EM1 and EM2. The proper way of controlling these power sources is determined by providing a solution to the energy management problem.

6.3.1 ICE operating point

As far as the ICE is concerned, two pieces of information are needed for the control of the considered hybrid vehicle: the maximum ICE torque $\tau_{ice_{max}}$ versus the ICE speed ω_{ice}, together with the ICE *minimum specific consumption path*, which gives the optimal ICE torque $\tau_{ice_{opt}}$ expressed as a function of the ICE speed ω_{ice}. Such pieces of information are graphically shown in Fig. 6.27, where the blue dashed curve represents the characteristic $\tau_{ice_{max}}$ vs ω_{ice}, and the magenta dashed curve represents the ICE *minimum specific consumption path* $\tau_{ice_{opt}}$ vs ω_{ice}. The colored areas in Fig. 6.27 represent portions of the ICE specific fuel consumption map for which the specific consumption is decreasing when moving from the red portions to the green portions (for which the minimum of the ICE specific consumption is achieved).

The meaning of the ICE *minimum specific consumption path* for a parallel architecture significantly differs from the one related to power-split hybrid architectures described in Sec. 6.1.1 and to series hybrid architectures described in Sec. 6.2.1. The presence of a planetary gear set in power-split architectures makes both the ICE speed ω_{ice} and the ICE torque τ_{ice} exploitable as degrees of freedom. Similarly, the lack of a direct coupling between the ICE and the transmission in series architectures makes both the ICE speed ω_{ice} and the ICE torque τ_{ice} exploitable as degrees of freedom. On the contrary, the ICE speed is always coupled to the vehicle speed in parallel architectures, meaning that it cannot be arbitrarily chosen.

It follows that the ICE *minimum specific consumption path* for a parallel archi-

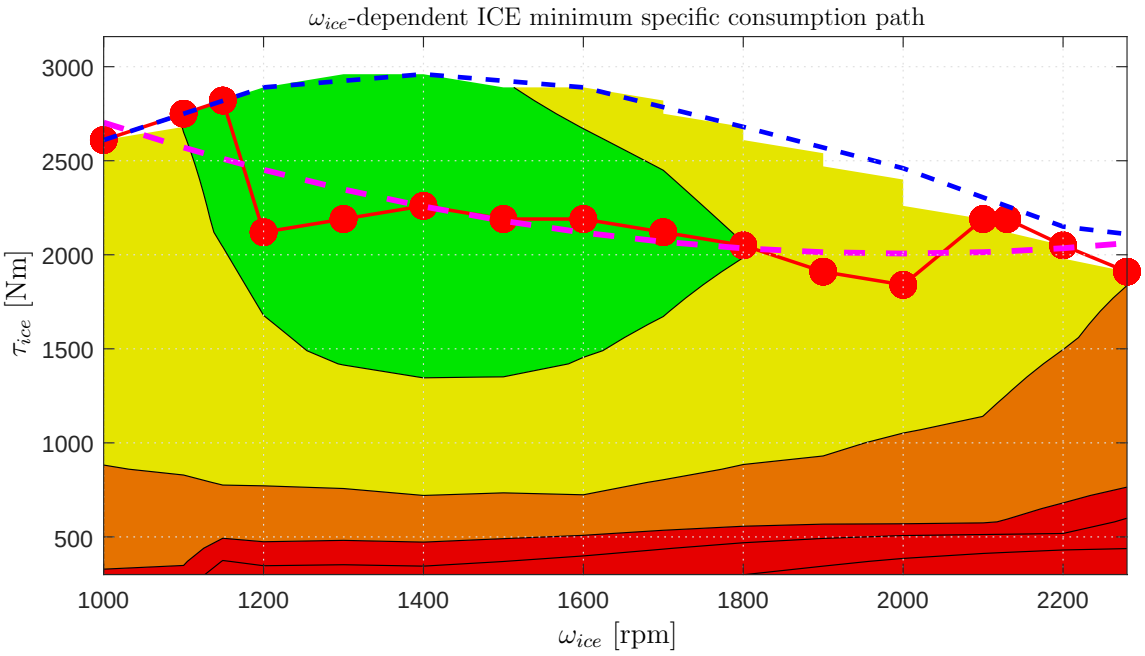

Figure 6.27: ICE minimum specific consumption path dependent on the ICE speed in the operating plane (ω_{ice}, τ_{ice}).

tecture is ω_{ice}-*dependent* and addresses the following issue: "what is the optimal ICE torque $\tau_{ice_{opt}}$ which minimizes the ICE specific fuel consumption over the whole ICE speed range $\omega_{ice} \in [\omega_{ice_{min}}, \omega_{ice_{max}}]$?".

The procedure for computing the ω_{ice}-dependent *minimum specific consumption path* of a parallel hybrid architecture requires to analyze the whole ICE speed range $\omega_{ice} \in [\omega_{ice_{min}}, \omega_{ice_{max}}]$. For each ICE speed point ω_{ice}, the ICE specific consumption map can be exploited in order to find the most suitable ICE torque τ_{ice} along the y-axis, see Fig. 6.27, that minimizes the specific fuel consumption of the ICE at the considered ICE speed ω_{ice}. The computed minimum specific consumption points for each ICE speed ω_{ice} are shown in Fig. 6.27 by red spots. The magenta characteristic in Fig. 6.27 is the actual ω_{ice}-dependent *minimum specific consumption path* that will be used. The latter exhibits transitions which are less abrupt compared to those

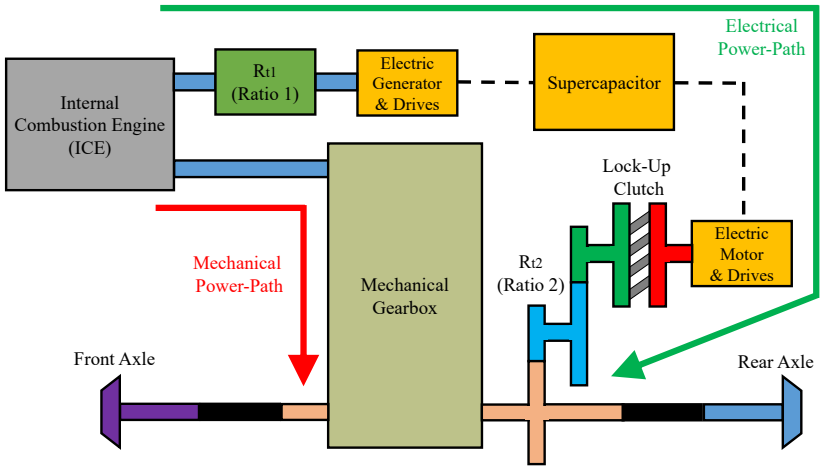

Figure 6.28: Structure of the considered parallel hybrid propulsion system.

in the red path, and has been obtained using the following relation:

$$\tau_{ice} = p_0 + \omega_{ice} p_1 + \omega_{ice}^2 p_2, \quad \text{where} \quad \begin{cases} p_0 = 4.79 \cdot 10^3 \\ p_1 = -26.64 \\ p_2 = 0.064 \end{cases}. \tag{6.8}$$

As far as the ICE speed range $\omega_{ice} \in [0,\ \omega_{ice_{min}})$ is concerned, the ICE optimal torque $\tau_{ice_{opt}}$ giving the minimum specific consumption is assumed to be linearly increasing from $\tau_{ice_{opt}} = 0$ at $\omega_{ice} = 0$ until the beginning of the *minimum specific consumption path*, i.e. until $\omega_{ice} = \omega_{ice_{min}}$.

Modeling

Fig. 6.28 shows the parallel hybrid architecture analyzed in this work, describing a parallel hybrid agricultural tractor, whereas Fig. 6.29 shows the associated Simulink block scheme.

The systems in the architecture of Fig. 6.29 are, ordered from the top/left to the bottom/right corner, the electric machine working as a generator (EM2 in Fig. 2.2), the inverter that controls this machine, the energy storage device (which is the supercapacitor named C_s), the inverter that controls the electric machine working as a motor, the electric machine working as a motor (EM1 in Fig. 2.2), the ICE, the

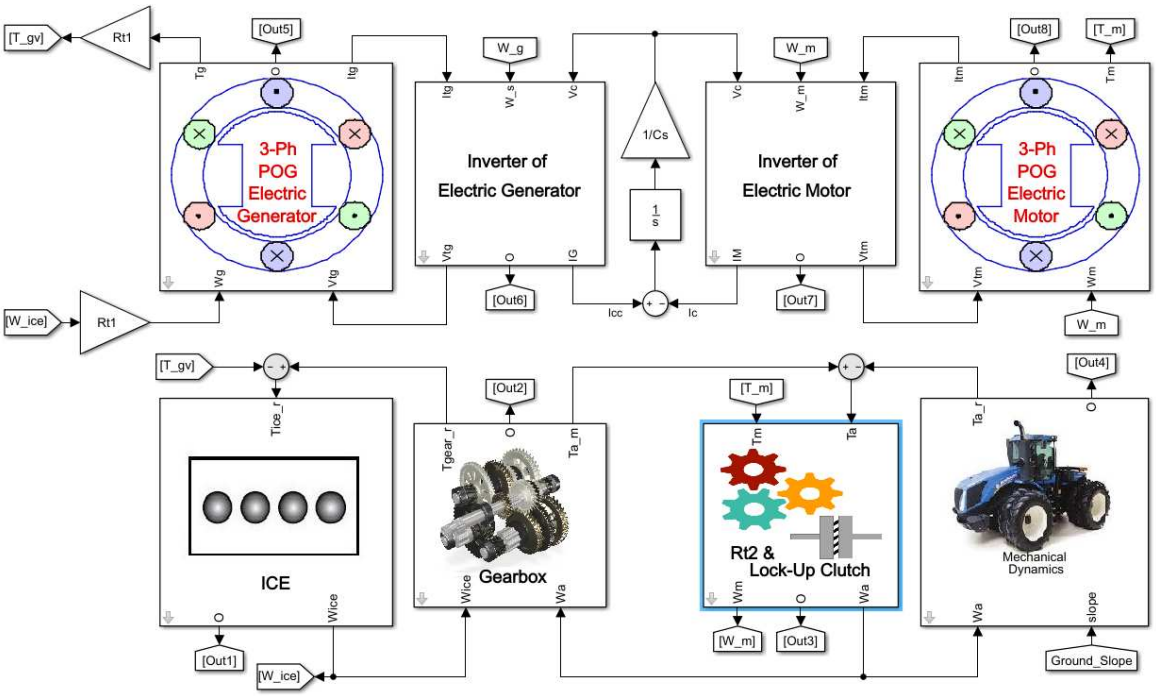

Figure 6.29: Simulink implementation of the parallel hybrid propulsion system shown in Fig. 6.28.

gearbox, the additional reduction ratio (which, in this case study, is equipped with a lockup clutch in order to be able to disconnect the electric path) and, finally, the mechanical transmission system of the vehicle. The considered electric machines EM1 and EM2 are PMSMs, and have been modeled using the POG technique, see Sec. 5. The machine model parameters have been estimated as in Sec. 5.3. The drives of EM1 and EM2 have been implemented using a vectorial control [37]. The vectorial control aims at minimizing the power dissipated because of the direct current component, see Sec. 5.2.1.

The dynamic model of the supercapacitor has been represented by means of the POG block in the center-top part of Fig. 6.29. The dynamic model of the vehicle transmission system [59] has been derived by considering the front and rear axles as a unique transmission axle, whereas the dynamic model of the lock-up clutch has been derived by applying the approach using the main and relative system dynamics described in [79].

6.3.2 Control strategy

In this section, the description of the control strategy developed for the parallel hybrid architecture under consideration is given. The load power demand is met using the two power paths in the system: the mechanical/electrical one and the mechanical one. Therefore, the energy management problem is solved by presenting the power sources control. The available power sources are: the ICE, the electric motor (EM1) and the electric generator (EM2). The control of the three power sources is handled by a control logic having two main purposes:

A) Determination of the current *vehicle state*, see Sec. 6.3.3;

B) ICE, EM2 and EM1 control according to the current *vehicle state*, see Sec. 6.3.4;

6.3.3 Determination of the vehicle state

The control logic makes a decision about the *state* of the vehicle at each time step on the basis of the current value of three *decision variables*: v_v, $\tau_{ice_{req}}$ and V_c, that are the vehicle speed, the torque which would be required to the ICE if there were no mechanical/electrical path (fully-mechanical operating mode) and the voltage drop across the supercapacitor, respectively. From now on, variable $\tau_{ice_{req}}$ will be referred to as "fictitious torque required to the ICE", since it coincides with the actual ICE demanded torque iff the mechanical/electrical path is disabled or EM1 is not required to provide its contribution.

The discriminating thresholds for the three *decision variables* v_v, $\tau_{ice_{req}}$ and V_c are called *decision parameters*: v_{v_t}, $\tau_{ice_{opt}}$, $V_{c_{low}}$ and $V_{c_{up}}$. The first decision parameter v_{v_t} is a constant representing the threshold vehicle speed above which the lock-up clutch opens, thus disabling the mechanical/electrical power path and the vehicle passes in fully-mechanical operating mode. The second decision parameter $\tau_{ice_{opt}}$ is a time-variant parameter representing the optimal ICE torque versus the ICE speed ω_{ice} given by the *minimum specific consumption path* according to (6.8). The third and fourth decision parameters $V_{c_{low}}$ and $V_{c_{up}}$ are two constant parameters representing the lower and upper thresholds of the voltage V_c across supercapacitor

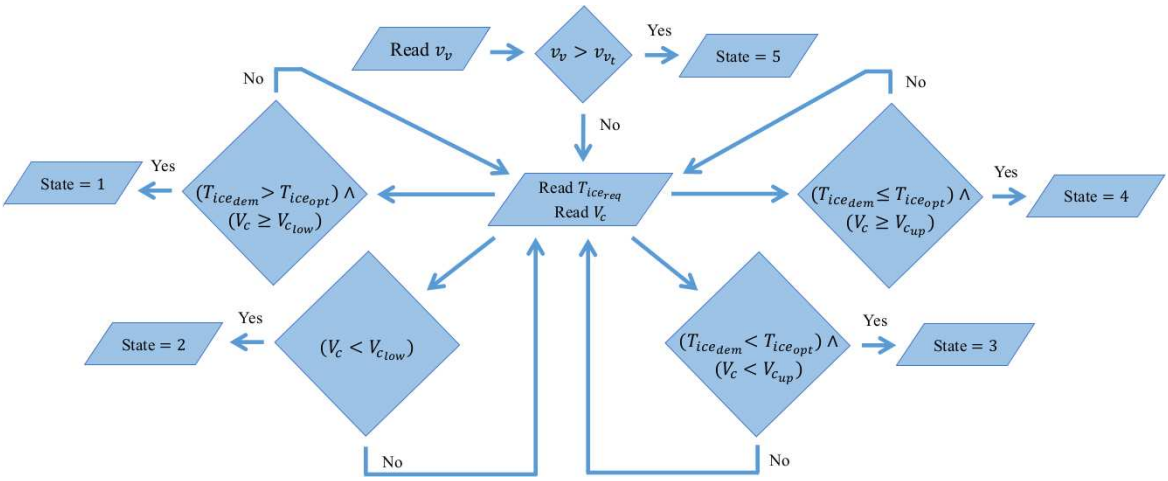

Figure 6.30: Flowchart describing the determination of the current vehicle state for the architecture implemented in Fig. 6.29.

C_s, the latter being related to the supercapacitor state of charge. Because of the dynamics of the considered system, a safety range is left between $V_{c_{low}}$, $V_{c_{up}}$ and the actual minimum and maximum thresholds $V'_{c_{low}}$ and $V'_{c_{up}}$, respectively, such that:

$$V'_{c_{low}} < V_{c_{low}} \quad \text{and} \quad V'_{c_{up}} > V_{c_{up}}.$$

The considered parallel hybrid architecture is characterized by five states: States from 1 to 4 are characterized by the vehicle operating in hybrid mode, whereas State 5 is characterized by the vehicle operating in fully-mechanical mode. The entering/exiting conditions according to which the control logic makes a decision about the current vehicle state are described in Fig. 6.30 with the aid of a flowchart.

6.3.4 Control of the power sources

A Proportional-Integral-Derivative (PID) controller is employed to translate the ICE speed error $\Delta_{\omega_{ice}} = \omega_{ice_{des}} - \omega_{ice}$ into the fictitious torque $\tau_{ice_{req}}$ required to the ICE. Thanks to the presence of the two parallel power paths, such fictitious torque $\tau_{ice_{req}}$ is properly split between the *actual* torque $\tau_{ice_{dem}}$ demanded to the ICE and the actual torque $\tau_{EM1_{dem}}$ demanded to EM1 depending on the vehicle state.

A proportional controller is employed to translate the supercapacitor voltage error $\Delta_{V_c} = V_{c_{ref}} - V_c$ into a desired torque $\tau_{EM2_{dem}}$ for EM2, in order to recharge the

supercapacitor when $V_c < V_{c_{low}}$. The reference value for the supercapacitor voltage $V_{c_{ref}}$ is defined as the arithmetic mean of the upper and lower voltage thresholds $V_{c_{up}}$ and $V_{c_{low}}$, $V_{c_{ref}} = (V_{c_{up}} - V_{c_{low}})/2$.

From these considerations about the determination of the demanded torques, the reader can evince that a *torque control* is applied to the three power sources.

The *vehicle state* uniquely determines the proper torque demands $\tau_{ice_{dem}}$, $\tau_{EM1_{dem}}$ and $\tau_{EM2_{dem}}$ for the three power sources ICE, EM1 and EM2 in order to fulfill the requirements: minimize the ICE specific fuel consumption, satisfy the power demand coming from the transmission and make sure that the supercapacitor voltage is always confined in between the minimum and maximum acceptable thresholds $V'_{c_{low}}$ and $V'_{c_{up}}$. The five possible vehicle states characterizing the considered parallel architecture and the corresponding control actions are discussed in the following.

State 1

The vehicle is in this state when the fictitious torque $\tau_{ice_{req}}$ required to the ICE is greater than the optimal one $\tau_{ice_{opt}}$ and the supercapacitor is sufficiently charged to sustain the operation of EM1, i.e. when $V_c \geq V_{c_{low}}$, see Fig. 6.30. In this state, the control logic imposes the following equalities:

$$\begin{cases} \Delta_{\tau_{ice}} &= \tau_{ice_{req}} - \tau_{ice_{opt}} \\ \tau_{ice_{dem}} &= \tau_{ice_{opt}} \\ \tau_{EM1_{dem}} &= \left(\dfrac{\Delta_{\tau_{ice}}}{R_g}\right) R_{t2} \\ \tau_{EM2_{dem}} &= 0 \end{cases}, \tag{6.9}$$

where R_g is the reduction ratio of the currently engaged gear and R_{t2} is the reduction ratio introduced by the gears placed downstream with respect to the lock-up clutch, see Fig. 6.28.

From (6.9), one can see that: the ICE actual demanded torque $\tau_{ice_{dem}}$ is determined so as to keep the ICE operating point along the *minimum specific consumption path*, the EM1 actual demanded torque $\tau_{EM1_{dem}}$ is determined in order to convert the additional ICE torque request $\Delta_{\tau_{ice}}$ into a request for EM1, and the EM2 actual

demanded torque $\tau_{EM2_{dem}}$ is set to zero in order not to make EM1 and EM2 operate at the same time.

State 2

The vehicle is in this state when the supercapacitor must be recharged, i.e. when $V_c < V_{c_{low}}$ (see Fig. 6.30) in order not to cause voltage V_c to go below the minimum threshold $V'_{c_{low}}$. In this state, the control logic imposes the following equalities:

$$\begin{cases} \Delta_{V_c} &= V_{c_{ref}} - V_c \\ \tau_{EM2_{dem}} &= -K\,\Delta_{V_c} \\ \Delta_{\tau_{ice}} &= -\tau_{EM2_{dem}}\,R_{t1} \\ \tau_{ice_{dem}} &= \tau_{ice_{req}} + \Delta_{\tau_{ice}} \\ \tau_{EM1_{dem}} &= 0 \end{cases} , \tag{6.10}$$

where K is the properly set gain of the proportional regulator converting the supercapacitor voltage error Δ_{V_c} into a torque $\tau_{EM2_{dem}}$ demanded to EM2.

From (6.10), one can see that the ICE actual demanded torque $\tau_{ice_{dem}}$ is determined in order to fully satisfy the request $\tau_{ice_{req}}$ to guarantee that the ICE and thus the transmission will follow the desired speed profile and in order to provide EM2 with the demanded torque level $\tau_{EM2_{dem}}$. The EM1 actual demanded torque $\tau_{EM1_{dem}}$ is set to zero in order not to make EM1 and EM2 operate at the same time, whereas the EM2 actual demanded torque $\tau_{EM2_{dem}}$ is determined in order to properly recharge the supercapacitor.

State 3

The vehicle is in this state when the fictitious ICE demanded torque $\tau_{ice_{req}}$ is lower than the optimal one $\tau_{ice_{opt}}$ and the supercapacitor voltage V_c is lower than the upper threshold $V_{c_{up}}$, see Fig. 6.30. In this state, the control logic imposes the following equalities:

$$\begin{cases} \Delta_{\tau_{ice}} & = & \tau_{ice_{opt}} - \tau_{ice_{req}} \\ \tau_{EM2_{dem}} & = & -\dfrac{\Delta_{\tau_{ice}}}{R_{t1}} \\ \tau_{ice_{dem}} & = & \tau_{ice_{opt}} \\ \tau_{EM1_{dem}} & = & 0 \end{cases} . \tag{6.11}$$

From (6.11) one can see that the ICE actual demanded torque $\tau_{ice_{dem}}$ is determined so as to keep the ICE operating point along the *minimum specific consumption path* and the EM1 actual demanded torque $\tau_{EM1_{dem}}$ is set to zero, in order not to make EM1 and EM2 operate at the same time.

The EM2 actual demanded torque $\tau_{EM2_{dem}}$ is determined in order to exploit the additional ICE torque $\Delta_{\tau_{ice}}$, which is not required by the transmission, in order to recharge the supercapacitor. The philosophy behind this choice is the following one: since the transmission torque request is such as to make the ICE torque lower than the optimal one, thus rising the specific fuel consumption of the ICE, and since the supercapacitor voltage is lower than $V_{c_{up}}$, it makes sense to improve the specific fuel consumption of the ICE by setting the ICE torque equal to the optimal one and to exploit the ICE extra torque to recharge the supercapacitor as much as its characteristics allow.

State 4

The vehicle is in this state when the fictitious ICE demanded torque $\tau_{ice_{req}}$ is lower than or equal to the optimal one $\tau_{ice_{opt}}$ and the supercapacitor voltage V_c is greater than or equal to the upper threshold $V_{c_{up}}$, see Fig. 6.30. In this state, the control logic imposes the following equalities:

$$\begin{cases} \tau_{ice_{dem}} & = & \tau_{ice_{req}} \\ \tau_{EM1_{dem}} & = & 0 \\ \tau_{EM2_{dem}} & = & 0 \end{cases} . \tag{6.12}$$

From (6.12), one can notice that the ICE actual demanded torque $\tau_{ice_{dem}}$ coincides with the fictitious torque $\tau_{ice_{req}}$ which would be required to the ICE if the

mechanical/electrical path were disabled, since both the EM1 and the EM2 actual demanded torques $\tau_{EM1_{dem}}$ and $\tau_{EM2_{dem}}$ are set to zero. $\tau_{EM1_{dem}}$ is set to zero because there is no need to perform torque compensation as the ICE demanded torque is lower than the optimal one; $\tau_{EM2_{dem}}$ is set to zero because it is not possible to exploit the fact that the ICE demanded torque is lower than the optimal one in order to recharge the supercapacitor, since it cannot be recharged any further (because $V_c \geq V_{c_{up}}$ is already verified, and $V_c < V'_{c_{up}}$ has to be guaranteed).

State 5

The vehicle is in this state when the vehicle speed v_v is greater than threshold v_{v_t} ($v_v > v_{v_t}$), therefore the control logic opens the lock-up clutch to disable the mechanical/electrical power path. In this case, the control logic imposes the following equalities:

$$\begin{cases} \tau_{ice_{dem}} = \tau_{ice_{req}} \\ \tau_{EM1_{dem}} = 0 \\ \tau_{EM2_{dem}} = 0 \end{cases} \quad \text{if} \quad V_c \geq V_{c_{ref}}$$

$$\begin{cases} \Delta_{\tau_{ice}} = \tau_{ice_{max}} - \tau_{ice_{req}} \\ \tau_{ice_{dem}} = \tau_{ice_{max}} \\ \tau_{EM2_{dem}} = -\dfrac{\Delta_{\tau_{ice}}}{R_{t1}} \\ \tau_{EM1_{dem}} = 0 \end{cases} \quad \text{if} \quad V_c < V_{c_{ref}} \qquad . \tag{6.13}$$

Relations (6.13) highlight that State 5 is decoupled into two substates:

- When $V_c \geq V_{c_{ref}}$, the ICE actual demanded torque $\tau_{ice_{dem}}$ is simply set to be equal to the ICE fictitious demanded torque $\tau_{ice_{req}}$, since this is exactly the case of fully-mechanical operating mode. Indeed, it is fully up to the ICE to satisfy the transmission torque request. The EM1 and EM2 actual demanded torques $\tau_{EM1_{dem}}$ and $\tau_{EM2_{dem}}$ are therefore set to zero.

- When $V_c < V_{c_{ref}}$, the ICE actual demanded torque $\tau_{ice_{dem}}$ is set to the maximum torque $\tau_{ice_{max}}$ available at the current ICE speed ω_{ice} until $V_c = V_{c_{ref}}$.

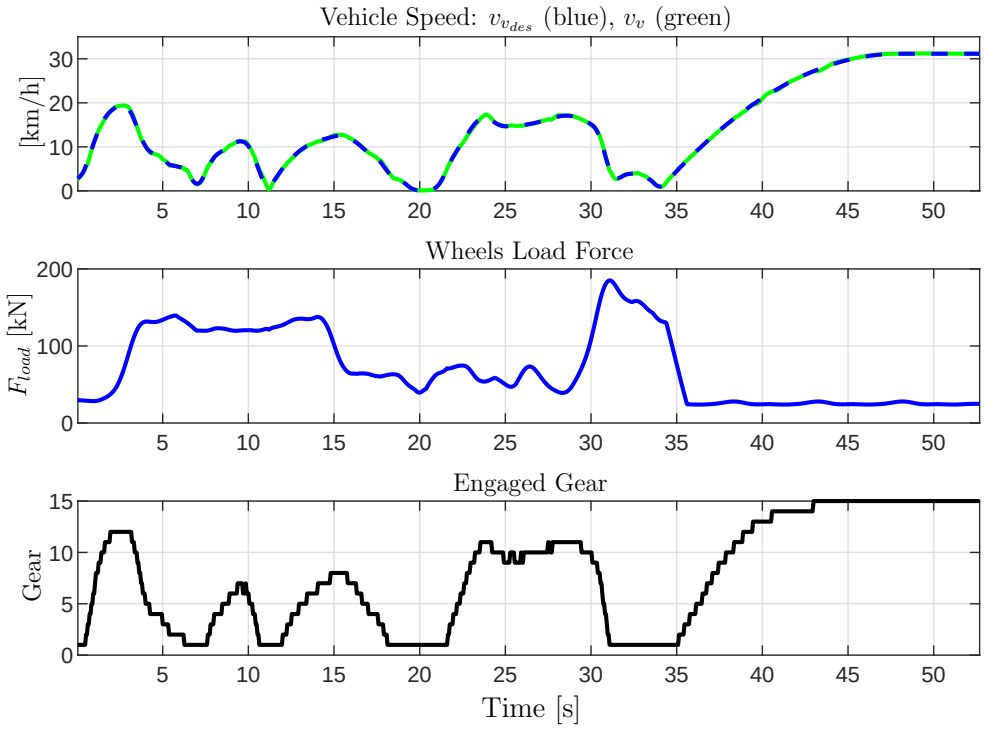

Figure 6.31: Desired and Actual Vehicle Speed; Wheels Load Force; Engaged Gear.

The EM1 actual demanded torque $\tau_{EM1_{dem}}$ is still set to zero, as the lock-up clutch is open. The EM2 actual demanded torque $\tau_{EM2_{dem}}$ is determined in order to exploit the additional ICE torque $\Delta_{\tau_{ice}}$ so as to recharge the super-capacitor, in order for it to be fully operative when the vehicle leaves State 5 and enters in hybrid mode again.

Simulation

The architecture whose Simulink scheme is shown in Fig. 6.29 has been simulated by making the tractor follow a determined speed profile. During the simulation, the vehicle is subject to a wheels load force associated with the tractor operation. The parameters values inserted in the model could not be shown because of trade secret. The simulation results are provided in Fig. 6.31, Fig. 6.32, Fig. 6.33, Fig. 6.34 and Fig. 6.35.

The upper subplot in Fig. 6.31 reports the desired vehicle speed profile $v_{v_{des}}$ (blue

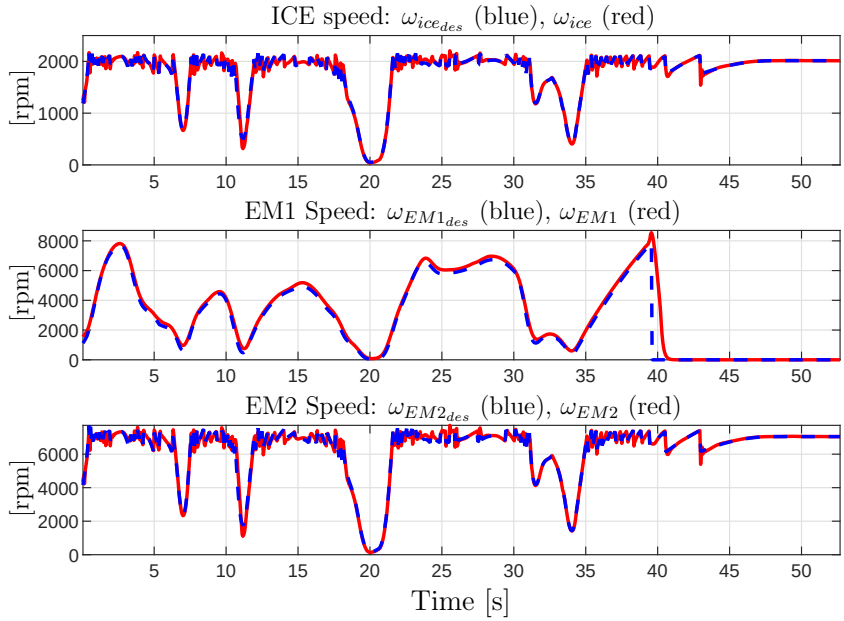

Figure 6.32: Desired and actual ICE speed; Desired and Actual EM1 Speed; Desired and Actual EM2 Speed; .

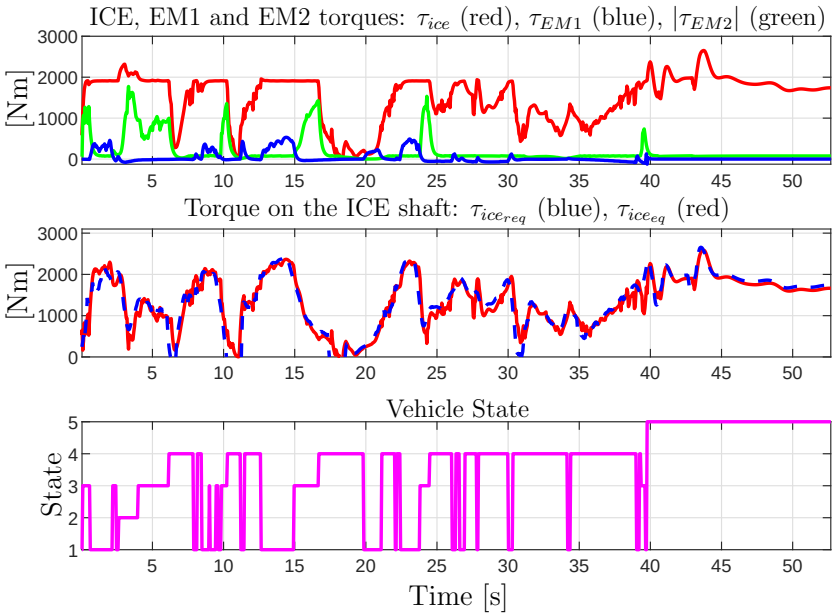

Figure 6.33: ICE, EM1 and EM2 torques reported on the ICE shaft; Fictitious and equivalent torque on the ICE shaft; State of the vehicle.

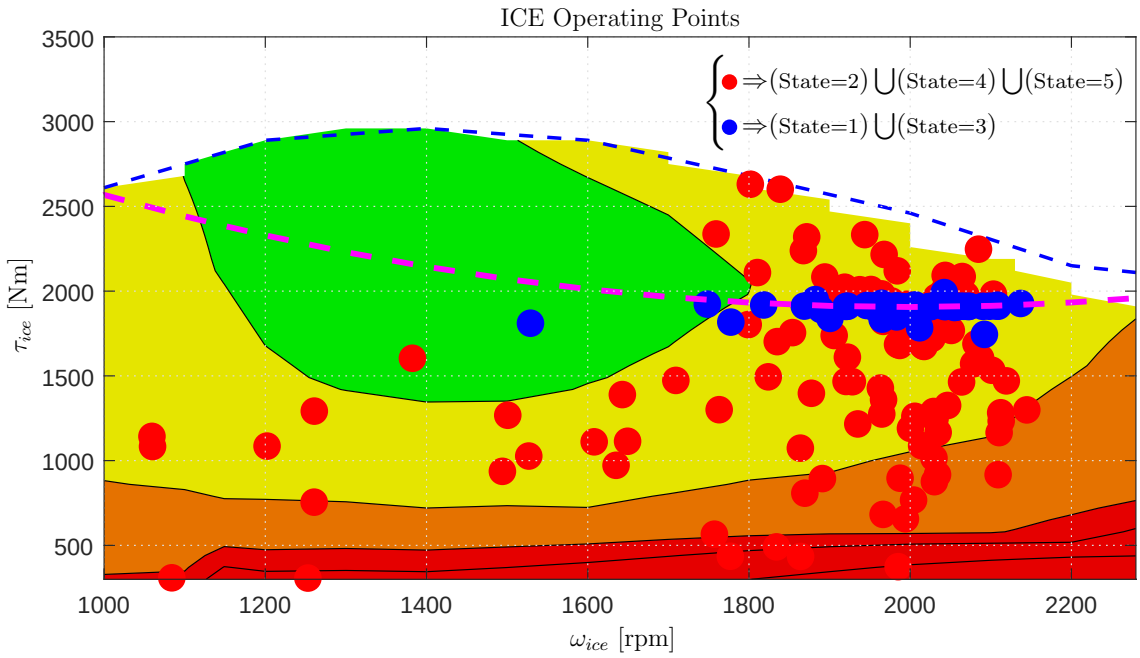

Figure 6.34: Operating points of the ICE on the specific fuel consumption map.

dashed line) and the actual vehicle speed v_v (green line). The middle subplot shows the wheels load force F_{load} that the vehicle is subject to during its operation. The lower subplot in Fig. 6.31 reports the gear signal, denoting which gear is engaged at different vehicle speed. The vehicle speed threshold above which the vehicle enters State 5, denoting the operation in fully-mechanical mode, is $v_{v_t} = 20$ [km/h]. This operating mode is activated when the tractor is traveling by road. In this case, the tractor is not operating on the field and is subject to a lighter load force, therefore no torque compensation by EM1 is needed.

The three subplots in Fig. 6.32 show, from top to bottom, the desired and actual ICE speeds $\omega_{ice_{des}}$ and ω_{ice}, the desired and actual EM1 speeds $\omega_{EM1_{des}}$ and ω_{EM1}, the desired and actual EM2 speeds $\omega_{EM2_{des}}$ and ω_{EM2}, where the desired profiles are plotted in blue dashed lines and the actual profiles are plotted in red lines. The actual speed profiles in Fig. 6.31 and Fig. 6.32 agree with the desired ones, showing how the joint contribution of the three power sources ICE, EM1 and EM2, which are properly controlled thanks to the developed control strategy, effectively satisfies

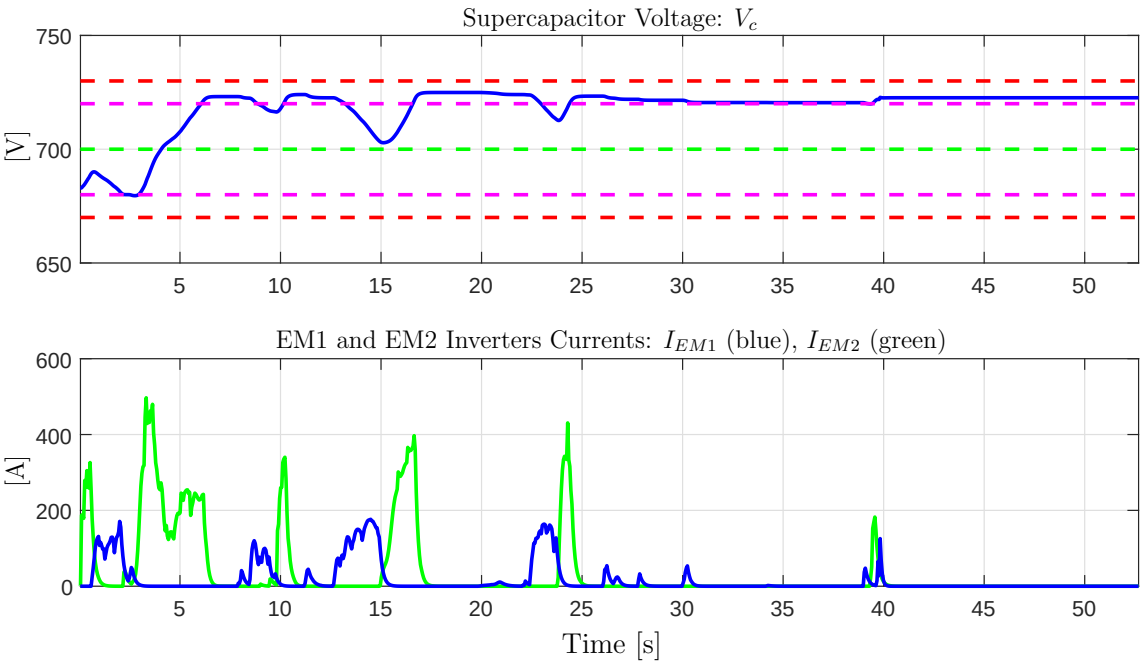

Figure 6.35: Supercapacitor voltage; EM1 and EM2 Inverters Currents.

the transmission power demand.

The upper subplot in Fig. 6.33 reports: the actual ICE torque τ_{ice} (red curve), the equivalent EM1 torque τ_{EM1} reported on the ICE shaft through the currently engaged gear R_g and ratio R_{t2} (blue curve) and the modulus of the equivalent EM2 torque τ_{EM2} reported on the ICE shaft through ratio R_{t1} (green curve). The actual values of τ_{EM2} are negative, denoting the operation of this electric machine as a generator. The middle subplot in Fig. 6.33 reports the fictitious ICE required torque $\tau_{ice_{req}}$ that the ICE should provide in fully-mechanical operating mode and the equivalent motive torque $\tau_{ice_{eq}}$ available on the ICE shaft, which is given by the algebraic sum of the three power sources torques reported in the upper subplot of Fig. 6.33. The lower subplot in Fig. 6.33 shows how the vehicle state changes during the simulation. The current vehicle state, determined by the control logic according to the algorithm described in Fig. 6.30, uniquely determines the ICE torque τ_{ice}, the EM1 torque τ_{EM1} and the EM2 torque τ_{EM2}, according to the strategy presented in Sec. 6.3.4.

Fig. 6.34 reports the operating points (ω_{ice}, τ_{ice}) of the ICE on its specific consumption map. It can be noticed that, when the vehicle is operating in States 1 and 3, the ICE torque τ_{ice} coincides with the optimal ICE torque $\tau_{ice_{opt}}$ according to (6.9) and (6.11). In these states, the ICE operating points are confined around the *minimim specific consumption path* in (6.8), see the blue spots in Fig. 6.34. The red spots in Fig. 6.34 show that, when the vehicle is operating in the remaining States 2, 4 and 5, the ICE leaves the *minimum specific consumption path* as required by the control logic, see (6.10), (6.12) and (6.13). Metrics giving the comparison of the obtained specific fuel consumption of the ICE with the one given by the non-hybrid agricultural tractor could not be shown because of trade secret.

Finally, the blue curve in the upper subplot of Fig. 6.35 represents the supercapacitor voltage V_c. The maximum, upper, reference, lower and minimum thresholds $V'_{c_{up}}$, $V_{c_{up}}$, $V_{c_{ref}}$, $V_{c_{low}}$ and $V'_{c_{low}}$ are shown in upper dashed red, upper dashed magenta, dashed green, lower dashed magenta and lower dashed red lines, respectively. The lower subplot in Fig. 6.35 reports the EM1 inverter current I_{EM1} discharging the supercapacitor (blue curve), as well as the EM2 inverter current I_{EM2} recharging the supercapacitor (green curve). By looking at Fig. 6.33 and Fig. 6.35, one can notice that the EM1 inverter current I_{EM1} is different from zero only in correspondence of those time frames where the EM1 torque τ_{EM1} is different from zero, as expected. A similar consideration can be made as far as the EM2 inverter current I_{EM2} and torque τ_{EM2} are concerned as well.

6.4 Conclusions

In this chapter, the modeling control and simulation of different Hybrid Electric Vehicles architectures of the series, parallel and power-split types are addressed. The involved physical elements are: ICE (Internal Combustion Engine), PMSMs (Permanent Magnet Synchronous Motors), supercapacitors acting as energy storage devices, planetary gear sets, and the transmission systems of the vehicles themselves from the gearbox all the way down to the vehicles wheels. The modeling of all the physical elements has been performed using the Power-Oriented Graphs modeling technique,

which allows to build block schemes that are easily and directly implementable in the Simulink environment. A solution for the energy management problem has been proposed for the different types of considered vehicles architectures, aiming at the minimization of the ICE specific fuel consumption, the charge sustaining operation of the vehicles, and the capability of satisfying the power demand from the vehicle transmission systems. The control of the ICE and of the electric machines in the considered vehicles architectures has then been described, and the effectiveness of the proposed solutions has been tested with the aid of some simulation results with reference to different driving cycles for the considered vehicles architectures.

Chapter 7

Conclusions

In this work of thesis, the mathematical modeling, control and simulation of Hybrid Electric Vehicles have been addressed. The work begins with a description of the main properties and characteristics of the main graphical formalisms BG, EMR and POG, giving particular emphasis to the POG modeling technique which is the one employed in this thesis for modeling physical systems. Next, the classification and description of the main architectures for Hybrid Electric Vehicles have been addressed, highlighting pros and cons of the different architectures. Particular emphasis has been given to the detailed modeling of three important physical elements. The first one is represented by planetary gear sets. In this case, a systematic procedure has been developed for the systematic modeling of any planetary gear set using a unified approach. Thanks to the proposed modeling approach, two system models can be obtained: a detailed full elastic model accounting for the gears elastic contact points and a reduced-order model suitable for real-time execution. For the latter, proof has been given that the tangential forces at the gears contact points can still be computed. The comparison of this method with the Lever Analogy has been addressed, and simulation results comparing the full and reduced models have been proposed with reference to a case study. Next, the modeling of multilevel flying-capacitor converters has been addressed. For the latter, a compact model has been proposed, together with a robustness assessment when the converter is controlled using a classical minimum distance control and with a new variable-step

control strategy able to guarantee capacitors voltages balancing. The effectiveness of the proposed variable-step control has been tested in simulation with reference to some case studies. The power-oriented modeling of permanent magnet synchronous motors has then been addressed, together with their efficiency analysis and with the model parameters estimation. Finally, some Hybrid Electric Vehicle architectures in the agricultural and construction fields have been modeled and proposed as case studies. A solution for the energy management problem has been studied for all these architectures, and simulation results have been reported and commented in detail.

The presented work of thesis allows to gain a deep knowledge of the dynamic behavior of some of the main physical elements present in Hybrid Electric Vehicles and in other engineering fields. The understanding of the physical element dynamic behavior is always the starting point for an engineer to develop a good and effective control strategy and to gather a full understanding of the system under consideration. For what concerns the future perspectives, the following steps are being addressed, in order to overcome the current limitations. The proposed systematic approach for modeling planetary gear sets can be extended to the modeling of any time-variant gear system with oblique rotation axes as well, and to the modeling of gear systems interacting with physical elements in other energetic domains too. The proposed variable-step control for multilevel flying-capacitor converters can be further improved in order to reduce the computational load and to carefully evaluate its real-time implementation. Furthermore, the proposed modeling approach and control algorithm can be extended to other multilevel converter topologies as well. As for the proposed efficiency analysis performed on permanent magnet synchronous motors, it can be extended to other physical systems as well, such as planetary gear sets for example, in order to also extend the field of application of the efficiency-based parameters estimation procedure. As far as the proposed HEVs energy management strategies are concerned, they can be further improved in order to further reduce the ICE consumption while also improving the driving experience. Furthermore, other new and innovative HEVs topologies can be investigated, in order to perform their accurate modeling and control to gain the maximum benefits.

Appendix A

Force vector computation: proof

Proof of Property 3: The first equation of (3.1) can be rewritten as follows:

$$\mathbf{R}^{\mathrm{T}}\mathbf{F} = \boldsymbol{\tau} - \mathbf{J}\,\dot{\boldsymbol{\omega}} - (\mathbf{B}_J + \mathbf{R}^{\mathrm{T}}\mathbf{B}_k\mathbf{R})\,\boldsymbol{\omega}. \tag{A.1}$$

When $\mathbf{K} \to \infty$, from (3.18) and (3.19) it follows: $\boldsymbol{\omega} = \mathbf{Q}_1\mathbf{x}_1$. Replacing $\boldsymbol{\omega}$ in (A.1), one obtains:

$$\mathbf{R}^{\mathrm{T}}\mathbf{F} = \underbrace{\boldsymbol{\tau} - \mathbf{J}\,\mathbf{Q}_1\dot{\mathbf{x}}_1 - \mathbf{B}_J\mathbf{Q}_1\mathbf{x}_1}_{\bar{\boldsymbol{\tau}}} - \mathbf{R}^{\mathrm{T}}\mathbf{B}_k\,\underbrace{\mathbf{R}\mathbf{Q}_1}_{\mathbf{0}}\,\mathbf{x}_1. \tag{A.2}$$

The last term of (A.2) is equal to zero because $\mathbf{R}\mathbf{Q}_1 = 0$, see (3.23). By substituting the time derivative $\dot{\mathbf{x}}_1 = \mathbf{L}_1^{-1}\mathbf{A}_1\,\mathbf{x}_1 + \mathbf{L}_1^{-1}\mathbf{B}_1\,\boldsymbol{\tau}$ obtained from the reduced system (3.21) in (A.2), one obtains:

$$\mathbf{R}^{\mathrm{T}}\mathbf{F} = (\mathbf{I} - \mathbf{J}\mathbf{Q}_1\mathbf{L}_1^{-1}\mathbf{Q}_1^{\mathrm{T}})\boldsymbol{\tau} - (\mathbf{B}_J\mathbf{Q}_1 + \mathbf{J}\mathbf{Q}_1\mathbf{L}_1^{-1}\mathbf{A}_1)\mathbf{x}_1. \tag{A.3}$$

By substituting the expressions of matrices $\mathbf{L}_1$ and $\mathbf{A}_1$ given in (3.22) within (A.3), one obtains the following relation:

$$\begin{aligned}\mathbf{R}^{\mathrm{T}}\mathbf{F} = (\mathbf{I} - \mathbf{J}\mathbf{Q}_1(\mathbf{Q}_1^{\mathrm{T}}\mathbf{J}\mathbf{Q}_1)^{-1}\mathbf{Q}_1^{\mathrm{T}})\boldsymbol{\tau} + \\ -(\mathbf{B}_J\mathbf{Q}_1 - \mathbf{J}\mathbf{Q}_1(\mathbf{Q}_1^{\mathrm{T}}\mathbf{J}\mathbf{Q}_1)^{-1}\mathbf{Q}_1^{\mathrm{T}}\mathbf{B}_J\mathbf{Q}_1)\mathbf{x}_1.\end{aligned} \tag{A.4}$$

The latter relation can be easily rewritten as follows:

$$\mathbf{R}^{\mathrm{T}}\mathbf{F} = \underbrace{(\mathbf{I} - \mathbf{J}\mathbf{Q}_1(\mathbf{Q}_1^{\mathrm{T}}\mathbf{J}\mathbf{Q}_1)^{-1}\mathbf{Q}_1^{\mathrm{T}})}_{\mathbf{M}_p}(\boldsymbol{\tau} - \mathbf{B}_J\mathbf{Q}_1\mathbf{x}_1). \tag{A.5}$$

Let functions $\mathrm{Im}(\mathbf{A})$ and $\ker(\mathbf{A})$ denote the image and the kernel of matrix $\mathbf{A}$, respectively. From linear matrix algebra, it is well known that matrix $\mathbf{M}_p$ in (A.5) is a projection matrix on $\ker(\mathbf{Q}_1^{\mathrm{T}})$ along $\mathrm{Im}(\mathbf{J}\mathbf{Q}_1)$. From (3.18) and (3.19), it follows that: $\mathbf{R}\,\boldsymbol{\omega} = \mathbf{0} \leftrightarrow \mathbf{R}\mathbf{Q}_1\mathbf{x}_1 = \mathbf{0} \leftrightarrow \mathbf{R}\mathbf{Q}_1 = \mathbf{0} \leftrightarrow \mathbf{Q}_1^{\mathrm{T}}\mathbf{R}^{\mathrm{T}} = \mathbf{0}$, which implies that $\ker(\mathbf{Q}_1^{\mathrm{T}}) = \mathrm{Im}(\mathbf{R}^{\mathrm{T}})$. Furthermore, it is true that $\mathrm{Im}(\mathbf{J}\mathbf{Q}_1) = \ker(\mathbf{S}^{\mathrm{T}})$, where $\mathbf{S}$ is a matrix such that $\mathrm{Im}(\mathbf{S}) = \ker[(\mathbf{J}\mathbf{Q}_1)^{\mathrm{T}}] = \ker(\mathbf{Q}_1^{\mathrm{T}}\mathbf{J})$. From $\mathbf{Q}_1^{\mathrm{T}}\mathbf{R}^{\mathrm{T}} = \mathbf{0}$, it follows that $\mathbf{Q}_1^{\mathrm{T}}\mathbf{J}\mathbf{J}^{-1}\mathbf{R}^{\mathrm{T}} = \mathbf{0}$, which implies that $\ker(\mathbf{Q}_1^{\mathrm{T}}\mathbf{J}) = \mathrm{Im}(\mathbf{J}^{-1}\mathbf{R}^{\mathrm{T}}) = \mathrm{Im}(\mathbf{S})$. From the previous considerations, it follows that $\mathbf{M}_p$ can be rewritten as reported in the following:

$$\mathbf{M}_p = \mathbf{R}^{\mathrm{T}}(\mathbf{S}^{\mathrm{T}}\mathbf{R}^{\mathrm{T}})^{-1}\mathbf{S}^{\mathrm{T}} = \mathbf{R}^{\mathrm{T}}(\mathbf{R}\mathbf{J}^{-1}\mathbf{R}^{\mathrm{T}})^{-1}\mathbf{R}\mathbf{J}^{-1}. \tag{A.6}$$

Substituting (A.6) in (A.5), one obtains:

$$\mathbf{R}^{\mathrm{T}}\mathbf{F} = \mathbf{R}^{\mathrm{T}}(\mathbf{R}\mathbf{J}^{-1}\mathbf{R}^{\mathrm{T}})^{-1}\mathbf{R}\mathbf{J}^{-1}(\boldsymbol{\tau} - \mathbf{B}_J\mathbf{Q}_1\mathbf{x}_1), \tag{A.7}$$

which directly implies the relation given in (3.25), since $\mathbf{R}^{\mathrm{T}}$ is a full rank matrix.

Appendix B

List of Publications

R. Zanasi, D. Tebaldi, "Planetary gear modeling using the power-oriented graphs technique", IEEE European Control Conference (ECC), Naples, Italy, Jun. 25-28, 2019.

R. Zanasi, D. Tebaldi, "Power flow efficiency of linear and nonlinear physical systems", IEEE European Control Conference (ECC), Naples, Italy, Jun. 25-28, 2019.

D. Tebaldi, R. Zanasi, "Modeling and control of a power-split hybrid propulsion system", IEEE 45th Annual Conference of the Industrial Electronics Society, Lisbon, Portugal, Oct. 14-17, 2019.

R. Zanasi, D. Tebaldi, "Study of the bidirectional efficiency of linear and nonlinear physical systems", IEEE 45th Annual Conference of the Industrial Electronics Society (IECON), Lisbon, Portugal, Oct. 14-17, 2019.

D. Tebaldi, R. Zanasi, "Modeling and simulation of a multiphase diode bridge rectifier", IEEE European Control Conference (ECC), St. Petersburg, Russia, May 12-15, 2020.

D. Tebaldi, R. Zanasi, "Instantaneous gearshift model based on gear-dependent angular momentum", IFAC World Congress, Berlin, Germany, Jul. 11-17, 2020.

D. Tebaldi, R. Morselli, R. Zanasi, "Estimation of physical parameters using a new discrete-time derivative algorithm", IFAC World Congress, Berlin, Germany, Jul. 11-17, 2020.

R. Zanasi, D. Tebaldi , "Power-oriented modeling of epicyclic gear trains", IEEE Vehicular Power and Propulsion Conference (VPPC), Gijón, Spain, Oct. 26-29, 2020.

D. Tebaldi, R. Zanasi, "Modeling control and simulation of a series hybrid propulsion system", IEEE Vehicular Power and Propulsion Conference (VPPC), Gijón, Spain, Oct. 26-29, 2020.

R. Zanasi, D. Tebaldi, "Modeling of complex planetary gear sets using power-oriented graphs", IEEE Trans. Veh. Technol., vol. 69, no. 12, pp. 14470-14483, Dec. 2020.

R. Zanasi, D. Tebaldi, "Modeling control and robustness assessment of multilevel flying-capacitor converters", Energies, vol. 14 (7), Mar. 2021.

D. Tebaldi, R. Zanasi, "Modeling control and simulation of a parallel hybrid agricultural tractor", Mediterranean Conference on Control and Automation (MED), Puglia, Italy, Jun. 22-25, 2021.

D. Tebaldi, R. Zanasi, "Modeling control and simulation of a power-split hybrid wheel loader", Mediterranean Conference on Control and Automation (MED), Puglia, Italy, Jun. 22-25, 2021.

Bibliography

[1] D. Tebaldi, R. Zanasi, "Instantaneous gearshift model based on gear-dependent angular momentum", IFAC World Congress, Berlin, Germany, Jul. 11-17, 2020.

[2] R. Zanasi, "The power-oriented graphs technique: system modeling and basic properties", IEEE Vehicle Power and Propulsion Conference (VPPC), Lille, France, Sep. 1-3, 2010.

[3] R. Zanasi, "POG modeler: the web power-oriented graphs modeling program", IFAC World Congress, Berlin, Germany, Jul. 11-17, 2020.

[4] R. Zanasi, G. H. Geitner, A. Bouscayrol, W. Lhomme, "Different energetic techniques for modelling traction drives", 9th International Conference on Modeling and Simulation of Electric Machines, Converters and Systems (ELECTRIMACS), Québec, Canada, Jun. 8-11, 2008.

[5] F. Freudenstein, A. T. Yang, "Kinematics and statics of a coupled epicyclic spur-gear train", Mechanism and Machine Throry, vol. 7, no. 2, pp. 263-275, 1972.

[6] H. L. Benford, M. B. Leising, "The level analogy: a new tool in transmission an alysis", SAE Transactions, vol. 90, no. 1, pp. 429-437, 1981.

[7] J. Liu, H. Peng, "Modeling and control of a power-split hybrid vehicle", IEEE Trans. Control Syst. Technol., vol. 16, no. 6, pp. 1242-1251, Nov. 2008.

[8] X. Zhang, C.-T. Li, D. Kum, H. Peng, "Prius$^+$ and Volt$^-$: configuration analysis of power-split hybrid vehicles with a single planetary gear", IEEE Trans. Veh. Technol., vol. 61, no. 8, pp. 3544-3552, Oct. 2012.

[9] X. Zhang, H. Peng, J. Sun, "A near-optimal power management strategy for rapid component sizing of multimode power split hybrid vehicles", IEEE Trans. Control Syst. Technol., vol. 23, no. 2, pp. 609-618, Mar. 2015.

[10] L. Yang, M. Hu, D. Qin, A. Zhou, C. Fu, M. Yu, "Analysis and optimization of a novel power-split hybrid powertrain", IEEE Trans. Veh. Technol., vol. 68, no. 11, pp. 10504-10517, Nov. 2019.

[11] J. Zhang, T. Shen, J. Kako, "Short-term optimal energy management of power-split hybrid electric vehicles under velocity tracking control", IEEE Trans. Veh. Technol., vol. 69, no. 1, pp. 182-193, Jan. 2020.

[12] R. Zanasi, D. Tebaldi, "Planetary gear modeling using the power-oriented graphs technique", IEEE European Control Conference (ECC), Naples, Italy, Jun. 25-28, 2019.

[13] R. Zanasi, D. Tebaldi, "Modeling of complex planetary gear sets using power-oriented graphs", IEEE Trans. Veh. Technol., vol. 69, no. 12, pp. 14470-14483, Dec. 2020.

[14] R. Zanasi, D. Tebaldi , "Power-oriented modeling of epicyclic gear trains", IEEE Vehicular Power and Propulsion Conference (VPPC), Gijón, Spain, Oct. 26-29, 2020.

[15] R. Zanasi, S. Cuoghi, "Model of soft-switching converter and power control of grid-connected photovoltaic systems", IECON Annual Conference of the IEEE Industrial Electronics Society, Melbourne, VIC, Australia, Nov. 7-11, 2011.

[16] H. Wu, T. Mu, H. Ge, Y. Xing, "Full-range soft-switching-isolated buck-boost converters with integrated interleaved boost converter and phase-shifted control", IEEE Trans. Power Electron., vol. 31, pp. 987-999, 2016.

[17] P. Azer, A. Emadi, "Generalized state space average model for multi-phase interleaved buck, boost and buck-boost DC-DC converters: transient, steady-state and switching dynamics", IEEE Access, vol. 8, pp. 77735-77745, 2020.

[18] R. Zanasi, S. Cuoghi, "Model of soft-switching converter and power control for smart grid applications", IEEE PES Innovative Smart Grid Technologies, Perth, WA, Australia, Nov. 13-16, 2011.

[19] A. H. Al-Badi, R. Ahshan, N. Hosseinzadeh, R. Ghorbani, E. Hossain, "Survey of smart grid concepts and technological demonstrations worldwide emphasizing on the oman perspective", Appl. Syst. Innov., vol. 3, no. 5, 2020.

[20] B. Wu, M. Narimani, "High-power converters and AC drives", Wiley-IEEE Press: Hoboken, NJ, USA, 2017.

[21] D. Tebaldi, R. Zanasi, "Modeling and simulation of a multiphase diode bridge rectifier", IEEE European Control Conference (ECC), St. Petersburg, Russia, May 12-15, 2020.

[22] M. Quraan, P. Tricoli, S. D'Arco, L. Piegari, "Efficiency assessment of modular multilevel converters for battery electric vehicles", IEEE Trans. Power Electron., vol. 3, pp. 2041-2051, 2017.

[23] J. Rodrìguez; J.-S. Lai; F. Z. Peng, "Multilevel inverters: a survey of topologies, controls, and applications", IEEE Trans. Ind. Electron., vol. 49, pp. 724-738, 2002.

[24] J. S. Rodrìguez Bernet, B. Wu, J. O. Pontt, S. Kouro, "Multilevel voltage-source-converter topologies for industrial medium-voltage drives", IEEE Trans. Ind. Electron., vol. 54, pp. 2930-2945, 2017.

[25] J. Rodrìguez, L. G. Franquelo, S. Kouro, J. I. Lèon, R. C. Portillo, M. A. M. Prats, M. A. Pèrez, "Multilevel converters: an enabling technology for high-power applications", Proc. IEEE, vol. 97, pp. 1786-1817, 2009.

[26] K. A. Corzine; J. R. Baker, "Multilevel voltage-source duty-cycle modulation: analysis and implementation", IEEE Trans. Ind. Electron., vol. 49, pp. 1009-1016, 2002.

[27] R. Zanasi, D. Tebaldi, "Modeling control and robustness assessment of multilevel flying-capacitor converters", Energies, vol. 14 (7), Mar. 2021.

[28] R. Zanasi, S. Cuoghi, "Dynamic Models of Multilevel Converters by using the Power Oriented Graph Technique", International Symposium on Power Electronics, Electrical Drives, Automation and Motion, Sorrento, Italy, Jun. 20-22, 2012.

[29] H. Tian; Y. W. Li, "Carrier-based stair edge PWM (SEPWM) for capacitor balancing in multilevel converters with floating capacitors", IEEE Trans. Ind. Appl., vol. 54, pp. 3440-3452, 2018.

[30] B. P. McGrath; D. G. Holmes, "Enhanced voltage balancing of a flying capacitor multilevel converter using phase disposition (PD) modulation", IEEE Trans. Power Electron., vol. 26, pp. 1933-1942, 2011.

[31] D.-W. Kang, B.-K. Lee, J.-H. Jeon, T.-J. Kim, D.-S. Hyun, "A symmetric carrier technique of CRPWM for voltage balance method of flying-capacitor multilevel inverter", IEEE Trans. Ind. Electron., vol. 52, pp. 879-888, 2005.

[32] X. Kou, K. A. Corzine; Y. L. Familiant, "Full binary combination schema for floating voltage source multilevel inverters", IEEE Trans. Power Electron., vol. 17, pp. 891-897, 2002.

[33] J. Huang, K. A. Corzine, "Extended operation of flying capacitor multilevel inverters", IEEE Trans. Power Electron., vol. 21, pp. 140-147, 2006.

[34] F. Grossi, "Dynamic modeling and control of hybrid automotive systems", PhD Thesis, University of Modena and Reggio Emilia, XXII Cycle.

[35] D. Tebaldi, "Modeling and control of a hybrid propulsion system for a wheel loader", Master's Degree Thesis, University of Modena and Reggio Emilia, Academic Year 2016/2017.

[36] M. Fei, R. Zanasi, F. Grossi, "Modeling of multi-phase permanent magnet synchronous motors under open-phase fault condition", IEEE International Conference on Control and Automation (ICCA), Santiago, Chile, December 19-21, 2011.

[37] R. Zanasi, F. Grossi, "Vectorial Control of Multi-phase Synchronous Motors using POG Approach", 35th Annual Conference of IEEE Industrial Electronics, Porto, Portugal, November 3-5, 2009.

[38] R. Zanasi, F. Grossi, "The pog technique for modelling multi-phase permanent magnet synchronous motors," 6th EUROSIM Congress on Modelling and Simulation, 2007.

[39] R. Zanasi, F. Grossi, "Multi-phase synchronous motors: POG modeling and optimal shaping of the rotor flux", ELECTRIMACS 2008, Québec, Canada, June 2008.

[40] D. Tebaldi, R. Morselli, R. Zanasi, "Estimation of physical parameters using a new discrete-time derivative algorithm", IFAC World Congress, Berlin, Germany, Jul. 11-17, 2020.

[41] R. Zanasi, D. Tebaldi, "Power flow efficiency of linear and nonlinear physical systems", IEEE European Control Conference (ECC), Naples, Italy, June 25-28, 2019.

[42] R. Zanasi, D. Tebaldi, "Study of the bidirectional efficiency of linear and nonlinear physical systems", IEEE 45th Annual Confer- ence of the Industrial Electronics Society (IECON), Lisbon, Portugal, Oct. 14-17, 2019.

[43] N. Jalil, N. A. Kheir, M. Salman, "A rule-based energy management strategy for a series hybrid vehicle", American Control Conference (ACC), Albuquerque, New Mexico, June, 1997.

[44] S. H. Mahyiddin, M. R. Mohamed, Z. Mustaffa, A. C. Khor, M. H. Sulaiman, H. Ahmad, S. Abdul Rahman, "Fuzzy logic energy management system of series hybrid electric vehicle", 4th IET Clean Energy and Technology Conference (CEAT), Kuala Lumpur, Malaysia, November 14-15, 2016.

[45] C. Jia, W. Qiao, L. Qu, "Modeling and control of hybrid electric vehicles: a case study for agricultural tractors", IEEE Vehicle Power and Propulsion Conference (VPPC), Chicago, IL, USA, Aug. 27-30, 2018.

[46] A. Hossein Eghbali, B. Asaei, "Efficient control strategy for reducing fuel consumption in parallel hybrid electric vehicles, based on engine and electric motor efficient operating points", IEEE Vehicle Power and Propulsion Conference (VPPC), Dearborn, MI, USA, Sep. 7-10, 2009.

[47] A. Kahrobaeian, R. Amiri, "Comparative investigation of charge-sustaining and fuzzy logic control strategies in parallel hybrid electric vehicles", IEEE Vehicle Power and Propulsion Conference (VPPC), Dearborn, MI, USA, Sep. 7-10, 2009.

[48] L. Qingkai, Z. Zhiguo, D. Haifeng, "Energy management strategy for single driveshaft parallel hybrid electric vehicle based on torque control", IEEE Vehicle Power and Propulsion Conference (VPPC), Dearborn, MI, USA, Sep. 7-10, 2009.

[49] S. A. Zulkifli, N. Saad, "Split-parallel in-wheel-motor retrofit hybrid electric vehicle", IEEE International Power Engineering and Optimization Conference (PEOCO), Melaka, Malaysia, Jun. 6-7, 2012.

[50] D. Sigmund, A. Lohner, M. Böh, "Simulation-based development of an energy-management-system for a drive train of a parallel hybrid electric vehicle", 16th International Power Electronics and Motion Control Conference and Exposition, Antalya, Turkey, Sep. 21-24, 2014.

[51] Yu-H. Cheng, Ching-M. Lai, J. Teh, "Memetic algorithm for fuel economy and low emissions parallel hybrid electric vehicles", IEEE 8th International Conference on Awareness Science and Technology (ICAST), Taichung, Taiwan, Nov. 8-10, 2017.

[52] J. Liu, H. Peng, "Control optimization for a power-split hybrid vehicle", American Control Conference (ACC), Minneapolis, Minnesota, USA, June 14-16, 2006.

[53] C. C. Lin, H. Peng, J. W. Grizzle, "A stochastic control strategy for hybrid electric vehicles", American Control Conference (ACC), Boston, MA, USA, June 30 - July 2, 2004.

[54] R. E. Bellman, Dynamic programming. Princeton, NJ, USA: Princeton Univ. Press, 1957.

[55] G. Paganelli, G. Ercole, A. Brahma, Y. Guezennec, G. Rizzoni, "General supervisory control policy for the energy optimization of charge-sustaining hybrid electric vehicles", JSAE Rev., vol. 22, no. 4, pp. 511-518, 2001.

[56] N. Kim, S. Cha, H. Peng, "Optimal control of hybrid electric vehicles based on pontryagin's minimum principle", IEEE Trans. Control Syst. Technol., vol. 19, no. 5, pp. 1279-1287, Sep. 2011.

[57] J. Wu, J. Ruan, N. Zhang, P. D. Walker, "An optimized real-time energy management strategy for the power-split hybrid electric vehicles", IEEE Trans. Veh. Technol., vol. 27, no. 3, pp. 1194-1202, May 2019.

[58] G. Buccoliero, P. G. Anselma, S. A. Bonab, G. Belingardi, A. Emadi, "A new energy management strategy for multimode power-split hybrid electric vehicles", IEEE Trans. Veh. Technol., vol. 69, no. 1, pp. 172-181.

[59] D. Tebaldi, R. Zanasi, "Modeling control and simulation of a series hybrid propulsion system", IEEE Vehicular Power and Propulsion Conference (VPPC), Gijón, Spain, Oct. 26-29, 2020.

[60] D. Tebaldi, R. Zanasi, "Modeling control and simulation of a parallel hybrid agricultural tractor", Mediterranean Conference on Control and Automation (MED), Puglia, Italy, Jun. 22-25, 2021.

[61] D. Tebaldi, R. Zanasi, "Modeling and control of a power-split hybrid propulsion system", IEEE 45th Annual Conference of the Industrial Electronics Society, Lisbon, Portugal, October 14-17, 2019.

[62] D. Tebaldi, R. Zanasi, "Modeling control and simulation of a power-split hybrid wheel loader", Mediterranean Conference on Control and Automation (MED), Puglia, Italy, Jun. 22-25, 2021.

[63] "Systemic design methodologies for electrical energy systems, analysis, synthesis and management", ISTE Willey editions, Oct. 2012, ISBN: 9781848213883.

[64] S. Lichiardopol, C. Sueur, "Duality in system analysis for bond graph models", J. Franklin Inst., vol. 347, no. 2, pp. 377-414, Mar. 2010.

[65] J. Zhao, D. Song, B. Zhu, Z. Chen, Y. Sun "Nonlinear backstepping control of electro-hydraulic brake system based on bond graph model", IEEE Access, vol. 8, pp. 19100-19112, Jan. 2020.

[66] S. Amirdehi, B. Trajin, P.-E. Vidal, J. Vally, D. Colin "Power transformer model in railway applications based on bond graph and parameter identification", IEEE Trans. Transport. Electrific., vol. 6, no. 2, pp. 774-783, Jun. 2020.

[67] K. Li, A. Bouscayrol, S. Han, S. Cui, "Comparisons of electric vehicles using modular cascade machines system and classical single drive electric machine", IEEE Trans. Veh. Technol., vol. 67, no. 1, pp. 354-361, Jan. 2018.

[68] Y. Liu, X. Gao, "Energetic macroscopic representation of self-air-cooling reciprocating compressor's cooling system", IEEE Access, vol. 8, pp. 61131-61137, Mar. 2020.

[69] B.-H. Nguy˜ên, R. German, J. Pedro F. Trovão, A. Bouscayrol "Real-time energy management of battery/supercapacitor electric vehicles based on an adaptation of pontryagin's minimum principle", IEEE Trans. Veh. Technol., vol. 68, no. 1, pp. 203-212, Jan. 2019.

[70] O. M. Govardhan, "Fundamentals and classification of hybrid electric vehicles", International Journal of Engineering and Techniques, vol. 3, no. 5, pp. 194-198, Sep.-Oct. 2017.

[71] J. M. Miller, "Hybrid electric vehicle propulsion system architectures of the e-CVT type", IEEE Trans. on Power Electronics, May. 2006.

[72] A. Zia, "A comprehensive overview on the architecture of Hybrid Electric Vehicles (HEV)", 19th International Multi-Topic Conference (INMIC), Islamabad, Pakistan, December 5-6, 2016.

[73] W. Hong-xing, K. Bao-quan, L. Li-yi, "The Research for power matching strategy of parallel hybrid vehicle", IEEE Vehicle Power and Propulsion Conference (VPPC), Harbin, China, Sep. 3-5, 2008.

[74] S. A. Syed, W. Lhomme, A. Bouscayrol, O. Pape, G. LeTrouher, "Modeling of power split device for heavy-duty vehicles", IEEE Vehicle Power and Propulsion Conference., Lille, France, Sep. 1-3, 2010.

[75] S. A. Syed, W. Lhomme, A. Bouscayrol, "Modeling of power split device with clutch for heavy-duty millitary vehicles", IEEE Vehicle Power and Propulsion Conference, Chicago, IL, USA, Sep. 6-9, 2011.

[76] W. Lhomme, A. Bouscayrol, S. A. Syed, S. Roy, F. Gailly, O. Pape, "Energy savings of a hybrid truck using a ravigneaux gear train", IEEE Trans. Veh. Technol., vol. 66, no. 10, pp. 8682-8692, Oct. 2017.

[77] Y. G. Liao, M.-Y. Chen, "Analysis of multi-speed transmission and electrically continuous variable transmission using lever analogy method for speed ratio determination", Advances in Mechanical Engineering, vol. 9(8), pp. 1-12, 2017.

[78] Q. Guo, C. Zhang, L. Li, J. Zhang, M. Wang "Maximum efficiency per torque control of permanent-magnet synchronous machines", Appl. Sci., vol. 6 (12), Dec. 2016.

[79] R. Zanasi, G. Sandoni, R. Morselli, "Simulation of variable dynamic dimension systems: The Clutch Example", European Control Conference (ECC), Porto, Portugal, Sep. 4-7, 2001.